A Geological And Geochemical Study Of The Fongo-tongo And Areally Related Bauxite Deposits, Western Highlands, Republic Of Cameroon.

Order Number 8729540

A geological and geochemical study of the Fongo-Tongo and areally related bauxite deposits, western highlands, Republic of Cameroon

Nyobe, Jean Blaise, Ph.D.

Lehigh University, 1987

U·M·I
300 N. Zeeb Rd.
Ann Arbor, MI 48106

PLEASE NOTE:

In all cases this material has been filmed in the best possible way from the available copy. Problems encountered with this document have been identified here with a check mark ✓.

1. Glossy photographs or pages ✓
2. Colored illustrations, paper or print _____
3. Photographs with dark background _____
4. Illustrations are poor copy _____
5. Pages with black marks, not original copy ✓
6. Print shows through as there is text on both sides of page _____
7. Indistinct, broken or small print on several pages ✓
8. Print exceeds margin requirements _____
9. Tightly bound copy with print lost in spine _____
10. Computer printout pages with indistinct print _____
11. Page(s) _____ lacking when material received, and not available from school or author.
12. Page(s) _____ seem to be missing in numbering only as text follows.
13. Two pages numbered _____. Text follows.
14. Curling and wrinkled pages ✓
15. Dissertation contains pages with print at a slant, filmed as received _____
16. Other _____

_____

_____

University
Microfilms
International

A GEOLOGICAL AND GEOCHEMICAL STUDY OF THE FONGO TONGO AND AREALLY RELATED BAUXITE DEPOSITS, WESTERN HIGHLANDS, REPUBLIC OF CAMEROON

by

JEAN BLAISE NYOBE

A Dissertation

Presented to the Graduate Committee

of Lehigh University

in Candidacy of the Degree of

Doctor of Philosophy

in

Geological Sciences

Lehigh University

1987

Approved and recommended for acceptance as a dissertation in partial fulfillment of the requirements for the degree of Doctor of Philosophy.

9/14/87
(date)

Charles B. Nolan
Professor in charge

Accepted 9/14/87
(date)

Special committee directing
the doctoral work of
Jean Blaise Nyobe

Charles B. Nolan
chairman

William L Greenwood

Dale R. Lange

Paul B. Myers Jr.

ACKNOWLEDGEMENTS

The author expresses his thanks to his advisor, Dr. Charles B. Sclar of Lehigh University to whom he ows his interest in economic geology, and who originally encouraged him to undertake the study of the bauxite deposits of the Cameroon Western Highlands. Dr. Sclar critically read the manuscript. The author was especially fortunate to have carried out this study at Lehigh University where he received his M. S. degree earlier. He is indebted to all the faculty of the Department of Geological Sciences at Lehigh Universiy for the guidance and assistance received throughout all these years. He expresses his thanks to the other members of his special committee, Dr. Paul B. Myers and Dr. Dale R. Simpson of Lehigh University, and Dr. William R. Greenwood of the Office of International Geology of the United States Geological Survey for their constructive advice. Dr. Sclar and Dr. Myers visited the author in the field in January, 1985.

This projet was supported by the Cameroon Institute for Geological and Mining Research (IRGM) of which the author is a staff member. To the Director of IRGM, Dr. Soba Djallo, and to the entire staff, he expresses his thanks for all the material and moral assistance he has received during the execution of this project.

The author is indebted to two of his undergraduate professors at the University of Yaounde, namely, Dr. Eno Belinga from whom he took his first bauxite geology course, and Dr. Felix Tchoua who introduced him to the Geology of the Cameroon Line in his junior year. Those introductory

courses proved useful throughout his career as a geologist and during this project. The author is also indebted to Francois Liboum of the University of Yaounde for his priceless laboratory assistance.

The study area was first visited in 1984 with Mr. John D. Fondzeyuf, a geologist of the Cameroon Ministry of Mines and Power, who had a good acquaintance with the area. The one-day field trip they had was a useful pre-requisite for the follow-up of this project. Other persons who made unpublished material available include, in addition to Mr. Fondzeyuf, Mr. Bienvenue Fouda and Mr. Djapa also of the Ministry of Mines and Power, and Mr. Morin of the University of Yaounde.

The author's sincere thanks go to Jean Nni, his colleague and field assistant during two field seasons. The many discussions they had in the field proved useful in understanding the geologic history of the study area. This work would have been impossible without the author's dedicated field drivers Nguimapi and Abdouraman Moussa, IRGM technicians Ndongue and Foue who helped prepare line drawings, Kankeu who did all the sample crushing and sieving, and E. Tanteh who made most of the thin sections.

He also thanks the staff of the Department of Geological Sciences at Lehigh University for their priceless assistance, especially Laurie Cambiotti Don Fluck and George Yasko.

The author is especially indebted to Paul Benoit, Steve Rice, and Lou Vittorio, fellow graduate students at Lehigh University, for all the help he received from them.

He acknowledges that his academic achievements at Lehigh University would probably have been less satisfactory without the

encouragement, during his first stay at Lehigh, of Dr. J. D. Ryan, former Chairman of the Department of Geological Sciences and Professor Emeritus.

Foremost, his sincerest thanks go to his wife Florence for having agreed to bear the burden of their household during his long and endless trips to the study area and to North America when this work was in progress, and to his children Annick Marie, Albert Blaise and Jacques Eithel.

TABLE OF CONTENTS

TABLE OF CONTENTS (cont.)

TABLE OF CONTENTS (cont.)

TABLE OF CONTENTS (cont.)

TABLE OF CONTENTS (cont.)

TABLE OF CONTENTS (cont.)

TABLE OF CONTENTS (cont.)

LIST OF FIGURES

LIST OF FIGURES (cont.)

LIST OF FIGURES (cont.)

LIST OF FIGURES (cont.)

LIST OF FIGURES (cont.)

LIST OF FIGURES (cont.)

LIST OF FIGURES (cont.)

LIST OF TABLES

LIST OF TABLES (cont.)

LIST OF PLATES

(in pocket)

ABSTRACT

The Fongo Tongo and areally related bauxite deposits are located on the southern flank of the Bambouto Mountains, a volcanic cone which belongs to the major NE-trending tectonic lineament known as the Cameroon Line.

The areal geology consists essentially of a thick sequence of trachytic flows, minor trachytic and phonolitic plugs and sills, ash-flow tuffs, and basaltic flows of Tertiary age which overlie the Precambrian crystalline basement. The Bambouto volcano collapsed into an 8-13 kilometer-wide crest caldera to the north of the study area. The collapse of the caldera resulted in the tilting towards the northwest of the volcanic sequence found in the study area.

Two discrete bauxitization stages were found in the area. The first one resulted in the development on top of the volcano of a saprolite cap which was largely eroded due to the collapse of the Bambouto caldera. A fraction of the resulting detrital saprolitic material accumulated downslope on trachytic flows where it forms small para-autochthonous bauxite deposits such as that at Melan. This saprolite has a relic trachytic texture with cryptocrystalline gibbsite aggregates pseudomorphous after sanidine microlites. It forms the Melan-type bauxite which is composed dominantly of gibbsite and minor to trace amounts of goethite, kaolinite, anatase, maghemite, hematite, and quartz.

Another fraction of the detrital saprolitic material was embedded as xenoliths in younger trachytic intrusives such as the Fongo Tongo dark trachyte during their emplacement. This sill together with the older volcanic flows was subsequently subjected to a second bauxitic weathering which resulted in the development of a residual lateritic bauxite or the Fongo Tongo-type bauxite which includes most of the present bauxite deposits.

The Fongo Tongo-type bauxite contains detrital clasts of saprolite. It forms a 9-11 meter-thick hardened cap or duricrust on top of gently sloping hills. Its has a colloform texture and overlies a soft mottled clay horizon which grades with depth into a whitish clayey horizon. This clayey horizon overlies the weathering front. These three horizons are characteristic of the vertical profile in the Fongo Tongo and related deposits. Local topographic conditions may result in the absence of one or the two lowermost horizons.

Mineralogical and geochemical studies of the vertical profile of the Fongo Tongo and genetically related bauxite deposits show that their duricrust is composed essentially of gibbsite, and that the other minerals are identical and present in the same proportions as those of the Melan saprolite. Silica is highly depleted whereas alumina is greatly enriched. The mottled clay horizon on the contrary shows a gradual increase with depth of kaolinite, which becomes a dominant mineral at the base of this profile, and a corresponding decrease of gibbsite. These trends reveal a breakdown with height of kaolinite in this horizon. The underlying clayey horizon is characterized by an increase with depth of the basal spacing of kaolinite which is

successively replaced by hydrated kaolinite, metahalloysite, and hydrated halloysite.

Residual profiles show manganese-oxide masses near the surface, and a residual enrichment of Ni, Cu, Pb, Co, Ti, V and P. The Mn-oxide bodies are composed of a mineral which resembles vernadite although chemical and crystallographic differences suggest that this may be a unique new mineral tentatively termed "cameroonite".

INTRODUCTION

The Fongo Tongo bauxite deposit was discovered in 1956 by the French Overseas Mining Bureau (BUMIFOM) during a bauxite exploration venture in the Cameroon Western Highlands. Between 1956 and 1958 a number of bauxite deposits of lower grade were found in the vicinity of the Fongo Tongo deposit, but no detailed study was undertaken because of the lack of interest in these bauxites.

In 1979 the Cameroon Ministry of Mines and Power launched an important bauxite exploration project in the Western Highlands in a joint venture with ALCAN International LTD. A number of potential bauxite and aluminous laterite deposits were discovered under this program, and the Fongo Tongo deposit was confirmed to be minable.

The purpose of this project was to study the origin and evolution of the Fongo Tongo and areally related bauxite deposits based on detailed geologic mapping and on mineralogical and geochemical investigations.

The study includes the geologic evolution of the southern flank of the Bambouto Mountains where these bauxite deposits are located, and the influence on bauxitization of intraplate tectonic movements associated with the Cameroon Line on which the Bambouto Mountains are located.

PHYSICAL ENVIRONMENT

LOCATION AND ACCESS

The Republic of Cameroon is located in Central Africa in the Gulf of Guinea between latitude 2°N and 12°30N and longitude 8°E and 16°E. The study area is situated in the Western Highlands of Cameroon and includes the township of Dschang (Fig. 1).

Five bauxite deposits are known in this area. The largest is the Fongo Tongo deposit which is situated about 20 kilometers northwest of Dschang. It is flanked on the west by the Fondjoumetah deposit and on the northeast by Melan, Djeu and the so-called Bambouto deposits. These latter four deposits are small and could only be mined as part of a Fongo Tongo mining project. Bauxite duricrusts have also been mapped around Djuttitsa in the course of this work, and they have been called the Djuttitsa deposit in this study.

Access to Dschang is best through the Mbo plain by a tarred road 200 kilometers long from Douala. The town can also be reached through Bafoussam. A railway 123 kilometers long links Douala to Nkongsamba, a township situated 60 kilometers south of Dschang on the Douala-Dschang road.

CLIMATE

The climatic pattern over the whole of Cameroon is essentially governed by the interaction between the maritime Saint-Helena austral anticyclone and the Saharan anticyclone (Genieux, 1958).

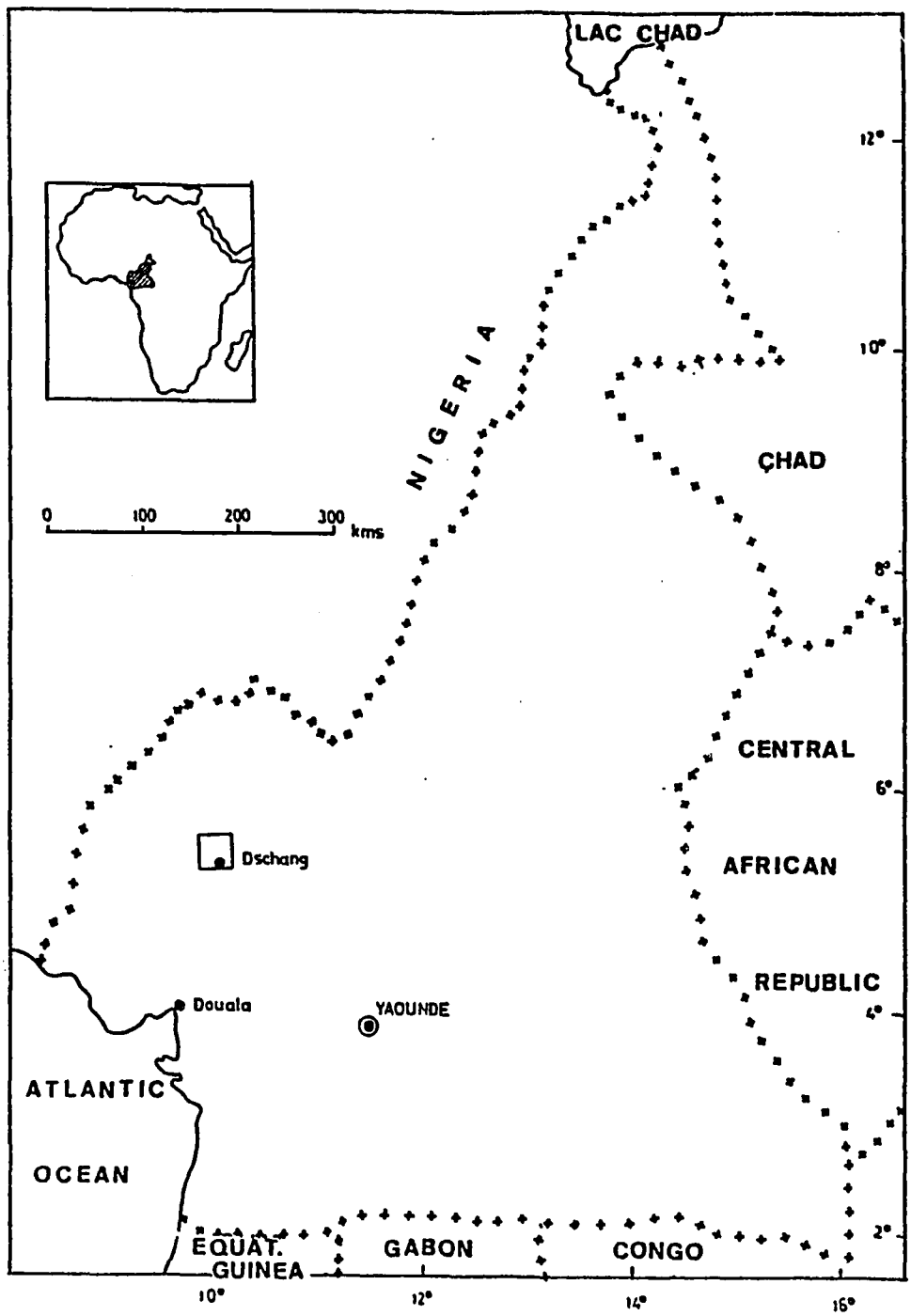

Fig. 1

Location of the study area

The Saint-Helena air mass blows northeastward from the Atlantic Ocean, and crosses the equator around July onto the African continent where it forms a very wet wind known as the Monsoon. The Saharan air mass blows southwestward across the saharan desert during dry season and is known locally as the Harmattan. It is very dry and disappears during the wet season.

The seasonal movement of the two air masses is shown in figs. 2a and 2b. The zone where they meet is known as the intertropical front (I.T.F.). The latitudinal position of the I.T.F. depends on the seasonal movement of the Saint-Helena and the Saharan anticyclones. The I.T.F. reaches its northernmost latitude of about 27°N in July, then reverses its progression between July and January and reaches its lowest latitude of about 10°N in January. Four meteorological zones are defined around the I.T.F., and their seasonal latitudes depend on the I.T.F. movements which vary considerably from year to year (Brunt and Hawkins, 1965). Zone "A", also called the Harmattan zone, is located north of the I.T.F. and has a nearly permanently clear sky. This zone theoretically never descends down to the latitude of the study area. Zone "B" is found immediately below the I.T.F. and has a relatively clear sky. It covers the study area during the dry season. Zone "C" is located south of "B" and is characterized by high humidity and cloudy skies with heavy rains. The study area is covered by this zone during the rainy season. Zone "D" is found south of "C" and has stratified clouds and less rain. This zone is constantly below the latitude of the study area.

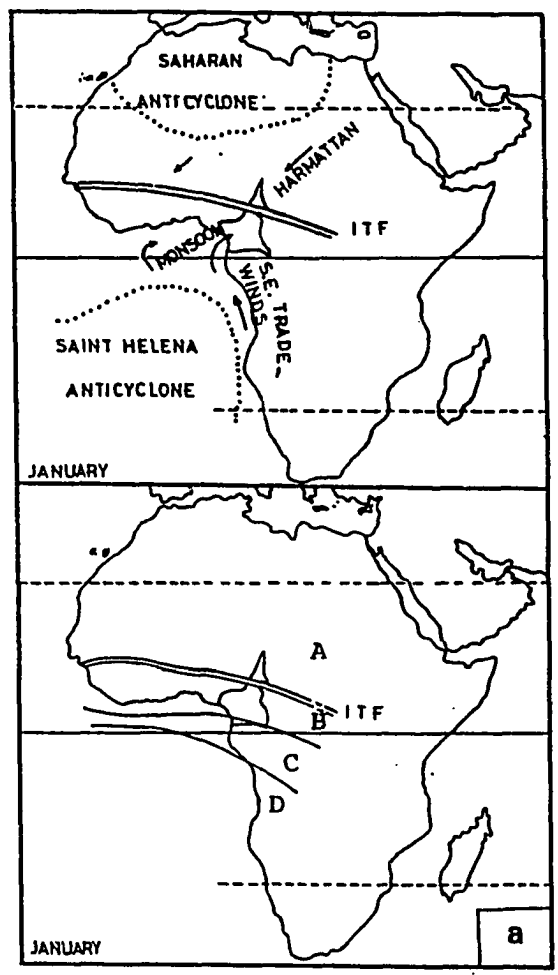

Fig. 2a
Location of the I.T.F. and
the meteorologic zones
in January

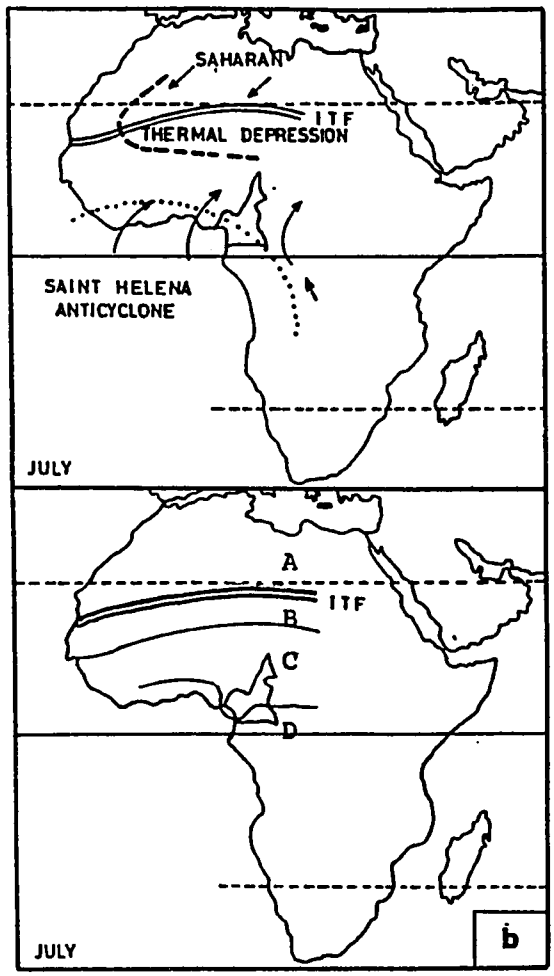

Fig. 2b
Location of the I.T.F. and
the meteorologic zones
in July

The shape of the I.T.F. and its position with respect to the Monsoon and the Harmattan are shown in a S-N cross-section through the air masses in fig. 3.

The weather is characterized locally by relatively high annual rainfall with a maximum between June and October and a minimum between December and February. Climatic characteristics can readily be assessed from the Dschang climatograph (Fig. 4). The average annual rainfall is 1,856.4 millimeters, and mean temperatures range between 19°C and 22°C.

VEGETATION

The vegetation is characterized by a savannah made up of open grass fields sometimes interspersed with eucalyptus forests. Hypparrhenia and Imperata cylindrica are the dominant grass species (Brunt and Hawkins, 1965). In lower elevations, streams are bordered with a vegetation of raphia, fern, and reed. Pennisetum purpureum, also known as elephant grass, is seasonal and grows on flooded areas in the rainy season (Brunt and Hawkins, 1965).

SOILS

The study area is partially underlain by a reddish-brown soil which develops on volcanic flows as well as on granites. There is little information available on complete residual soil profiles including the parental bedrock. Nevertheless the upper part of several profiles has

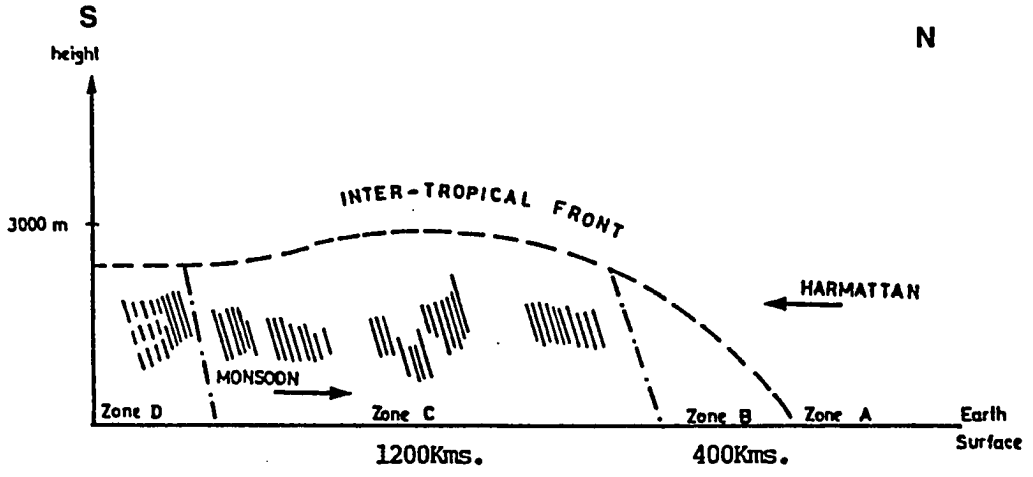

Fig. 3

S-N cross-section through the air masses across Cameroon showing the I.T.F. and its position with respect to the Harmattan and the Monsoon. Meteorologic zones are also shown. After Génieux, 1958.

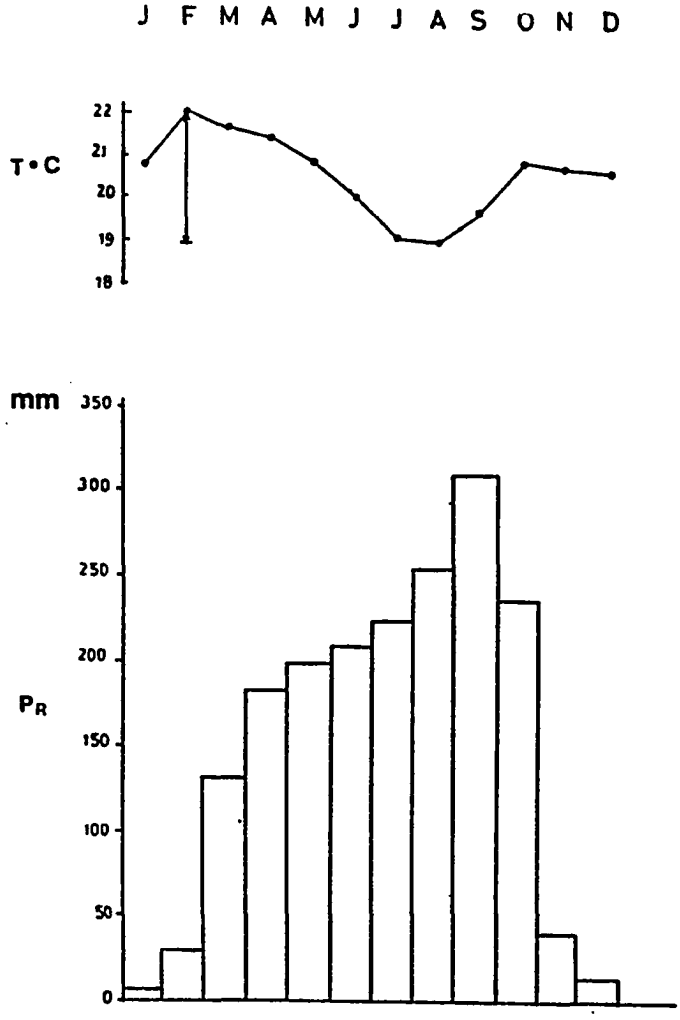

Fig. 4

Climatograph for Dschang
(1969 - 1975)

been investigated by pedologists (Mohr et al., 1972) who conclude that the soil-forming process has a podzolic tendency in the study area.

A soil profile studied at Djuttitsa (Mohr et al., 1972) is an oxisol without plinthite, a high level humic representative of an intergrade between ferrisol and ferralsol. The profile developed on a slightly convex but otherwise flat plateau underlain by basalts, at an elevation of 1,900 meters above sea level. Clay content increases with depth, and the profile seems to be a result of strong desilication accompanied by podzolic soil-forming processes (Mohr et al., 1972).

DRAINAGE

The stream flow is permanent throughout the year. It reaches its lowest volume during the dry season which extends from December to March. The longitudinal profile of streams is marked by numerous falls and rapids corresponding to lava flow-fronts.

The rivers which drain the study area belong to the Sanaga and the Cross river basins. They include, respectively, the Menoua tributaries, which flow radially from the Bambouto heights, and the Manyu river.

As far as the area of study is concerned, the overall external drainage is linear, most rivers flowing NNE-SSW or south along the southern flank of the Bambouto Mountains. A pseudo-radial drainage is nevertheless noticeable in the Fongo Tongo Mountains area.

Internal drainage in the volcanic highlands of Cameroon was studied in detail by Le Marechal (1976). According to his findings, a

siphon-shaped underground water circuit channels both descending meteoric waters and ascending waters which emerge as springs.

Within the uppermost descending part of the siphon a downward flowage of meteoric waters takes place, through the weathered profile, down to the water table which overlies the bedrock. It then continues through fractures, faults and joints within the bed rock.

A reverse ascending movement of waters takes place through deep-seated faults under the action of water vapor and CO_2-rich gases of magmatic origin (Le Marechal, 1976). These faults belong to the Cameroon Line, a major structural feature described below.

TOPOGRAPHIC SETTING

The area of study owes its topographic appearance to a series of trachytic and basaltic flows which terminate southward in abrupt cliffs (fig. 5) in which well-developed columnar jointing occur. The relief is young and the streams are still very actively down-cutting. The following two topographic units can be singled out in the area:

Unit I: from 1,200 meters to 1,600 meters

Unit II: from 1,600 meters to 2,500 meters

Unit I:

This unit includes the Dschang granites of the Precambrian basement, accumulations of ash-flow tuffs north of the granites, and basaltic flows. The unit forms a relatively flat-lying peneplain with the exception of a few small basaltic cones. The streams have reached

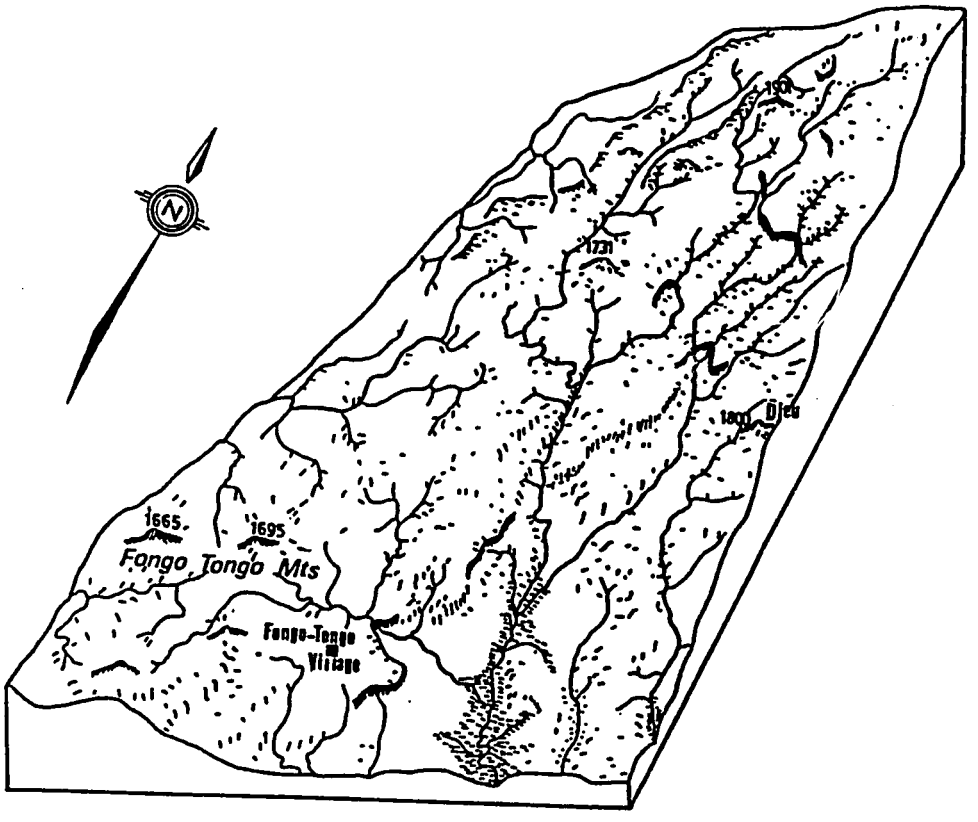

Fig. 5

BIock diagram of Fongo Tongo area
and vicinity

maturity as readily observed along the Menoua river which passes through Dschang. Limited bauxitic weathering has taken place on basaltic flows.

Unit II:

This very important unit includes all the bauxite deposits investigated in this study. It is underlain by a thick sequence of trachytic flows. The streams in the Fongo Tongo area are approaching early maturity whereas the longitudinal profile of those found in the Melan sector shows numerous waterfalls and rapids.

GEOLOGIC OUTLINE OF THE AREA OF INVESTIGATION

Geologic field investigations in Cameroon go back to the German colonial days when the first reconnaissance studies were carried out (Guillemain and Harbort, 1909; Passarge, 1910; Mann, 1913). However the first nationwide mapping program did not start until the end of the Second World War.

The national mapping program launched by France soon after the Second World War resulted in the publication of fifteen reconnaissance quadrangles on a scale of 1:500,000 between 1953 and 1971. Two reconnaissance geologic maps were also published in the nineteen fifties as part of this program by the Cameroon Department of Mines and Geology, namely, a 1:2,000,000 map (Nickles and Hourcq, 1952), and a 1:1,000,000 map (Gazel, Hourcq and Nickles, 1956). This work was part of a regional geologic mapping program covering the whole of the former French Equatorial Africa.

More recent investigations include a revision of the 1:1,000,000 geologic map by the Ministry of Mines and Power, the ongoing geologic mapping of Cameroon at 1:50,000 by the Center for Geological and Mining Research, and various unpublished reports mainly by petroleum and mining companies.

SUMMARY OF THE GEOLOGY OF CAMEROON

Over 80% of Cameroon is underlain by Precambrian granites and high-rank metamorphic rocks (fig. 6). The major geologic entities can be summarized as follows:

The Ntem Complex

The northwestern end of the Congo craton terminates in southern Cameroon (Fig. 7) where it constitutes the Ntem complex. This complex is made up of various igneous rocks, and is bordered on the north by granulites of the Nyong series. Recent U-Pb zircon age determinations in these rocks gave Archean ages of 2.85 Ga for the complex, and 2.6 Ga for the surrounding granulites (Van Schmus et al., in preparation).

The Basement Complex

This complex forms a SW-NE trending belt of granites, granodiorites, migmatites, gneisses and amphibolites. U-Pb zircon age determinations recently made in the complex at Kribi, Yaounde, and Ngaoundere consistently give a Panafrican age of 550 Ma to 650 Ma (Van Schmus et al., in preparation). The Basement complex underlies most of Cameroon.

The Intermediate Series

This group includes the low- to medium- grade Precambrian Series of Poli, Lom, Mbalmayo-Bengbis, Ayos, and Yokadouma. The stratigraphic and structural relationship between these series and the basement complex is still poorly understood. The basement complex and the lower grade intermediate series form the SW-NE trending Central African mobile belt (Rocci, 1965; Bessoles and Trompette, 1980) of Panafrican age.

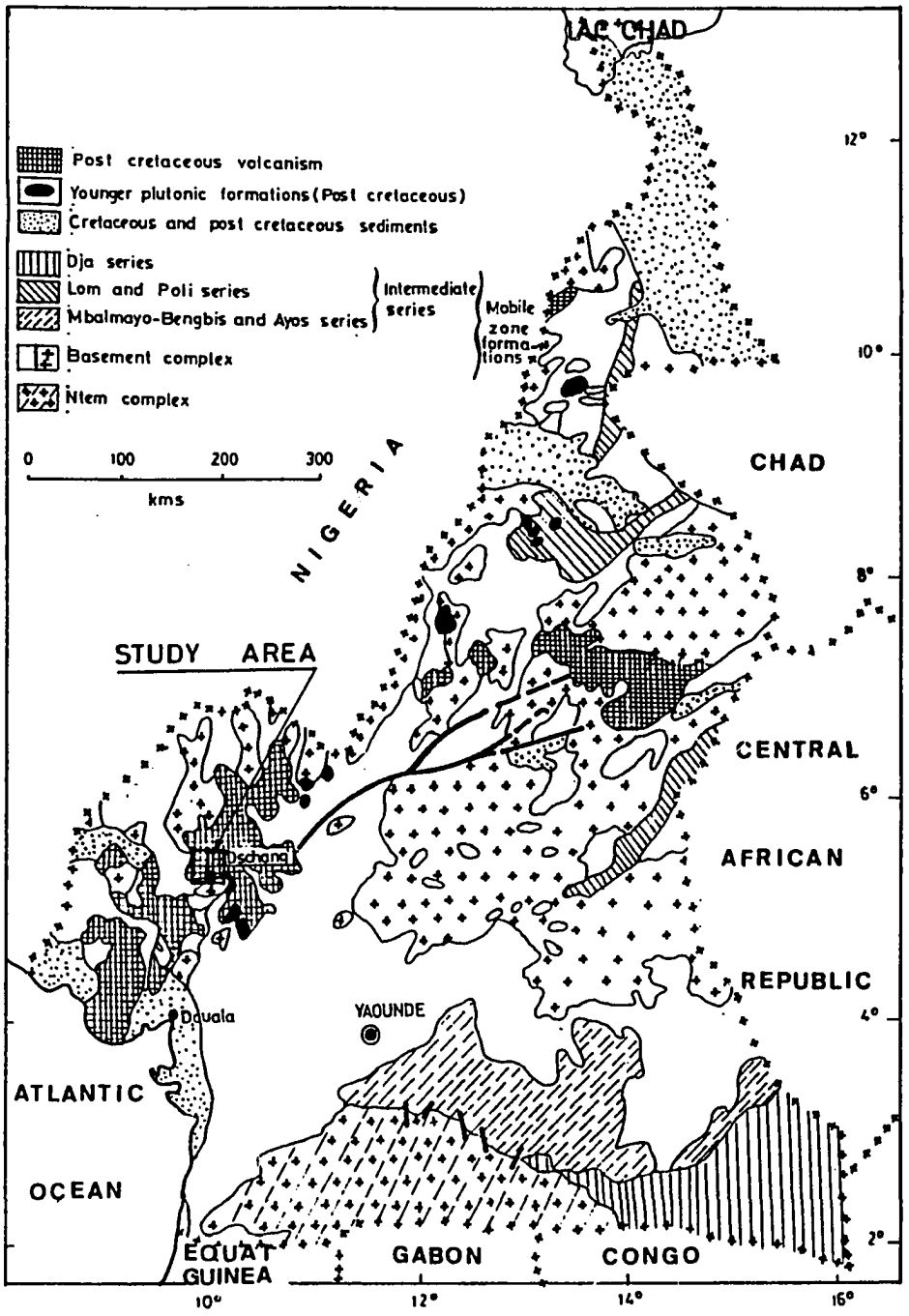

Fig. 6

Geologic map of Cameroon
(modified after Bessoles and Lasserre, 1977)

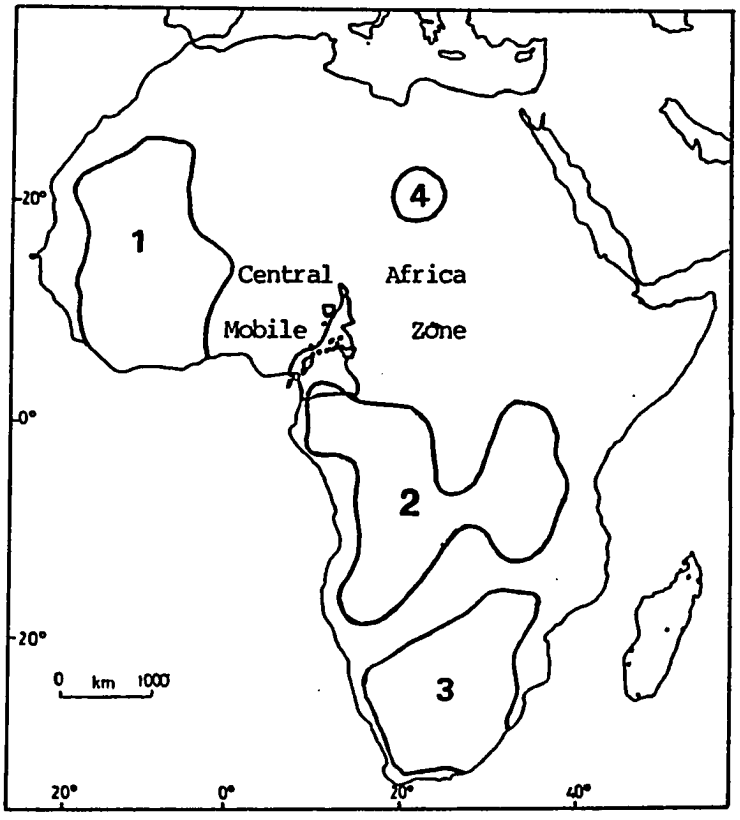

Fig. 7

Structural Units of Africa
(from EKODECK, 1984)

1 : Northwest African Craton
2 : Congo Craton
3 : Kalahari Craton
4 : Nilotic Craton

The Lower Dja Series

This series is located in the southeast corner of Cameroon and includes a tillite complex, a diabase complex and a complex of quartzites and schists known as the Bek complex. The series is Uppermost Proterozoic in age (Bessoles and Lasserre, 1977) and has a very low metamorphic grade.

The Mangbei Series

This volcano-sedimentary series is located in the northern part of the country where it overlies unconformably the basement complex and the Poli series (Nyobe, 1984). It is composed of polygenic conglomerates, basaltic, rhyolitic and trachytic volcanics, microconglomeratic and arkosic sandstones. This series is thought to be of Silurian age (Bessoles and Lasserre, 1977).

The Blanket Formations and Late Intrusions

The blanket formations include the Atlantic sedimentary basin of Cretaceous, Tertiary and Quaternary deposits, the Chad sedimentary basin which is essentially Tertiary, a number of Cretaceous continental basins such as the Benue basin, and a thick Tertiary volcanic sequence which is located along the Cameroon Line (Fig. 8).

The "late intrusions" are anorogenic and usually form small granite or syenite ring complexes of a few kilometers in diameter. These intrusions were emplaced at the close of the Cretaceous and in the Tertiary during subvolcanic activity associated with the Cameroon Line (Dunlop, 1983). Rb-Sr ages obtained from some of them range from 30 Ma for Bana to 77-74 ± 2 Ma for Namboe (Lasserre, 1978).

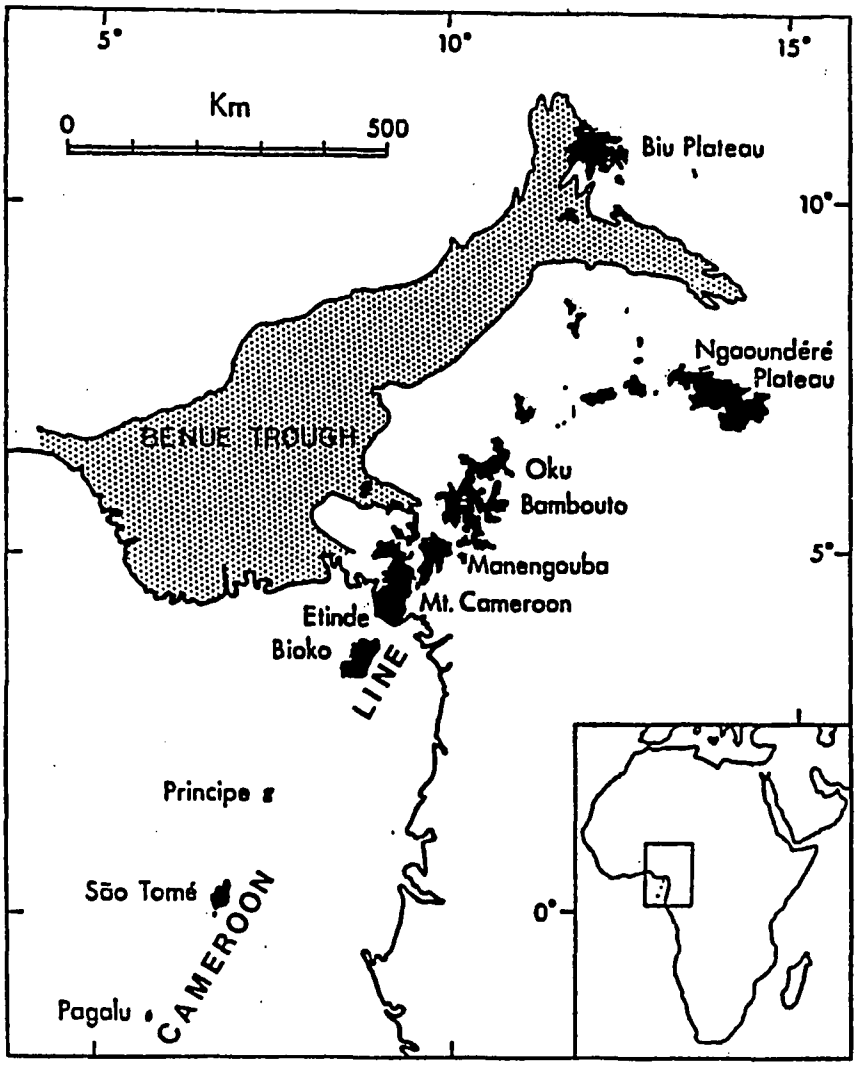

Fig. 8

Position of the Cameroon Line and the neighbouring Benue Trough. Dunlop, 1983.

GEOLOGY OF THE STUDY AREA

Nature and Origin of the Cameroon Line

The study area is located on a Tertiary-to-Recent chain of transitional to strongly alkaline (Dunlop, 1983) intraplate volcanoes 1,600 kilometers long known as the Cameroon Line (Fig. 8). This line extends from the Pagalu-Sao-Tome-Principe volcanic archipelago in the Atlantic ocean abyssal plain, through Bioko island (formerly Fernando-Po) on the continental shelf, into the continent. Dunlop (1983) has also tentatively associated the Cameroon Line with the islands of St. Helena (African plate) and/or Ascension (American plate) in the South Atlantic. On the continent, the Cameroon Line includes all the major Recent Cameroon volcanic cones such as Mt. Cameroon, Mt. Manengoumba, the Bambouto Mountains, and the Oku Massif. According to recent investigations in this area (Dunlop, 1983), the Cameroon Line splits into two branches north of Oku. One branch trends northward to the Biu Plateau in northern Nigeria and the other runs eastward to the Ngaoundere Plateau in Cameroon.

In early studies, the Cameroon Line was described as a deep-seated basement fracture of Panafrican age which trends N30°E and runs through the major Cameroon volcanic cones. This interpretation prevailed for over three decades. Fitton (1980) recently found that volcanism along the Cameroon Line does not seem to have been controlled by pre-existing basement fractures. Inasmuch as the eastern branch of the Cameroon Line runs oblique to a series of large scale basement faults, Fitton (1980) suggests that it must be the product of mantle processes unmodified by

the structure of the overlying crust, and that it cannot simply be interpreted as a deep seated fracture.

A number of plate-tectonic models have recently been proposed to explain the genesis of the Cameroon Line. These include:

(1). The model of membrane tectonics of Turcotte and Oxburgh (1973) according to which the Cameroon Line results from membrane stresses generated by the northward movement of the African plate over a non spherical earth (Freeth 1978a,b; 1979).

(2). The model of an oceanic transform which may stretch into the African continent (Hedberg, 1968; Burke, 1969; Le Pichon and Hayes, 1971; Gorini and Bryan, 1976; Wright, 1976; Mascle, 1975).

The first model, which requires peripheral extension of the African plate north of the equator in post-Eocene times as a result of a rapid northward movement, was rejected by Dunlop (1983) on the basis of evidence suggesting that the African plate has been stationary for the past 45 Ma or so. Fitton (1980) and Dunlop (1983) also rejected the second model because of the lack of correlation between the Cameroon Line and pre-existing lineaments or fractures. Instead, they propose a rapid 7° clockwise rotation of the African plate about a Sudan pole which brought the area now occupied by the Cameroon Line on top of a Y-shaped mantle plume originally overlain by the nearby Benue trough, a linear depression filled with 6,000 meters or more of Cretaceous, mainly marine sediments (Burke et al., 1972). According to Fitton (1980) this rotation took place during a relatively short period of time, between the end of tectonic activity in the Benue trough 80 Ma ago and the beginning of magmatic activity along the Cameroon Line (66 Ma). Fitton

(1980) has shown that the Cameroon Line and the Benoue trough may be superimposed perfectly by the rotation of one with respect to the other by 7° about a pole at 12.1°N, 30.2°E (Fig. 9). The identical geometry shared by the Benue trough and the Cameroon Line strongly favors this plate-tectonic interpretation of the origin of the two structures.

Geologic Setting of the Study Area

The study area has undergone regional uplift in excess of 1,000 meters (Burke et al., 1972; Black and Girod, 1970). Its geologic outline is as follows:

Basement Granites:

These rocks form a WSW-ENE trending belt of medium- grained muscovite-biotite granites and porphyritic muscovite granites with oligoclase phenocrysts.

Volcanic Rocks:

The study area covers the southern flank of the Bambouto Mountains, an elliptical volcanic cone which culminates at Mt. Meletan (2,740 meters) situated on the boundary between the former British and French Cameroons. Its long axis is parallel to the Cameroon Line, and is approximately 45-50 kilometers in length.

The area owes its present morphology to superimposed trachytic lava flows which were extruded southward from a SW-NE trending horse-shoe shaped caldera (Geze, 1943) 8-13 kilometers wide resulting in plains and cliffs underlain by a sequence of trachytic flows. According to Tchoua (1974), this caldera is made up of two calderas (the western caldera and the eastern caldera) separated by a sinous line of trachytic and phonolitic dikes and plugs. Tchoua states that trachytic volcanism

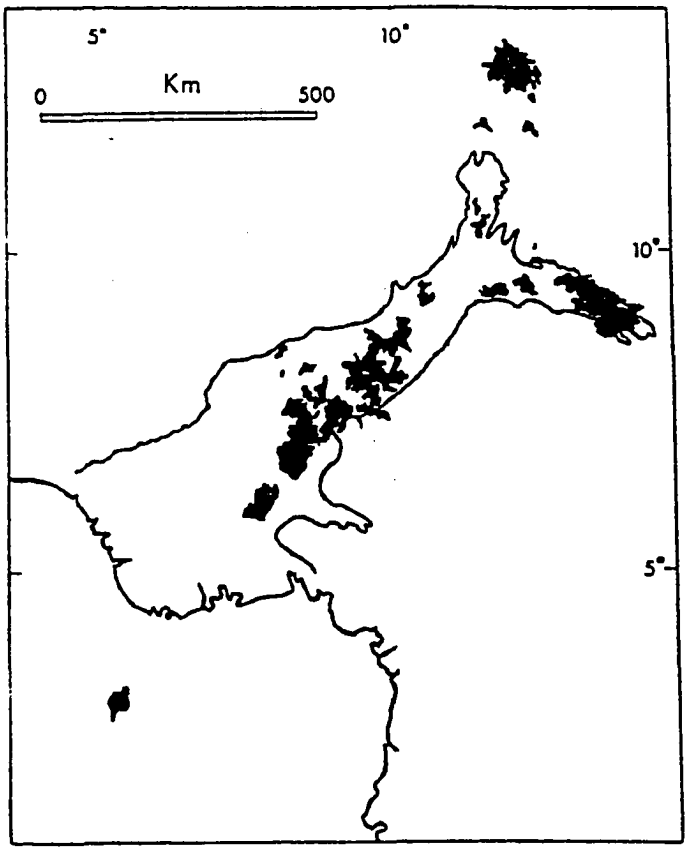

Fig. 9

The Cameroon Line superimposed on the Benue trough by rotating the former clockwise relative to the latter by 7° about a pole at 12.2°N, 30.2°E. After Fitton, 1980

took place at the site of a former basaltic shield, and that trachytic lavas flowed out through circular fractures after the collapse of the calderas, and ran along the southern flank of the mountain. Some of the flows reach a thickness of over 100 meters. They terminate in abrupt cliffs where numerous waterfalls occur.

Tchoua (1974) describes a S-N cross-section from Dschang to the heights of the Bambouto Mountains as follows:

(1). Migmatite and granite basement covered locally by ignimbrites and lignites.

(2). Aphyric and porphyritic basalts (including the shield and the plateau basalts). Trachytic dikes are found at the base of basalt flows.

(3). Trachytic cliffs sometimes underlain by volcanic tuffs.

(4). A series of flat areas made up of porhyritic basalts alternating with trachytic cliffs.

(5). Trachytic flows at the upper part of the mountain associated with minor basalt and phonolite dikes and plugs.

This cross-section has been modified on the basis of information obtained from the geologic mapping of the study area, and a different cross-section is proposed in a subsequent chapter of this document.

OBJECTIVES, METHODS, AND ANALYTICAL PROCEDURES

CONCEPT OF BAUXITIZATION AND THE BAUXITE PROBLEM IN WESTERN CAMEROON HIGHLANDS

The term "laterite" was first used nearly two centuries ago by Buchanan (1807) who defined it as "indurated clay ... without any appearance of stratification ... It is full of cavities and pores and contains a very large quantity of iron in the form of red and yellow ochres ... In the mass, while excluded from the air, it is ... soft ... It soon after becomes as hard as brick ...". Laterites develop over a wide variety of parent rocks and are extremely heterogenous in composition (Mohr, 1944). A historical review of the development of the concept of lateritization is beyond the scope of this investigation, but it is necessary to define its meaning as it is used in this study, as well as the meaning of such terms as bauxite and bauxitization.

Buchanan's original definition of laterite changed greatly over the years and today's apparent inconsistency in the literature regarding laterite and laterization is due to the fact that these words came to mean different things to geologists, pedologists, civil engineers and other soil scientists, each one of these groups having its own definition of this material according to their needs.

Laterites were defined by Schellman (1969) as "products of intense subaerial rock weathering ... They consist predominantly of mineral assemblages of goethite, hematite, aluminum hydroxides, kaolinite

minerals and quartz". Bardossy (1982) defines *lateritization* as a form of superficial weathering resulting in an increase of aluminum, titanium and iron and a decrease of alkali, alkaline earths and silica.

During an early reconnaissance of the goldfields of the Southern Appalachians of the U.S.A., Becker (1895) noticed that the weathered sequence was made up of two separate units, a lower untransported unit which retained the exact texture of the parent rock and an upper unit which showed evidence of partial transport. He proposed the term *saprolite* for the lower unit as opposed to *laterite* for the upper one. His study of the weathering profile revealed that above the saprolite, the soil was usually reworked by plant roots and had lost its characteristic parental texture.

According to most authors *bauxitization* is just a special case of lateritization which results in the development of *bauxite*, a rock characterized by high aluminum enrichment. Bardossy (1982) defines it as a geologic process which leads to the formation of a "residual or sedimentary rock in which the aggregate of the oxide and/or hydroxide minerals of aluminum, iron and titanium is greater than 50%, and aluminum minerals are more abundant than the minerals of the two other elements together".

The genetic term lateritic bauxite was proposed by Vadasz (1951) in order to emphasize the role played by lateritic weathering in the development of this type of bauxite.

The above definitions of laterite and bauxite are in accord with the conclusions drawn by various authors regarding the Cameroon Western Highlands bauxites which have consistently been described as residual

products of the weathering of volcanic rocks (Weeksteen, 1957; Hieronymus, 1971, 1972, 1980, Hieronymus and Bildgen, 1981; Porter and Bliss, 1981; Pascual, 1983).

However, many key factors regarding bauxitization in the study area have not been addressed in the studies listed above. Some of the most critical issues not yet resolved are the following:

(1). **The issue of parent rock(s)** has been given limited attention in the past, and the relationship between each deposit and its substratum has not yet been investigated.

(2). **The issue of transport** deserves careful attention inasmuch as some deposits show evidence of both autochthonous and para-autochthonous character. It is essential that an investigation of these rocks covers the role of in situ bauxitization and/or the contribution of para-autochthonous or allochthonous material, and that the provenance of transported material (if any) be studied as well as its mode of transport.

(3). **Intracontinental plate-tectonic movements** in the Tertiary in this part of Africa and their potential effect on the history of bauxitization in the study area is a highly important issue and should be considered.

All of these issues were investigated in this study by means of a comprehensive geologic study of the southern flank of the Bambouto Mountains.

STATEMENT OF PROBLEMS AND OBJECTIVES

Scientific contributions to the understanding of the geological development of Western Cameroon bauxite deposits has been rather limited ever since their discovery despite their potential economic attraction, fairly easy access to the area, and the availability of hydroelectric energy.

In an earlier report on these deposits, Weeksteen (1957) concluded that they were the product of in situ bauxitization of post-trachytic volcanics. The result of a 1:500,000 reconnaissance mapping of the area led Dumort (1968) to different conclusions. According to him, bauxitization occured on the so-called old Bambouto Mountains shield basalts which were believed to predate trachytic volcanism in the study area. A later geologic study of the area by Tchoua (1974) resulted in similar conclusions. According to these authors, bauxite developed on old basalt inliers. Hieronymus (1971, 1972) described bauxitic profiles on basalts as well as on trachytes in the Fongo Tongo area, but did not add any new data on the geology of the bauxite protoliths in the study area. In this connection, Tchoua (1974), who also described similar profiles on basalts as well as on trachytic rocks, notes that only bauxite developed on basalts shows potential economic value, and that bauxitic weathering of trachytes would normally be hampered by their high silica content.

Pascual (1983) reported the existence in the Fongo Tongo area of basaltic and trachytic lavas but gave no indication of the geologic setting and areal extent of the two types of flows. Using

geomorphologic, relic mineral, and trace elements data, he concluded that bauxitization in the Fongo Tongo area was solely due to the weathering of basaltic rocks. However, he failed to explain the process by which selective bauxitization of basalts may have taken place.

Different conclusions were reached by Fondzeyuf (1983) who showed that there was a textural relationship between the Djeu bauxite and the underlying trachytes. A similar relationship was found in the Melan-Djeu-Bambouto sector by Alcan geologists (Porter and Bliss, 1981).

As is evident from these divergent conclusions, no agreement to date has been reached concerning the geological evolution of these bauxites. In undertaking this project, the aim was to try and resolve these differences and to develop field and laboratory evidence in order to improve our understanding of the origin and evolution of each of these deposits in conjunction with the geology of the southern flank of the Bambouto Mountains. An improved understanding of the geological setting of these deposits should help in further bauxite prospecting in this part of the country.

METHODOLOGY

Geologic Mapping

One of the reasons why the various investigations on the geology of the Fongo Tongo area bauxite deposits resulted in conflicting conclusions is the lack of a detailed geologic map of the area. None of the studies mentioned above included geologic mapping of the entire area

and, as a result, the various conclusions reached can only have limited relevance to the region as a whole.

Since the publication of the "Douala Ouest" quadrangle reconnaissance geologic map at a scale of 1:500,000 (Dumort, 1968) of which this study area is a part, no other geologic mapping has been initiated in this region. Using the lithostratigraphy proposed by Geze (1943) for the volcanic formations of Western Cameroon, Dumort (1968) described two series in the Bambouto Mountains volcanic sequence, namely, a "Lower Black Series" made up of a huge basaltic flow and an overlying "Middle White Series" composed of trachytic tuffs, aphyric and porphyritic trachytes, trachy-andesites, rhyolites, and trachy-phonolites.

This stratigraphy was not in accord with field observations made during this author's first trip in the area in 1984. Contrary to the conclusions reached by previous workers, two different bauxite macrotextures were recognized. Furthermore, the geologic setting of the various deposits suggested that they did not develop from a single parent rock. In addition to this, some deposits also show evidence of para-autochthony or limited transport of bauxitic material. It then became obvious that any investigation of the origin and evolution of these bauxites had to include a comprehensive geologic study of the entire area inclusive of the basement rocks and the volcanics.

Consequently, a geologic mapping program of the southern flank of the Bambouto Mountains at a scale of 1:50,000 was carried out in this study.

Geologic Sampling

Surface geologic sampling was done on all the rock units throughout the study area. In addition to this sampling, a drilling program was set up in order to provide continous drill cores through some bauxite deposits for the study of mineralogical and geochemical trends. Five sites were chosen on the basis of accessibility as follows: two at Fotendza in the Fongo Tongo sector, one at Melan, and two at Fondjoumetah. A limited-range Louis Menard core drill was used, and a total of 43.4 meters were drilled. Nevertheless these drillings failed to reach the underlying fresh volcanics in most cases because of mechanical limitations, with one exception at the shallow Melan deposit.

Drilling was complemented by two crest pits dug at the Djeu and Melan deposits, and one flank pit dug south of the Fongo Tongo deposit. Over 250 samples were collected in three field seasons for laboratory analyses.

Analytical Procedures

Rock-sample preparation was largely done in Cameroon at the Center for Geological and Mining Research in Garoua. About 200 thin sections of rock and ore samples were made, and nearly 100 samples of fresh and weathered rocks were crushed and sieved for whole-rock analyses, x-ray diffractometry, differential thermal analyses and infrared spectrometry.

Petrographic studies were carried out in Garoua and at Lehigh University. Thin sections of friable material and polished thin sections were made at Lehigh University. X-ray diffractometry, scanning electron microscopy, electron microprobe and infrared spectrometry were also done at Lehigh.

X-ray diffractometry was done on powdered samples of bauxite, fresh volcanics, and other residual or partially weathered material for mineral identification. A Philips APD-3600 computer-assisted x-ray powder diffractometer was used. A random-orientation mounting technique was used for all the samples.

Analytical scanning electron microscopy was done on broken surfaces of bauxite and partially weathered rocks by means of an ETEC Autoscan scanning electron microscope equipped for energy dispersive (EDS) spectrometry. Some electron microprobe analysis was carried out on polished thin sections of fresh parent rocks in order to determine the chemical composition of some of the aluminum- and iron-bearing major minerals present in these rocks. Infrared spectrometry was used for the study of "cameroonite", a potential new manganese hydroxide mineral which was found in the study area during this investigation.

Twenty seven powdered samples were sent to Marseille (France) for x-ray fluorescence whole-rock analysis of major, minor and trace elements. They included surface samples of bauxite and less weathered material, as well as fresh rocks. In addition to these samples, five surface samples and twenty nine core samples from the S2 and S4 drillings were sent to X-Ray Assay Laboratories, Don Mills, Ontario, Canada, for the same purpose.

The facilities of the Department of Physical Chemistry of the University of Yaounde (Cameroon) were used for differential thermal investigations. The samples studied by DTA methods included surface bauxite samples from various locations and core samples from the S2 and S4 drillings.

GEOLOGY OF THE SOUTHERN FLANK OF THE BAMBOUTO MOUNTAINS

The southern flank of the Bambouto Mountains consists essentially of two groups of rocks: (1) the Precambrian crystalline basement made up of granites, biotite-hornblende gneisses and quartzo-feldspathic gneisses, and (2) the overlying Tertiary volcanics made up of trachytes, basalts, ash-flow tuffs and minor phonolites. In addition to these formations, a tiny continental sedimentary basin is located south of Dschang. It is partly overlain by plateau basalts.

CRYSTALLINE BASEMENT

The crystalline basement crops out in the southern half of the study area. It was peneplained during the Jurassic (Geze, 1943) into a planation surface known as the Gondwana Surface (Martin and Segalen, 1966) prior to the magmatic activity along the Cameroon Line. Outcrops are made up of dominant granites and minor biotite-hornblende gneisses and quartzo-feldspathic gneisses. The description of the various rock units is as follows:

Granites

These granites show a variety of textures and compositions ranging from a subequigranular muscovite granite to a porphyritic monzonite granite. The grain boundaries are heavily sutured and show triple junctions. The minerals are fractured.

Muscovite Granite

The muscovite granite crops out in the southeastern part of the study area, east of the plateau basalts. It is heavily weathered and mostly hidden under a thick blanket of overburden material. No fresh outcrops were found in the area. This granite is characterized by large muscovite flakes which reach 4 centimeters in diameter and equally large euhedral albite crystals. Its contact with the monzonite granite was not located.

Monzonite Granite

The monzonite granite is the dominant granitic facies. It is located in the central and western part of the study area, and is characterized by microcline and plagioclase phenocrysts 1 to 4cms in size in a medium-grained groundmass of quartz, microcline, plagioclase and biotite.

Microcline occurs as anhedral to subhedral phenocrysts and also appears in the matrix where it shows highly sutured boundaries with interstitial anhedral quartz grains. In places, it is microperthitic.

Oligoclase is the principal plagioclase. It forms subhedral phenocrysts with inclusions of quartz and biotite. It is also present in the groundmass.

Orthoclase is difficult to distinguish from untwinned microcline. It forms anhedral crystals of intermediate size and contains inclusions of quartz. Some crystals exhibit microperthitic texture.

Quartz constitutes about 25% of the rock and most often fills interstitial space between feldspar crystals. It is also found as

inclusions in feldspar phenocrysts. Quartz grains have undulatory extinction.

Biotite occurs as euhedral to subhedral crystals which show a weak preferred orientation, and in places fill W-E to WSW-ENE trending cracks in the rock with their "c" axes normal to the crack.

Green hornblende is a minor constituent.

Accessories include apatite, zircon and opaques.

Muscovite is only a minor secondary in the biotite granite in which it occurs along some feldspar grain boundaries. Other secondaries found in the monzonite granite are sericite, chlorite, and epidote which occurs as irregular patches.

Biotite-Hornblende Gneisses

The monzonite granite contains xenoliths of biotite-hornblende gneisses with alternating mafic and felsic layers. The felsic layers have a medium-grained equigranular to porphyritic texture with anhedral mesocrysts of orthoclase which contain inclusions of biotite and quartz, subhedral to anhedral crystals of oligoclase with well developed albite twins, and minor subhedral biotite. The mafic layers are subordinate and contain elongated subhedral crystals of biotite with inclusions of sphene and quartz, anhedral crystals of oligoclase-andesine, elongated quartz grains with inclusions of sphene, and minor subhedral to anhedral clusters of hornblende with inclusions of quartz.

Sphene is the major accessory, but the rock also contains zircon and opaques. Secondary chlorite is present and results from the breakdown of biotite and hornblende.

Quartzo-Feldspathic Gneisses

Quartzo-feldspathic gneisses are limited to sporadic bands within the monzonitic granite. In thin section, they have a medium-grained granular texture. The mineral components are essentially anhedral with the exception of biotite, and consist of oligoclase, perthitic microcline, greenish-brown biotite and quartz. Myrmekitic intergrowths are fairly common and consist of worm-like quartz inclusions in a plagioclase host. Traces of secondary muscovite are present along feldspar grain boundaries, cleavage planes and fractures. Zircon is the major accessory.

High grade gneisses and granites similar to those studied in Dschang have been investigated in different places in Cameroon. They form the basement complex described above and were developed during the Panafrican orogeny. The granites may have resulted from incomplete granitization of basement migmatites and gneisses. They underlie younger sedimentary and volcanic units.

SEDIMENTARY FORMATIONS

A tiny basin was mapped about three kilometers south of Dschang. It is partly capped by basaltic flows. Only the uppermost units of its volcano-sedimentary sequence were investigated during this study. They consist of greyish volcanic ash and fine-grained sand underlain by argillaceous clays.

This basin was studied by Geze (1943), Caponi (1944), Dumort (1968) and others. A complete stratigraphic section from top to bottom is as follows (Dumort, 1968):

(1). Basalt capping

(2). Sands and sandstones

(3). Argillaceous clays

(4). Argillaceous sandstones

(5). Conglomeratic tuffs

(6). Conglomeratic sandstones

Only the argillaceous clay and the sand and sandstone units were investigated during this study. Argillaceous clays reach a thickness of about 10 meters and contain minor lignite deposits (Dumort, 1968). Plant fossils occur in this basin. They were not identified during this study but are believed to be related to recent species (Tchoua, 1974). According to Tchoua, these volcano-sedimentary deposits are Cretaceous, but they were earlier correlated with the Nigerian "Lignite Group" of post Lower Eocene to Miocene age (Geze, 1943).

VOLCANIC COVER

About 60% of the study area is overlain by volcanic flows which, in turn, underlie all the bauxite deposits. One of the objectives in this mapping project was to study the lithostratigraphy of the volcanic rocks. As will be shown, this step was essential to understanding the sequence of geologic events related to the process of bauxitization in this area.

According to Tchoua (1974), the Bambouto Mountains are essentially composed of a thick ash-flow sheet covered by basaltic flows. Together they form an asymmetric shield volcano which has erupted trachytic

lavas. Late differentiation of this trachytic magma resulted in the formation of a limited volume of phonolite (Tchoua, 1974).

The southern flank of these mountains consists of superimposed trachytic flows which extend across the area of study. With the exception of the Fondjoumetah deposit which overlies ash-flow tuffs, all the bauxite deposits in the area of study are underlain by trachytes. South of the trachytic sequence lies a blanket of ash-flow tuffs which comes into contact southward with the crystalline basement. The remaining volcanic rocks consist of dikes of dark and greyish trachytes, trachytic plugs, and basaltic flows and dikes.

Ash-Flow Tuffs

These rocks were previously investigated by Tchoua (1974). According to the stratigraphy proposed by Tchoua, they form the lowermost volcanic unit in the area of study.

This unit belongs to a group of volcanic rocks known variously as ash-flows, welded tuffs, glowing avalanche deposits, incadescent tuff flows, ignimbrites, etc. This confusion of terminology seems to result from the nature of these volcanics which lend themselves so easily to differences in description and interpretation. A semantic discussion of their nomenclature and terminology is beyond the scope of this work. The choice of the term "ash-flow tuffs" as defined by Ross and Smith (1961) seemed more appropriate to the field and laboratory observations made in this study. These authors define ash-flow tuffs as "consolidated deposits of volcanic ash resulting from an ash-flow". The adjective "ash-flow" is meant to indicate the dispersal mechanism, and "tuffs" indicates the state and particle size of the material. The term is

inclusive of consolidated ash-flow beds that "may or may not be either completely or partly welded" (Ross and Smith, 1961).

The term "ignimbrite" has been more extensively used by previous investigators in the study area. It was proposed by Marshall (1935) who defined it as volcanic-derived material "deposed from immense clouds or showers of extensively heated, but generally minute fragments of volcanic magma".

No agreement has been reached so far on the geology of these ash-flow tuffs. Tchoua (1974) first observed that they rest on top of the basement, and that they are older than the trachytic sequence. Eno Belinga and Ossah (1974) reached different conclusions in the Bamenda area where they described a cliff of ash-flow tuffs underlain by trachytes. Other investigators such as Gouhier et al. (1974) contended that there were no ash-flow tuffs in the study area. Dunlop (1983) concluded that the rocks Tchoua termed "ignimbrites" or ash-flow tuffs are instead trachytes or rhyolites. He suggested the possibility of interfingering of trachytes and the so-called rhyolite flows.

The relationship between the ash-flow tuffs and the trachytic sequence is indeed complex. According to the results of this study, no direct field observation suggests that the ash-flow tuffs underly the trachytic sequence in the study area, even though this interpretation may be considered. Nevertheless, the trachytic clasts found in the groundmass of the ash-flow tuffs suggest that the ash-flow tuffs may be younger than the nearby greenish trachyte.

In addition to these trachytic clasts, the ash-flow tuffs also contain clasts of basement rocks, as well as organic matter probably

derived from the areal volcano-sedimentary Cretaceous lacustrine basins. This observation was made at many outcrops, in particular at Fondjoumetah and east of the Mamy Watta falls.

Field observations also suggest that the ash-flow tuffs are older than the greyish trachyte. This relationship is shown by the ash-flow tuffs xenoliths occasionally found in the matrix of the greyish trachyte (Fig. 10), and by an outcrop north of the Fongo Tongo market place where the ash-flow tuffs are overlain by the greyish trachyte. At that outcrop, the ash-flow tuffs are compact, highly consolidated, and have a greasy luster. Their pumice fragments are flattened horizontally as a result of compaction.

In places, the ash-flow tuffs show a layered appearance in different zones of a single unit. This pseudo-layering is apparently due to local non-uniform welding in different parts of the unit, i.e. some parts remain unconsolidated whereas others are slightly or even strongly welded (Ross and Smith, 1961). According to these authors, this pseudo-layering can be accentuated further by subsequent effects such as weathering and metamorphism.

When the ash-flow tuffs unit is not overlain by younger volcanic ones, its texture is largely uncollapsed and still retains a high percentage of pore space.

The microscope reveals that the ash-flow tuffs have a glassy matrix composed of weakly oriented fragments of elongated shards and relatively large devitrifying pumice fragments. The pumice fragments are uncollapsed in areas where compaction has not occurred. They are occasionally surrounded by a shell of devitrified glass composed of a

Fig. 10

Photograph of a xenolith of ash-flow tuff in a greyish trachyte flow

fine intergrowth of feldspar and cristobalite. In places, entire fragments of pumice have been devitrified. Crystals of quartz, plagioclase and sanidine are also present in the matrix. In addition, the tuffs contain clasts of trachyte and basement granite. Many flows were emitted as evidenced by ash-flow tuff clasts found in the matrix of younger flows. Extreme compaction, such as that found north of the Fongo Tongo market place, leads to the development of a microtexture characterized by subparallel flattened pumice fragments in a glassy groundmass of shards (Fig. 11). Other minerals present include euhedral plagioclase, quartz, and opaques.

Greenish Trachyte

This unit covers nearly 60% of the volcanic terrain and consists of a pile of superimposed greenish trachyte flows which terminate in abrupt cliffs with poorly developed columnar joints. It has well-developed flowage planar structure and shows a constant 20 to 30°NW dip with a SW-NE strike paralleling the direction of the Cameroon Line.

The rock is generally green and locally shows phenocrysts of K-feldspar in a fine-grained matrix. The K-feldspar phenocrysts range in length from a few millimeters to one centimeter.

In thin section, the microscope shows that the rock is composed of euhedral phenocrysts of sanidine in a groundmass of sanidine microlites. The sanidine phenocrysts are tabular and developed parallel to (010). In the groundmass, sanidine forms strongly aligned elongated microlites which are commonly twinned by the carlsbad law. X-ray powder diffraction (appendix 2) reveals the presence of Na in the structure of the sanidine and suggests a composition of $(Na_{0.61}K_{0.39})AlSi_3O_8$. This composition, in

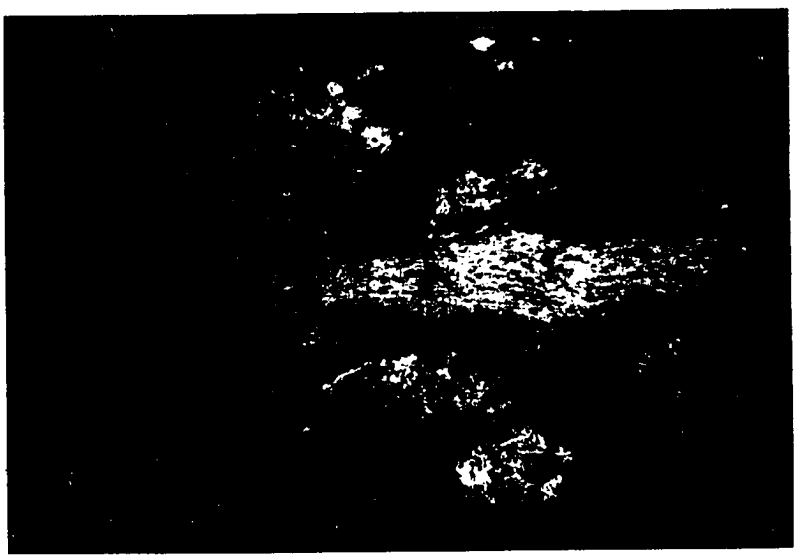

Fig. 11

Photomicrograph of ash-flow tuff
53x

the solid solution between sanidine and high albite, was confirmed by electron microprobe analysis (Table 1) which also revealed the presence in the structure of small amounts of iron and calcium. These results were verified by EDS qualitative analysis except for calcium which was not detected by this technique (fig. 12a). The composition suggested by micro-probe analysis is $(Fe_{0.03}Na_{0.56}K_{0.36}Ca_{0.05})Al_{1.1}Si_{2.9}O_8$.

In addition to sanidine, the greenish trachyte has minor pyroxene and hornblende, and traces of cristobalite, ilmenite and magnetite.

It was difficult to investigate pyroxene optically because most crystals are altered. The crystals are subhedral and are pleochroic in shades of brownish-green to brownish-yellow. According to x-ray powder diffraction and EDS qualitative analyses, it is a clinopyroxene of the aegirine-augite series which contains Mg, Ti, Mn and Fe (fig. 12b).

Green hornblende forms tiny elongated crystals which, together with chlorite, are responsible for the parting observed in these rocks. It contains Mn and Ti (fig. 12c).

Cristobalite was found to be present in trace amounts by x-ray powder diffractometry, its major peak being just above the background.

Accessories are ilmenite and magnetite. Of the two, ilmenite is the dominant. Qualitative EDS study of ilmenite grains reveals the presence of minor Mn in its structure (fig. 12d).

The greenish trachyte sequence has a northwest dip, but its dip is not related to the flowage direction which was south to southeast. It is suggested that this dip is a result of a regional uplift which may have caused the collapse of the Bambouto caldera.

Table 1

Electron microprobe analysis of sanidine crystals in the greenish trachyte. Total iron expressed as FeO.

Na_2O	3.19	4.52	5.25	4.42	5.36	6.58
MgO	0.00	0.00	0.05	0.06	0.00	0.00
Al_2O_3	20.71	21.35	22.51	20.04	20.55	19.85
SiO_2	60.99	65.64	70.81	66.01	71.73	71.50
TiO_2	0.07	0.02	0.00	0.09	0.14	0.07
FeO	0.60	0.31	0.31	7.40	0.69	1.26
K_2O	8.86	6.64	4.67	5.19	5.13	6.31
CaO	0.41	1.12	1.74	1.24	0.16	0.00
Sum	94.83	99.60	105.34	104.46	103.76	105.57

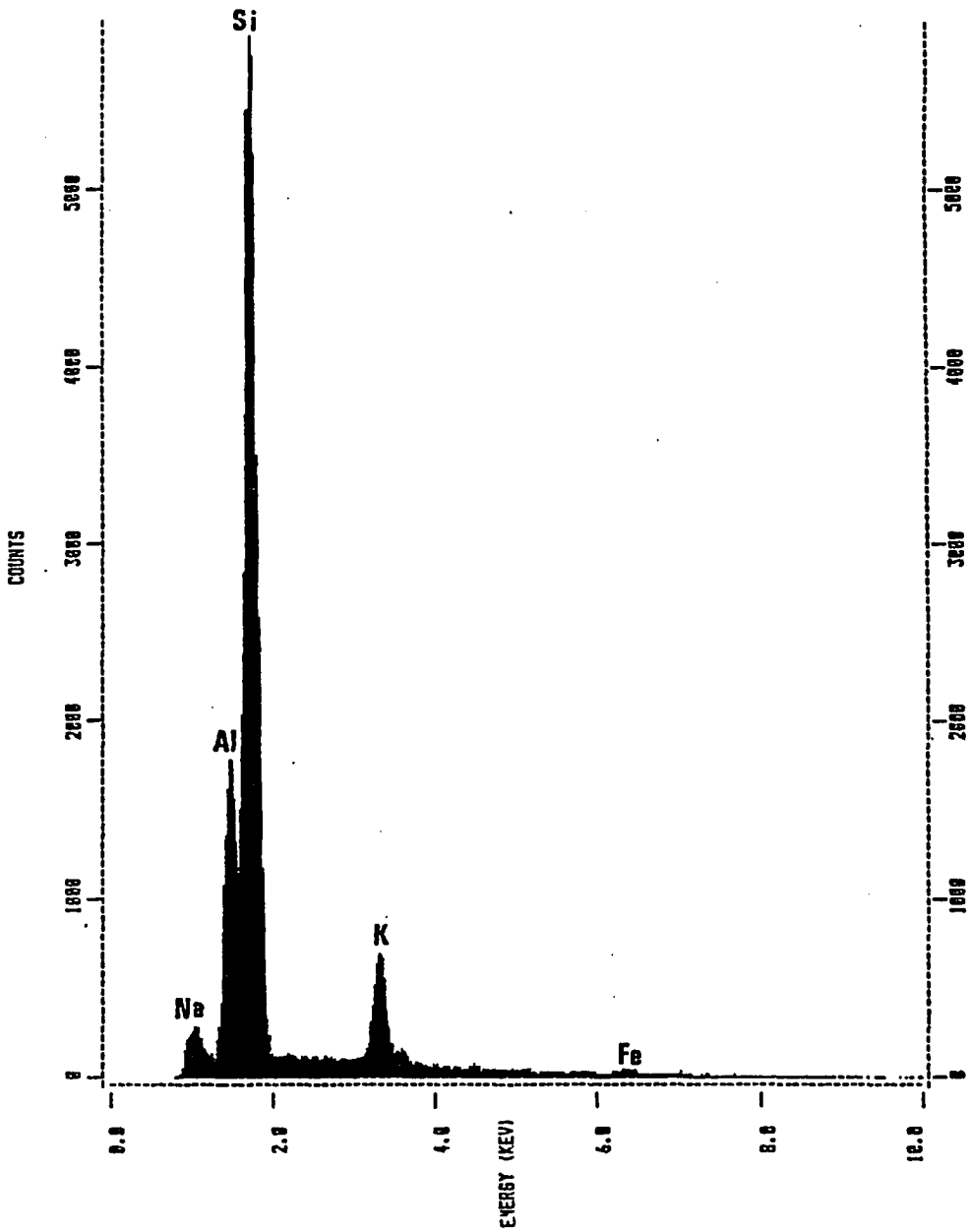

Fig. 12a

EDS spectrum of sanidine

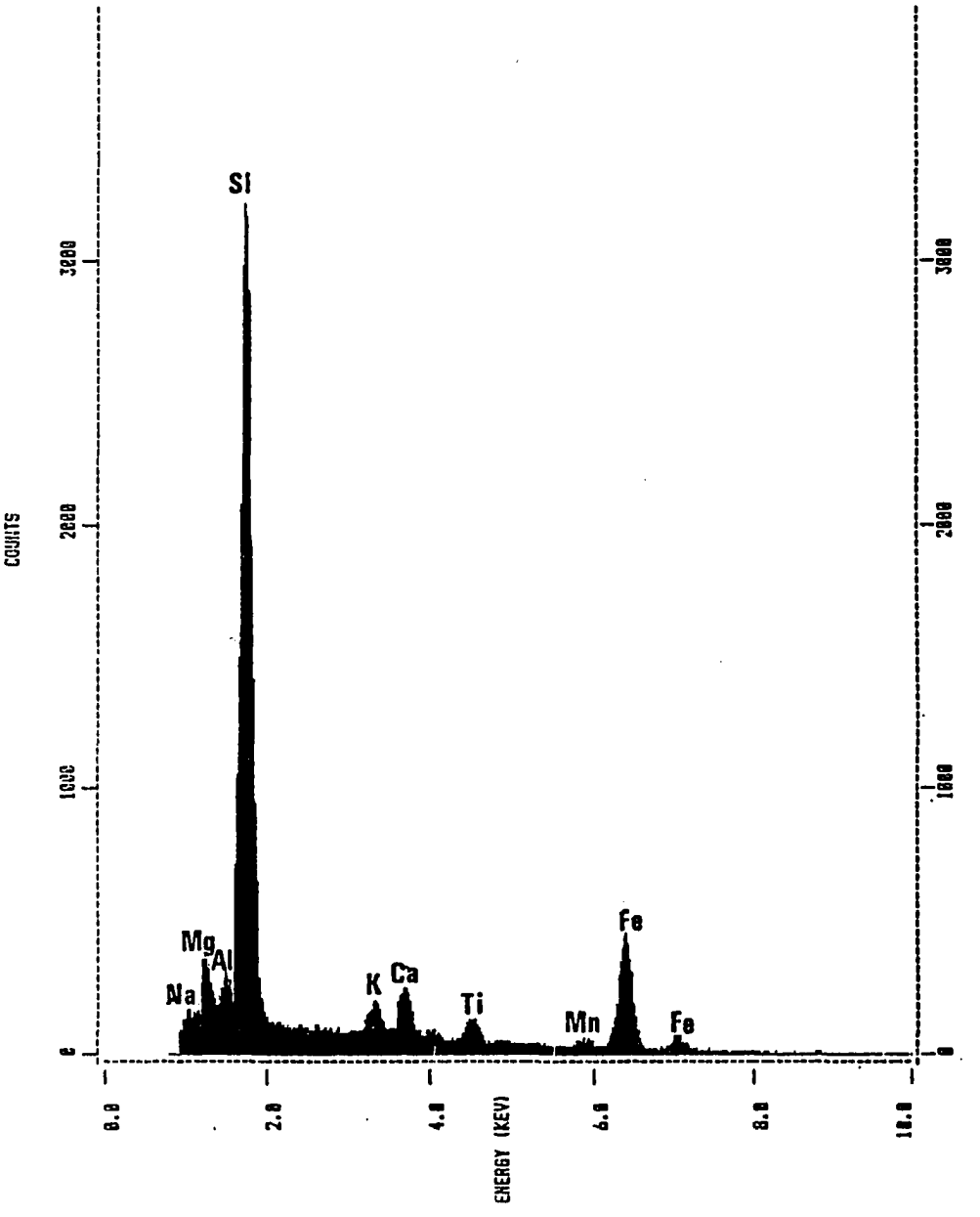

Fig. 12b

EDS spectrum of aegirine-augite

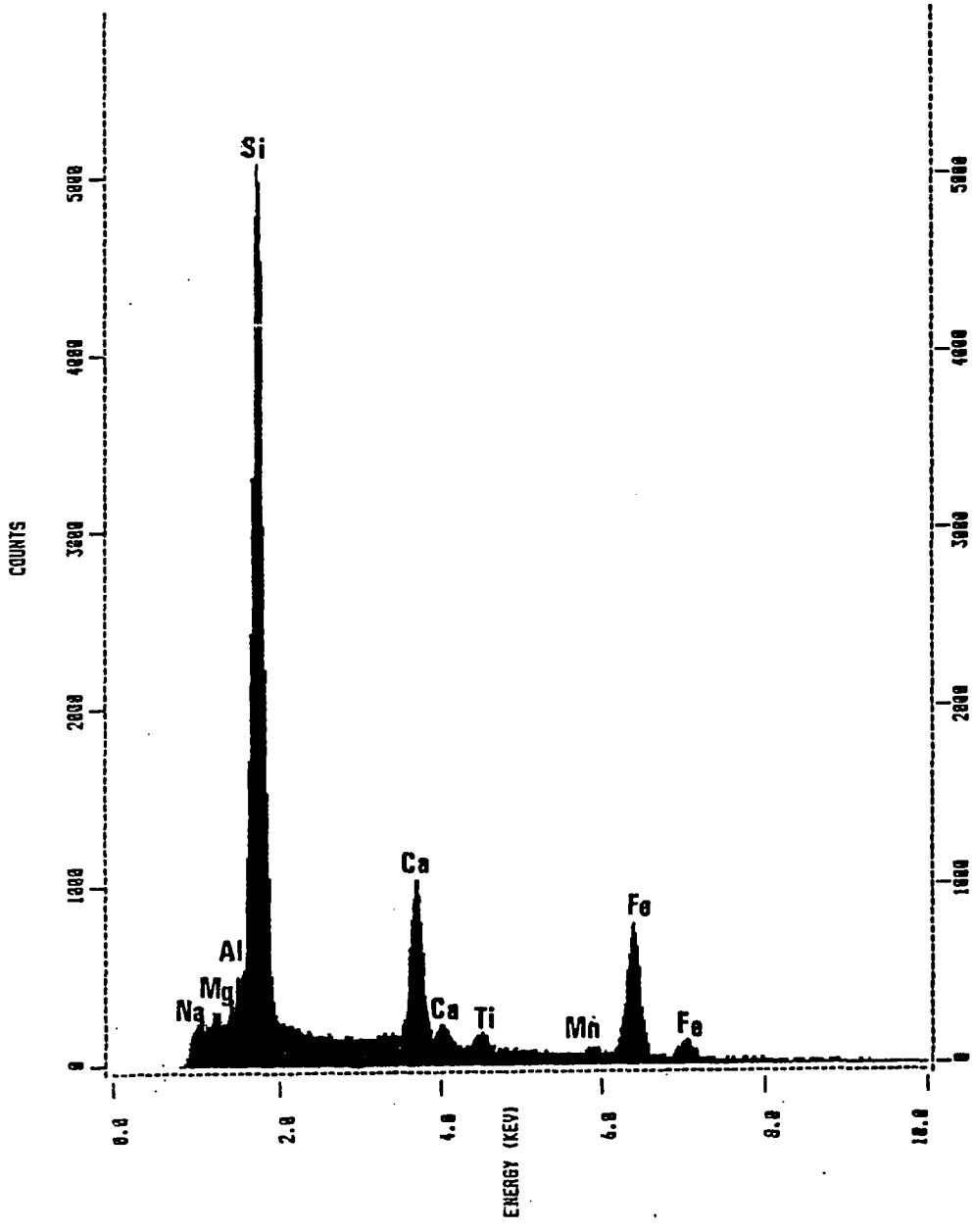

Fig. 12c

EDS spectrum of hornblende

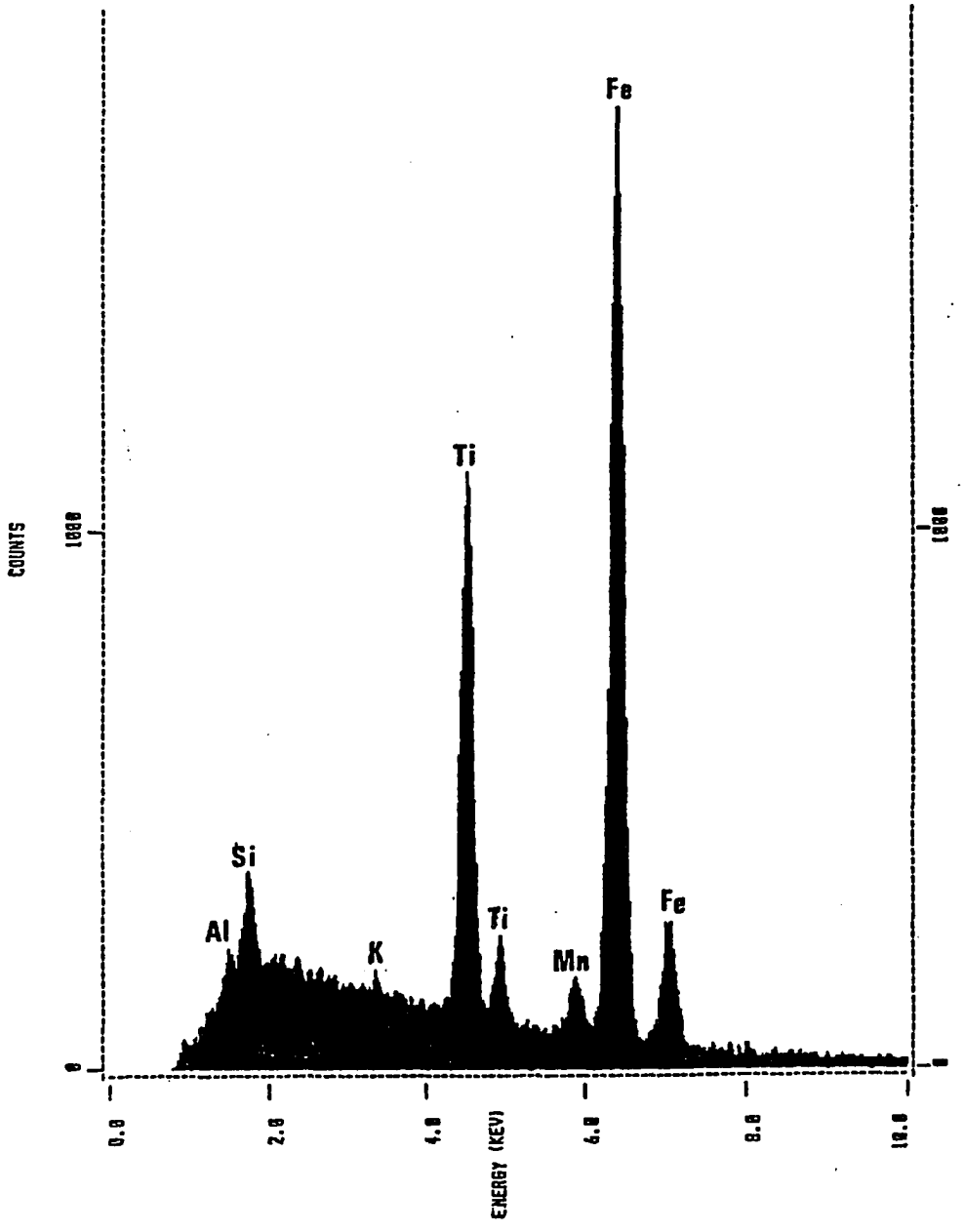

Fig. 12d

EDS spectrum of ilmenite

Greyish Trachyte

This light-grey compact trachyte crops out east of the Fongo Tongo deposit and in the northern part of the study area where it forms the "rocher rond" mountain. Most greyish trachyte bodies seem to form northeast- or northwest-trending dikes.

This trachyte contains clasts of ash-flow tuffs and basement rocks. It is generally massive, but sometimes shows flowage layering. Field relationships with the dark trachyte (see below) are difficult to see due to the lack of good contacts between the two units. The greyish trachyte develops a columnar structure. It does not underly any bauxite deposit, but incipient bauxitic weathering is displayed east of the Fongo Tongo Mountains.

The dominant texture is microcrystalline. Porphyritic texture is subordinate and marked by euhedral macroperthitic K-feldspar crystals in an aphanitic groundmass. Under the microscope, two different feldspar phenocrysts are seen, namely, an optically homogeneous sanidine and a feldspar which shows a plagioclase core with discrete albite twinning surrounded by an outer shell of K-feldspar. The groundmass consists of randomly oriented sanidine microlites, augite and actinolite. Augite also forms subhedral phenocrysts with opaque inclusions. Actinolite occurs as bluish-green bladed crystals, and probably is the result of secondary replacement of augite. Actinolite is, in turn, altered to chlorite and a deep-brown to opaque iron oxide.

Fongo Tongo Dark Trachyte

This trachyte underlies the Fongo Tongo bauxite deposit. It was also mapped west of the "Rocher rond" mountain and at the northeast

corner of the study area. Like the greyish trachyte, it seems to form a northeast-trending dike which runs from the Fongo Tongo Mountains to the northern part of the study area. The northeast trend of both the greyish trachyte dikes and the dark trachyte dikes suggests that all these dikes may belong to a major local structural feature.

In the area where bauxitic weathering has taken place, outcrops of the dark trachyte are scarce due to the thickness of the weathering profile. This study provides the first field data on the areal extent of the dark trachyte, its characterization, and its relationship with the surrounding greenish trachyte.

The dark trachyte is a compact microcrystalline rock traversed by vertical joints. A subhorizontal joint system, probably related to the thermal gradient of the lava, was also observed south of the Fongo Tongo deposit along a road cut. These well developed joints together with the morphology of the Fongo Tongo dike seem to be responsible for the high degree of weathering in this area, as they provided excellent channeling for descending meteoric water.

This rock has a glomeroporphyritic microtexture with clusters of anhedral K-feldspars in a matrix of poorly aligned sanidine microlites, epidote, chlorite, augite, ilmenite and magnetite. A network of parallel microfractures coated with secondary minerals is present throughout the rock. The K-feldspar clusters are made up of irregularly shaped and highly sutured crystals of microcline and orthoclase with undulatory extinction. Individual orthoclase crystals have a clouded nucleus surrounded by an overgrowth of clearer K-feldspar. These clusters are

considered to be xenoliths of granitic basement rocks enclosed in the lava.

The mineralogy is dominated by sanidine which constitutes over 55% of the modal composition. Its chemical composition of $Na_{0.6}K_{0.4}AlSi_3O_8$ (Hieronymus, 1980) is identical with that of sanidine from the greenish trachyte. Augite forms anhedral to subhedral greenish-yellow and non pleochroic mesocrysts with opaque inclusions. It is sometimes optically zoned, and is found as inclusions in feldspar phenocrysts.

The dark color of this trachyte is related to its higher content in augite, ilmenite and magnetite.

Basalts

The geology of these basalts was investigated in an earlier report by Tchoua (1974) who described two different basaltic lavas in the study area:

"Shield" Basalt

This porphyritic basalt was described by Tchoua (1974) west of the "Pastorale de Djuttitsa" along the Djuttitsa-Mbranka road where it is believed to underlie the greenish trachyte. This outcrop was visited and mapped. The position of this locality, which is situated at a high altitude close to the uppermost greenish trachyte flows, is not in accord with Tchoua's lithostratigraphy. It is concluded that this outcrop is most likely a dike within the greenish trachyte sequence. Furthermore the geologic map reveals that all the porphyritic basalt outcrops in the study area are northeast trending dikes of various sizes. These dikes strike parallel to the NE-trending faults which dissect the greenish trachyte sequence. The porphyritic basalt occurs,

therefore, within the greenish trachyte sequence in the form of dikes and not as flows at the base of the greenish trachyte sequence. The thermal effect normally expected on the greenish trachyte in contact with these basaltic dikes was not investigated because of the small size of most of the dikes. Nevertheless, this stratigraphic and structural relationship between the two units is supported by additional field data such as a xenolith of greenish trachyte which was found in this basalt at an outcrop located south of Djuttitsa.

Under the microscope the porphyritic basalt is made up of euhedral phenocrysts of augite, olivine and Ca-rich plagioclase in a groundmass of olivine, labrador, clinopyroxenes and opaques. Olivine crystals are intersected by a network of fractures filled with several unidentified secondary phyllosilicates. These fibrous greenish minerals are probably the result of hydrothermal alteration. Augite is usually optically zoned and contains olivine inclusions. Brown hornblende is a minor constituent.

Plateau Basalt

This dominantly aphyric basalt forms a huge blanket which covers the southern part of the study area. It also occurs in its northeast corner. Careful study of the topography reveals small volcanic cones within this unit. Three such cones appear in the southeast part of the study area. They are aligned along a 60°E trend which probably indicates a major fracture through which lavas were extruded. Columnar jointing is common in this basalt.

The plateau basalt is a microcrystalline olivine basalt composed of subparallel laths of plagioclase, euhedral olivine, and magnetite in

a much finer groundmass of feldspars, opaques, and barely resolvable ferromagnesian minerals. Zeolites fill irregularly shaped voids, and have a radial-fibrous texture.

The time relationship between the two types of basalts was not resolved during this investigation, but the aphyric basalt is considered to be younger than the porphyritic basalt (Tchoua, 1974).

Bauxitic profiles have locally developed on aphyric basalt flows in areas with low slope. One such profile is located outside the map area, about 3.5 kilometers south of Dschang.

Vesicular Basalt

In addition to the two types of basalt described above, a cone of vesicular basalt was also found in the study area, south of the "Rocher rond" mountain, on the left hand side (south) of the road which goes from Djuttitsa to Mbranka. The cone is small, and its relationship with the surrounding greenish trachyte is not yet known. This basalt is highly vesicular, altered, and contains olivine phenocrysts.

Geochronology and Stratigraphy of the Volcanic Sequence of the Southern Flank of the Bambouto Mountains

The first geochronologic study of the Bambouto volcanics was done by Geze (1943) who equated the mafic rocks in the area to his so-called "Lower Black Series" and grouped the ash-flow tuffs and all the trachytes and phonolites in the younger "Middle White Series". A more complex picture was proposed by Tchoua (1974) who described a complete stratigraphic profile of these volcanics starting from the ash-flow tuffs which rest on top of the Precambrian basement. Ash-flow tuffs are overlain by basalts. Overlying these basalts are thick piles of

trachytic flows. The sequence given by Tchoua (1974) based on his study terminates with minor trachytic and phonolitic plugs located in the vicinity of the caldera.

A revised geochronology and stratigraphy of the study area is proposed in this study on the basis of available data and field observations made in this study.

According to a recent geochronologic study (Dunlop, 1983), the oldest volcanic unit in the area is trachytic and has an age between 22.00 ± 1.24 Ma and 23.44 ± 1.58 Ma. Ash-flow tuffs, which Dunlop calls rhyolites, have a younger age of 18.34 Ma to 18.75 ± 0.38 Ma. A second series of trachytes dated by Dunlop has an age span of 15.26 ± 0.40 Ma to 16.40 ± 0.38 Ma. The fourth volcanic unit he reports includes basaltic rocks which have an age of 13.84 ± 0.38 to 14.33 ± 0.31 Ma.

Despite the fact that Dunlop did not characterize petrographically the trachytic units that he dated, there seem to be a match between his data and the results of this study: His oldest volcanic unit presumably corresponds to the greenish trachyte sequence whereas his second series of trachytic rocks presumably corresponds to the greyish and the dark trachytes. The two series of trachytes are separated in time by ash-flow tuffs as shown by this study and Dunlop's data. This volcanism was followed by the extrusion of basaltic dikes and flows. Volcanic activity in the area was terminated by the intrusion of phonolites which have a K/Ar age of 10.58 Ma (Tchoua, 1974).

A NNW-SSE cross-section through the study area is shown in fig. 13a. It runs from the southern edge of the caldera to the plateau basalts east of Dschang, and displays a volcanic sequence tilted

Fig. 13a

NNW-SSE cross-section through the southern flank of the Bambouto Mountains

J. B. Nyobe, 1987

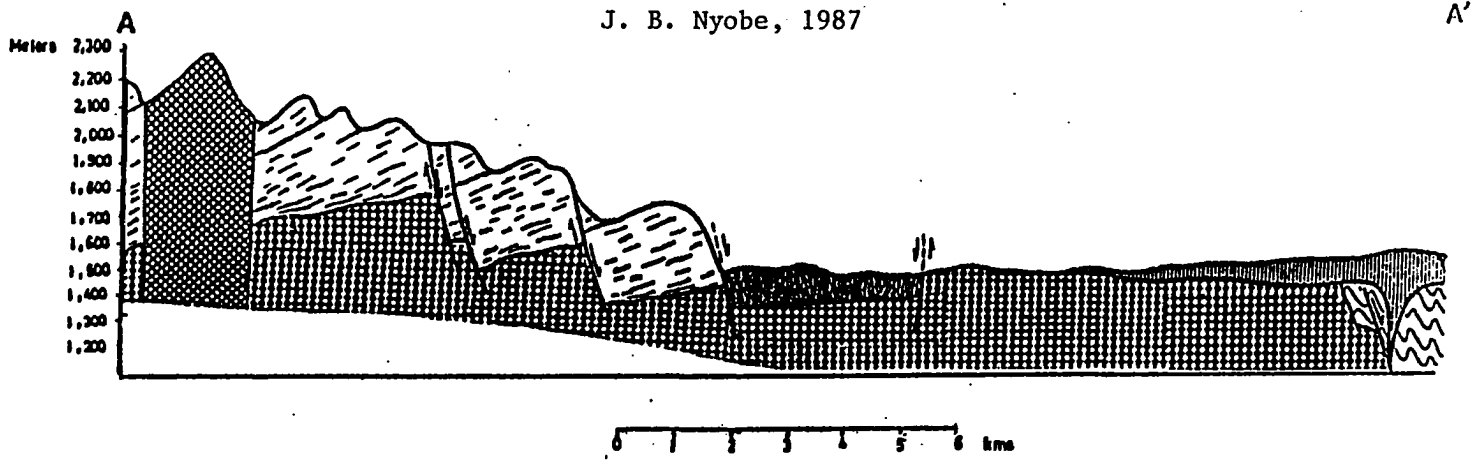

$$\text{Ratio: } \frac{\text{Vertical scale}}{\text{Horizontal scale}} = 5.3$$

Legend

- Greenish trachyte
- Dark trachyte
- Ash-Flow tuffs
- Basalts
- Granites
- Migmatites

Fig. 13b

NW-SE cross-section across the
Fongo Tongo deposit
(J. B. Nyobe, 1987)

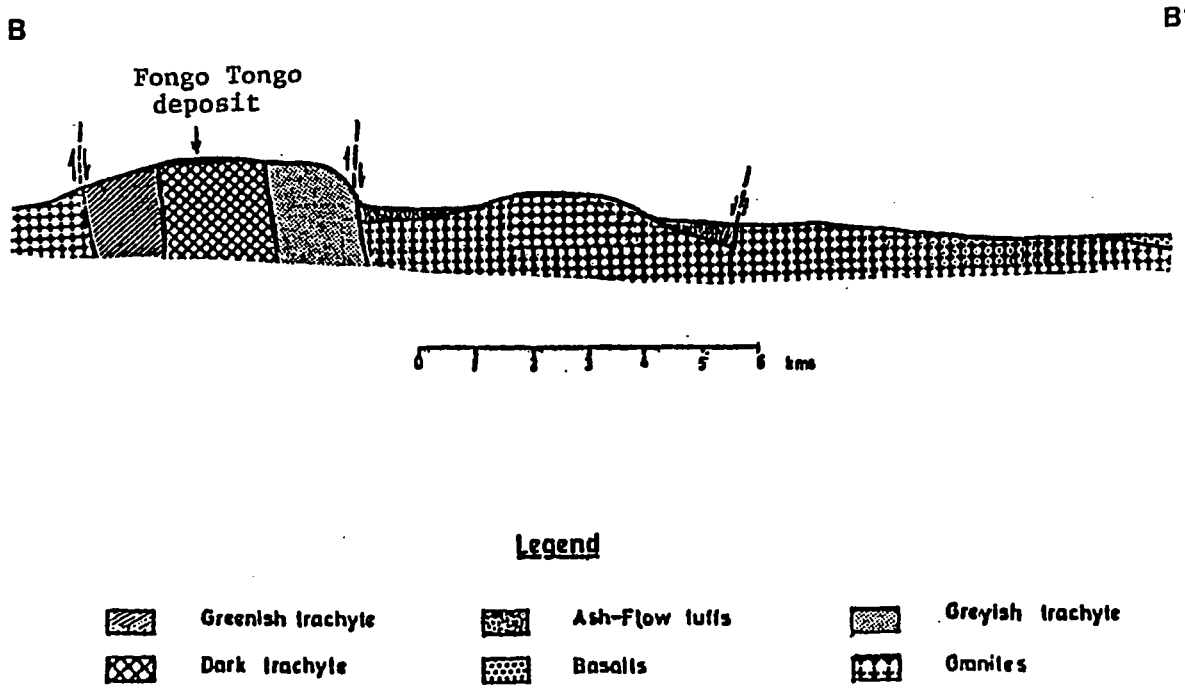

northwestward. This sequence overlies Precambrian granites and is made up of greenish trachyte flows which are cut by a dark trachyte dike. The plateau basalts are considered to have been poured out through deep seated faults. The NW-SE cross-section shown in Fig. 13b shows both the dark trachyte and the greyish trachyte and their relationship with the surrounding greenish trachyte. Different stratigraphic interpretations may be given to the field data obtained during this study. The ash-flow tuffs could for example underly the volcanic sequence as proposed by Tchoua (1974), but additional field data in support of this interpretation are still to be found.

Despite the apparent agreement between the geochronologic data and the field results of this study, a number of uncertainties still exist on many key issues such as the nature of Dunlop's rhyolites and trachytes. It is recommended that new K-Ar ages be obtained on geologically and petrographically well-characterized samples.

GEOCHEMISTRY AND PETROLOGY OF THE SOUTHERN FLANK OF THE BAMBOUTO MOUNTAINS

Twenty samples of volcanic rocks were analysed for all major elements and 10 trace elements, and CIPW norms were calculated on an anhydrous basis. In addition, sixteen analyses of volcanic rocks from the study area reported by Tchoua (1974) were added to these data. All of these analyses are given in appendix 1. The chemistry of the volcanic rocks is included in this study in order to facilitate correlation between the various bauxite deposits and the country rocks.

The flows are composed essentially of silica-saturated peraluminous trachytic rocks and ash-flow tuffs and metaluminous to peraluminous basalts.

GEOCHEMISTRY OF SALIC ROCKS

These rocks are silica saturated. Ash-flow tuffs have the highest mean silica content of 69.2 wt%, whereas trachytes range between 66.44 and 60.42 wt% SiO_2. TiO_2 is low and only averages 0.60 wt% in the two rock types. Ash-flow tuffs contain <0.30 wt% of MgO and their CaO content is only in the range of 0.2 wt%. Trachytes contain <1.1 wt% of MgO. CaO averages 0.29 wt% in the greenish and greyish trachytes and 2.44 wt% in the dark trachyte. Mean alkali values in the salic rocks are

5.89 wt% for Na_2O and 5.05 wt% for K_2O. Total iron (FeO + Fe_2O_3) averages 7.48 wt% in the Fongo Tongo trachyte and 5.58 wt% in the other trachytes and the ash-flow tuffs.

All of these rocks contain normative hypersthene which, in some samples, exceeds 10.0 wt%. The amount of normative quartz (up to 74.88%) obtained in the various ash-flow tuffs suggests that they have rhyolitic and trachytic components. As for the quartz-trachytes, they range in composition from minor miaskitic to dominant agpatic trachytes (Tchoua, 1974). The areally minor phonolites in this group were not studied during this investigation. Unlike the trachytes and ash-flow tuffs, they are nepheline-normative (Tchoua, 1974).

GEOCHEMISTRY OF MAFIC ROCKS

The basaltic rocks are undersaturated with respect to silica which averages 43.52 wt%, and are nepheline-normative. Titania is higher than in the salic rocks and ranges between 2.95 and 4.15 wt%. MgO and CaO are also relatively high with respective values of 8.15 and 8.9 wt%. Na_2O and K_2O are, on the other hand, comparatively low and only average 3.18 and 1.58 wt% respectively. Total iron (FeO + Fe_2O_3) is high with a mean value of 12.14 wt%. It is nearly 1.5 times the amount of iron reported in the Fongo Tongo trachyte, and is twice as high as that of the other salic rocks.

These rocks are free of normative quartz. Their chemical analyses give normative nepheline and olivine in average proportions of 6.92 and 17.44 respectively.

IGNEOUS PETROLOGY OF THE STUDY AREA

The data reported in the preceeding sections of this study suggest that the geology of the areal volcanics consists essentially of two rock suites, a mafic suite characterized by undersaturated nepheline-normative olivine basalts, and a felsic suite made up of hypersthene-normative oversaturated trachytes and ash-flow tuffs. Also reported in the area are nepheline-normative phonolites.

Chemical variation within the volcanic rocks of the study area is shown in fig. 14 which is a rectangular plot of the sum of the weight percents of normative (or + ab + ne) reported on the abscissa against Na_2O, K_2O, MgO, CaO and total Fe. Basaltic rocks essentially plot towards the low values of or + ab + ne, whereas felsic rocks show a much higher salic component index. The nearly continous trends obtained are partly consistent with a fractional crystallization model, but the plots show a gap which reflects a difference in chemistry between the salic rocks and their mafic counterparts. A plot of total iron, magnesia and soda + potash on the triangular diagram FeO - MgO - $Na_2O + K_2O$ (Fig. 15) also suggests that these rocks underwent fractional crystallization, but fails to explain the gap which exists between the two rock suites. Moreover CIPW norms obtained on the various samples do not favor this

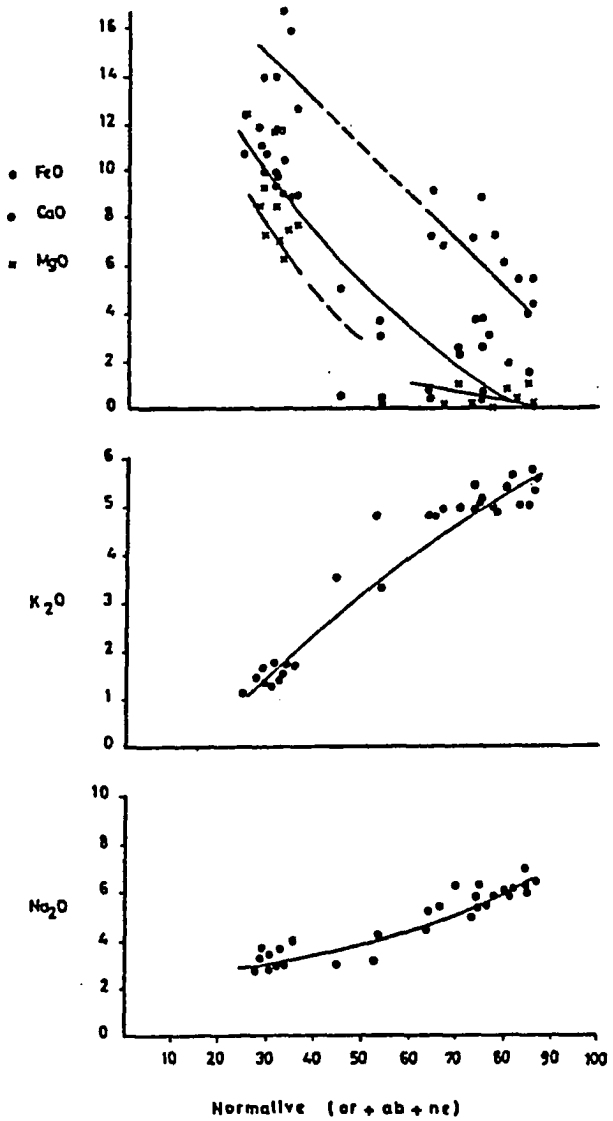

Fig. 14

Chemical variation in the lavas of the Bambouto Mountains Southern flank (Total iron plotted as FeO)

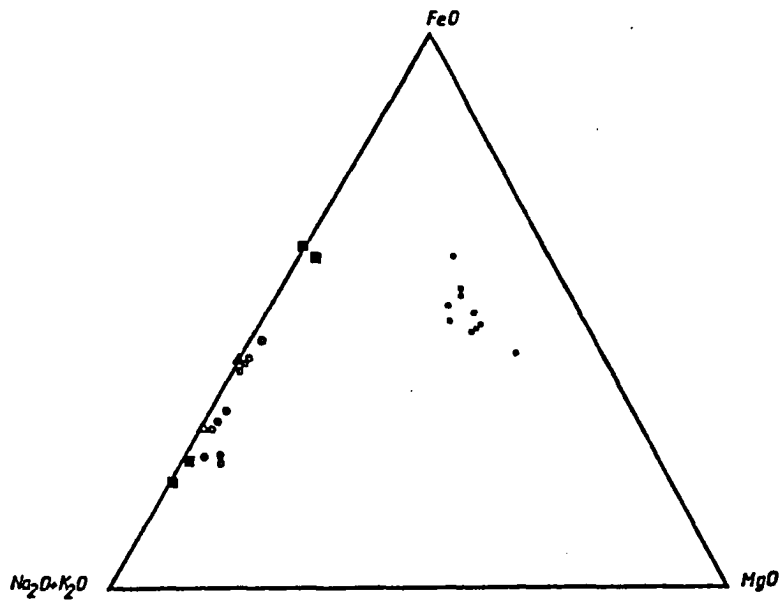

Fig. 15

- • Basalts
- o Trachytes
- ■ Ash-flow Tuffs
- △ Rhyolitic Ash-flow Tuffs

(Total iron plotted as FeO)

Triangular variation diagram for alkali, iron and magnesium in the lavas of the Bambouto Mountains southern flank.

model in the production of trachytes and related rocks from the areal mafics.

Although some crystal fractionation is suggested by the chemical data, an additional geologic process must have prevailed during the formation of silica-saturated magma. Dunlop (1983) suggested that the trachytes result from combined low-pressure fractionation of the mafic rocks and their contamination by radiogenic crustal material before or during fractionation in a crustal magma chamber. Dunlop also stated that ash-flow tuffs resulted from the fusion of crustal material.

Indeed, the absence in the study area of volcanic rocks of intermediate composition suggests that fractionation products were contaminated by a significant volume of crustal material during the evolution of the trachytic magma. This may be the reason why all the trachytes are hypersthene-normative as are the ash-flow tuffs which are also believed to originate by partial fusion of crustal rocks (Dunlop, 1983). Chemical data reveal the existence of two kinds of ash-flow tuffs, namely a trachytic ash-flow tuff which is chemically close to trachyte, and a rhyolitic ash-flow tuff which may have developed by partial fusion of crustal material solely under the action of radiogenic heat. The areally limited nepheline-normative phonolites, on the other hand, may have been derived from olivine basalts through fractional crystallization without any contamination (Dunlop, 1983).

The conclusions reached by Tchoua (1974), which are generally in accord with those of this report, led him to suggest the existence of two different magmas in this area, namely, a mantle-derived basaltic magma and a trachytic magma which was formed in the crust by partial

fusion. Nevertheless, in accord with Dunlop (1983), it is concluded that there is only one truly original magma in the study area, namely, the basaltic magma, that the trachytic magma should be regarded as a product of combined crystal fractionation and crustal contamination, and that crystal fractionation evolved to phonolites where contamination was minimized.

CONCLUSIONS ON THE GEOLOGY OF THE SOUTHERN FLANK OF THE BAMBOUTO MOUNTAINS

The bauxite deposits of the Cameroon Western Highlands are located on the southern flank of the Bambouto Mountains, a volcanic cone made up of a pile of trachytic flows, ash-flow tuffs, and basaltic rocks which developed from continental volcanic activity associated with the Cameroon Line. Crustal uplift reportedly reached 1,000 meters or more along this structural line (Burke et al., 1972; Black and Girod, 1970).

Volcanism along the Cameroon Line may have been activated by a branch of the same Y-shaped hot zone which initiated the opening of the South Atlantic ocean (Fitton, 1980). The Cameroon Line lineaments were perhaps controlled by a mantle plume, and not by reactivated Panafrican faults as previously thought (Gazel, 1958). According to Dunlop (1983), the only significant Panafrican crustal effect imposed on the Cameroon Line volcanism may be the combination of extreme fractionation and crustal contamination which resulted in the formation of trachytes and ash-flow tuffs.

The Bambouto Mountains form an elliptical cone with its long axis parallel to the Cameroon Line. Trachytes are the dominant rocks in the study area and form superimposed lava flows which terminate in cliffs. The study area also has ash-flow tuffs, basaltic flows and dikes, and phonolite plugs. The central part of the volcano has collapsed into a

horse-shoe shaped crest caldera where trachytic and phonolitic plugs occur.

The geology of the study area is made up of a Precambrian crystalline granitic basement of Panafrican age (about 550 to 650 Ma) which is overlain by the following Miocene volcanic units:

(1). A quartz-normative unit of ash-flow tuffs which underlies the Fondjoumetah deposit. It also borders the southern limit of the greenish trachyte sequence.

(2). A thick unit of greenish trachyte flows covers nearly 40% of the study area and represents about 60% of the volcanic suite. It consists of superimposed flows which terminate abruptly in major cliffs with poorly developed columnar joints. Chemical analyses of this trachyte give a quartz-normative composition. This trachytic unit forms the oldest volcanic sequence in this area.

The greenish trachyte unit underlies a number of small bauxite deposits such as Melan, Djeu, Bambouto and Djuttitsa. More detailed mapping of this unit may reveal additional small bauxitic deposits.

(3). Quartz-normative greyish trachyte and dark trachyte dikes and plugs are found in the area of study. No bauxitic profile has been found on any of the greyish trachyte intrusions. The dark trachyte in the Fongo Tongo area was subjected to intense bauxitic weathering.

The age relationship between the greyish trachyte and the dark trachyte was not investigated during this study

(4). A blanket of an aphyric plateau basalt covers the southern part of the study area and its northeast corner. Dikes of a porphyritic basalt are also found within the greenish trachyte unit. They follow NE

trending fractures which can be traced across the entire area. All of these basaltic rocks have similar chemical compositions (Appendix 1) and seem to be younger than their trachytic counterparts according to field observations and the few available absolute-age data. All of the basalts are undersaturated nepheline- and olivine-normative, higher than the felsic rocks in total iron, lime, magnesia and titania, and lower than the felsic rocks in silica and total alkali. Minor bauxite bodies have been found south of Dschang directly on the plateau basalt. Additional absolute age determinations on the two basalts are needed for a better correlation with the other areal volcanic units. A cone of a vesicular olivine-basalt was mapped in the northern part of the study area. Its relationship with the porphyritic basalt and the aphyric basalt is not yet known.

Field data suggest that the northwest tilt of the greenish trachyte sequence is most likely due to the faulting of the underlying granitic basement along the northeast trend, and the rotation to the northwest of the resulting granitic blocs. This crustal disturbance may have resulted in the collapse of the Bambouto caldera. The magma chamber apparently collapsed along a SW-NE axis. Magmatic activity continued after the collapse of the caldera with the emplacement of trachytic dikes and plugs.

MORPHOLOGICAL FEATURES OF WEATHERING IN THE STUDY AREA

The thickness of the weathering zone is variable and decreases with increase in slope. It reaches a maximum in the Fongo Tongo and Fondjoumetah deposits.

A characteristic weathering profile has been observed south of the Fongo Tongo deposit along a road cut (fig. 16). Here, the weathering front of the dark trachyte is overlain by a relatively thick layer of soft greyish-white friable material. The thickness of this layer may reach 1.0 meter or more. It has a sharp contact with the overlying laterite and appears to be the first weathering product of the dark trachyte.

Sheeting has been observed in granitic terrain, as well as concentric weathering which is characterized by rounded blocks of rock rimmed by concentric layers of weathering product. The inner layers are tough, whereas the outer ones are friable.

In the volcanic terrain, weathering seems to proceed from the fractures bounding the polygonal columns towards the center of individual columns. The resulting boulders are progressively rounded by the spalling off of a series of concentric shells of rock. According to Leet et al. (1978), this spalling off is due to the chemical breakdown and hydration of primary minerals, with the resulting secondary minerals occupying a greater volume. It is this increase in volume that creates the stress responsible for concentric weathering.

Fig. 16

Photograph of a weathering profile of the dark trachyte along a road cut south of the Fongo Tongo deposit.

1.0 meter

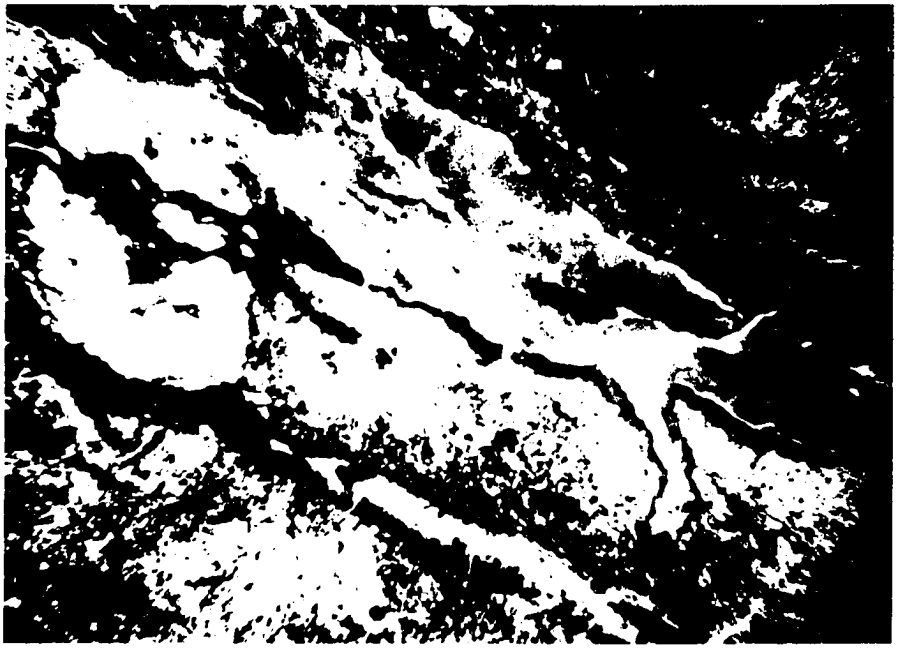

Fig. 17

Photomicrograph of incompletely weathered dark trachyte from the Fongo Tongo Mountains
44.5x

Microscopic examination of a moderately weathered trachyte from the Fongo Tongo Mountains also reveals that weathering proceeds along fractures, mineral cleavages and grain boundaries which serve as channels through which ground water moves, and along which hematite, colloidal goethite and gibbsite veinlets develop (fig. 17). The absence of kaolinite at this site is attributed to an extremely good movement of ground water which has resulted in a complete removal of silica from the weathered area.

GEOLOGIC SETTING OF THE BAUXITE DEPOSITS

Bauxite occurs in the study area at relatively high elevations, within the range of 1,400 meters to 2,000 meters, on a variety of volcanic rocks. The deposits are nevertheless restricted to a few gently convex hills with maximum gradients of about 5°.

THE FONGO TONGO DEPOSIT

This deposit rests on top of the Fongo Tongo dark trachyte within a fairly narrow elevation range of 1600 meters to 1700 meters. It forms a NE trending narrow strip 5 kilometers long made up of a number of discontinous hard caps. The core of the deposit has been narrowed considerably by downslope transport and, as a result, is partly surrounded by an apron of loose bauxitic material which reaches a thickness of 11.0 meters or more at Fotendza. Fig. 18 is a map of the Fongo Tongo deposit showing the various bauxite caps and the prospection trench dug by the BRGM in 1959. This deposit has long been known to be the most economically attractive of the deposits in the study area (Gazel, 1957). This statement was confirmed by Lorer (1980) who calculated a total of 34 x 10^6 recoverable washed tons of ore based on a reconnaissance evaluation of the deposit.

Two bore holes were drilled in this deposit, the first one, S1, at Fotendza village (Fig. 18), along the eastern flank of the deposit

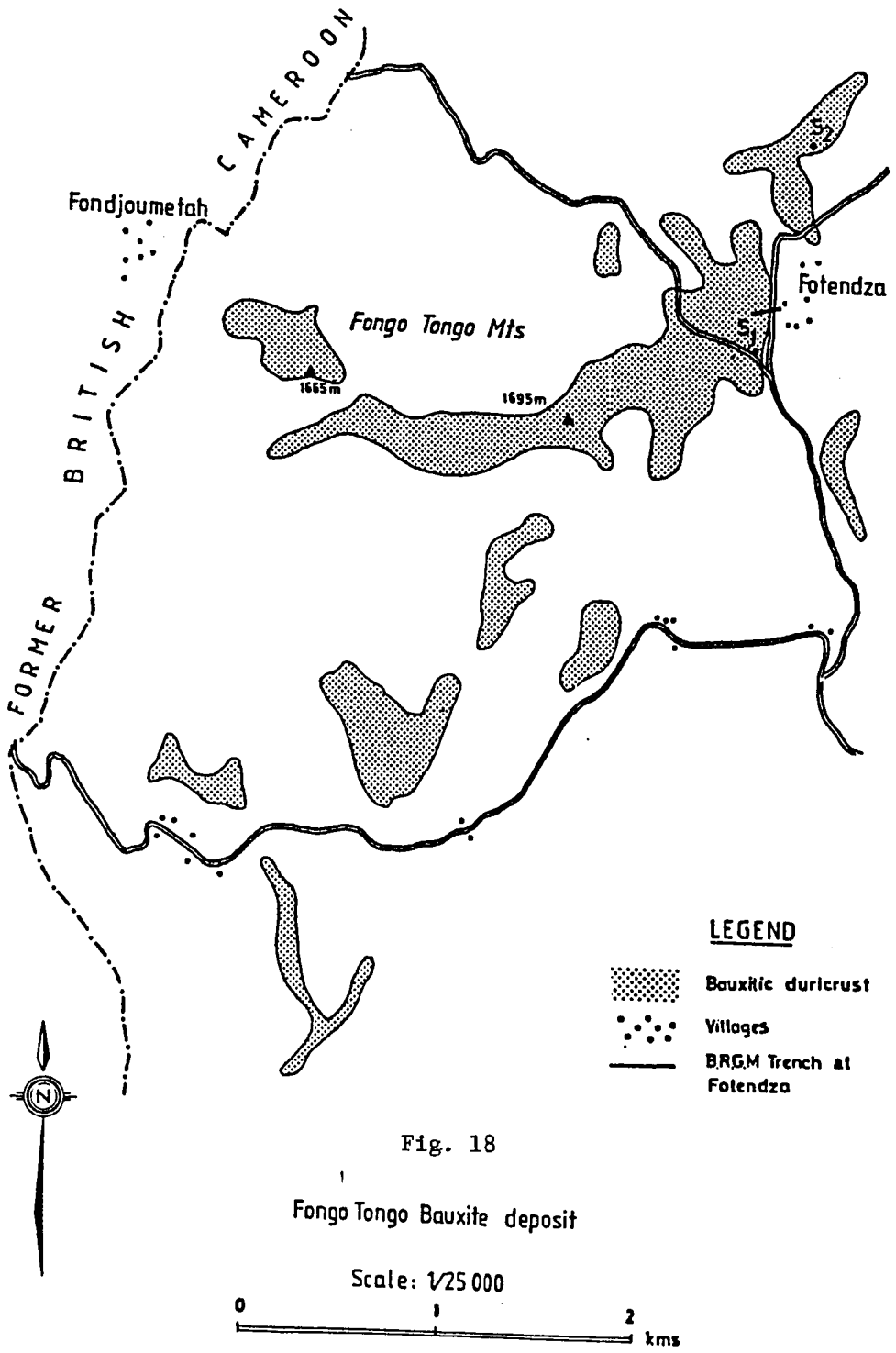

Fig. 18

Fongo Tongo Bauxite deposit

Scale: 1/25 000

through loose bauxitic gravel, and the second one, S2, north of this locality on top of the hard cap (Fig. 18). The profile found at S2 (Fig. 19) consists of a thick porous reddish-brown to deep-red hard cap or duricrust which extends from the surface down to a depth of about 10.0 meters and is broken into subrounded concretions in its upper part. Its lowermost part is consists of irregular blocks enclosed in a clayey matrix. These blocks vary in diameter from less than 1 centimeter to more than 5 centimeters. The duricrust forms the economically useful horizon of the profile. It overlies a massive mottled clay horizon with loose duricrust fragments and brownish nodules in its upper part.

The Fongo Tongo duricrust has a spongy porous texture. Many outcrop samples also have a breccia-like texture with coarse and fine-grained angular fragments in a reddish matrix (fig. 20).

The duricrust is exposed on the hill tops (Fig. 21). On the hill sides, it is partly masked by a thin humic soil rich in bauxite concretions. In places, where it underlies a stream bed, it is covered by relatively thick alluvial clayey deposits. This situation can be observed along the SW-NE cross-section in Fig. 22 which follows the BRGM trench. The duricrust can be divided into two parts as follows:

(1). Part "A" is located on the highest elevations of the duricrust, i.e. on hill tops. It has a nearly homogeneous hard cap jointed into irregular blocks which show little or no evidence of transport.

(2). Part "B" is restricted on hill flanks and consists of an apron of loose bauxitic gravel. It corresponds to bore hole S1 and forms the outer part of the deposit.

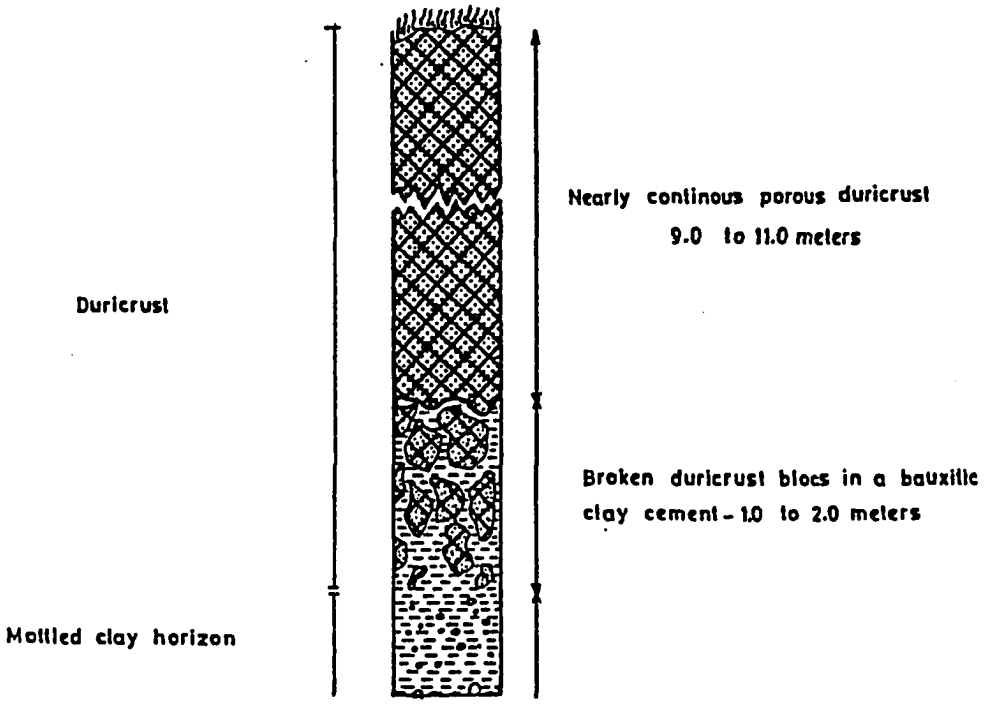

Fig. 19

Profile S2

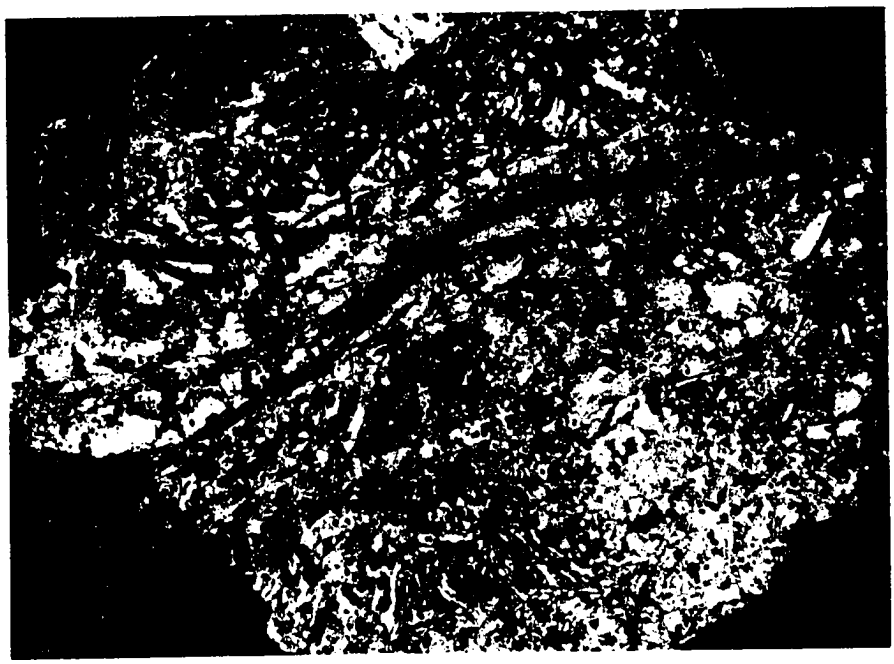

Fig. 20

Photograph of a hand specimen of
the Fongo Tongo bauxite

5.0 cm

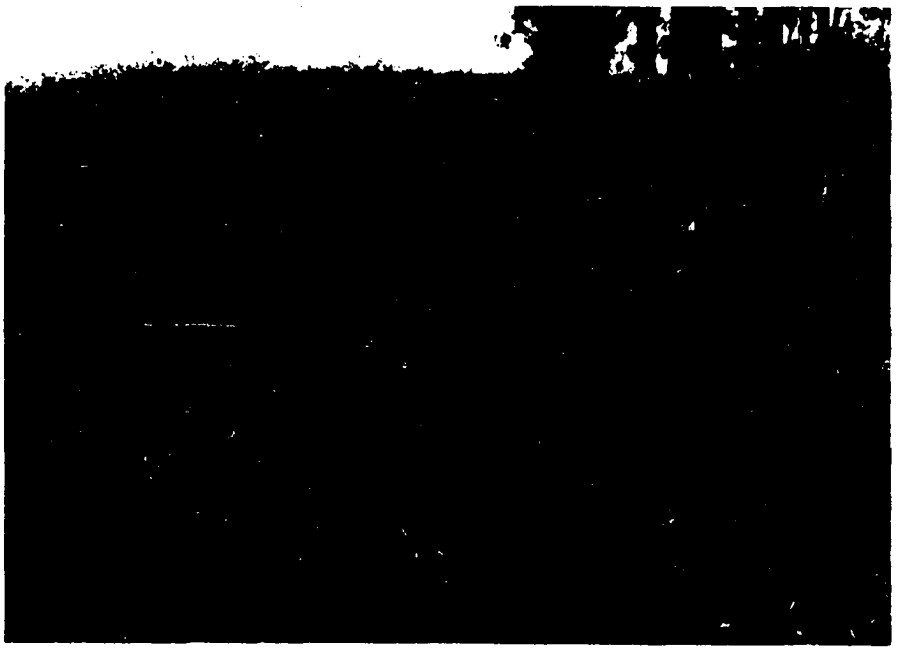

Fig. 21

Outcrop of the Fongo Tongo duricrust on top of the Fongo Tongo Mountains

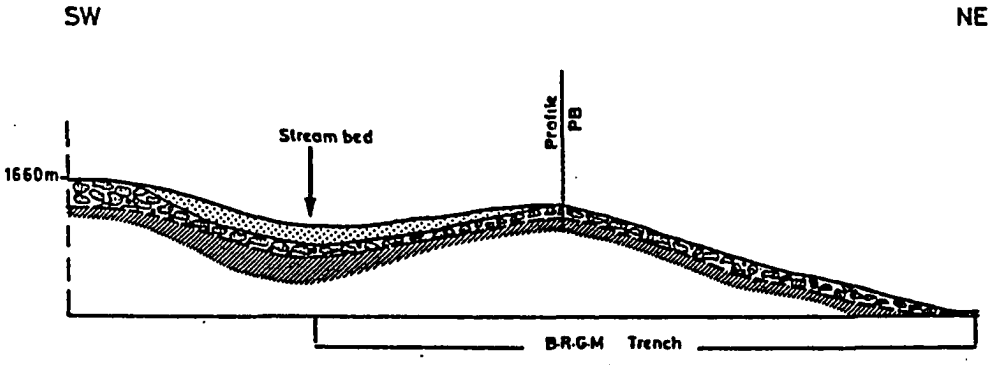

Fig. 22

SW-NE cross-section through the northern edge of the Fongo Tongo deposit showing the duricrust and the position of profile Pb, modified after Pascual, 1983. The BRGM trench at Fotendza is included in this cross-section.

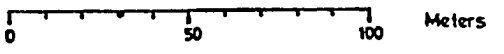

In summary, the Fongo Tongo deposit is a NE trending strip made up of narrow bauxitic hard caps situated on gently sloping hills on top of the dark trachyte also called the Fongo Tongo trachyte. It is essentially composed of a porous concretionary red-brown to deep-red duricrust and fragmented on the hill slope into chunks loosely held together by a clayey soil rich in bauxite concretions. The duricrust overlies a mottled clay horizon.

THE MELAN DEPOSIT

This small deposit is situated NE of Fongo Tongo at an elevation of nearly 2,000 meters. It is composed of a small pale-pinkish bauxite cap and a much smaller reddish cap about 400 meters NE. The southern cap was drilled whereas the northern one was studied by sinking a pit. Profile S3 from the southern cap is shown in fig. 23. These bauxitic horizons rest on nearly flat surfaces on top of gently convex plateaus.

The Southern Cap

Bore hole S3 went through about 3.0 meters of loosely bound bauxite boulders and entered a substratum made up of fresh greenish trachyte flows. A sharp unconformity coated with ferric iron oxides and hydroxides separates the trachyte and the overlying bauxite cap. There is no vertical zonation within the bauxite cap (Fig. 23).

This bauxite is a saprolite with a very well preserved trachytic texture similar to the texture of the underlying trachyte. It is composed of euhedral gibbsite aggregates pseudomorphous after sanidine

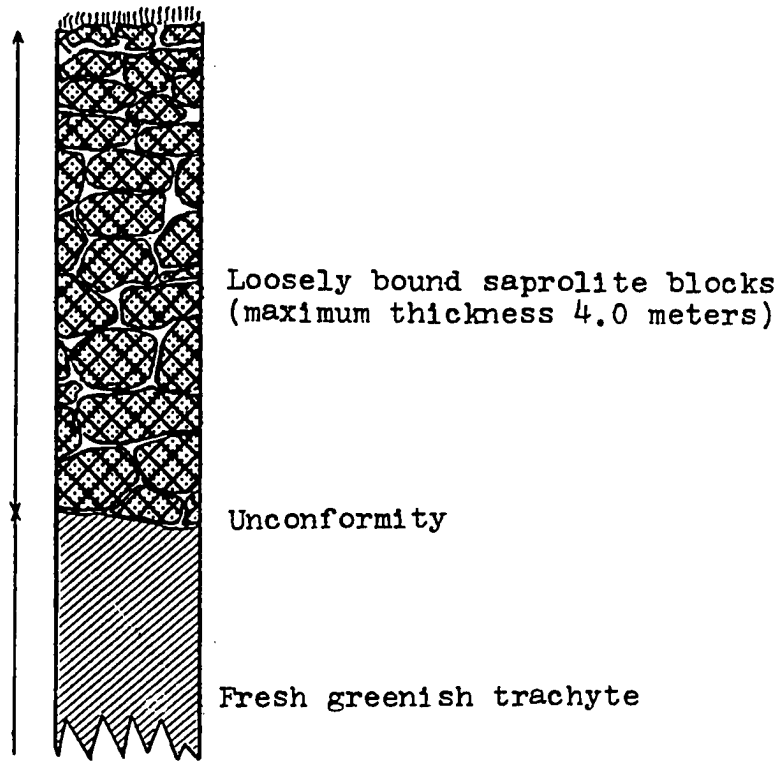

Fig. 23

Profile S3 of the southern cap of Melan deposit

phenocrysts in a matrix of very fine gibbsite crystals and minor opaques (fig. 24). The textural similarity between the saprolite boulders of the Melan deposit and the underlying greenish trachyte suggests that these boulders result from the dismantling of a saprolitic horizon which capped the greenish trachyte at higher elevations. The resulting boulders moved downslope to their present site. The saprolite was faulted (Fig. 25), and its dismantling is probably the result of a major tectonic event.

Hand specimens of the saprolite show voids left by dissolved sanidine phenocrysts. These voids retain the square or rectangular sanidine morphology. They are usually coated with ferric iron oxides which apparently did not migrate from the rather homogenous matrix into the voids. EDS and electron microprobe studies of fresh sanidine crystals from the greenish trachyte reveal the presence of iron in the structure of the sanidine. Therefore, it is suggested that the iron which coats the voids described in the saprolite was derived by chemical decomposition of the sanidine, and, because of its relative insolubility, iron oxide precipitated in the voids left by dissolved sanidine crystals. In places, thin lamellae of gibbsite aggregates have crystallized along former (001) planes of the sanidine crystals (Fig. 24).

In its lower part, this cap contains small rounded deep-red porous pebbles of a lateritic bauxite.

The Northern Cap

The northern cap is composed of a 3- to 4- meter-thick pile of unsorted fragments of saprolite and a deep-red porous lateritic bauxite

Fig. 24

Photograph of a hand specimen of
the Melan saprolite

4.0 cm

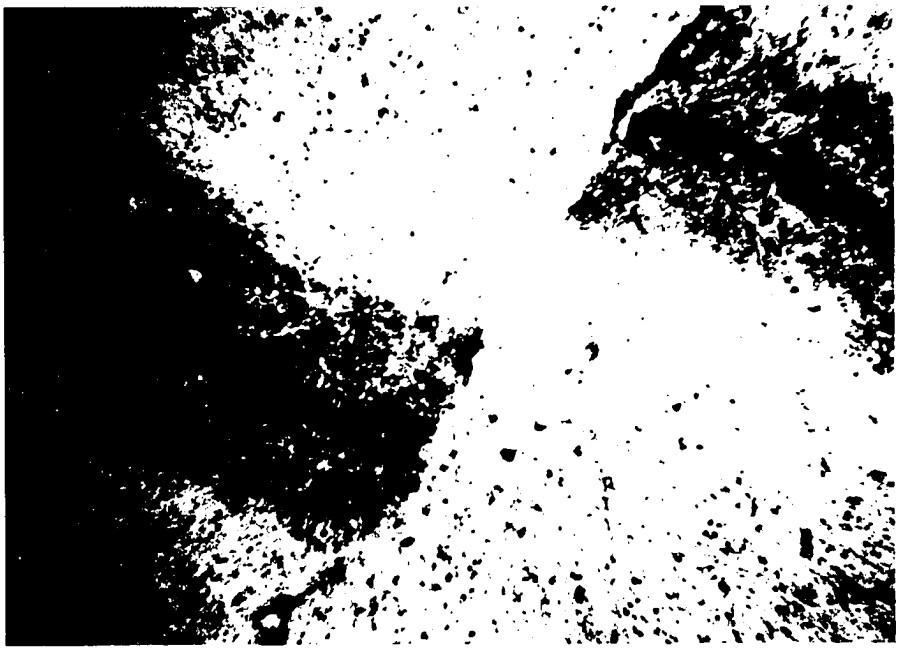

Fig. 25

Photomicrograph showing a microfault in
the Melan saprolite
40x

loosely held in a clayey matrix. The pit did not reach the underlying greenish trachyte, but this bauxitic material has clearly been transported to its present site.

The presence of loose porous lateritic bauxite fragments at Melan suggests that at its original site, the saprolite may have been overlain by a lateritic bauxite horizon. Such a vertical weathering sequence is not uncommon and has been described in several places (Valeton, 1981; Gilkes and Suddiprakaran, 1981).

Field data, therefore, favor a para-autochthonous origin for the Melan deposit.

THE DJEU DEPOSIT

This deposit is made up of small caps which are located on a number of NS to NE-SW trending ridges in the vicinity of the village Djeu which lies about 6 kilometers northeast of Fongo Tongo. Its elevation averages 1,800 meters. A 5.0 meter-deep crest pit was dug through a porous concretionary duricrust on the northernmost cap. The outcrop morphology and the weathering profile are identical to that of the Fongo Tongo deposit.

THE BAMBOUTO DEPOSIT

This deposit is situated approximately 1.5 kilometers north of

Melan, and is made up of a thin horizon of saprolite boulders in a bauxitic clay matrix. The bauxite is thin and economically unattractive (Porter and Bliss, 1981). It rests on flat-lying areas over a greenish trachyte flow which terminates abruptly southward. It has the highest elevation which ranges between 1,920 meters and 2,030 meters.

The saprolite boulders have a trachytic texture and resemble those described at Melan. They are rounded and sometime form a 10- to 30-centimeter-thick continous horizon. Pebbles similar to these were found at much higher elevations, near the southern edge of the caldera.

It is suggested that all the saprolite clasts found in the study area resulted from the dismantling of a saprolitic horizon which once capped the Bambouto Mountains. The dismantling may have been a consequence of a major tectonic event such as the collapse of the Bambouto caldera. Any event of lesser magnitude would probably have caused only a partial dismantling of the saprolite.

THE DJUTTITSA DEPOSIT

This deposit, which is described here for the first time, includes a number of small plateaus located in the vicinity of Djuttitsa township with elevations ranging between 1,760 meters and 1,780 meters. Bauxite is currently being quarried from many of these plateaus by the local branch of the Highway Department for road material.

The bauxite caps consist of broken pieces of a very hard crust. The pieces tend to have platy shapes, and the larger ones still retain

their original subhorizontal orientation (Fig. 26a). Refilling of duricrust cracks by gibbsite is frequent (Fig. 26b).

The bauxite horizon at Djuttitsa has a maximum thickness of 2.5 meters. Its lower contact is diffuse as clayey material is mixed with platy bauxite fragments. This profile apparently developed on the underlying greenish trachyte flows and shows no evidence of transport.

THE FONDJOUMETAH DEPOSIT

This deposit is located west of the Fongo Tongo deposit on top of a small hill 1,500 meters high, near Fondjoumetah village. Due to the lack of a base map for this part of the study area at the time when field work was carried out, this deposit is not shown on the geologic map. The Fondjoumetah hill is made up of ash-flow tuffs which overlie the granitic basement.

Two bore holes were drilled, the first, S4, at the foot of Fondjoumetah hill, and the second, S5, on top of the hill. A cross-section through the northern flank of the hill is shown in fig. 27.

Bore hole S4 starts at the surface with a detrital sequence 10.0-meter-thick composed of polygenic pebbles with bauxite clasts dominant and subordinate to minor ash-flow tuff and granitic clasts. The pebbles are loosely held in a reddish clay-sized matrix. This detrital sequence is underlain by a thick clayey horizon which continues down to the bottom of the hole. The parent rock was not reached, but incompletely

Fig. 26a

Photograph of a bauxitic profile
near Djuttitsa

1.0 m

Fig. 26b

Photograph showing the filling of duricrust cracks by gibbsite

20.0 cm

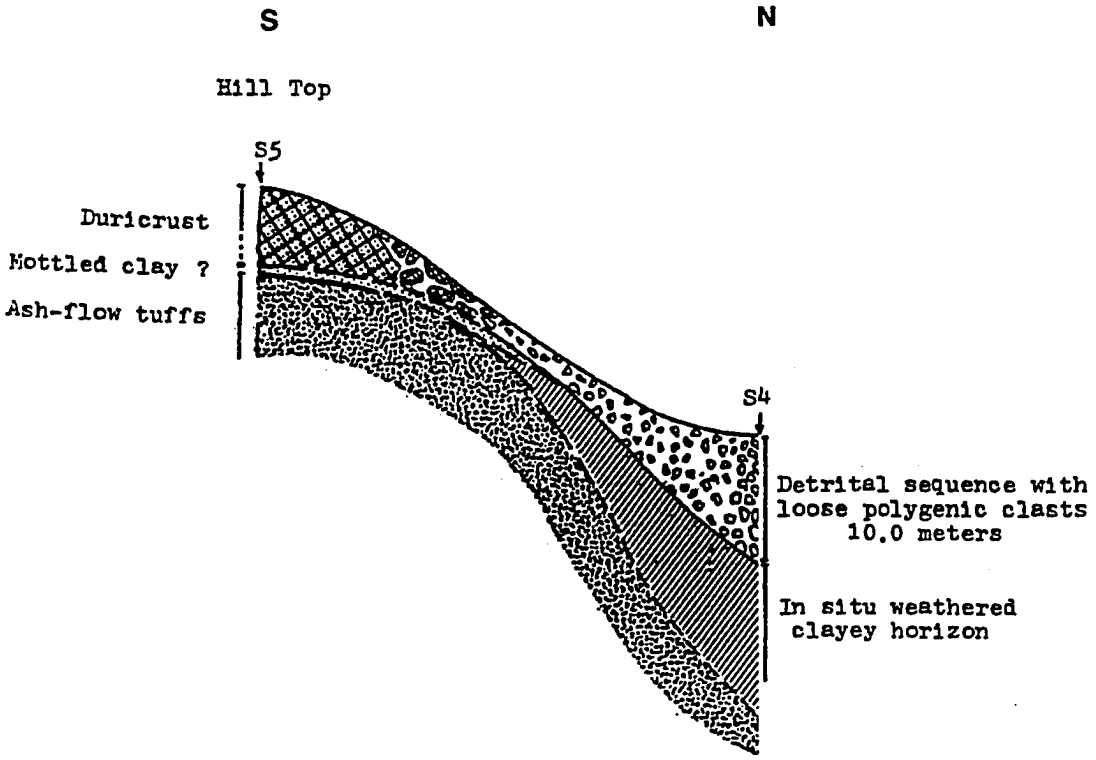

Fig. 27

S-N cross-section through the northern flank of Fondjoumetah hill between bore holes S4 and S5

weathered ash-flow tuff clasts were recognized at the base of the bore hole.

Bore hole S5 is 7.5 meters deep and was drilled on top of the hill in a porous concretionary duricrust similar to the one described at Fongo Tongo and Djeu. The duricrust was not transsected but the areal geology reveals that it overlies the ash-flow tuffs. The nature and thickness of the substrate for the duricrust remains unknown, but because of the high gradient of the hill slope, it is probably a thin mottled clay horizon transitional into the underlying ash-flow tuffs. There is no evidence of transport of the duricrust.

The Fondjoumetah deposit thus developed through in situ weathering of the underlying ash-flow tuffs. No genetic relationship was found between the ore and the nearby basement granites as suggested by Porter and Bliss (1983) and there is no evidence for granite-derived bauxitic crust in the area.

OTHER BAUXITE DEPOSITS

Small bauxitic hard caps have also been located at lower elevations south of the study area. One of these lies about 3.5 kilometers south of Dschang at an elevation of 1450 meters. It rests on a flat-lying basaltic flow.

CONCLUSIONS ON THE GEOLOGIC SETTING OF THE BAUXITE DEPOSITS

The bauxite deposits of the study area are situated on the southern flank of the Bambouto Mountains, on top Tertiary lava flows.

Bauxitization occured at high elevations between 1,400 meters and 2,000 meters, on flat to gently sloping hill tops. Most deposits have an in situ weathering profile, and consist of a duricrust cap overlying a mottled clay horizon. In places the duricrust is disrupted into clasts on its flanks. With increase in slope, the clasts of bauxite undergo limited downslope transport. A few very small deposits are composed of a horizon of para-autochthonous rounded saprolite pebbles held together by a clayey matrix and resting on top of fresh volcanic rocks from which they are separated by a sharp unconformity. The saprolite pebbles have a well-preserved trachytic texture with abundant polycrystalline aggregates of gibbsite pseudomorphous after sanidine.

Two texturally different kinds of bauxites coexist, therefore, in the area of study. The dominant one is rich in iron oxides and has a spongy or porous texture; the subordinate one is a pale pink saprolite. The first texture characterizes the Fongo Tongo, Djeu, Djuttitsa and Fondjoumetah deposits, whereas the second one is found at the Bambouto and Melan deposits.

MICROTEXTURE AND PETROGRAPHY OF THE BAUXITE DEPOSITS

In the preceeding section the various bauxite deposits of the study area have been divided into two groups according to their texture and mode of occurence. The dominant group includes deposits with a residual weathering profile and a porous texture whereas the second group consists of deposits with para-autochthonous features and a saprolitic texture. This section deals with the microtexture and petrography of each of the two groups. The first group is hereafter termed the "Fongo Tongo-type bauxite " and the second termed the "Melan-type bauxite" after the two most characteristic occurrences.

THE FONGO TONGO-TYPE BAUXITE

The Fongo Tongo-type bauxite consists essentially of a fine-grained matrix composed of minute gibbsite crystals and iron oxides. The bauxite is very porous and contains numerous voids and a network of interconnected tubules coated with alternating collophorm layers of goethite and gibbsite (Fig. 28). It is cut by veins of goethite and gibbsite. Saprolite clasts with the texture of trachyte or ash-flow tuff are found locally in the matrix (Fig. 29). The mineralogy is as follows:

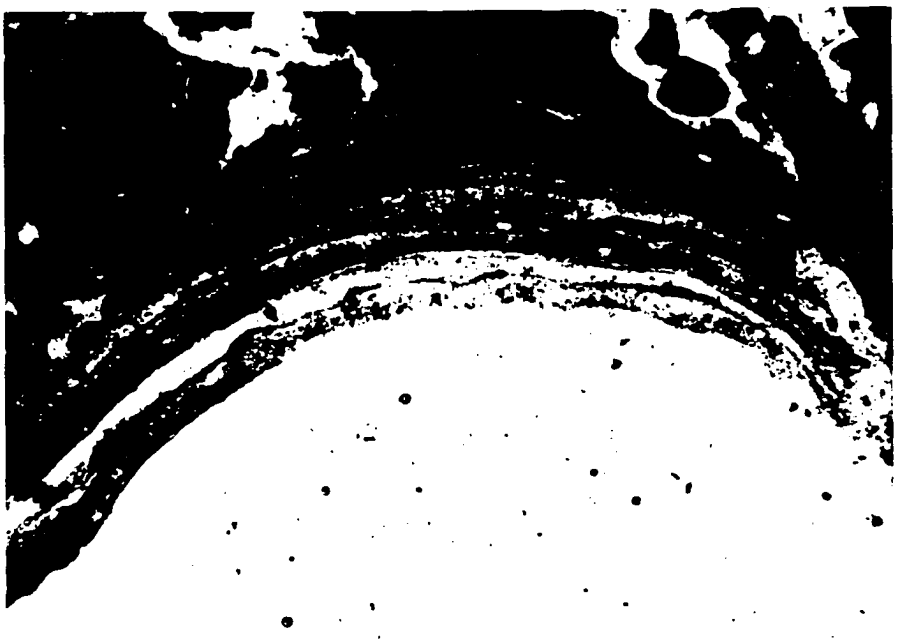

Fig. 28

Photomicrograph showing alterning collophorm gibbsite and goethite layers in the Fongo Tongo bauxite

40x

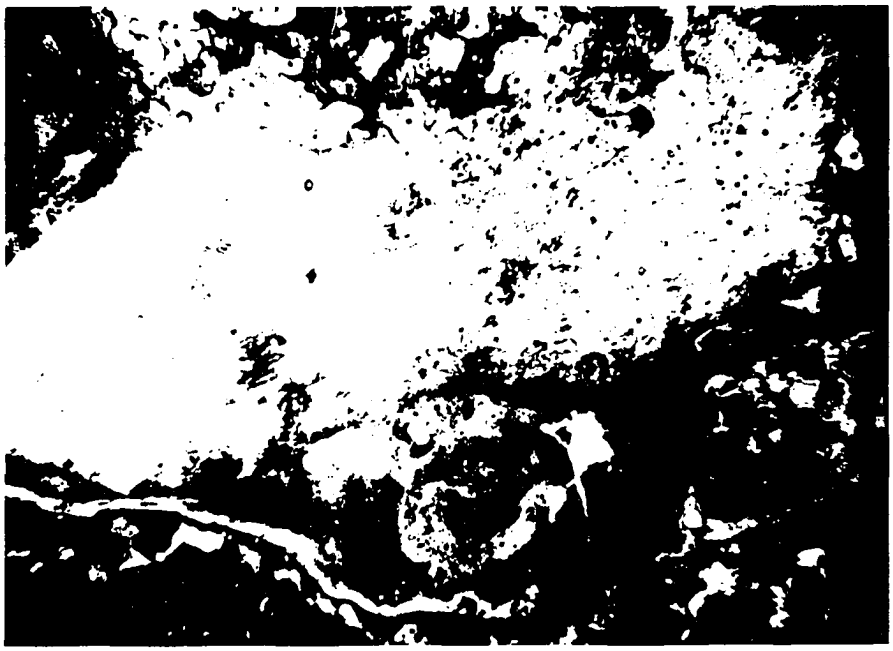

Fig. 29

Photomicrograph of a saprolite chunk in the colloidal matrix of the Fongo Tongo bauxite

40x

Aluminum Hydroxides

"Free alumina" was found exclusively in the form of gibbsite ($Al(OH)_3$), or aluminum oxide trihydrate which constitutes the dominant mineral species. Boehmite (AlO.OH) was reported on the hill slopes (Pascual, 1983), but no evidence for this mineral was found in this study. If present, boehmite probably plays little or no role in the evolution of the weathering profile. Gibbsite shows two different textural occurrences, each one being related to a specific development stage as follows:

Poorly crystallized white to yellow gibbsite forms the major component of the gel-like matrix. In places, it crystallizes in polycrystalline aggregates which fill the former sites of primary minerals. This gibbsite also forms alterning layers with goethite. It has a spherical or flaky habit. Normally white when pure, this gibbsite becomes yellow when it is intimately associated with goethite in the colloidal matrix, probably due to limited atomic substitution of Fe^{3+} for Al^{3+} in the structure of gibbsite.

Gibbsite is also found in voids and cracks where it forms relatively large euhedral crystals (Fig. 30 a, b). These gibbsite crystals are twinned on (001), and multiple twinning is common. They grow with their twin planes normal to the walls of the voids. Stacking of two or three layers of gibbsite crystals is common. These crystals are much whiter than those which have grown in the colloidal groundmass, probably because of a lower Fe^{3+} content. Figs. 31.a and 31.b are scanning electron micrographs a broken bauxite surface showing cryptocrystalline gibbsite crystals (31.a) and a void filled with

Fig. 30a

Filling of a void in the Fongo Tongo bauxite
124x

Fig. 30b

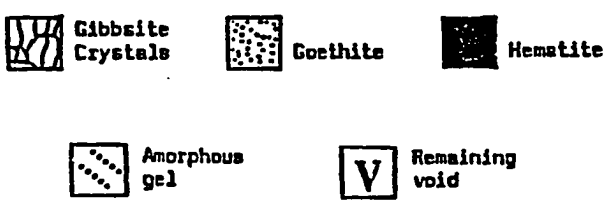

Filling of a void in the
Fongo Tongo-type bauxite
168x

Fig. 31a

Scanning electron micrograph of a broken bauxite surface showing the filling of a void by euhedral gibbsite crystals

Fig. 31b

Scanning electron micrograph of a broken bauxite surface showing the crystal habit of euhedral gibbsite crystals grown in a void in the Fongo Tongo duricrust

euhedral gibbsite crystals (31.b). The euhedral crystals in the void are composed of a stacking of superimposed tabular sheets with monoclinic symmetry. Individual layers can be recognized.

Goethite

The principal iron oxide in this type of bauxite is goethite (α-FeO.OH) which occurs in various colors ranging from yellow to brownish-orange. It constitutes the second major mineral after gibbsite. It occurs in intimate association with gibbsite in the colloidal matrix, and also fills shrinkage cracks and cross-cutting veins, sometimes in association with fine grained cryptocrystalline gibbsite. The duricrust has locally developed iron-rich concretions which are held together in a polygonal network of cracks filled with gibbsite (Fig. 32). Pisoliths are also developed. They are composed of concentric alternating gibbsite and/or goethite shells (Fig. 33). Pisolithization seems to be localized in the uppermost part of the duricrust.

Gibbsite veins commonly cut goethite veins and, therefore, seem to be younger. This observation is in accord with the development of gibbsite-cemented concretions described above. Qualitative EDS analyses of these veins has also revealed the presence of traces of silicon which is in the form of silica and kaolinite according to mineralogical the studies below.

Maghemite

Maghemite (γ-Fe_2O_3) was found by reflected-light microscopy. It is the second most important iron-oxide mineral after goethite, and occurs as irregular particles throughout the profile. It is bluish-grey in oil immersion and isotropic. The few slightly anisotropic maghemite crystals

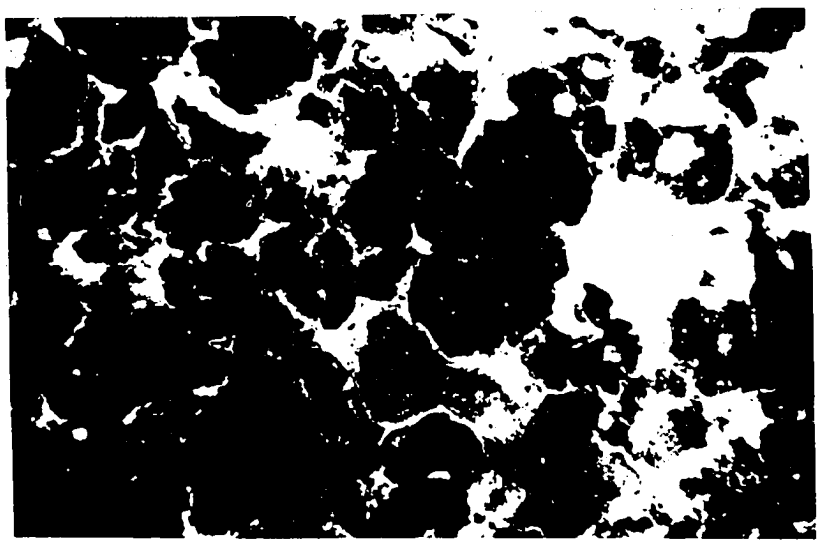

Fig. 32

Photomicrograph showing the development of concretions in the duricrust

40x

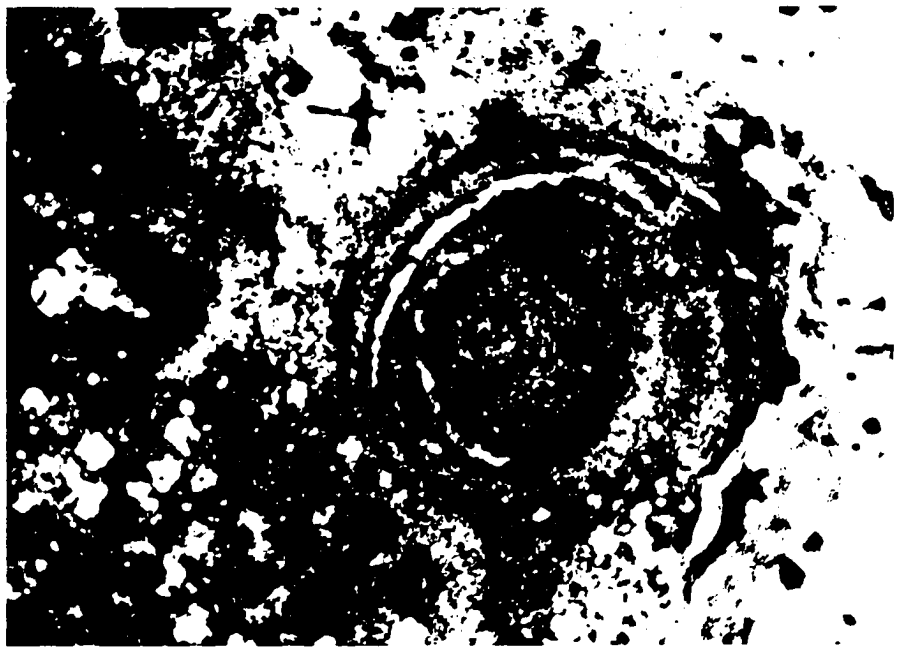

Fig. 33

Photomicrograph showing the pisolithization
of the duricrust

124x

which were observed suggest a transition to hematite. Subhedral crystals are probably pseudomorphous after magnetite through oxidation.

Hematite

Hematite (α-Fe_2O_3) is a minor iron-oxide constituent, which was found by reflected-light microscopy. In oil immersion it is grey-white with a distinct anisotropy. It sometimes crystallizes along the (111) planes of magnetite and forms a square grid when the optical axis of the microscope is perpendicular to the (100) planes of the magnetite.

THE MELAN-TYPE BAUXITE

This bauxite is composed essentially of coarse saprolite pebbles characterized principally by the preservation of the macro- and micro-fabric of the parent rock(s). A dominant trachytic texture is displayed with subparallel gibbsite crystallites pseudomorphous after sanidine microlites. Relic flow banding is well preserved through the alignment of sanidine microlites which is particularly distinctive where they follow the outline of voids formerly occupied by sanidine phenocrysts (Fig. 34). The mineralogy of this saprolite is as follows:

Gibbsite

Gibbsite is the dominant mineral and is responsible for the preservation of relic textures. Sanidine has been completely transformed into polycrystalline gibbsite aggregates in which gibbsite outlines the shape and cleavages of former sanidine crystals (Fig. 35). Pseudomorphous replacement of sanidine by gibbsite is also shown in fig.

Fig. 34

Photomicrograph of the Melan saprolite

40x

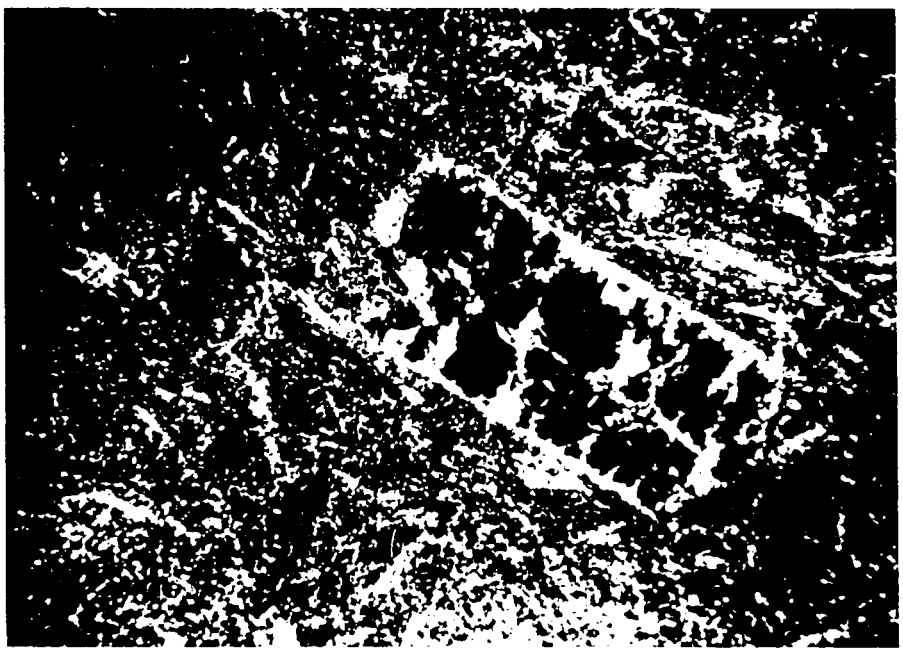

Fig. 35

Photomicrograph showing the development of gibbsite aggregates along the cleavage planes of a former sanidine phenocryst in the Melan saprolite

40x

36 which shows a relatively fresh remnant of a former sanidine crystal surrounded by gibbsite aggregates. The surrounding groundmass has undergone an identical transformation.

Goethite

Goethite is subordinate to minor in this bauxite, and usually fills the interstitial space between polycrystalline gibbsite aggregates. Thin films of goethite also form thin selvages that coat gibbsite-lined cleavages developed along the (001) and (010) of former sanidine crystals.

Maghemite

Maghemite is identical to that described in the Fongo Tongo-type bauxite and occurs only in trace amounts in the Melan-type bauxite.

SUMMARY OF THE MICROTEXTURE AND PETROGRAPHY OF THE FONGO TONGO- AND MELAN- TYPE BAUXITES

All the bauxite deposits situated in the area of study can be divided into two groups according to their microtextural and petrographic features. The first group, also named the "Fongo Tongo-type bauxite" is composed of a reddish-brown to deep-red spongy material with a colloidal-sized matrix of platy gibbsite crystals and goethite. It has a porous texture characterized by numerous voids and a network of interconnected tubules coated with layers of euhedral gibbsite crystals and/or goethite, and is cut by numerous veins of both minerals. This

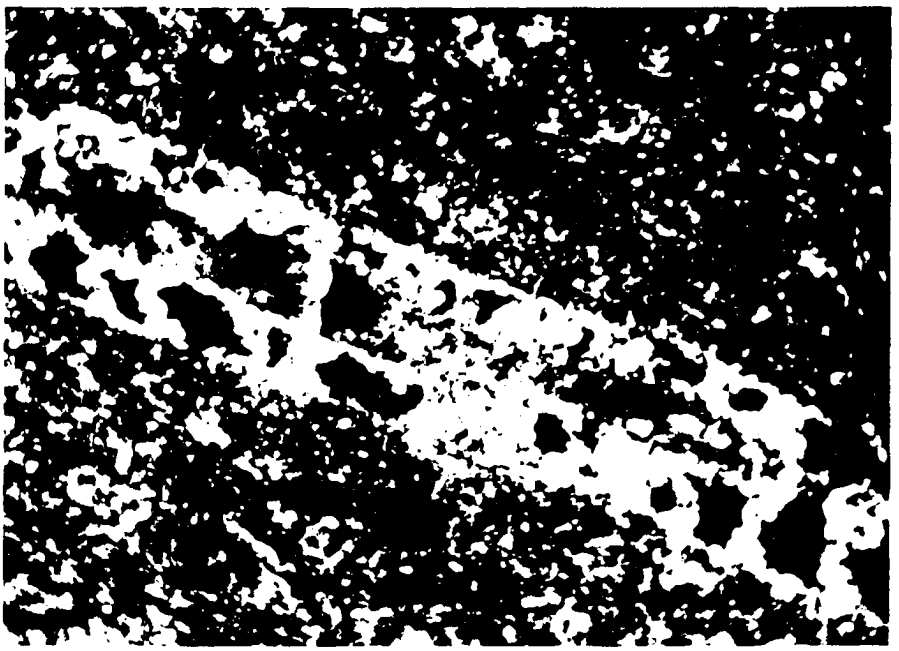

Fig. 36

Photomicrograph showing direct gibbsitization of a sanidine phenocryst

124x

bauxite locally contains saprolite clasts with either a trachytic texture or that of an ash-flow tuff.

The second group, the "Melan-type bauxite", consists of a pale-pinkish saprolite with a dominant trachytic texture and a minor ash-flow tuff texture. The trachytic texture consists of subparallel gibbsite aggregates pseudomorphous after sanidine microlites.

TIME CORRELATION BETWEEN THE FONGO TONGO- AND MELAN-TYPE BAUXITES

The textural similarity between the saprolite pebbles which make up the Melan bauxite on the one hand, and those which are embedded in the Fongo Tongo bauxite on the other suggests that they may both have been derived from the same saprolitic horizon which predates the formation of the Fongo Tongo bauxite. Bauxitization in the study area might, therefore, have taken place in at least two discrete stages. The first stage resulted in the development on top of the Bambouto Mountains of a pinkish saprolite. This saprolite was subsequently destroyed following the collapse of the Bambouto caldera and some of the resulting loose bauxitic clasts mechanically moved downslope along the southern flank of the mountain. This stage was followed by the emplacement of trachytic and phonolitic dikes and plugs, and the outpouring of basaltic flows in the Dschang area. Some saprolite chunks were incorporated in the Fongo Tongo trachyte during its emplacement. The second stage of

bauxitic weathering was one during which lateritic bauxite developed at Fongo Tongo, Fondjoumetah, Djeu, Djuttitsa and near Dschang.

The possibility that there were two discrete stages of bauxitization raises a question regarding the controlling factors which may have led to the development of two texturally different bauxitic profiles. To provide an answer to this question, a detailed study of the mineralogy and geochemistry of these bauxites was carried out, and the results of this study follow.

SEMI-QUANTITATIVE MINERALOGY OF THE BAUXITE DEPOSITS

The general mineralogy of the Fongo Tongo and areally related bauxite deposits has been discussed in the section on microtexture and petrography. Two distinctive microtextures were described, each representing one of the two types of bauxites found in the area. Both of these types of bauxites are composed essentially of gibbsite and minor goethite, other minerals being present in trace amounts only. Maghemite and hematite were found by reflected-light microscopy. No other minerals were identified optically. With these limitations in mind, additional mineralogical studies were undertaken using x-ray powder diffraction, differential thermal analysis, scanning electron microscopy and infrared spectroscopy.

X-RAY POWDER DIFFRACTION STUDIES

Method

X-ray powder diffraction studies were carried out on 50 samples from three bore holes and various outcrops. A Philip APD-3600 computer-assisted x-ray powder diffractometer equipped with a Cu tube was used. All the samples were finely powdered and mounted evenly in the cavity of a sample holder. Then the upper surface of the sample was flattened with a glass slide by applying slight pressure. Generator settings were 45kv and 30ma. A step size of 0.020 degrees 2θ was used with a 1.20 second

count time for most samples. Slower scan rates were selectively used for solving specific problems.

Results

The secondary minerals identified were gibbsite, goethite, anatase, maghemite, hematite, kaolinite, hydrated halloysite, metahalloysite and quartz. Only the 001 basal reflections of halloysite and metahalloysite have *hkl* indices. The remaining diffraction peaks of halloysite and metahalloysite have *hk* indices, and their spacings can approximately be listed as *hk*0 even though they do not correspond exactly to *hk*0 positions in reciprocal space (Brindley and Brown, 1980). In addition to these minerals, primary minerals from fresh or slightly altered volcanics were also examined; these minerals were identified as high sanidine, aegirine-augite, hornblende, albite, magnetite, ilmenite and cristobalite. Cristobalite was also identified in some weathered samples in the vicinity of the weathering front. A semi-quantitative estimation of the mineralogy of each deposit was made using the relative intensity of the strongest line of each mineral identified in the diffraction patterns. The resulting x-ray powder diffraction analyses are given in appendix 2. The intensity scale on each diffractogram is logarithmic. The minerals estimated based on their characteristic diffraction maxima and the relative intensities of these maxima are as follows:

gibbsite	d_{002} 100
kaolinite	d_{001} 100
metahalloysite	d_{001} 100
goethite	d_{110} 100, d_{130} 30

hematite	d_{104} 100, d_{110} 71
maghemite	d_{220} 100
anatase	d_{101} 100
quartz	d_{101} 100

When an unresolved maximum shared by two different minerals was used in estimating one of the two minerals, the next strongest maximum of that mineral was used in the analysis in order to minimize the error. For instance the main goethite d_{110} maximum was used together with its d_{130} reflection, because the goethite d_{110} and the kaolinite d_{111} maxima overlap.

Each mineral was classified in one of the following four groups: dominant (++), minor (+), trace (+0), absent (0). When the relative intensity of a characteristic maximum was between 100 and 15, the corresponding mineral was classified as dominant. When this intensity was between 15 and 5, the mineral was considered to be minor, and when it was lower than 5, the mineral was classified as a trace. The resulting mineralogy is as follows:

Profile S2

Bore hole S2 was drilled through a thick duricrust at Fotendza in the Fongo Tongo area. It reached the underlying mottled clay horizon. Its mineralogy is shown in fig. 37 and table 2.

Gibbsite is dominant throughout the entire profile. Its most intense peaks in descending order of intensity are associated with the d_{002}, the d_{110} and the d_{200} reflection planes. Additional lines recorded are d_{112}, d_{112}, d_{103}, d_{021}, d_{213}, d_{311}, d_{312}, d_{114}, d_{313} and d_{204}. Below a depth of about 11.7 meters, there is a sharp decrease in the relative

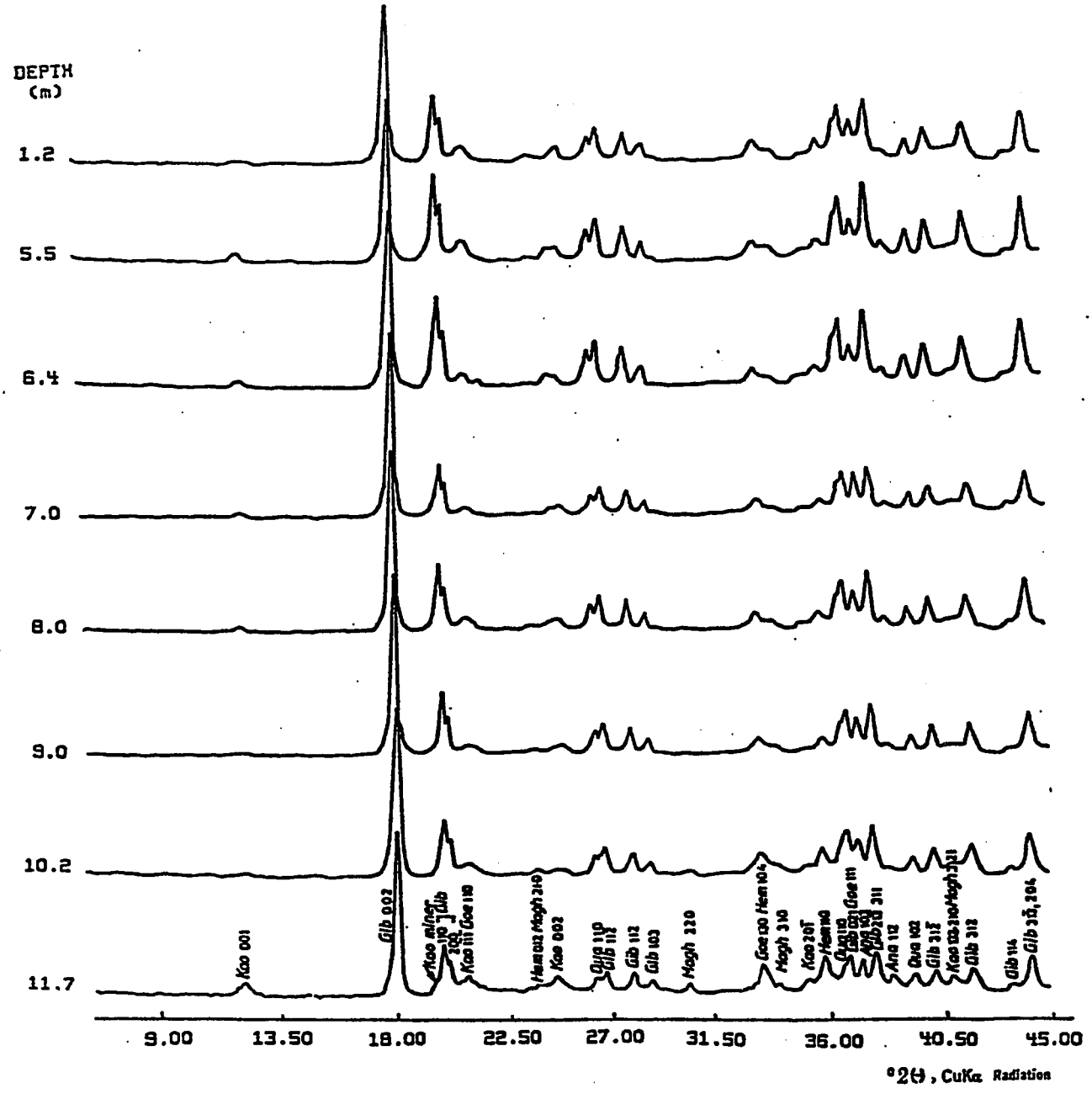

Fig. 37

X-Ray powder diffraction patterns along profile S2 at Fotendza

Table 2

Semi-quantitative mineralogy of profile S2 using x-ray powder diffraction data

++	dominant
+	minor
+0	trace
0	absent

SAMPLE NUMBER	gib	kao	goe	hem	magh	ana	qua	metah
S2/1.2	++	+0	+	+0	+0	+0	+	0
S2/2.7	++	0	+0	+0	+0	+0	+0	0
S2/4.0	++	+0	+	+0	+0	+0	+0	0
S2/5.5	++	+0	+0	+0	+0	+0	+	0
S2/6.4	++	+0	+0	+0	+0	+0	+	0
S2/7.0	++	+0	+0	+0	+0	+0	+0	0
S2/8.0	++	+0	+0	+0	+0	+0	+0	0
S2/9.0	++	+0	+0	+0	+0	+0	+0	0
S2/10.2	++	0	+0	+0	+0	+0	+0	0
S2/11.7	++	+0	+0	+	+0	+0	+0	0
S2/13.2	++	+	+	+	+0	+0	+0	0

intensity of the peaks which indicates a drop in gibbsite concentration. The drop in gibbsite represents the transition from the duricrust into the underlying mottled clay horizon. Despite this drop in concentration, gibbsite remains the dominant mineral in the mottled clay horizon.

Goethite also occurs in the entire profile, but it is a minor to trace mineral. Its major peak is associated with the d_{110} plane. This peak is rounded, probably as a result of poor crystallinity. Additional diffraction planes of goethite are d_{130} and d_{111}. The intensity of the d_{110} peak is relatively constant throughout the profile.

Kaolinite is revealed by its d_{001} reflection. Almost absent in the duricrust, it increases sharply within the mottled clay horizon. Additional reflection planes are d_{111}, d_{002} and d_{201}.

Hydrated Poorly Crystalline Alumino-Silicates: In the mottled clay horizon, the gibbsite d_{110} peak has a shoulder on its low angle side which reveals the presence of a poorly crystalline mineral of the kaolinite family.

Anatase occurs as a trace mineral. The relative intensity of its d_{101} peak shows a remarkable constancy throughout the profile.

Maghemite, Hematite and Quartz: Maghemite is present throughout the profile in trace amounts with peaks barely above the background. Traces of hematite and quartz are also revealed along the profile.

The mineralogy of the major part of profile S2 consists, therefore, very dominantly of gibbsite followed by minor-to-trace goethite and traces of kaolinite, anatase, maghemite, hematite and quartz. Gibbsite has a relatively constant concentration within the duricrust but decreases sharply in the mottled clay horizon. Kaolinite,

by contrast, has a very low concentration and is relatively constant in the duricrust, but it is much more abundant in the mottled clay horizon. Maghemite, hematite, quartz and anatase occur only in trace amounts.

Profile S3

This bore hole was drilled through a 3.0 meter-thick saprolite cap at Melan. It also penetrated the underlying greenish trachyte. The mineralogy of recovered cores is shown in fig. 38 and table 3 and can be summarized as follows:

Mineralogy of the Saprolite

The 3.0 meter-thick saprolite blanket is made up dominantly of *gibbsite*, minor to trace *goethite*, *quartz* and *hematite*, and of trace amounts of *kaolinite*. The last two minerals are nearly absent in the underlying trachyte. Goethite is exceptionally abundant near the unconformity with the underlying greenish trachyte, probably as a result of oxidation by ground water of ferrous iron contained in the primary minerals of the underlying trachyte.

Mineralogy of the Greenish Trachyte

High sanidine is only found in the trachyte where it is the dominant mineral. Its estimated composition from x-ray powder diffraction is $Na_{0.61}K_{0.39}AlSi_3O_8$. *Aegirine-augite* and *Hornblende* are minor constituents. *Oligoclase* and *cristobalite* were found in trace amounts, as well as *goethite* and *kaolinite* which result from the weathering of primary minerals.

Ilmenite and *magnetite* are the two accessories found in the trachyte. The relative intensity of the d_{102} peak of ilmenite decreases

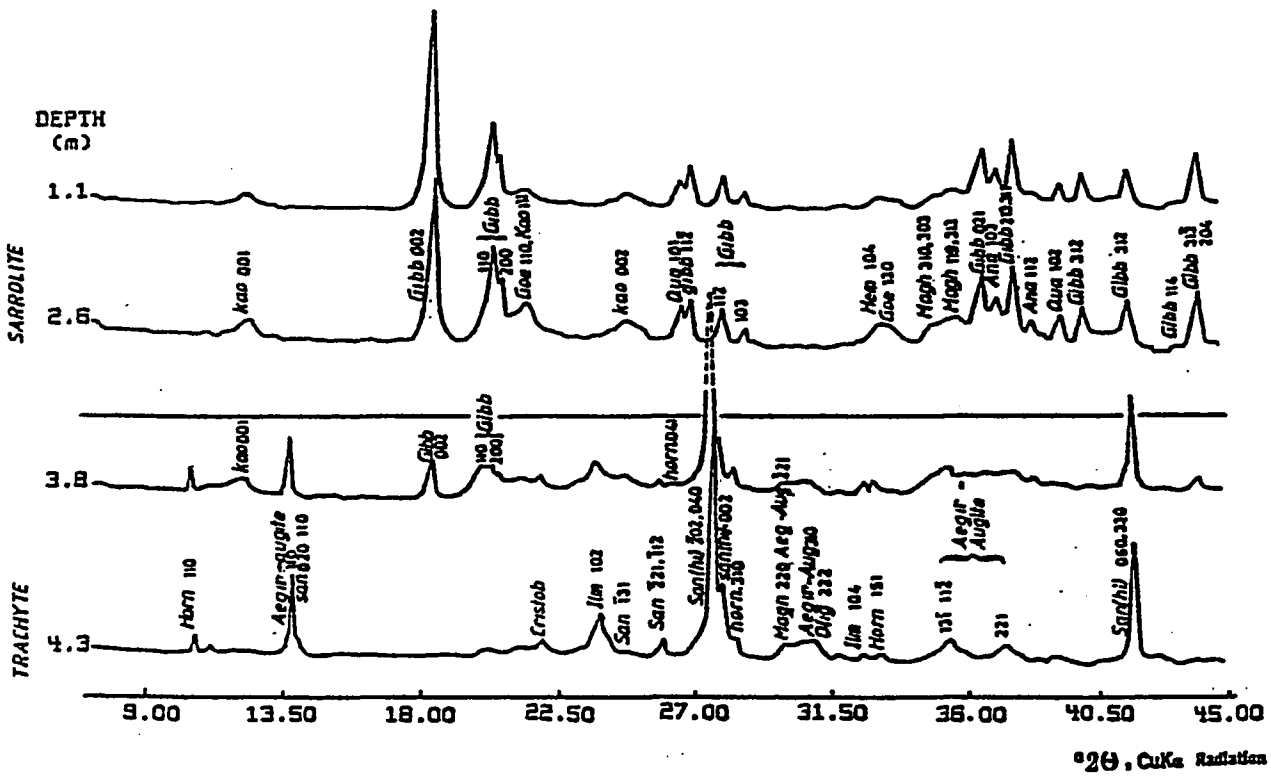

Fig. 38

X-Ray powder diffraction patterns along profile S3 at Melan

Table 3

Semi-quantitative mineralogy of profile S3 using x-ray powder diffraction data

++ dominant
+ minor
+0 trace
0 absent

SAMPLE NUMBER	gib	kao	goe	hem	magh	ana	qua	metah
S3/1.1	++	+0	+0	+0	+0	+0	+0	0
S3/2.6	++	+0	+	+	+0	+0	+	0
S3/3.85	+	+0	+0	0	0	0	+0	0
S3/4.35	+0	0	+0	0	0	0	+0	0
S3/5.5	0	0	+0	0	0	0	+0	0

with height, probably due to its breakdown to anatase and iron oxides and hydroxides.

The mineralogy of bore hole S3, therefore, reveals that there are two different rock units in the profile. The upper one is composed dominantly of gibbsite, minor goethite, and traces of kaolinite, anatase, maghemite, hematite and quartz. Underlying this unit is a relatively fresh trachyte composed dominantly of high sanidine, minor aegirine-augite, and hornblende, oligoclase, ilmenite, magnetite, cristobalite, goethite and kaolinite in trace amounts. The goethite and kaolinite of the lower unit are only found near the contact between the two units. They decrease rapidly with depth.

Profile S4

This bore hole was drilled through non-bauxitic weathered material at the foot of Fondjoumetah hill. Its mineralogy was included in this study in order to help in understanding the evolution of a number of minerals associated with bauxitization processes in the area of study. The profile is composed of two separate horizons, an underlying *in situ* weathering profile, and an upper detrital horizon 8.0 meters thick made up dominantly of bauxite clasts and subordinately of polygenic pebbles derived from the basement and the volcanic rocks of the area.

This study was essentially limited to the underlying weathered horizon. The results of x-ray powder diffractometry are shown in fig. 39. The mineralogy is given in table 4 and can be summarized as follows:

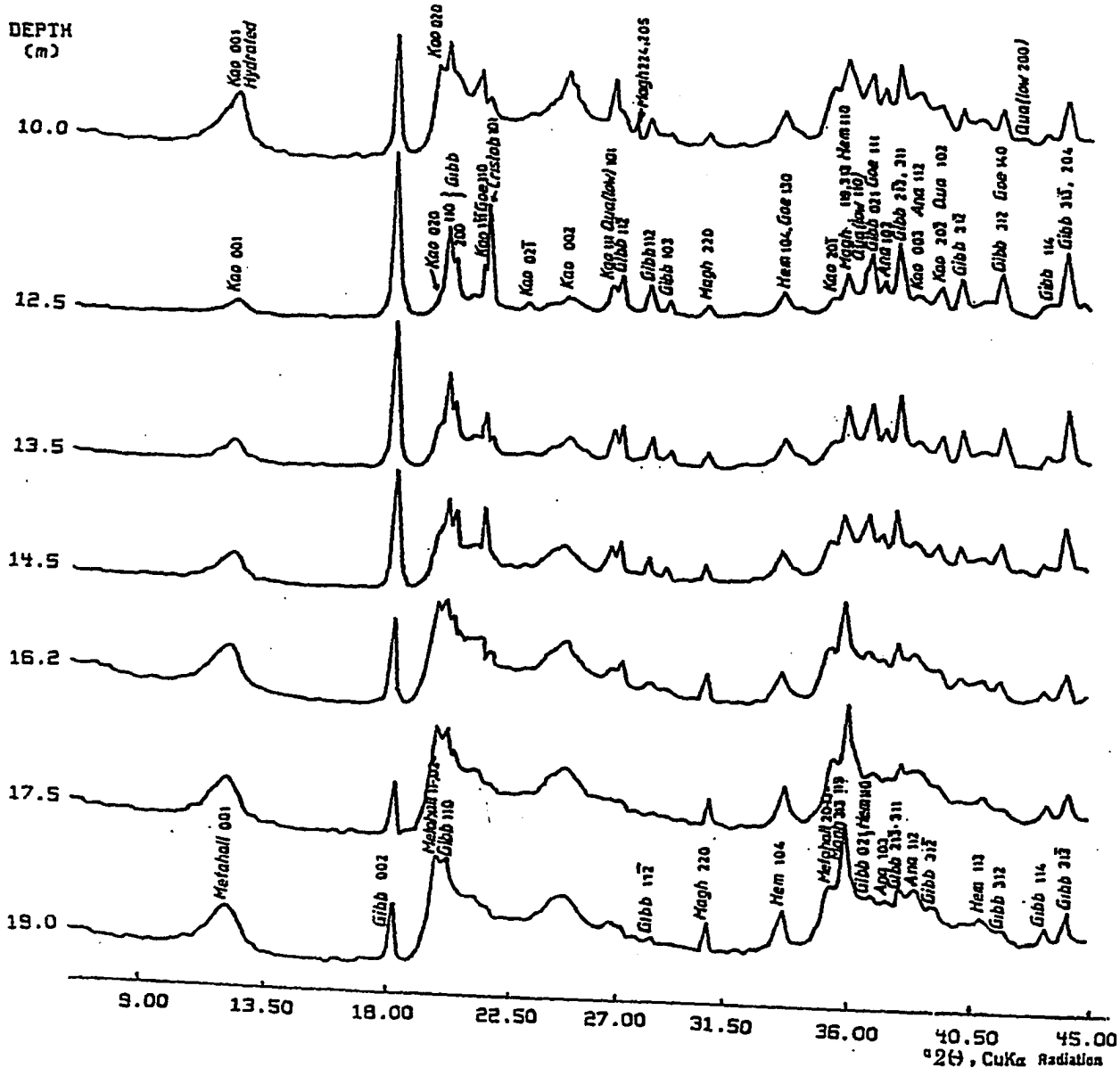

Fig. 39

X-Ray powder diffraction patterns along the lower horizon of profile S4 at Fondjoumetah

Table 4

Semi-quantitative mineralogy of profile S4 using x-ray powder diffraction data

++ dominant
+ minor
+0 trace
0 absent

SAMPLE NUMBER	gib	kao	goe	hem	magh	ana	qua	metah
S4/1.1	++	+	+	+	+0	+0	++	0
S4/2.4	++	+	++	+	+0	+0	++	0
S4/5.0	++	+0	++	+0	+0	+0	+	0
S4/6.0	++	0	+	+0	+0	+0	+	0
S4/7.0	++	+	+	+0	+0	+0	+	0
S4/8.5	++	++	++	+0	+0	+0	++	0
S4/10.0	++	++	++	+	+	+0	++	0
S4/13.5	++	0	++	+0	+0	+0	+	+0
S4/14.5	++	+	0	+	+0	+0	+	0
S4/16.2	++	0	0	++	+	+0	+0	++
S4/17.5	++	0	0	++	+	+0	0	++
S4/20.5	++	+0	0	+	+0	+0	0	0

Gibbsite and *goethite* are depleted in the lower part of the profile. They are primarily concentrated in the overlying detrital (transported) zone.

Metahalloysite is absent in the detrital zone. It is the dominant hydrated alumino-silicate in the lower half of the underlying weathered horizon. It is poorly crystallized and shows broad basal plane spacings which are suggestive of an irregular stacking sequence.

Fig. 40 shows a gradual increase with depth, in the weathered horizon of profile S4, of the basal-plane spacing of metahalloysite. This d-spacing changes from 7.228 Å half way into the weathered horizon to 7.326 Å at the base of the profile.

According to Brindley and Robinson (1948), the decrease of the basal spacing of metahalloysite is controlled by relative humidity, and is due to a decrease in the percentage of hydrated layers with respect to that of dehydrated layers.

Kaolinite is found in the detrital sequence and in the upper half of the underlying weathered clayey horizon. Its basal-plane spacing also increases with depth (Fig. 40) which is probably due to an increase of hydrated layers. The basal-plane spacing ranges from 7.118 Å near the surface to 7.14 Å at the base of the detrital horizon. It continues to increase with depth in the underlying weathered horizon, and reaches the value of 7.20 Å at a depth of 16.2 meters. Below this depth kaolinite is replaced by metahalloysite. A transition, therefore, takes place with increasing depth from kaolinite to metahalloysite. This transition is shown in fig. 40.

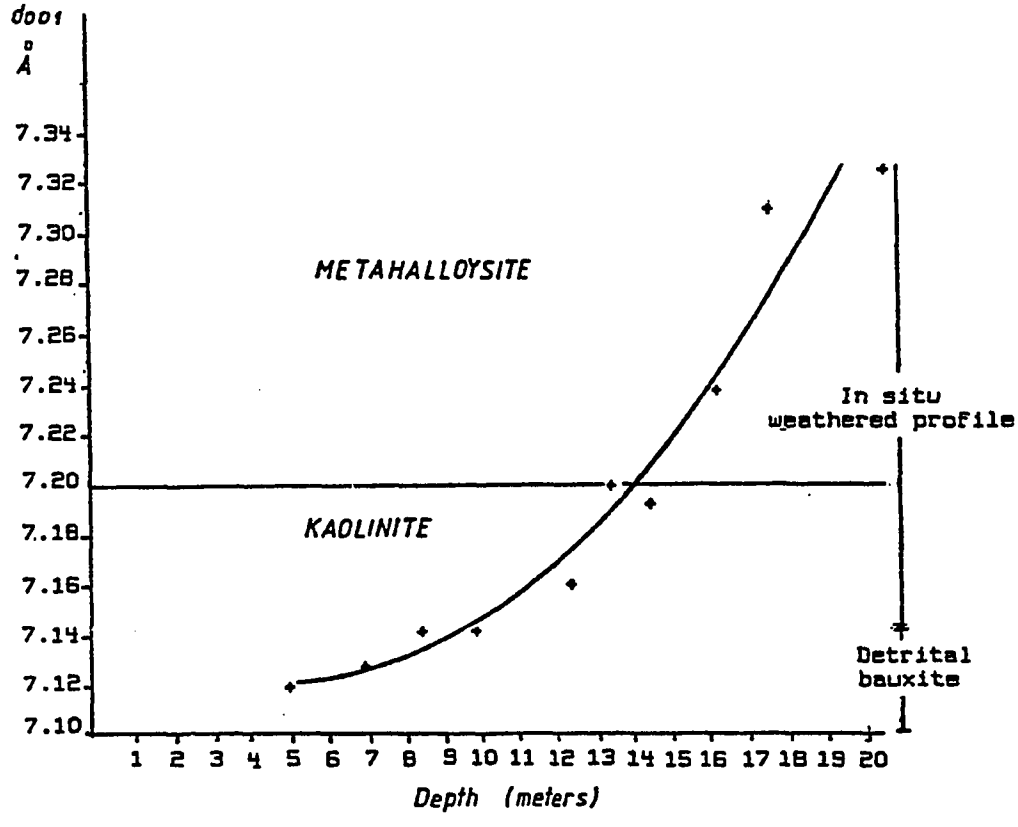

Fig. 40

Change with depth of the d001-spacing of metahalloysite and kaolinite along profile S4 at Fondjoumetah

The diffractograms suggest that kaolinite may have been concentrated near the surface perhaps through the kaolinitization of gibbsite. The reaction gibbsite + silica = kaolinite is known to be reversible (Valeton, 1972), and its evolution towards kaolinite is essentially a function of silica concentration in meteoric waters. Silica leached from the highest elevations may accumulate at the foot of the hill where it can react with gibbsite according to the following equation (Valeton, 1972):

$$Al_2O_3.3H_2O + 2H_4SiO_4 = 2SiO_2.Al_2O_3.2H_2O + 5H_2O$$

The behavior of the remaining minerals in the lower horizon of the profile is as follows:

Anatase occurs in trace amounts along the profile, but seems to increase with height. This apparent increase is perhaps attributable to an increase in crystallinity with height.

Hematite is a dominant mineral in the lower horizon of the profile. The relative intensity of its strongest diffraction maximum reaches 24 at the depth of 17.5 meters. Below this depth, it is progressively replaced by *maghemite*.

Cristobalite and *quartz* are present in trace amounts throughout most of the profile, but free silica is believed to have been underestimated because of the likely presence in the profile of x-ray amorphous silica.

Profile S5

This 7.5 meter-deep bore hole is located at the crest of Fondjoumetah hill, on top of a small bauxite hard cap which forms part of the Foundjoumetah deposit. The bore hole did not go any deeper because of mechanical problems with the drilling equipment. As a result, the bottom of the duricrust was not reached. The mineralogy of profile S5 is shown in fig. 41 and table 5, and is identical to that found in the duricrust of S2 at Fongo Tongo.

X-Ray Powder Diffraction Study of Loose Whitish Material from Above the Dark Trachyte Weathering Front South of the Fongo Tongo Deposit

A weathering profile of the Fongo Tongo dark trachyte was described above. This profile is located along a road cut south of the Fongo Tongo deposit (Fig. 16). It shows a friable white weathering product that overlies the weathering front of the Fongo Tongo dark trachyte, and locally rims fresh trachyte blocks. This material was sampled, and its x-ray powder diffraction pattern is shown in fig.42.

The powder diffraction pattern has two poorly defined broad maxima at the angular intervals 2° to 10° and 20° to 22° 2θ using CuKα radiation. A slow scan over the low-angle range shows poorly defined maxima at d-values of 26.1, 21.0, 15.8, and 10.0 Å, but, given the low resolution of d-values at very small angles, the 26.1 Å and 21.0 Å d-values were discarded. The high-angle (20° to 22° 2θ) maximum has a d value of 4.44 Å. Two discrete minerals are suggested by this pattern, namely, a 10.0 Å clay mineral and an unknown poorly crystallized phase as indicated by d-values in the angular range of 20° to 22°. Additional

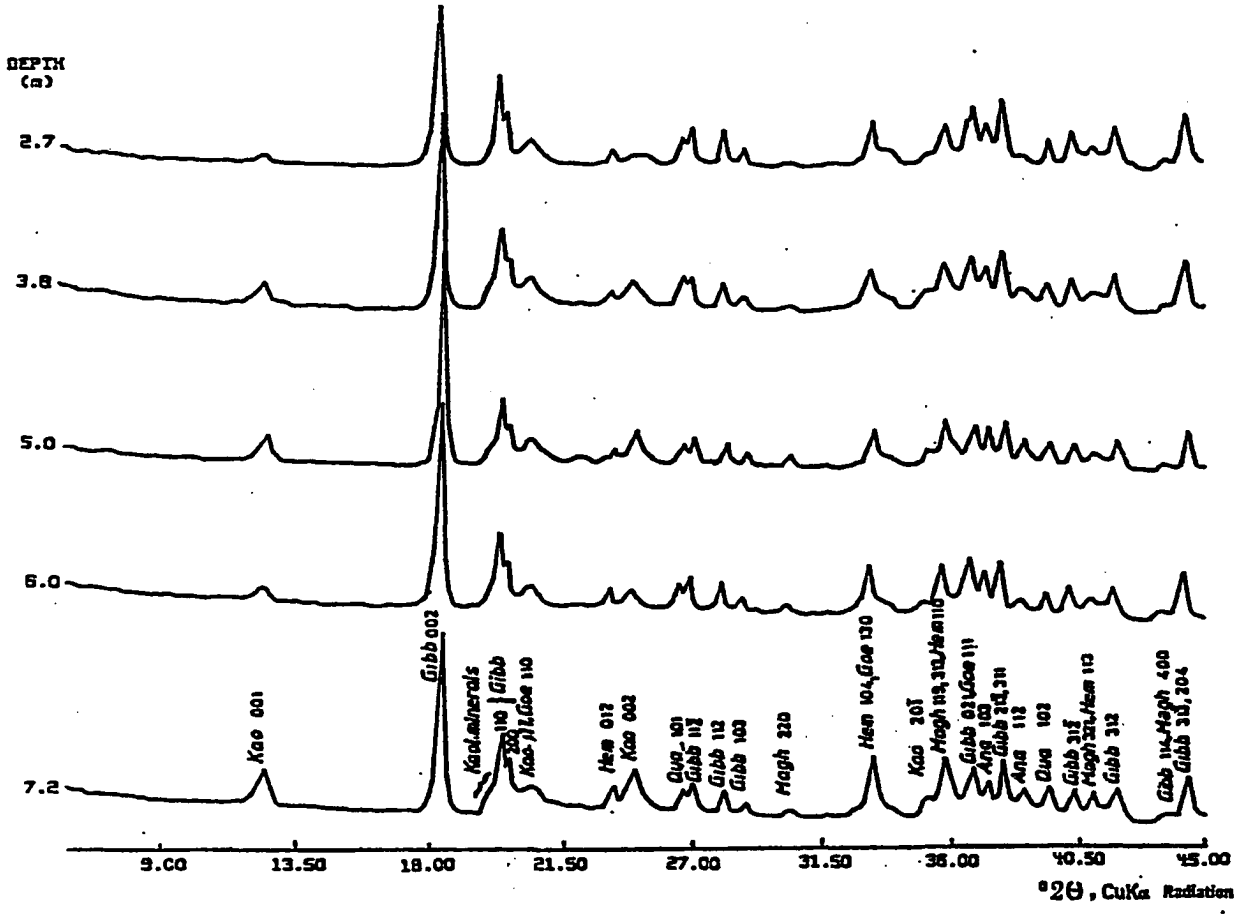

Fig. 41

X-Ray powder diffraction patterns along profile SS at Fondjoumetah

Table 5

Semi-quantitative mineralogy of profile S5 using x-ray powder diffraction data

++ dominant
+ minor
+0 trace
0 absent

SAMPLE NUMBER	gib	kao	goe	hem	magh	ana	qua	metah
S5/2.5	++	+0	+0	+	+0	+0	+	0
S5/3.2	++	+0	+0	+	+0	+0	+	0
S5/5.0	++	+0	+0	+0	+0	+0	+0	0
S5/6.0	++	+0	+0	+	+0	+0	+0	0
S5/7.2	++	+	+0	+	+0	+0	+0	0

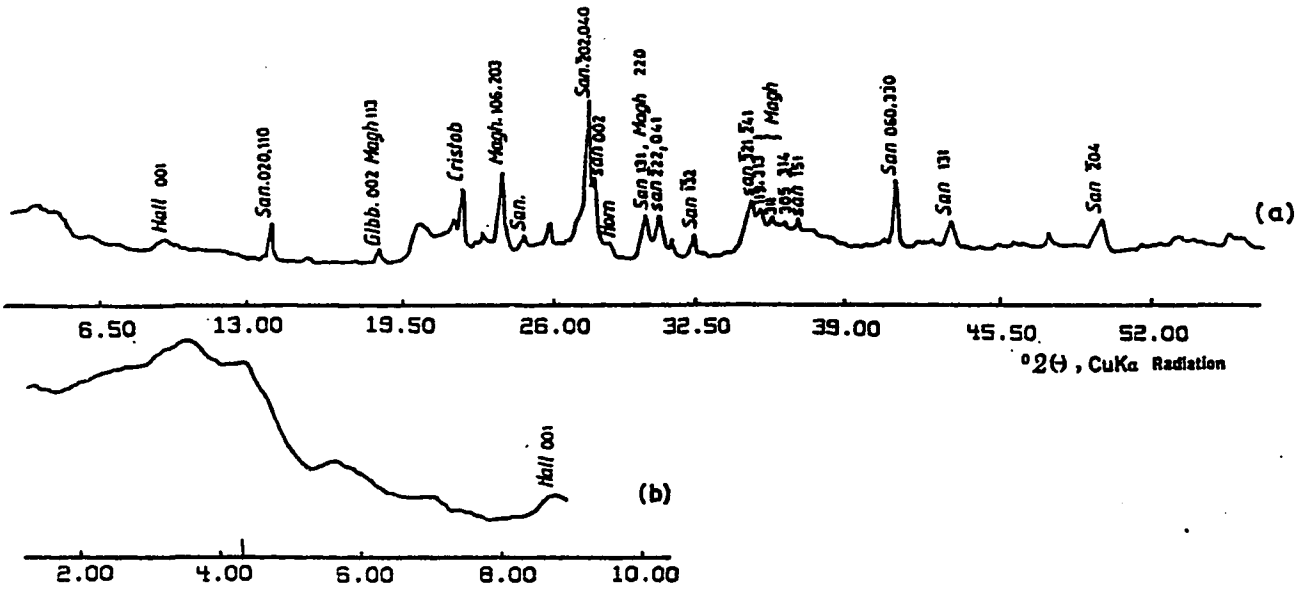

(a) Fast scan
(b) Slow scan

Fig. 42

X-Ray powder diffraction patterns of whitish friable material sampled above the weathering front of the dark trachyte

d-spacings suggest that the 10.0 Å-clay mineral is *hydrated halloysite*. The reflections obtained for this mineral are: d_{001}, d_{11} and d_{20}.

Further examination of the data reveals that the broad maxima obtained at the higher angle range correspond to those assigned by Wada and Yoshinaga (1969) to imogolite, a poorly crystalline hydrated aluminum silicate. Transmission electron microscopy, however, failed to confirm the presence of this mineral in the sample.

This sample also contains subordinate maghemite and minor gibbsite, as well as residual high sanidine and hornblende from the underlying dark trachyte.

Three sample fractions were heated at 80°C, 230°C and 380°C respectively for 3 hours to determine phase changes with increase in temperature.

After heating in air at 80°C, the sample gives an x-ray diffraction pattern with a characteristic maximum which corresponds to the (001) reflection plane of dehydrated halloysite (Fig. 43a). The d_{001} spacing obtained is 37 Å. Additional dehydrated halloysite reflections shown by the pattern are $d_{20,13}$ and $d_{33,06}$.

Heat treatment of the sample at 80°C, therefore, results in the collapse of the basal spacing of hydrated halloysite from 10.0 Å to that of a 7.35 Å dehydrated halloysite.

When the sample is heat treated at 230°C, metahalloysite dehydrates into kaolinite. Kaolinite reflections obtained are the followings: d_{001}, d_{002}, $d_{201,130}$, d_{004} and $d_{060,331}$.

When heat treated at 380°C the kaolinite d_{001} peak becomes sharper, which indicates an increase in crystallinity (Fig. 43b), and

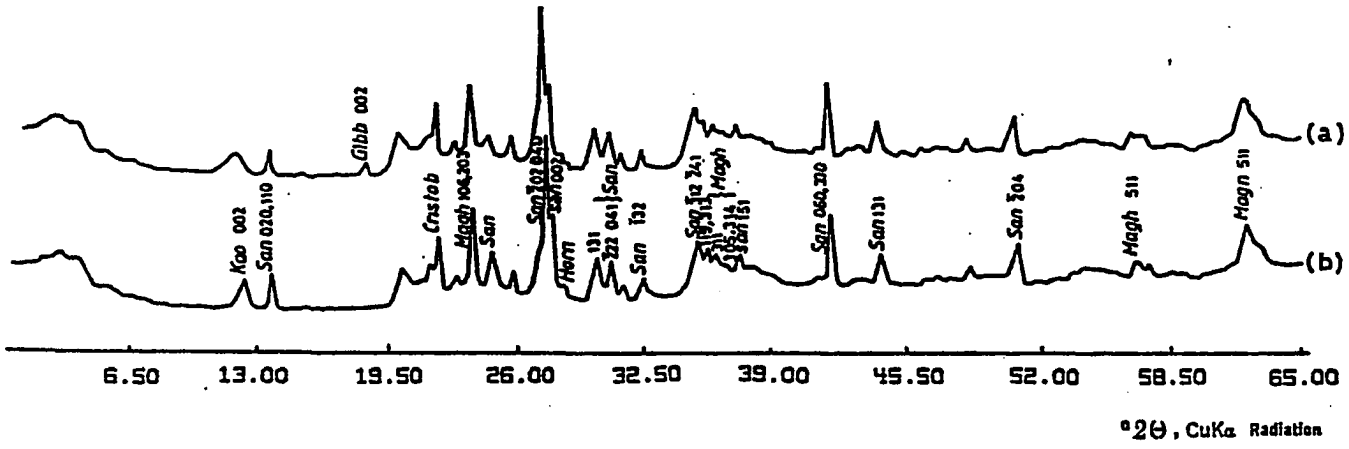

Fig. 43

X-Ray powder diffraction patterns of the dark trachyte weathering product heated respectively at 80°C (a) and 380°C (b).

the d_{002} gibbsite peak disappears. The presence of reflections at 2.05, 1.60, and 2.55 Å d-spacings suggests that gibbsite has dehydrated into corundum.

To sum up the results of these experiments, the hydrated secondary aluminum minerals identified above the weathering front of the Fongo Tongo trachyte are the following:

(1). *Hydrated Halloysite*: This mineral has a very low degree of crystallinity and dehydrates rapidly with increase in temperature, yielding a 7.35 Å halloysite also known as metahalloysite. With increasing temperature, metahalloysite dehydrates into kaolinite.

(2). *Gibbsite*: This mineral is present in limited quantities in the sample.

The field and laboratory data, therefore, suggest that hydrated halloysite is the first hydrated alumino-silicate produced during the weathering of the Fongo Tongo trachyte. The paragenesis suggested experimentally for hydrated alumino-silicates is as follows:

Hydrated halloysite ⇒ metahalloysite ⇒ kaolinite

The x-ray powder diffraction data obtained from the samples collected at the base of bore hole S4, which is collared at the foot of Fondjoumetah hill, have also shown that metahalloysite forms before kaolinite in that area. It is concluded that hydrated halloysite would have been found below the bottom of this profile had the drilling gone any deeper.

The above hydrated alumino-silicate paragenesis may, therefore, be generalized for all the weathering profiles in the study area, regardless of the nature of the parent rocks.

According to these findings, the various weathering stages which lead to bauxitization in the Fongo Tongo and related areas may be summarized as follows:

(1). Weathering begins with the breakdown of the parent rock and the formation of a gel from which hydrated halloysite nucleates.

(2). Hydrated halloysite undergoes a progressive decrease in basal-plane spacing with decrease in depth, as a result of dehydration, and ultimately yields kaolinite.

(3). Kaolinite, in turn, undergoes desilication and breaks down into gibbsite. This stage is demonstrated in the mottled clay horizon of S2 profile.

(4). A fourth stage, which has been described in the section on microtexture and petrography, is related to lateral and vertical transportation of Al^{3+} and Fe^{3+} ions through the duricrust and their subsequent reprecipitation in voids and cracks as hydrated oxides of aluminum and iron.

Gibbsite has been found near the protolith, together with halloysite, but this assemblage is unstable as will be shown in a subsequent section.

The paragenesis of ferric oxide minerals was also studied along the profiles. From bottom to top, the ferric oxide minerals found along profile S4 are successively maghemite, hematite and goethite. Replacement of magnetite by maghemite during weathering of the parent

rocks is indicated by these results. A fraction of the maghemite may also have been formed from iron transported during weathering. Maghemite is subsequently replaced by hematite higher in the profile, and hematite by goethite upon hydration at even higher levels in the profile.

Conclusions Based on X-Ray Powder Diffraction Studies

The mineralogy of the Fongo Tongo and genetically related bauxite deposits consists of the following: gibbsite, goethite, kaolinite, hydrated halloysite, metahalloysite, magnetite, maghemite, hematite, anatase and quartz. Study of the paragenesis of aluminum- and iron-bearing minerals in these deposits suggests an *in situ* weathering profile. A theoretical cross-section from the top to the bottom of the profile includes, respectively, a duricrust, a mottled clay horizon, and a soft clayey horizon which overlies the weathering front. The mineralogy of the duricrust is dominated by gibbsite, the other minerals being present in minor or trace amounts. The mottled clay horizon is characterized by kaolinite and gibbsite which vary antipathetically with height. The whitish clayey horizon beneath the mottled clay horizon is characterized by the presence of halloysite in its lower section and by the presence of metahalloysite in the upper part.

Field observations and laboratory experiments suggest that hydrated halloysite is the first hydrated alumino-silicate to form during the breakdown of parent rocks, and that hydrated halloysite undergoes dehydration with height in the weathering profile and successively gives way to metahalloysite and kaolinite at higher levels.

By contrast, the mineralogy of profile S3 at Melan shows that there is no gradation between the upper 3.0 meter-thick unit which

consists of saprolite boulders on the one hand, and the underlying fresh greenish trachyte on the other. Furthermore, the two lithologic units are separated by a sharp unconformity on top of which the saprolite boulders were deposited.

The following section is a discussion on the stability of the aluminum- and iron-bearing mineral assemblages found in the Fongo Tongo and similar areas. This discussion is based on the current literature and on the conclusions reached in the preceeding sections, and allows a better understanding of the various mineral assemblages found in the Fongo Tongo and areally related bauxite deposits.

PARAGENESIS OF ALUMINUM- AND IRON-BEARING MINERALS IN THE FONGO TONGO AND RELATED BAUXITE DEPOSITS

Paragenesis of Aluminum-Bearing Minerals

The following secondary aluminum-bearing mineral assemblages have been found in the weathering profile of Fongo Tongo and similar deposits from top to bottom:

(1). In the duricrust:

gibbsite, kaolinite (minor, trace or absent)

(2). In the mottled clay horizon:

kaolinite, gibbsite

(3). In the whitish clayey horizon:

metahalloysite, gibbsite

(4). Above the weathering front:

hydrated halloysite, gibbsite

In order to predict the stability of these assemblages along the weathering profile, a thermodynamic approach proposed by Kittrick (1969) is used here. This approach uses the stability diagram of various hydrated aluminum minerals in the Al_2O_3 - SiO_2 - H_2O system at 25°C and 1 atm. The minerals chosen for this study are halloysite, kaolinite, gibbsite and amorphous silica. Amorphous silica has been added here because it is a key constituent in weathering environments (Kittrick, 1969).

According to Kittrick (1969), the solubility values for amorphous silica range between 115 ppm and 150 ppm SiO_2, which corresponds to the pH_4SiO_4 ($-\log H_4SiO_4$) range of 2.60 to 2.72. If $pH_4SiO_4 = X$, the solubility range for amorphous silica can be expressed as follows:

$$2.60 \leq X \leq 2.72 \qquad (1)$$

Kaolinite and halloysite can be considered as hydrated aluminosilicate polymorphs having different standard free energies. Their hydrolysis reaction is as follows:

$$Al_2Si_2O_5(OH)_4 + 6H^+ = 2Al^{3+} + 2H_4SiO_4 + H_2O \qquad (2)$$

$$k = [Al^{3+}]^2[H_4SiO_4]^2/[H^+]^6$$

$$\log k = 2\log[Al^{3+}] + 2\log[H_4SiO_4] - 6\log[H^+]$$

$$\log k - 2\log[H_4SiO_4] = 2\log[Al^{3+}] - 6\log[H^+]$$

$$1/6\log k - 1/3\log[H_4SiO_4] = -\log[H^+] + 1/3\log[Al^{3+}]$$

$$-1/6pk + 1/3pH_4SiO_4 = pH - 1/3pAl^{3+} \qquad (3a)$$

The quantity $pH - 1/3pAl^{3+}$ is the aluminum hydroxide potential (Kittrick, 1969). Equation (3) is of the form

$$y = ax + b \quad \text{with } y = pH - 1/3pAl^{3+} \qquad (3b)$$

$$x = pH_4SiO_4$$

$$a = 1/3$$

$$b = -1/6pk$$

From equation (2) the standard free energy can be written as follows (Kittrick, 1969):

$$G^\circ_f = 2G^\circ_{Al} + G^\circ_{H4SiO4} + G^\circ_{H2O} - 6G^\circ_H - G^\circ_{kao/halloy}$$

For the calculation of $G_o\zeta$, the following standard free energy values (Krauskopf, 1979) have been used:

G°_{Al} = -116 kcal/mole G°_{H4SiO4} = 312.5 kcal/mole

G°_H = 0 " G°_{H2O} = -56.7 "

G°_{kao} = -903.0 " G°_{halloy} = -898.6 "

For a reaction at 25°C, the relation between the standard free energy and the equilibrium constant is:

$$G^\circ = 1.364pk \qquad \text{(Krauskopf, 1979)}$$

For kaolinite, G°_f = -10.7 kcal/mole = 1.364pk

and pk = -7.845

From equation (3b) we obtain:

$$y_{kao} = 1/3x + 1.36 \qquad (4)$$

For halloysite, G°_f = -15.1 kcal/mole = 1.364pk

and pk = -11.07

From equation (3b) we obtain:

$$y_{halloy} = 1/3x + 1.84 \qquad (5)$$

Equations (4) and (5) delineate the stability of kaolinite and halloysite.

Gibbsite hydrolysis reaction is as follows:

$$Al(OH)_3 + 3H^+ = Al^{3+} + 3H_2O \qquad (6)$$

$$k = [Al^{3+}]/[H^+]^3$$

$$\log k = \log[Al^{3+}] - 3\log[H^+]$$

$$-1/3\log k = \log[H^+] - 1/3\log[Al^{3+}]$$

$$-1/3pk = pH - 1/3pAl^{3+} = y$$

$$y_{gibb} = -1/3pK \qquad (7)$$

From (6), $H°_f = 3G°_{Al} + 3G°_{H2O} - G°_{gibb} - 3G°_{H+}$

with $G°_{gibb} = -273.4$ kcal/mole (Krauskopf, 1979),

$$G°_f = -11.7 \text{ kcal/mole} = 1.363pk$$

$$pk = -8.58$$

$$y_{gibb} = 2.86 \qquad (8)$$

Equation (8) delineates the stability line for gibbsite. When plotted, equations (1), (4), (5) and (8) represent the stability diagram for amorphous silica, kaolinite, halloysite and gibbsite in the Al_2O_3 - SiO_2 - H_2O system at 25°C and 1 atm (Fig. 44). Since this is a three-component system and each one of the stability lines represents two phases, the mineral and the solution, the system theoretically has three degrees of freedom. But in the weathering environment, two degrees of freedom are fixed, pressure and temperature as we have stated above. This leaves the system with only one degree of freedom, namely composition.

The intersection between two stability lines represents an invariant point where the two corresponding minerals are at equilibrium with the solution. The most stable mineral supports the lowest aluminum hydroxide potential for a given H_4SiO_4 activity (Kittrick, 1969). Halloysite is therefore metastable throughout the entire pH_4SiO_4 range. It is indeed known to be a rapidly formed metastable precursor to

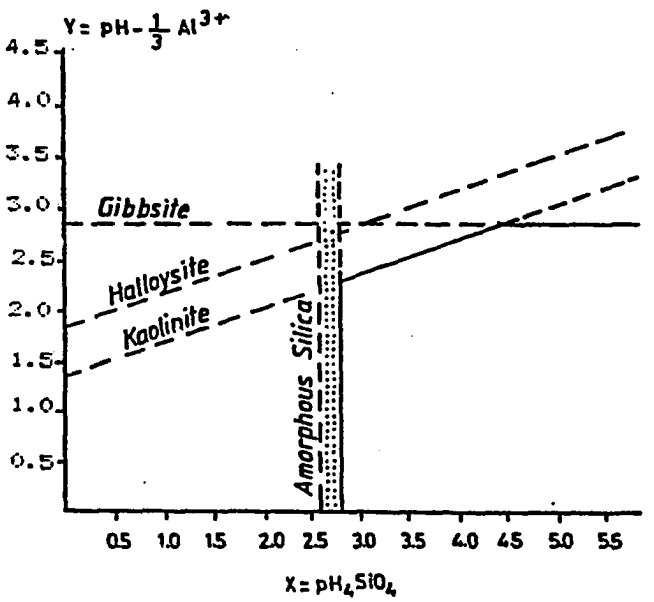

Fig. 44

Stability diagram for amorphous silica, kaolinite, halloysite and gibbsite after Kittrick, 1969. The stability line of each mineral is solid in the area where it is the most stable mineral. The solubility of amorphous silica ranges between x values of 2.60 and 2.72.

crystalline kaolinite (Kittrick, 1969). According to Kittrick and based on the x-ray diffraction results of this study, there is a gradation within the weathering profile from halloysite to kaolinite. The stable range of the stability lines has been drawn with a solid line. Based on the conclusions reached through this discussion, the only stable assemblage is kaolinite-gibbsite. Halloysite-gibbsite is metastable under weathering conditions

Transitional hydrated aluminum mineral assemblages, therefore, exist along the weathering profile of the Fongo Tongo and similar deposits. The kaolinite-gibbsite assemblage is met in the mottled clay horizon, but kaolinite decreases gradually with height in this horizon due to the removal of silica. According to the x-ray powder diffraction data, the invariant point between the stability lines of kaolinite and gibbsite is only found in the duricrust.

Paragenesis of Iron-Bearing Minerals

The following paragenesis was found along the profiles from bottom to top for secondary iron oxides and hydroxides:

maghemite ⇒ hematite ⇒ goethite

The transition from magnetite to maghemite occurs through a continous but metastable solid-solution series which exists between these two end-members (Lindsley, 1976). Maghemite is characterized by an iron deficient (vacancy) spinel structure which may form during the breakdown of magnetite-bearing rocks through oxidation of magnetite under hydrous conditions (Lindsley, 1976) as follows:

$$Fe^{2+}Fe_2^{3+}O_4 \rightarrow Fe_2^{3+}Fe_{2/3}^{3+}()_{1/3}O_4 \quad \text{or } \gamma\text{-}Fe_2O_3$$

Maghemite is, in turn, metastable with respect to hematite under surficial conditions (Mason, 1943). This paragenetic relationship has been confirmed in the present study, i.e. maghemite is located in the vicinity of the parent rocks and in the bottom of the bore holes; it disappears with height in the weathering profile and is replaced by hematite.

Under the influence of exogenic conditions, hematite is replaced by goethite. The transition from hematite to goethite is a climate-dependent reversible reaction which involves very little energy, its enthalpy being only 4.0kcal (Bardossy, 1982). The reaction is as follows:

$$\alpha\text{-}Fe_2O_3 + H_2O = 2FeO.OH$$

hematite goethite

The reason why the early gel first evolves towards the dehydrated solid solution maghemite-hematite is probably related to the low polarizing power of Fe^{3+} ions, which, according to Gastuche et al. (1964), seem unable to fix hydroxyls from water. Goethite later starts crystallizing with height in the profile when more OH^- ions are provided by meteoric water, and a corresponding decrease in hematite is noticed in the profile.

MINERALOGY AND CRYSTALLOGRAPHY OF "CAMEROONITE",

A SUPERGENE MANGANESE HYDROXIDE

X-Ray Powder Diffraction and Electron Microscopy Studies

Blue-black aphanitic blocks of a secondary mineral occur within the bauxite profile, about 1.5 to 2.0 meters below the surface. They vary in size and shape, and some reach 30 centimeters in diameter. An x-ray powder diffraction pattern of this material (Fig. 45) shows that its diffraction lines correspond to those assigned to vernadite, a poorly crystalline supergene manganese hydroxide with the approximate formula $MnO_2.nH_2O$ (Betekhtin, 1937; 1940).

According to the description by Betekhtin, vernadite has a chocolate-brown streak with a resinous luster. Its diffraction pattern with the most ordered structure shows three characteristic reflections at d ≃ 2.4 Å, d ≃ 2.2 Å and d ≃ 1.4 Å (Chukhrov et al., 1978).

The corresponding reflections in Angstrom units of the unknown mineral occur at 2.387(121), 2.197(240), and 1.4239(002). This unknown mineral also has additional reflections at 3.102(130), 2.829(141), 2.15(301) and 1.544(251). Most of its reflections correlate with those assigned to vernadite in the JCPDS file in which vernadite is defined as pseudo-tetragonal with the following lattice parameters (McClune et al., 1980):

$a_0 = 9.866$ Å $\qquad c_0 = 2.844$ Å

Vernadite was subsequently redefined in a recent study (Chukhrov and Gorshkov, 1981) as a hexagonal mineral, with the following unit cell parameters:

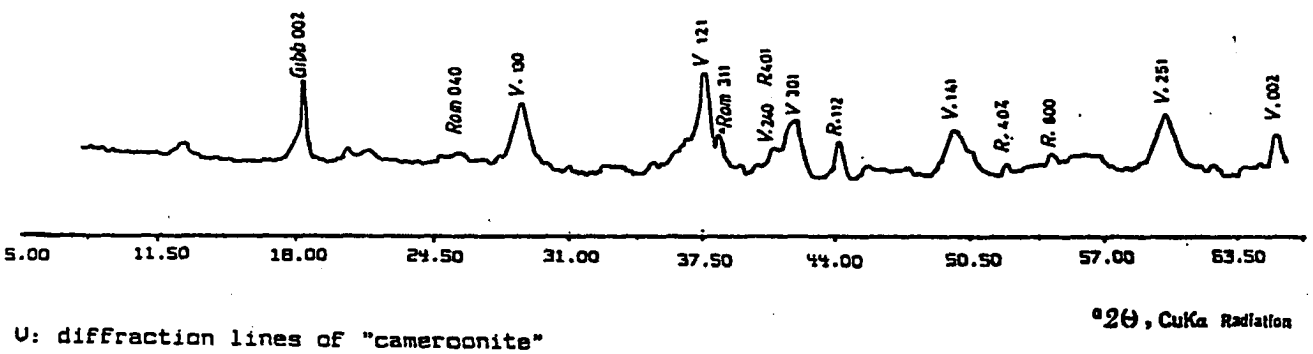

V: diffraction lines of "cameroonite"

Fig. 45

X-Ray powder diffraction pattern of "cameroonite"

a_0 = 2.86 Å c_0 = 4.7 Å

In order to determine whether the lattice parameters of the unknown mineral are identical with those recently reported for vernadite by Chukhrov and Gorshkov (1981), they were refined using the revised Appleman-Evans least-squares computer refinement program (Benoit, 1987). The results obtained reveal that the lattice parameters of this mineral do not match those found by Chukhrov and Gorskhov for vernadite. When the lattice parameters given in the JCPDS file are used for a tentative match, and a tetragonal symmetry is assigned to the unknown mineral, the following unit cell parameters are obtained for this mineral:

a_0 = 9.84 Å c_0 = 2.846 Å

These findings suggest that this mineral has a tetragonal symmetry, and that its unit cell parameters are closer to the ones originally assigned to vernadite. The EDS qualitative analysis (Fig. 46) and whole rock analyses (Table 6) of this unknown manganese mineral reveal a relatively high potassium content. It contains 1.74 wt% K_2O as opposed to 0.23 wt% to 0.60 wt% in vernadite. Vernadite contains between 2 wt% and 5 wt% CaO (Chukhrov and Gorskhov, 1981), whereas the unknown mineral has only 0.03 wt% CaO. EDS qualitative analysis also shows that the unknown mineral contains a fairly high amount of barium, but the percentage of barium was still unknown at the time of this writing . Nevertheless, the chemical analyses reported in table 6 suggest that the proportion of barium in the unknown mineral may reach 16 wt%. Because of these chemical and crystallographic differences, it is probable that we are dealing with a new manganese mineral. The name "cameroonite" will be proposed for this mineral. "Cameroonite" could be

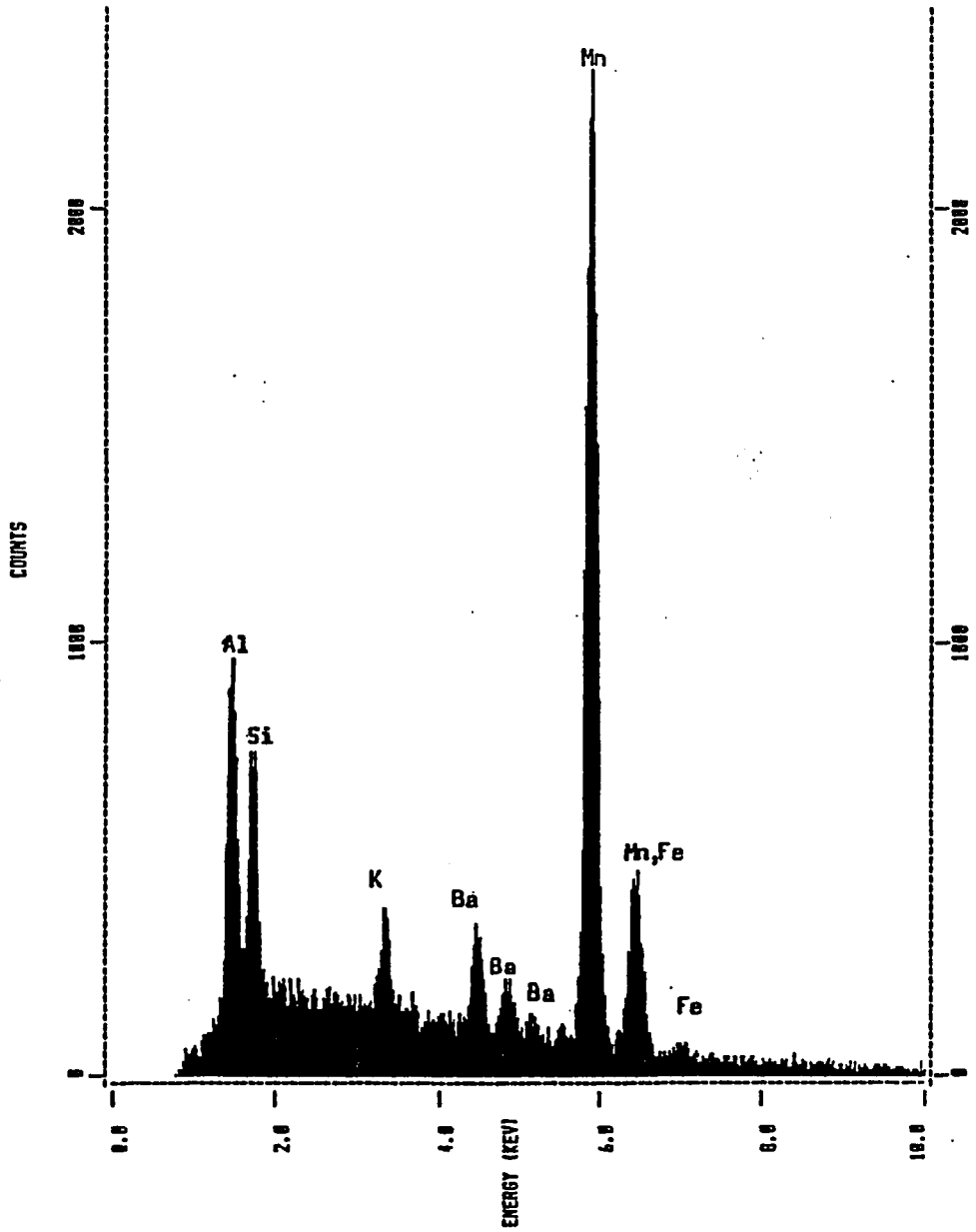

Fig. 46

EDS Qualitative analysis of "Cameroonite"

Table 6

Chemical analyses of "cameroonite" and vernadite
(*) Chukhrov et al., 1980

	"cameroonite"	vernadite(*)	
SiO_2	5.58	0.80	1.30
Al_2O_3	8.79	1.00	1.00
CaO	0.03	2.15	5.17
MgO	0.01	2.62	0.28
K_2O	1.74	0.60	0.23
Fe_2O_3	11.7	10.45	7.00
FeO			<0.1
MnO_2	47.8	46.47	56.45
MnO		1.09	4.81
P_2O_5	0.08	0.00	1.30
H_2O^+	1.1	6.94	3.00
H_2O^-	7.1	18.50	15.33
SrO		0.00	0.33
BaO		0.00	1.93
CoO		3.41	0.00
NiO		0.95	0.00
PbO		0.34	0.00
TiO_2		1.50	0.00
CO_2		0.00	3.70
Cl		1.19	0.00
	83.93	100.32	100.15

a chemical variant of vernadite, and may result from the distorsion of vernadite lattice due to the presence of large cations (K, Ba). Small peaks of romanechite, a manganese-bearing oxy-hydroxide, were also identified in the pattern. At the time of this writing, no technique seems appropriate to separate romanechite from the unknown mineral, but romanechite is only present in trace amounts.

Infrared Spectroscopy of "cameroonite"

Principles of Infrared Spectroscopy

When a molecule is irradiated with infrared light, it may absorb a given radiation if that radiation has the same energy as the vibration or rotation transitions of the molecule (Van der Marel and Beutelspacher, 1976). Vibrations are of two kinds, namely, the stretching vibrations which are characterized by extension and contraction of the chemical bond, and deformational vibrations which result from a periodic bending of the bond.

A vibration is infrared-active if a change in the dipole moment of the molecule occurs during vibration. The frequency of a vibration in a molecule depends on the mass of the atoms, the forces acting between them and the interaction with the surroundings (Van der Marel and Beutelspatcher, 1976). The unit commonly used is the number of waves per centimeter, also called wavenumber (cm^{-1}).

Mineral identification using infrared spectra is done by comparing unknown and known spectra. The nature of the frequencies can usually be assigned, and the structure of the unknown may be inferred.

Study of the "cameroonite" Spectrum

The study of the infrared spectrum of this mineral (Fig.47) has led to the identification of the following absorption bands:

Hydrogen Bonds

Absorption bands related to the stretching vibrations of O-H occur between $3200cm^{-1}$ and $3720cm^{-1}$. Two sharp bands are present, one centered at $3620cm^{-1}$ and the other at $3690cm^{-1}$. Molecular water is also present. It is expressed in the region of bending vibrations by an absorption band centered at $1660cm^{-1}$.

Comparative Study with Known Spectra

Comparative study of the spectrum of "cameroonite" with that of pyrolusite, friedelite, yellow-ocher limonite and hematite (Ferraro, 1982) led to the following correlations:

(1). The vibration bands of "Cameroonite" and pyrolusite (MnO_2) (Fig. 48b) show a match in the area between $400cm^{-1}$ and $700cm^{-1}$ where the main "cameroonite" absorption band lies. The band is bifurcated and shows two minima. The first minimum centers at $700cm^{-1}$ for both minerals. The second minimum occurs in the $600cm^{-1}$ - $400cm^{-1}$ region, but the single absorption band in the pyrolusite spectrum is doubled in the "cameroonite" spectrum, perhaps because of a more complex distribution of MnO_6 octahedra in this mineral or perhaps because of the presence in the "cameroonite" sample of limited admixtures of romanechite, another manganese bearing mineral. This correlation, therefore, suggests that "cameroonite" vibration bands in this region are due to the interaction between tetravalent manganese (Mn^{4+}) and oxygen as in pyrolusite, and that manganese is also in 6-fold coordination.

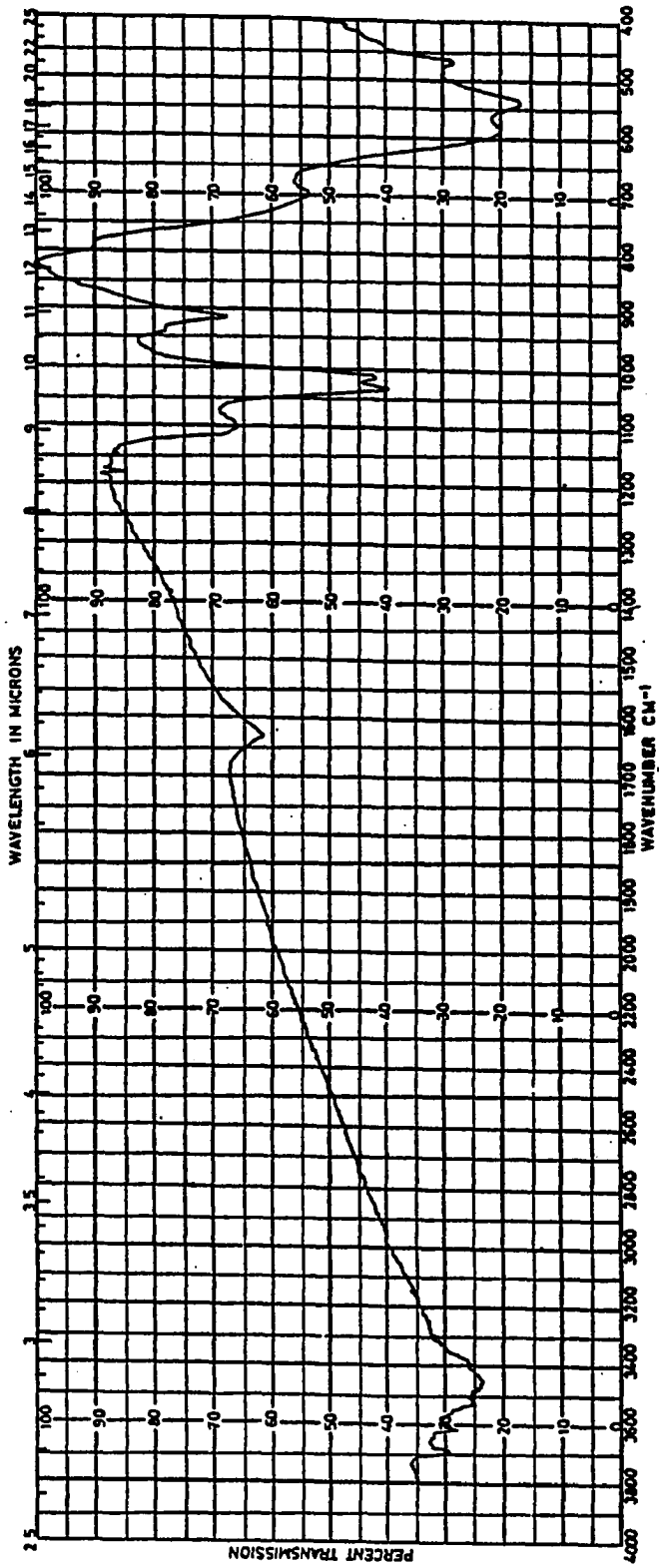

Fig. 47

Infrared spectrum of "cameroonite"

(2). The vibration bands in the region between 700cm^{-1} and 1200cm^{-1} correlate well with those of friedelite [$(Mn,Fe)_8Si_6O_{18}(OH,Cl)_4 3H_2O$] in the same range (Fig. 48c). One sharp doublet is located between 1000cm^{-1} and 1050cm^{-1} on both spectra. A discrete band which appears on the friedelite spectrum at 960cm^{-1} correlates with an equally small one found at 940cm^{-1} on the "cameroonite" spectrum. A similar correlation has been found in the same range between the spectrum of "cameroonite" and that of the yellow ocher variety of limonite $HFeO_2$ (Fig. 48d). Both spectra have the same characteristic band at about 900cm^{-1}, and a doublet in the 1000cm^{-1} - 1100cm^{-1} range. The similarities shared by the spectra of "cameroonite", friedelite and yellow ocher limonite are considered to be due to Fe^{3+} which is present in the three minerals. This conclusion is supported by the infrared spectrum of hematite which has similar absorption bands, one in the 1000cm^{-1} - 1100cm^{-1} range, and the other at 910cm^{-1} (Fig. 48e).

Comparative Study of "Cameroonite" and Vernadite Infrared Spectra

A comparative study of the infrared spectrum of "cameroonite" and that of vernadite (Fig. 49) results in the following:

(1). Both minerals have absorption bands assigned to their molecular water. This water is revealed in the "cameroonite" spectrum by an absorption band centered at 1633cm^{-1}. This absorption band is doubled in the vernadite spectrum and shows two minima at 1630cm^{-1} and 1550cm^{-1} (Chukhrov et al., 1978).

(2). The "cameroonite" spectrum has absorption bands in the 3200cm^{-1} - 2720cm^{-1} region which are considered to be due to a weak hydrogen bond between the MnO_6 octahedra and the hydrogen of molecular

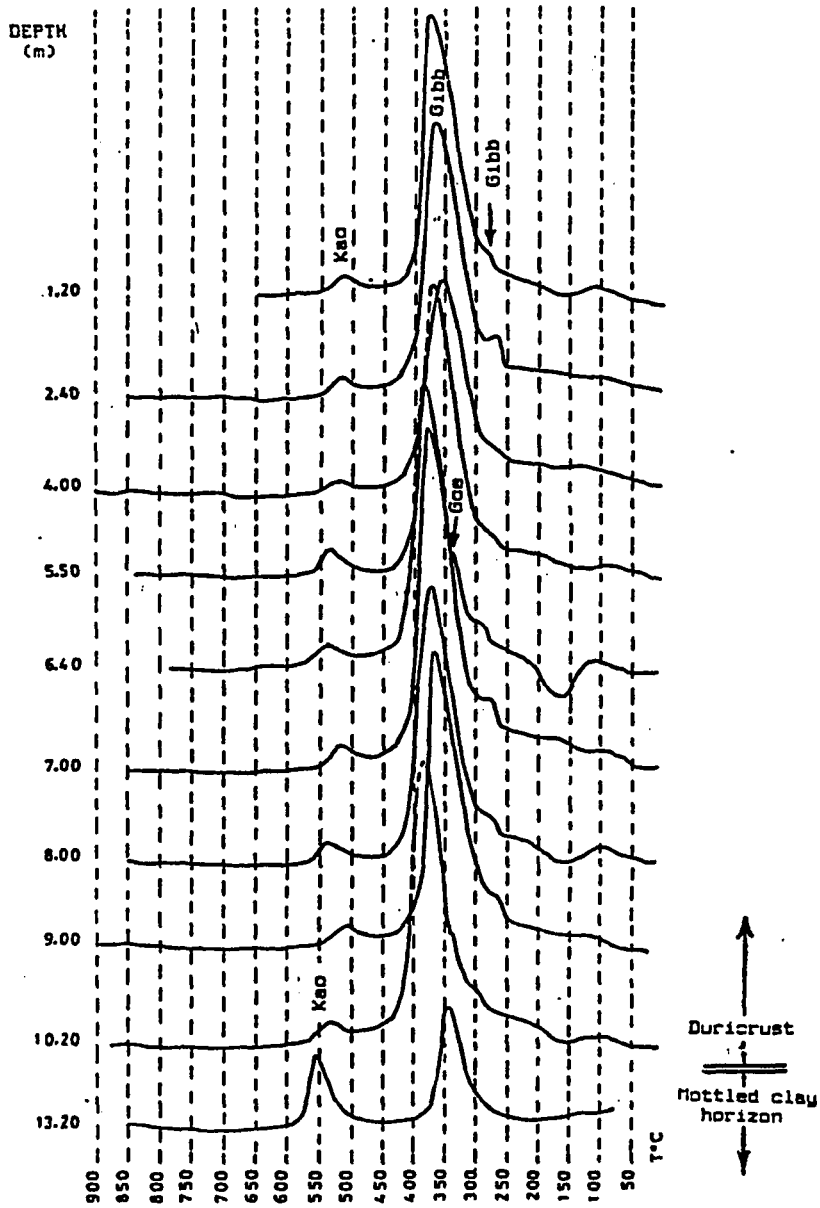

Fig. 50

DTA curves of samples from profile S2

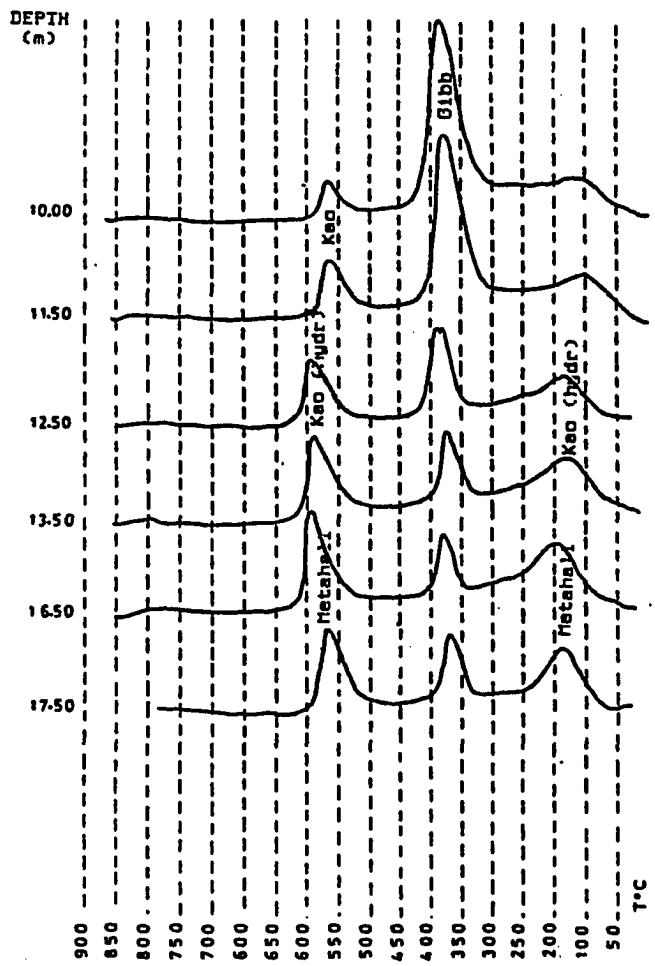

Fig. 51

DTA curves of samples from profile S4

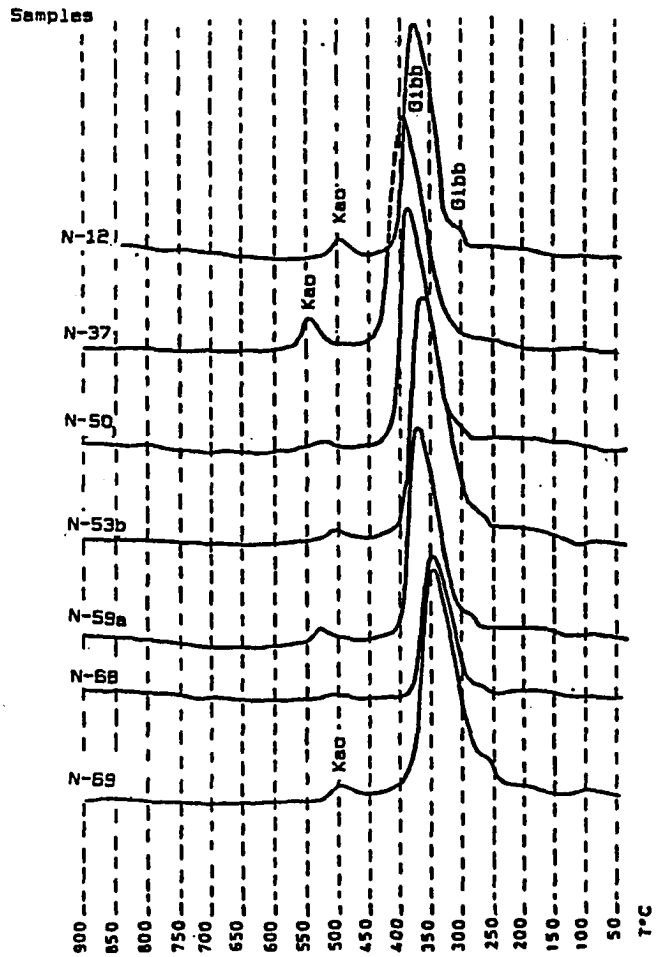

Fig. 52

DTA curves of bauxite outcrop samples

Goethite

Goethite has an unresolved thermal peak which sometimes forms a shoulder on the low-temperature slope of the gibbsite main peak. However the peak provides little information on the concentration of this mineral along the profile.

Profile S4

Additional analytical data on the paragenesis of hydrated aluminum minerals are provided by the DTA study of the weathered horizon of profile S4. This horizon underlies a 10-meter-thick detrital sequence made up of colluvial material. The results of this study are as follows:

Metahalloysite

This mineral is dominant in the lowermost four meters (16.20m - 20.50m) of profile S4. It is characterized by two endothermic peaks, and a small exothermic peak.

The first endothermic peak is broad. It commences below 100°C (in some samples as low as 47°C) and ends at about 170- to 180°C. The average temperature of its maximum is 111.8°C. The size of this peak decreases with height. Above a depth of 16.20 meters, metahalloysite changes into a poorly crystallized kaolinite. The average (001) d-spacing found by x-ray powder diffraction for this kaolinite is 7.19 to 7.20 Å. The thermograms of this kaolinite suggest that it is a hydrated kaolinite. This mineral was previously reported in the study area by Hieronymus and Bildgen (1981).

The second endothermic peak is sharper, and the average temperature at its maximum height is 571°C. This temperature decreases with height.

These two peaks are the most distinctive for metahalloysite. The small exothermic peak occurs at about 980°C.

Kaolinite

Two polymorphic varieties of kaolinite have been identified in the profile, namely hydrated kaolinite which is described in the section on metahalloysite, and crystalline kaolinite. Hydrated kaolinite is exclusively found in the upper half of the weathered horizon of the profile. Like metahalloysite, hydrated kaolinite has an endothermic peak slightly above 100°C. This peak is probably due to incomplete withdrawal of interlayer water from the parental metahalloysite.

The second endothermic peak of hydrated kaolinite has been described in the section on profile S2. It is the main kaolinite peak. It is common to metahalloysite, hydrated kaolinite, and kaolinite, and occurs at around 564°C.

The small exothermic peak is also common to all three polymorphic varieties.

The crystalline kaolinite is essentially found in the bauxitic clasts of the detrital sequence which overlies the weathered horizon.

The main difference between kaolinite on the one hand, and metahalloysite and hydrated kaolinite on the other, is the absence in the differential thermal curve of kaolinite of the low-temperature endothermic peak located in the 47-to-200°C region of metahalloysite and hydrated kaolinite thermograms.

Gibbsite

Gibbsite is ubiquitous throughout the profile. The mean temperature of its main endothermic peak decreases steadily with depth.

The decrease in temperature may be due to a decrease with depth of the crystallinity of gibbsite.

Goethite

The temperature of the characteristic endothermic peak of goethite in these samples is in the lower part of the range 304°C to 313°C. This relatively low temperature suggests poor crystallinity. The peak is unresolved, and sometimes appears as a shoulder on the low-temperature side of the main gibbsite endothermic peak. In one thermogram, both peaks are partially resolved, and form a doublet.

Outcrop Samples

The mineralogy of bauxite outcrop samples is similar to that of the samples selected from the duricrust of profile S2. No systematic lateral trend was revealed by the study of these samples.

Conclusion on DTA Studies

The differential thermal investigation of profile S2 has resulted in the division of this profile into two separate units, an upper one also called the duricrust, which is underlain by the lower unit, a mottled clay horizon. The ratio of kaolinite/gibbsite is less than 0.1 in the duricrust of profile S2, but rises sharply when the mottled clay horizon is reached, and averages 0.66 at the base of this profile.

As the depth increases, below the mottled clay horizon, kaolinite is replaced by more stable polymorphic forms which are characterized by a higher amount of interlayer water. Kaolinite is thus successively replaced with depth by hydrated kaolinite and metahalloysite.

Hydrated kaolinite and metahalloysite are characterized by a low-temperature endothermic peak located between 47°C and 180°C on their

Table 7

Variation with depth of the mean temperature of the main gibbsite endothermic peak

SAMPLE (m)	DEPTH	PEAK T°C	HORIZON
Average T°C for outcrop samples	0.0	362	duricrust
S2/1.2	1.2	379	duricrust
S2/2.7	2.7	369	duricrust
S2/4.0	4.0	354	duricrust
S2/5.5	5.5	375	duricrust
S2/6.4	6.4	373	duricrust
S2/7.0	7.0	381	duricrust
S2/8.0	8.0	372	duricrust
S2/9.0	9.0	336	duricrust
S2/10.2	10.2	372	duricrust
S2/11.7	11.7	356	duricrust
S2/13.2	13.2	345	mottled clay hor
S4/11.7	11.7	343.5	clayey horizon
S4/12.5	12.5	334.5	clayey horizon
S4/13.5	13.5	328.5	clayey horizon
S4/16.5	16.5	320	clayey horizon
S4/17.5	17.5	319	clayey horizon
S4/19.0	19.5	314	clayey horizon

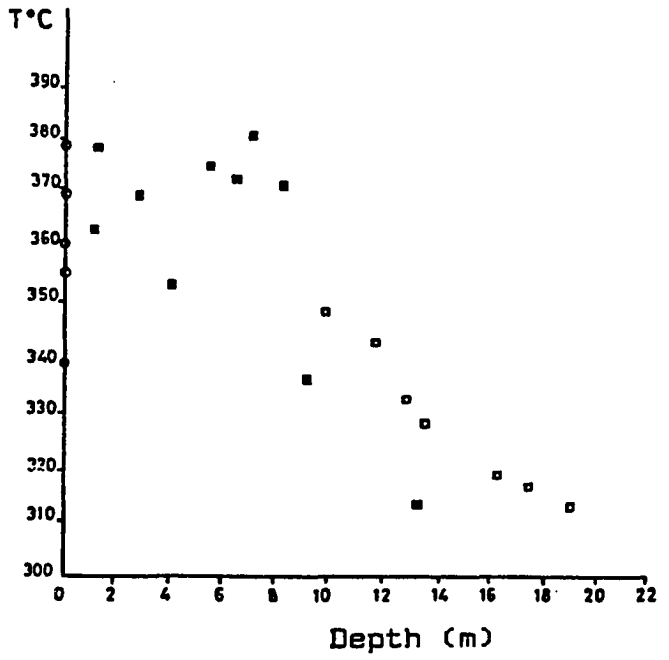

Fig. 53

Variation with depth of the mean temperature of the gibbsite main endothermic peak

- Profile S2
- Profile S4
- Outcrop sampling

thermal curves. This peak is absent in the kaolinite thermal curves. Hydrated kaolinite and metahalloysite have been separated from each other on the basis of their basal-plane spacings obtained from x-ray diffraction, the boundary between the two minerals having been set at 7.20 Å.

DTA data (Table 7) also show that the mean temperature of the gibbsite main endothermic peak decreases with depth. Fig. 53 is a plot of this temperature as a function of depth, along profiles S2 and S4. DTA data obtained from bauxite outcrop samples were also plotted. The highest temperatures of this peak have been registered in the duricrust, where gibbsite attains its maximum crystallinity as shown by petrographic observations. These data, therefore, suggest that the mean temperature of the gibbsite main endothermic peak varies proportionally to the crystallinity of this mineral.

QUANTITATIVE MINERALOGY

This section is a quantitative assessment of gibbsite, goethite and kaolinite which cumulatively constitute more than 95% of these bauxites based on estimates from x-ray powder diffractometry.

X-RAY POWDER DIFFRACTION

Because the "intensities" of x-ray powder diffraction maxima due to each crystalline phase in a mixture depend on the proportion of that phase in the mixture (Cullity, 1978), a quantitative assessment of the mineralogy of a mixture can be done by means of x-ray powder diffraction. This approach is theoretically valid in specific cases, but has practical limitations as will be discussed below.

The intensity of an x-ray powder diffraction maximun from a compound "c" in a mixture is given by the equation

$$I_c = K_c . W_c / u_c$$

where I_c is the integrated intensity per unit length of the diffraction maximum, K_c is a constant which depends on the nature of the crystalline phase, the particular reflection (hkl) considered, and the experimental arrangement (Brindley, 1980), W_c is the weight fraction of "c" in the mixture, and u_c is the mass absorption coefficient of "c".

The use of external standards of gibbsite, goethite and kaolinite was first considered to be an appropriate technique for a quantitative

estimation of these minerals applying the above equation. If the mixture of mass absorption coefficient u_m is assumed to be composed of "c" in the matrix of all the other components, this equation can be rewritten as follows:

$$I_c = K_c.W_c/[W_c.u_c + (1-W_c)u_m] \qquad (1)$$

If this equation is applied to an external standard of known weight composed of a single phase component "c" it becomes:

$$I^\circ_c = K_c/u_c \quad \text{with } W_c=1 \qquad (2)$$

A ratio of (1) and (2) gives:

$$I_c/I^\circ_c = W_c/[W_c(1-u_m/u_c) + u_m/u_c]$$

$$= W_c/[W_c(1-a) + a] \quad \text{with } a = u_m/u_c \qquad (3)$$

Equation (3), which was first derived by Alexander and Klug (1948), is applied in fig. 54 for the determination of the proportion of quartz in different mixtures. With a mixture such as quartz-cristobalite which has two components with the same mass absorption coefficient (Cullity, 1978), a=1 and the equation (3) becomes linear. But the assumption that a=1 is only true in a few cases (Brown, 1980), and the mass absorption coefficient of a mixture is usually different from that of a single phase external standard. In this connection, Brown (1980) notes that if the analysis of all the components of a mixture is based on the assumption that a=1, then the proportion of the components with a<1 (those with a large mass absorption coefficient) will be overestimated, and the proportion of the components with a>1 (those with a small mass absorption coefficient) will be underestimated. This is clearly demonstrated in fig. 54.

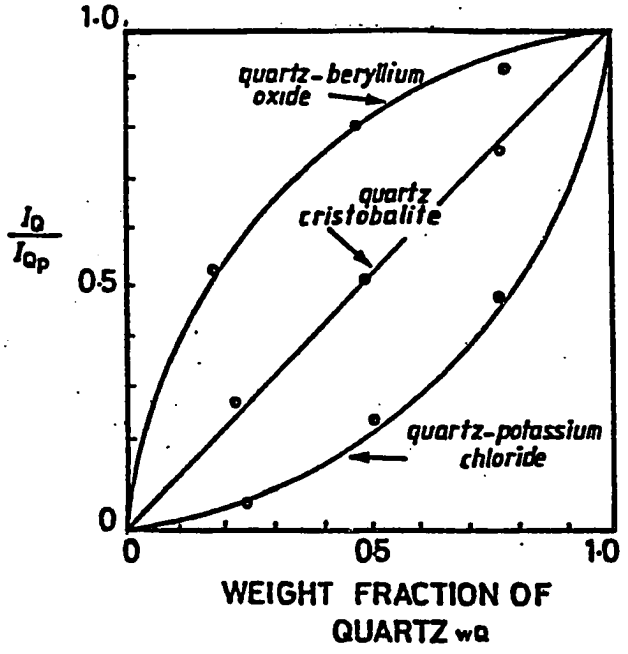

Fig. 54

Diffractometer measurements made with CuK_α radiation on binary mixtures. I_Q is the intensity of the reflection from the d = 3.34 Å planes of quartz in a mixture. I_{Qp} is the intensity of the same reflection from pure quartz. After Alexander and Klug (1974).

In other words, the relationship between I_c/I°_c and W_c is generally non-linear with the exception of a few mixtures such as quartz and cristobalite, anatase and rutile, kaolinite and dickite (Brown, 1980), and the use of equation (3) in the quantitative analysis of a component in a mixture may lead to an underestimation or an overestimation of its proportion.

Therefore, the best that could be expected from this approach was a semi-quantitative estimate of the mineralogy. This limitation rendered the method less suitable for the purposes of this study.

The use of an internal standard also proved to be inadequate. In this method, the diffraction maximum of an unknown mineral is compared with a diffraction maximum from a standard mixed with the sample in known proportions. But because of the high dependency of the Lorentz-polarization factor on the orientation of crystals in a mixture (Cullity, 1978), the use of this method in quantitative determination of minerals with a sheet structure, such as gibbsite, kaolinite, and goethite, would require an internal standard with identical crystallographic habit. Even then, a quantitative comparison between the reference lines and the unknown lines would be hampered by the Bragg-angle dependency of integrated intensities. Integrated intensities are indeed greater for larger and smaller values of the Bragg angle than for intermediate values, other things being equal (Cullity, 1978).

These limitations of x-ray powder diffraction methods in quantitative analysis led to a consideration of the alternative analytical methods discussed below.

DIFFERENTIAL THERMAL ANALYSIS

As early as 1939 it was found that the area under a peak on a differential thermal curve is approximately proportional to the amount of reacting material (Norton, 1939). Accordingly, DTA peaks can be used for the quantitative estimation of the minerals present in a sample. This is done in practice by comparing the area under a peak of a single-phase sample of known weight with the corresponding peak area of the same mineral in a mixture. The use of this technique was nevertheless prevented by analytical limitations such as (1) the base-line drift between the gibbsite and goethite endothermic peaks, (2) the largely unresolved small gibbsite endothermic peak on the low-temperature side of the gibbsite main peak, and, to some extent, (3) the unresolved gibbsite-goethite peak from which gibbsite could be removed by chemical dissolution with NaOH (Munoz, 1953). Furthermore, this technique requires that the thermal conductivity be identical for all the test samples (Mackenzie, 1957).

Consequently, a chemical method successfully applied earlier in the study of Arkansas bauxite (Thoenen et al., 1945) was used. This method is developed in the following section.

QUANTITATIVE MINERALOGY BY DIRECT CHEMICAL CALCULATIONS

Principle

When x-ray powder diffraction and DTA methods involve uncertainties or limitations such as those described above, the proportion by weight percent of aluminum-bearing minerals in a bauxite can be quantitatively estimated by distributing the alumina in a quantitative chemical analysis between all aluminum-bearing minerals present in relation to the weight percent of combined silica. Prior qualitative mineral determination is therefore required. This method was developed in the course of the study of Arkansas bauxites (Thoenen et al., 1945). Its accuracy depends on the absence of free silica. The remaining minerals are grouped under "impurities".

This method is suitable for the study of the Cameroon Highlands bauxites, which, like the Arkansas bauxite, are devoid of aluminous minerals other than gibbsite and kaolinite. Nevertheless, unlike the Arkansas bauxite, they contain trace amounts of quartz as revealed by x-ray powder diffraction. Free silica was found in the chemical analyses of bauxite samples from profile PB (Pascual, 1983) where it ranges from 0.01 to 0.20 wt%, and averages 0.09 wt%. However, given this very low quartz concentration, all the silica may be considered to be combined in kaolinite and the error involved is negligible.

The percentages of gibbsite and kaolinite in a given bauxite sample are related to its alumina and combined silica content, and can be found using the composition of these minerals as follows:

Kaolinite: $2SiO_2.Al_2O_3.2H_2O$ containing

46.5 wt% SiO_2

39.5 wt% Al_2O_3

14.0 wt% H_2O

100.0

The weight ratio of alumina to silica in kaolinite is:

$$Al_2O_3/SiO_2 = 0.85$$

The weight ratio of combined water to silica in kaolinite is:

$$H_2O/SiO_2 = 0.30$$

The weight percent of kaolinite may be determined from these relations as follows:

$$\text{wt\% Kaolinite} = SiO_2 + (0.85)SiO_2 + (0.30)SiO_2$$

$$= (2.15)SiO_2$$

Gibbsite: $Al_2O_3.3H_2O$ containing

65.4 wt% Al_2O_3

43.6 wt% H_2O

100.0

The weight ratio of combined water to alumina in gibbsite is:

$$H_2O/Al_2O_3 = 0.53$$

The alumina combined in gibbsite equals the total alumina minus the alumina combined in kaolinite

$$Al_2O_{3(gibb)} = Al_2O_{3(total)} - Al_2O_{3(kaol)}$$

$$= Al_2O_{3(total)} - (0.85)SiO_2$$

$$\text{wt\% Gibbsite} = Al_2O_{3(gibb)} + (0.53)Al_2O_{3(gibb)}$$

$$= [Al_2O_{3(total)} - (0.85)SiO_2] +$$

$$0.53[Al_2O_{3(total)} - (0.85)SiO_2]$$

$$= (1.53)Al_2O_{3(total)} - (1.7)SiO_2$$

Impurities: The percentage of impurities is found as follows:

wt% Impurities = 100% - (%kaolinite + %gibbsite)

Results

The calculations were done using x-ray fluorescence whole-rock analyses of samples from profile S2 and from the various outcrop samples. In addition, chemical analyses from profile PB (Pascual, 1983) were also used. The resulting calculated percentages of kaolinite, gibbsite and impurities in the samples processed are given in tables 8, 9, and 10.

Example: Sample N.49b from Fongo Tongo Mountains

Al_2O_3 = 49.63 wt.%

SiO_2 = 3.83 wt.%

wt% kaolinite = $(2.15)SiO_2$ = 8.23

wt% gibbsite = $(1.53)Al_2O_{3(total)} - (1.7)SiO_2$

= 69.43

wt% impurities = 100% - (8.23% + 69.43%)

= 22.34

Comments on the Method and its Limitations

The reliability of the results depends essentially on the accuracy of the chemical analyses and on the absence of free silica (quartz and amorphous silica) from the profile. The last condition is probably met in the duricrust where free silica is nearly absent. The situation is different in the mottled clay horizon where continous breakdown with height of kaolinite is expected to provide additional free silica. An

Table 8

Quantitative estimation of kaolinite, gibbsite and the "impurities" along profile S2

SAMPLE NUMBER	Al_2O_3 wt%	SiO_2 wt%	kao %	gib %	impur %
S2/1.2	54.9	2.08	4.47	80.46	15.07
S2/2.7	54.5	1.60	3.44	80.66	15.90
S2/4.0	52.4	3.03	6.51	75.02	18.47
S2/5.5	54.8	4.27	9.18	76.58	14.24
S2/6.4	60.5	3.71	7.98	86.26	5.76
S2/7.0	59.0	2.30	4.94	86.36	8.70
S2/8.0	56.4	3.30	7.09	80.68	12.23
S2/9.0	58.5	2.28	4.90	85.63	9.47
S2/10.2	54.8	2.72	5.85	79.22	14.93
S2/11.7	51.8	10.50	22.57	61.40	16.03
S2/13.2	33.3	14.40	30.96	26.47	42.57

Table 9

Quantitative estimation of kaolinite, gibbsite and the "impurities" along profile PB

SAMPLE NUMBER	Al_2O_3 wt%	SiO_2 wt%	kao %	gib %	impur %
CAM-134_1	48.57	1.64	3.53	71.52	24.95
CAM-134_2	47.87	1.75	3.76	70.27	25.97
CAM-135	51.13	1.67	3.59	75.39	21.02
CAM-136	42.60	1.72	3.70	62.25	34.05
CAM-137	49.20	1.94	4.17	71.98	23.85
CAM-138	54.68	2.32	4.99	79.72	15.29
CAM-139	45.02	1.72	3.70	65.96	30.34
CAM-140	51.40	2.78	5.98	73.61	20.41
CAM-141	48.43	3.01	6.48	68.99	24.53
CAM-145	42.70	5.26	11.31	56.69	32.00
CAM-142	53.90	2.69	5.78	77.89	16.33
CAM-143	46.32	6.13	13.18	60.45	26.37
CAM-143_1	33.40	14.70	31.60	26.11	42.29
CAM-143_2	32.16	7.50	16.12	36.46	47.42
CAM-144_1	46.25	26.02	55.94	26.53	17.53
CAM-144_3	30.37	28.81	61.94	0.00	38.06

Table 10

Quantitative estimation of kaolinite, gibbsite and the "impurities" in some bauxite outcrops

SAMPLE NUMBER	Al_2O_3 wt%	SiO_2 wt%	kao %	gib %	impur %
N49b	49.63	3.83	8.23	69.43	22.34
N50e	48.0	0.1	0.21	73.27	26.52
N53b	54.01	3.94	8.47	75.94	15.59
N59a	46.80	3.66	7.87	65.08	27.05
N63b	56.15	8.22	17.67	71.93	10.4

underestimation of gibbsite and a corresponding overestimation of kaolinite is therefore expected in this horizon, unless free silica is separately estimated and deducted from total silica. Nevertheless, this method is suitable for the purposes of this study.

The lack of quantitative information on what has been termed "impurities" does not allow a full account of the mineralogy. Quantitative data reveal that "impurities" represent in weight percent between 4.29 and 44.43 of the bulk composition with averages of 14.28 and 24.95 in profiles S2 and PB, respectively. The high proportion of "impurities" in profile PB is probably due to a higher percentage of goethite. The original distribution of goethite along the 27-year-old trench from which this profile was sampled is believed to have changed because of the expected relatively high mobility of ferric iron along the trench. Indeed, chemical analyses show a higher weight percent of iron along this profile. It is, therefore, important to individually quantify these "impurities" inasmuch as they may reveal additional information regarding the source rock and the geochemistry of the weathering profile.

In order to resolve this difficulty, additional calculations were carried out using a norm calculation method which was designed to include the major bauxite components, a few unweathered residual minerals, as well as a large number of oxides, hydroxides, secondary silicates and free silica. This normative method is described below in order to allow a better understanding of the results.

QUANTITATIVE MINERALOGY USING NORM CALCULATIONS

Definition of the Normative Method Used

The calculations reported here are based on a procedure described by Ekodeck (1984) which in turn is based on the well-known CIPW method (Cross et al., 1903). The CIPW norm calculations were developed primarily for the classification of igneous rocks. They are based on normative chemical formulae which are calculated on a weight percent basis.

The variation described by Ekodeck (1984) is based on a combination of 12 major chemical constituents including Loss on Ignition (LOI), and leads to a set of 21 minerals commonly encountered in weathering profiles. This variation of Ekodeck has been modified here in order to apply the method specifically to the study of bauxitic profiles. The normative minerals used were selected on the basis of petrography, x-ray powder diffraction, infrared spectrometry and other analytical data obtained in the course of this study.

(1). The mineralogy of the profiles investigated is limited to a few species. The following minerals were identified in thin and polished thin sections: gibbsite, goethite, hematite and maghemite. In addition to these minerals, x-ray powder diffraction and DTA studies revealed kaolinite, metahalloysite, halloysite, anatase and quartz. Of the three hydrated alumino-silicates identified in the profiles, only kaolinite is used in the calculations.

(2). Chemical analyses show that the weathering profiles are poor in alkalis and alkaline earth elements due to nearly complete leaching

during bauxitic weathering. Nevertheless, a few silicates of common monovalent and divalent cations were incorporated in the normative suite for the calculation of possible residual and secondary silicates.

(3). Ferrous iron is absent in the weathering profile, but appears in the chemical analyses of outcrop samples of bauxite. It is probably due to surficial biogenic reduction of ferric iron, and has not been considered in these calculations. All the Ti is expressed as anatase, but if Fe^{2+} is also present normative ilmenite may be calculated.

(4). Manganese is reported in all the whole rock analyses of bauxites and other weathering products. It is essentially tetravalent according to data obtained from infrared spectrometry.

The following minerals were accordingly selected for the normative calculations:

a- Residual accessory

Anatase ..... TiO_2

b- Residual silicates

Anorthite ..... $2SiO_2.Al_2O_3.CaO$

Albite ..... $6SiO_2.Al_2O_3.Na_2O$

Sericite ..... $6SiO_2.3Al_2O_3.K_2O.2H_2O$

c- Secondary silicates

Kaolinite ..... $2SiO_2.Al_2O_3.2H_2O$

Chlorite ..... $3SiO_2.Al_2O_3.5MgO.H_2O$

d- Oxides and hydroxides

Magnetite ..... $FeO.Fe_2O_3$

Hematite ..... Fe_2O_3

Goethite ..... $Fe_2O_3.H_2O$

Corundum ..... Al_2O_3

Gibbsite ..... $Al_2O_3.H_2O$

Pyrolusite ..... MnO_2

e- Silica

Amorphous silica ..... $SiO_2.nH_2O$

Quartz ..... SiO_2

Calculation Procedures

The calculation procedures used here are based on those proposed by Ekodeck (1984) for the study of weathering profiles. Nevertheless, many steps in these calculations have been changed, and those proposed here only apply to the study of bauxite.

It should be recognized that normative minerals are not meant to be a substitute for the mode of a specimen. The norm gives only hypothetical mineral assemblages which are derived from formalized calculations. The following calculations were devised for bauxite in which gibbsite is the only hydrated aluminum oxide. Loss on ignition is expressed as H_2O in the calculations. The method is divided into several steps as follows:

(1) Transform chemical analyses into molecular proportions by dividing the weight percent of each oxide by its gram-molecular weight, e.g. SiO_2 3.94 wt% divided by 60 gives a molecular proportion of 0.066. It is common practice to multiply these numbers by 10^3.

(2) If residual FeO is present, form ilmenite. Remaining FeO is termed FeO'.

(3) Assign remaining TiO_2 to anatase.

(4) Assign FeO' to magnetite. Remaining Fe_2O_3 is termed Fe_2O_3'.

(5) If K_2O is present, assign it to sericite.

(6) If Na_2O is present, assign it to albite.

(7) If CaO is present ,assign it to anorthite.

(8) If MgO is present, assign it to chlorite.

(9) If MnO_2 is present, assign it to pyrolusite

(10) Calculate the remaining alumina, water, and silica to be termed $Al_2O_3^{(1)}$, $H_2O^{(1)}$, and $SiO_2^{(1)}$, respectively.

If $H_2O^{(1)} < 2Al_2O_3^{(1)}$, proceed to (21)

If $H_2O^{(1)} > 2Al_2O_3^{(1)}$, proceed to (11)

(11) Form kaolinite. Excess water and alumina are termed $H_2O^{(2)}$ and $Al_2O_3^{(2)}$, respectively.

(12) Assign Fe_2O_3 to goethite. Excess water is termed $H_2O^{(3)}$.

If $Al_2O_3^{(2)} = X$, the number of water molecules neccessary for its hydrolysis into gibbsite is equal to 3X.

(13) If $3X > H_2O^{(3)}$, form gibbsite and corundum.

(14) If $3X = H_2O^{(3)}$, form gibbsite.

(15) If $3X < H_2O^{(3)}$, form gibbsite. Excess water is termed $H_2O^{(4)}$.

(16) Use $H_2O^{(4)}$ for partial or total hydrolysis of kaolinite as follows in (17), (18) and (19).

$Al_2O_{3(K)}$ = alumina in kaolinite

$H_2O_{(K)}$ = water in kaolinite

$H_2O^{(4)}$ = excess H_2O from (15)

If $Al_2O_{3(k)} = X_1$, the number of water molecules necessary for its hydrolysis into gibbsite is equal to $3X_1$.

(17) If $3X_1 > H_2O^{(4)} + H_2O_{(K)}$, form kaolinite, gibbsite and quartz. The number of kaolinite and gibbsite molecules to be formed,

termed (kao) and (gibb), respectively, are related to avalaible alumina (Al) and water (H) molecules as follows (Ekodeck, 1984):

$$kao = 3Al\text{-}H$$

$$gibb = H\text{-}2Al$$

(18) If $3X_1 = H_2O^{(4)} + H_2O_{(K)}$, hydrolyse kaolinite into gibbsite, then form quartz and proceed to (26).

(19) If $3X_1 < H_2O^{(4)} + H_2O_{(K)}$, change kaolinite into gibbsite. Excess water is combined with silica to form amorphous silica.

(20) Form quartz with excess silica and proceed to (26).

(21) Form kaolinite. Excess water and alumina are respectively termed $H_2O^{(2)}$ and $Al_2O_3{}^{(2)}$.

(22) If $Fe_2O_3{}^{(1)} = 0$, form gibbsite and corundum.

(23) If $Fe_2O_3{}^{(1)} > H_2O^{(2)}$, form goethite, hematite and corundum.

(24) If $Fe_2O_3{}^{(1)} = H_2O^{(2)}$, form goethite and corundum.

(25) If $Fe_2O_3{}^{(1)} < H_2O^{(2)}$, form goethite, gibbsite and corundum.

(26) Report resulting molecular proportions on the Bauxite Norm Calculation Chart (Fig. 55).

(27) Change molecular proportions into normative weight percents by multiplying the molecular proportions by the molecular weight of the corresponding mineral. The number is then divided by 10^3. For instance in the case of goethite in sample S2/1.2, the molecular proportion is 71, and the normative percent of goethite would be:

$$(71 \times 178)/10^3 = 12.64$$

Results

The results of the norm calculations for profiles S2, PB, for outcrop samples, and for profile S4 are reported in tables 11, 12, 13

SAMPLE N°		PROVENANCE :					DEPTH :			PARENT ROCK :						
Constituents		SiO_2	Al_2O_3	LO.I.	MgO	MnO_2	CaO	Na_2O	K_2O	Fe_2O_3	FeO	TiO_2	P_2O_5	MOLECULAR PRO	NORM %	MOLECULAR WT.
Molecular wt.		60	102	18	40	87	56	62	94	160	72	80	142			
weight %																
Molecular Proportions																
Anatase	TiO_2															80
Magnetite	$FeO.Fe_2O_3$															232
Sericite	$6SiO_2.3Al_2O_3.K_2O.2H_2O$															796
Albite	$6SiO_2.Al_2O_3.Na_2O$															524
Anorthite	$2SiO_2.Al_2O_3.CaO$															278
Chlorite	$3SiO_2.Al_2O_3.5MgO.4H_2O$															554
Kaolinite	$2SiO_2.Al_2O_3.2H_2O$															258
Pyrolusite	MnO_2															87
Goethite	$Fe_2O_3.H_2O$															179
Gibbsite	$Al_2O_3.3H_2O$															156
Corundum	Al_2O_3															102
Hematite	Fe_2O_3															160
Amorph. Sil.	$SiO_2.nH_2O$															
Quartz	SiO_2															60
SUM																

Fig. 55

Bauxite norm calculation chart

Table 11

Quantitative mineralogy of profile S2 using norm calculations (each sample number is preceeded by the indentification S2)

SAMPLE NUMBER	1.2	2.7	4.0	5.5	6.4	7.0
Ana	1.76	1.86	2.59	1.82	1.19	1.64
Mag	0.0	0.0	0.0	0.0	0.0	0.0
Ser	0.0	0.8	0.0	0.0	0.0	0.0
Alb	0.0	0.0	0.0	0.0	0.52	0.0
Ano	0.28	0.0	0.0	0.0	0.0	0.0
Chl	0.0	0.0	0.0	0.55	0.0	0.0
Kao	5.42	2.5	5.16	8.78	7.22	4.9
Pyr	0.0	2.67	0.0	0.0	0.0	0.0
Goe	12.64	11.57	14.42	9.97	5.52	7.65
Gib	70.04	79.87	77.22	78.31	80.65	80.96
Cor	0.0	0.92	0.0	0.0	4.79	4.08
Hem	0.0	0.0	0.0	0.0	0.0	0.0
Am.S	6.06	0.0	0.0	0.0	0.0	0.0
Qua	0.0	0.0	0.72	0.0	0.0	0.0
SUM	96.2	100.19	100.11	99.43	99.9	99.23

SAMPLE NUMBER	8.0	9.0	10.2	11.7	13.2
Ana	1.84	1.61	1.26	1.13	1.6
Mag	0.0	0.0	0.0	0.0	0.0
Ser	0.0	0.0	0.0	0.0	0.0
Alb	0.0	0.0	0.0	0.0	0.0
Ano	0.0	0.0	0.0	0.0	0.0
Chl	0.0	0.0	0.0	0.0	0.0
Kao	6.97	4.9	5.93	22.7	30.96
Pyr	0.09	0.0	0.18	0.18	0.09
Goe	9.08	8.01	14.95	12.64	34.18
Gib	80.65	81.74	73.94	56.16	31.2
Cor	1.02	3.06	4.08	6.12	0.71
Hem	0.0	0.0	0.0	0.0	0.0
Am.S	0.0	0.0	0.0	0.0	0.0
Qua	0.0	0.0	0.0	0.0	0.0
SUM	99.65	99.32	100.34	98.93	98.74

Table 12

Quantitative mineralogy of profile PB using norm calculations (each sample number is preceeded by the identification CAM)

SAMP NUMB	134_1	134_2	135	136	137	138	139	140
Ana	1.76	1.9	1.46	2.62	2.12	1.87	2.68	2.26
Mag	0.0	0.0	0.0	0.0	0.0	0.0	0.0	0.0
Ser	0.0	0.0	0.0	0.0	0.0	0.0	0.0	0.0
Alb	0.0	0.0	0.0	0.0	0.0	0.0	0.0	0.0
Ano	0.0	0.0	0.0	0.0	0.0	0.0	0.0	0.0
Chl	0.0	0.0	0.0	0.55	0.0	0.0	0.0	0.0
Kao	3.35	3.61	3.61	3.1	4.13	4.9	3.61	5.93
Pyr	0.18	0.18	0.09	0.52	0.27	0.0	0.09	0.09
Goe	22.6	23.32	19.76	33.29	22.25	15.3	27.23	17.98
Gib	70.98	70.2	74.2	56.94	69.57	77.53	65.21	73.94
Cor	0.82	0.51	1.33	4.08	2.04	2.04	0.92	1.33
Hem	0.0	0.0	0.0	0.0	0.0	0.0	0.0	0.0
Am.S.	0.0	0.0	0.0	0.0	0.0	0.0	0.0	0.0
Qua	0.1	0.24	0.06	0.12	0.0	0.0	0.06	0.12
SUM	99.81	99.96	100.51	101.22	100.38	101.64	99.8	101.65

SAMP NUMB	141	145	142	143	143_1	143_2	144_1	144_3
Ana	2.12	2.0	2.06	2.03	2.3	2.48	2.1	3.1
Mag	0.0	0.0	0.0	0.0	0.0	0.0	0.0	0.0
Ser	0.0	0.0	0.0	0.0	0.0	0.0	0.0	0.0
Alb	0.0	0.0	0.0	0.0	0.0	0.0	0.0	0.0
Ano	0.0	0.0	0.0	0.0	0.0	0.0	0.0	0.0
Chl	0.0	0.0	0.55	0.55	0.0	0.0	0.0	0.0
Kao	0.45	11.09	5.16	12.64	0.0	0.0	50.83	0.0
Pyr	0.09	0.0	0.0	0.09	0.0	0.18	0.0	0.09
Goe	21.18	28.48	15.31	22.25	29.37	35.96	4.8	21.36
Gib	70.2	58.19	76.29	62.71	51.0	49.14	39.93	46.49
Cor	0.0	0.2	1.84	0.20	0.0	0.0	0.0	0.0
Hem	0.0	0.0	0.0	0.0	0.0	0.0	0.0	0.0
Am.S.	0.1	0.0	0.0	0.0	3.93	10.66	0.0	2.02
Qua	0.12	0.12	0.12	0.12	12.24	0.8	2.4	27.5
SUM	100.26	100.08	101.33	100.6	98.85	99.22	100.06	100.56

Table 13

Quantitative mineralogy of some bauxite outcrop samples using norm calculations

SAMPLE NUMBER	N49b	N53b	N59a	N63b	N68
Ana	1.44	1.02	4.57	1.12	5.22
Mag	0.0	0.0	0.0	0.0	0.0
Ser	0.0	0.0	0.0	0.0	0.0
Alb	0.0	0.0	0.0	0.0	0.0
Ano	0.0	0.0	0.0	0.0	0.0
Chl	0.0	0.0	1.1	0.0	0.28
Kao	8.26	8.5	6.96	17.54	1.55
Pyr	0.0	0.0	0.09	0.0	0.0
Goe	19.05	14.60	21.72	7.48	30.44
Gib	69.29	77.38	59.90	73.6	58.03
Cor	1.12	0.0	4.79	1.02	2.55
Hem	0.0	0.0	0.0	0.0	0.0
Am.S	0.0	0.0	0.0	0.0	0.0
Qua	0.0	0.0	0.06	0.0	0.0
SUM	99.16	101.5	99.19	100.76	98.07

Table 14

Quantitative mineralogy of profile S4 using norm calculations (each sample number is preceeded by the identification S4)

SAMP NUMB	1.1	2.4	7.0	8.5	10.0	11.5
Ana	1.32	1.34	0.82	0.9	0.85	1.07
Mag	0.0	0.0	0.0	0.0	0.0	0.0
Ser	0.8	0.8	0.8	0.0	0.0	0.0
Alb	0.0	0.0	0.0	0.52	0.0	0.0
Ano	0.0	0.0	0.28	0.56	0.0	0.0
Chl	0.0	0.0	0.55	0.0	0.0	0.0
Kao	5.67	21.16	31.22	10.32	28.64	17.29
Pyr	0.09	0.0	0.09	0.18	0.09	0.09
Goe	16.83	18.62	8.4	12.17	10.56	13.6
Gib	65.2	44.3	42.9	45.71	58.97	55.69
Cor	0.0	0.0	0.0	0.0	0.0	0.0
Hem	0.0	0.0	0.0	0.0	0.0	0.0
Am.S	0.0	0.0	0.0	0.0	0.09	0.09
Qua	9.78	15.0	15.24	28.8	0.3	12.0
SUM	99.69	101.22	100.3	99.16	99.5	99.83

SAM NUM	12.5	13.5	14.5	16.2	17.5	19.0	20.5
Ana	1.19	1.18	1.19	1.2	1.16	1.24	1.13
Mag	0.0	0.0	0.0	0.0	0.0	0.0	0.0
Ser	0.0	0.0	0.0	0.0	0.0	0.0	0.0
Alb	0.0	0.0	0.0	0.0	0.0	0.0	0.0
Ano	0.0	0.3	0.0	0.0	0.28	0.0	0.0
Chl	0.0	0.0	0.0	0.0	0.0	0.0	0.0
Kao	8.25	14.45	15.0	17.3	8.25	10.84	14.2
Pyr	0.09	0.09	0.09	0.18	0.09	0.09	0.09
Goe	14.14	13.25	14.32	14.14	15.0	16.47	12.35
Gib	52.57	44.3	39.16	40.25	43.99	39.62	37.75
Cor	0.0	0.0	0.0	0.0	0.0	0.0	0.0
Hem	0.0	0.0	0.0	0.0	0.0	0.0	0.0
A.S	0.09	0.0	0.0	0.09	0.0	0.0	0.0
Qua	22.38	25.8	29.0	26.34	29.0	30.1	32.64
SUM	98.71	99.37	98.76	99.50	97.77	98.36	98.16

and 14. The normative minerals include those previously identified by petrographic and x-ray methods such as gibbsite, kaolinite, goethite anatase and quartz, as well as normative trace minerals related to the presence in the weathering profile of minute amounts of monovalent and divalent cations. This second group includes sericite and chlorite. Normative oxides reported are pyrolusite and corundum, the latter being due to residual aluminum after the formation of all the aluminum-bearing normative minerals listed on the chart.

Comparative examination of these results and those obtained from chemical calculations indicates reasonably good correlation for kaolinite and goethite throughout the duricrusts of the S2 and PB profiles (Figs. 56 and 57). However, a downward increasing discrepancy was found in the mottled clay horizon of profile PB, with higher values for normative gibbsite, and corresponding lower values for normative kaolinite. The difference at the bottom of profile PB between the two sets of results is +19 wt% for gibbsite and -32 wt% for normative kaolinite. This discrepancy can be explained by the presence in the mottled clay horizon of PB of unreported free silica which was by calculation incorporated in kaolinite using the chemical method. The discrepancy diminishes with height in the mottled clay horizon, which suggests a decrease in the same direction of free silica. The use of the two methods may prove helpful in testing the presence of unreported amorphous silica in whole rock analyses of bauxites.

The mineralogy of these bauxites is dominated by gibbsite which averages between 61.7 and 87.7% by weight in the duricrust. Kaolinite, the second most abundant aluminum-bearing mineral, is present in much

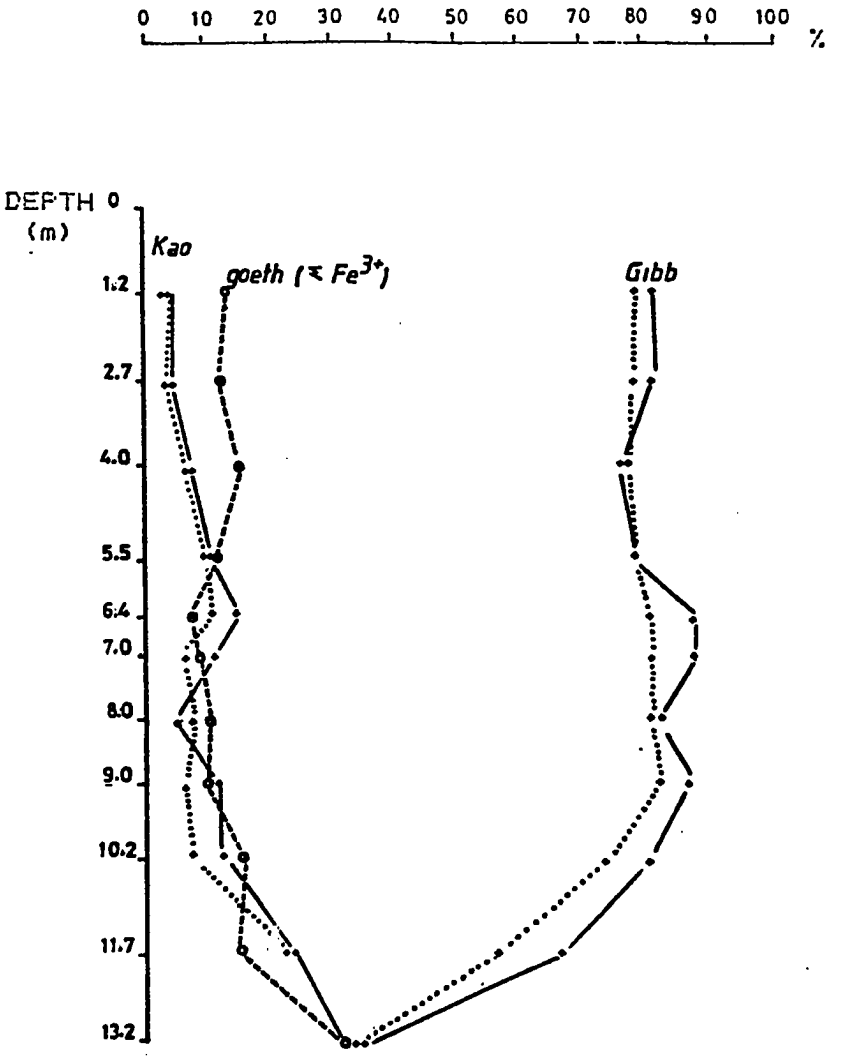

Fig. 56

Mineralogical Trends along Profile S2

——— Normative goethite
..... Normative kaolinite and normative gibbsite
_____ Quantitative estimation by chemical methods of kaolinite and gibbsite

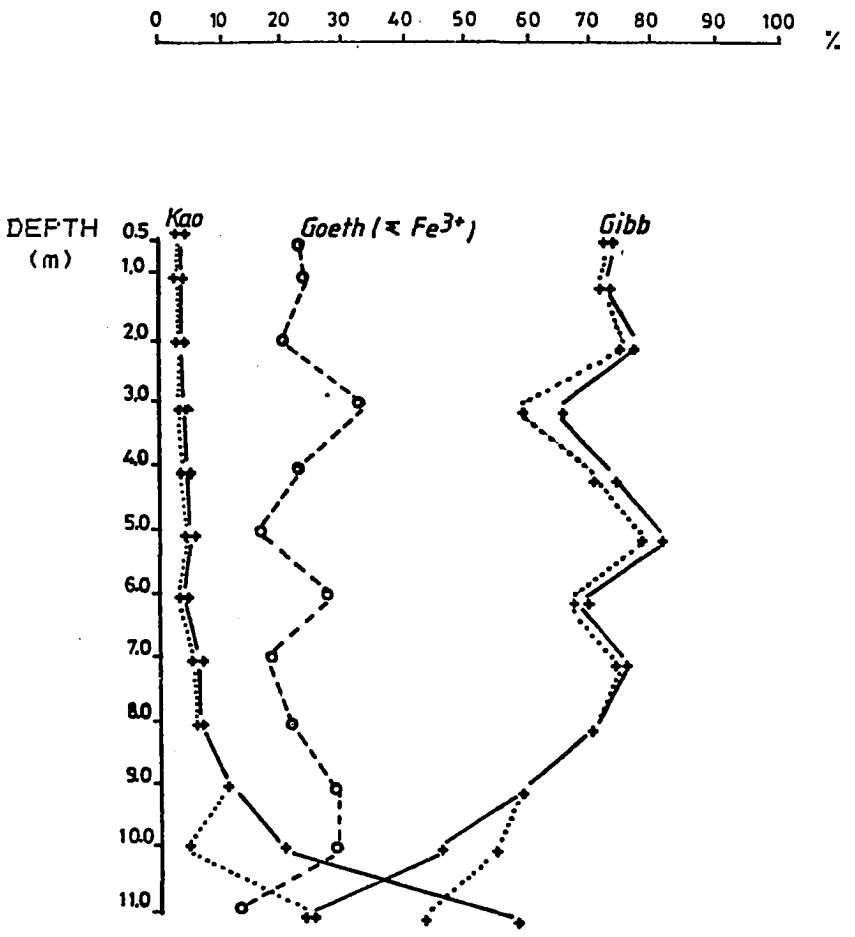

Fig. 57

Mineralogical Trends along Profile PB

------ Normative goethite
..... Normative kaolinite and normative gibbsite
——— Quantitative estimation by chemical methods of kaolinite and gibbsite

lower concentrations in the duricrust where it ranges between 0.2 and 9.2 wt%. Nevertheless, it reaches 58 wt% at the base of profile PB, in the mottled clay horizon. Quantitative estimation of the remaining minerals was done using their normative weight percents. The results are as follows:

(1). Goethite is the major "impurity" and averages 10.4 wt% in the duricrust of S2. Outcrop samples from Fongo Tongo and Djeu tend to be higher in normative goethite with values of 19 and 26 wt%, respectively.

(2). Normative anatase is ubiquitous and varies between 1.2 and 2.6 wt% along profile S2, and between 1.4 and 3.1 wt% along profile PB. Higher values of 3.4 and 3.8 wt% were recorded in two outcrop samples from Djeu.

(3). Normative corundum ranges between 0 and 6.2 wt%.

(4). Normative sericite, albite and anorthite are nearly absent, and normative chlorite is low and never exceeds 0.3 wt%.

(5). Normative quartz (plus normative amorphous silica) is low as expected, and averages 0.07 wt% and 0.08 wt% along the S2 and PB profiles respectively.

(6). Maghemite which is part of the "impurities" was not calculated because all the ferric iron was assigned to normative goethite.

The duricrust of Fongo-Tongo is composed, therefore, of gibbsite and kaolinite which constitute 61.8 to 87.7 wt% and 0.2 to 9.2 wt%, respectively. The average normative percentages of the remaining minerals is 10.4 wt% for goethite, 1.7 wt% for anatase, 0.08 wt% for quartz (plus amorphous silica), 2.0 wt% for corundum. Normative chlorite

and normative pyrolusite average 0.09 wt% and 0.2 wt%, respectively. Normative sericite and normative albite are less than 0.05 wt%. Normative anorthite is absent in the duricrust.

The limited quantitative method used in the section on "quantitative mineralogy by direct chemical calculations" for the estimation of kaolinite, gibbsite and the "impurities" could not be applied in the study of profile S4 due to the presence of significant amounts of quartz based on x-ray powder diffraction.

Anatase, kaolinite, gibbsite, goethite and quartz were essentially the only normative minerals found along profile S4. Normative sericite was only found in three samples in percentages not exceeding 0.8%, and normative pyrolusite is virtually absent.

CLASSIFICATION OF THE BAUXITES OF THE SOUTHERN FLANK OF THE BAMBOUTO MOUNTAINS

A number of classifications have been proposed for bauxites and related rocks, and the choice of which classification to use must be based on the purpose of the study and the data avalaible.

A simple geochemical classification based on the distinction of "free aluminum" (aluminum oxide hydrates) and "bound aluminum" (aluminum silicates) was proposed by Pedro (1966) who classified the various types of bauxite and related materials according to their free aluminum content which was determined using an index called the K_i coefficient. This parameter was defined by Harrassowitz (1926) as follows:

$$K_i = \text{wt\% } SiO_2 \; / \; \text{wt\% } Al_2O_3 \times 1.7$$

The factor 1.7 allows the transformation of weight into molecular percentages (Harrassowitz, 1926). K_i has a maximum value of 2.0. The resulting classification developed by Pedro (1966) is as follows:

bauxite	$K_i = 0.0 - 0.6$	free Al_2O_3: 70 - 100%
clayey bauxite	$K_i = 0.6 - 1.0$	free Al_2O_3: 50 - 70%
bauxitic clay	$K_i = 1.0 - 1.6$	free Al_2O_3: 20 - 50%
clay	$K_i = 1.6 - 2.0$	free $Al_2O_3 < 20\%$

The major drawback of this otherwise straightforward classification is that it provides no information on non-aluminous minerals. This group of minerals, which has been termed "impurities" in the preceeding section of this report, is made up dominantly of goethite

and includes minor amounts of anatase, hematite, maghemite and quartz, and averages a total weight percent of 13.1 in the S2 profile and almost twice that in the duricrust of PB. Thus the incorporation of "impurities" in the classification of bauxite makes it more useful for their specification with regard to iron oxides and hydroxides and silica-bearing minerals. Because of this limitation, the classification proposed by Konta (1958) and modified by Bardossy (1963, 1982) and Valeton (1972) is preferred. This classification is based on quantitative mineralogy and uses a triangular diagram. Each apex of this diagram represents one of the following mineral groups: (a) aluminum hydroxides, hydrous oxides and oxides, (b) iron hydroxide, hydrous oxides and oxides, (c) clay minerals.

Anatase was added into apex (a) as proposed by Bardossy (1982) because of its close association with aluminum hydroxides, hydrous oxides and oxides. The remaining "impurities" can be considered to be essentially iron oxides and hydrous iron oxides, the samples being nearly free of residual and secondary silicates and free silica.

The percentages of gibbsite, kaolinite and "impurites" obtained from chemical calculations (tables 7, 8 and 9) were used instead of the semi-quantitative DTA and x-ray diffraction data. The reliability of these quantitative data was tested in the preceeding section by comparing them with the data obtained from norm calculations. Anatase was estimated from its normative weight percentage; this estimation is considered to be accurate inasmuch as no other Ti-bearing minerals were found to be present in the samples.

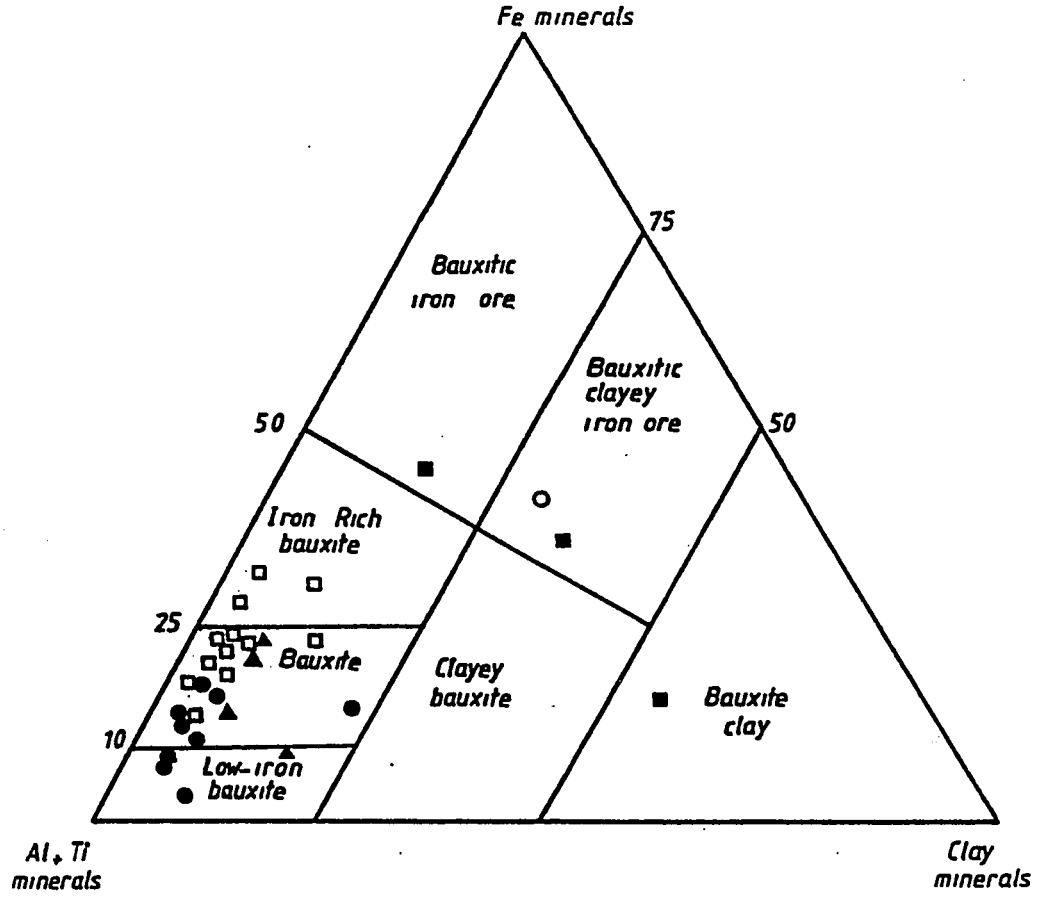

Fig. 58

Classification of bauxites from Fongo Tongo, Djeu, and Melan deposits.

▲ Surface samples

□ PB } duricrust
● S2 }

○ S2 } mottled clay
■ PB }

These data were plotted in fig. 58 according to the new classification of bauxites by Bardossy (1982) which has the advantage of including the central field of the ternary diagram where the composition of transitional material falls. The data from the S2 and the PB profiles were plotted, as well as data from outcrop samples collected at Fongo Tongo, Djeu and Melan. These samples include the two types of bauxites identified in the study area.

The results shown in fig. 58 show that the bauxites of the study area are essentially pure bauxite as defined by Bardossy (1982). They are subdivided into low-iron bauxite, bauxite sensu stricto, and iron-rich bauxite. These subdivisions represent respectively about 16%, 72% and 12% of the bauxite duricrust. The mottled clay horizon is made up of a clayey material with a composition ranging from bauxite clay to bauxitic clayey iron ore.

MINERALOGICAL TRENDS

The objective of this section is to study the evolution of the weathering profiles of Fongo Tongo and similar deposits using the trends displayed by some of the minerals identified along these profiles. The three profiles studied were S2, S4 and PB. The first two are located in the Fongo Tongo deposit which is the most important by volume and the most representative of the group, and the third profile is located at Fondjoumetah. The quantitative mineralogy of these profiles (fig. 59, 60 and 61) was obtained from norm calculations. The resulting conclusions may be extended to similar deposits.

GIBBSITE

The proportion of gibbsite is relatively constant throughout the duricrust of S2 and PB, and then decreases sharply downward in the mottled clay horizon to about one third of its value in the duricrust. Reported wt% values of gibbsite in the 10-meter-thick duricrust of profile S2 range from 76.2 and 87.7; gibbsite then follows a steady decrease with increasing depth in the mottled clay horizon reaching 32.2 wt% at the depth of 13.2 meters. An identical pattern is found along profile PB: gibbsite here varies within the narrow range of 62.9 to

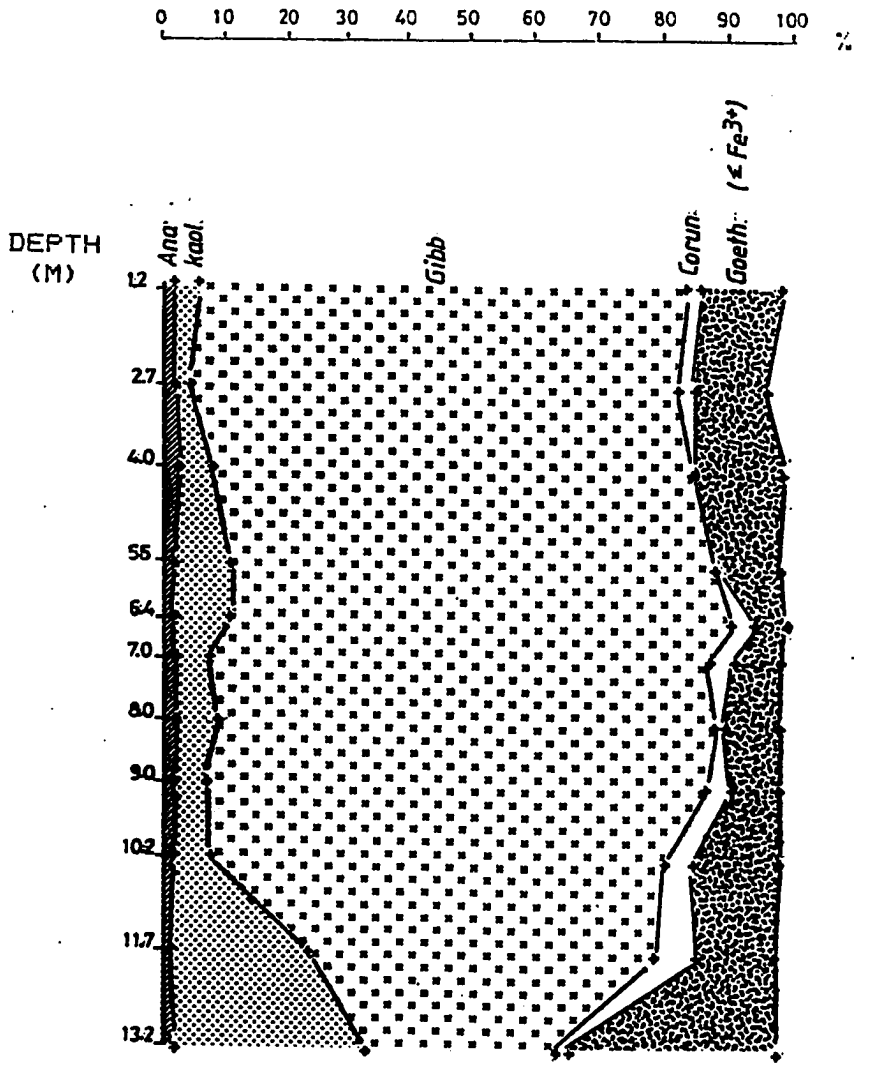

Fig. 59

Cumulative weight percents of normative minerals along profile S2.

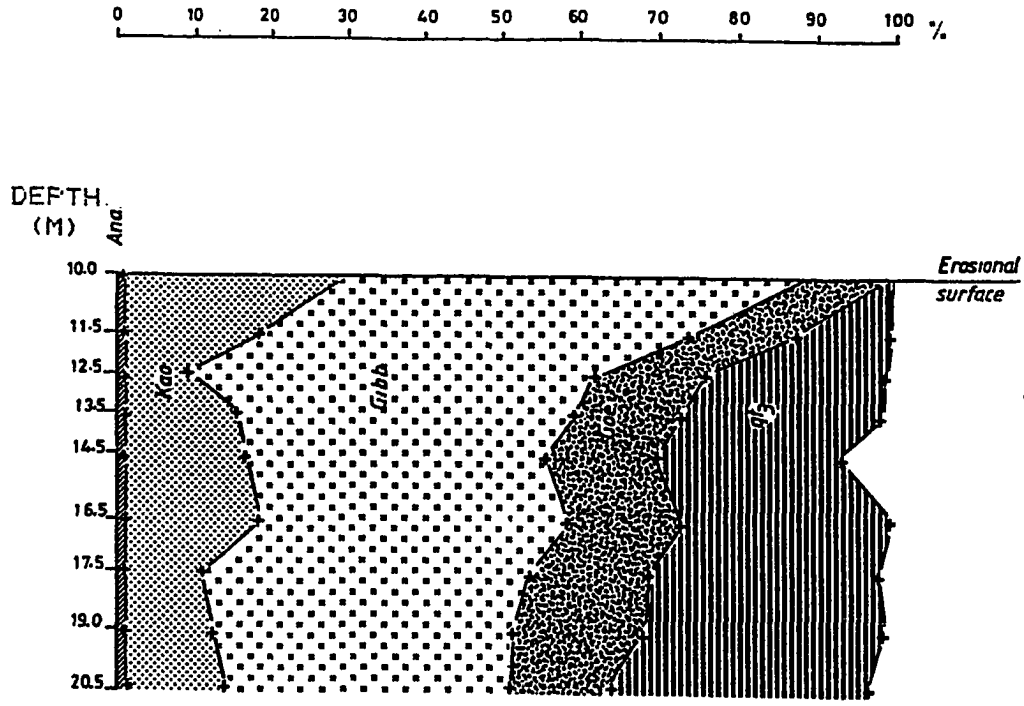

Fig.60

Cumulative weight percents of normative minerals along profile S4.

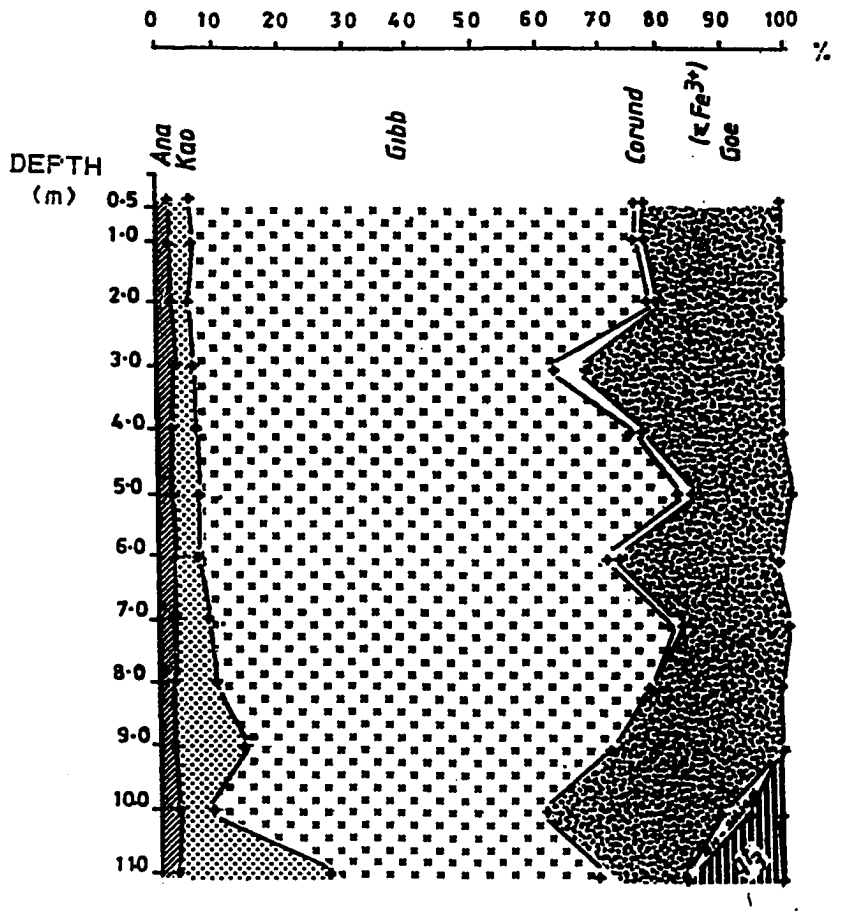

Fig. 61

Cumulative weight percents of normative minerals along profile PB.

80.6 wt% in the 8.0 meter-thick duricrust, and then falls abruptly in the mottled clay horizon reaching 23 wt% at the depth of 11.0 meters.

KAOLINITE

Kaolinite is present in the duricrust of profiles S2 and PB as a minor mineral, in normative proportions not exceeding 9.6 wt.%. Nevertheless, it increases rapidly with depth below the duricrust. Its wt% value of 31.0 at the base of the S2 profile is nearly ten times higher than that in the duricrust. A similar trend is shown along profile PB where normative kaolinite averages 30 wt% at the base of the profile. This trend indicates that kaolinite is a major mineral constituent in the mottled clay horizon.

There is an apparent discrepancy between the amount of kaolinite found in the mottled clay horizon using norm calculations and DTA techniques on the one hand, and the amount of kaolinite estimated in the same horizon by x-ray powder diffraction on the other. X-ray powder diffraction gives weak and broad maxima for the major (001) kaolinite reflection in samples for which norm calculations and DTA suggest much higher proportions of kaolinite. For example, sample S2/13.2 collected at the base of profile S2 yields 31.0 wt% for normative kaolinite. DTA data obtained on the same sample also suggest that the area under the kaolinite peak is at least equal to 2/3 of that under the gibbsite-

goethite unresolved maximum. And yet the ratio of their strongest diffraction maxima - $I(kao.d_{001})/I(gibb.d_{002})$ - is only 0.08.

To sum up, it appears that the kaolinite signature in the mottled clay horizon obtained using x-ray powder diffraction is much weaker than that given by the other analytical techniques. This discrepancy is attributed to the poor crystallinity of kaolinite in this horizon which is supported by the broadening of its (001) maximum.

The trends of kaolinite and gibbsite in the mottled clay horizon are anthipathetic and suggest that the increase with height of gibbsite is related to the breakdown of kaolinite. A similar relationship between these two minerals was noted by Rao and Krishmamurthy (1981) who concluded that gibbsite develops directly from kaolinite during bauxitization.

The behavior of kaolinite and gibbsite is somewhat different in the clayey horizon of profile S4. Here, kaolinite (and its polymorphs) increases with height in amount and crystallinity according to normative calculations, x-ray powder diffraction, and DTA data. Normative gibbsite also increases correspondingly. The trend and crystallinity of kaolinite (and its polymorphs) along this profile suggests that kaolinite originates from amorphous precursors which are formed at greater depths. The soft white material collected above the weathering front of the Fongo Tongo dark trachyte, south of the main deposit (Fig. 16), is considered to be the gel which results from the breakdown of the underlying parent rock. This gel is devoid of kaolinite and instead contains amorphous to cryptocrystalline hydrated halloysite. With increase in temperature, it has been shown in the section on

"qualitative mineralogy" that this mineral is successively replaced by metahalloysite and kaolinite. The same paragenetic sequence was found along profile S4 from bottom to top.

FREE SILICA

Free silica is present as low-cristobalite in the gel which results from the direct breakdown of the parent rocks. The relative intensity of the d_{101} reflection of low-cristobalite in this gel is equal to 27% in the Fongo Tongo area, south of the deposit. Free silica decreases with height throughout the entire weathering profile.

GOETHITE

The trend of normative goethite is essentially opposite to that of gibbsite. It appears to be closely related to that of kaolinite in the mottled clay horizon and in the duricrust.

ANATASE

Anatase is fairly constant along the profiles, and its trend is non-instructive as far as bauxitization is concerned.

CONCLUSIONS ON MINERALOGICAL TRENDS

The trends of the five important minerals encountered along the weathering profile of the Fongo Tongo and similar deposits have been examined in this section. These trends were not obtained from a single continous bore hole, but from a number of profiles. The information collected from all of these profiles was found to be complementary, and has allowed a full reconstruction of the vertical trends of gibbsite, kaolinite and associated polymorphs, free silica, goethite and anatase. The last mineral did not provide useful information on the evolution of the weathering profile. The first four, however, have helped to understand some of the critical aspects of the process of bauxitization in the study area. Their trends are summarized in fig. 62 which shows the theoretical weathering profile of Fongo Tongo and similar deposits. This profile may be divided into the following three horizons:

(1). The first and lowermost horizon is made up of a soft whitish gel which results from the breakdown of the parent rock. Its thickness varies from one to about ten meters depending on the topography. It is called the *pale-yellow-to-white homogeneous clayey horizon*. It is situated directly above the weathering front, and is characterized by the presence of hydrated halloysite in its lower part, and by metahalloysite in its upper part. Because of its mineralogy, it is believed to develop under conditions of hydration. It also contains some gibbsite.

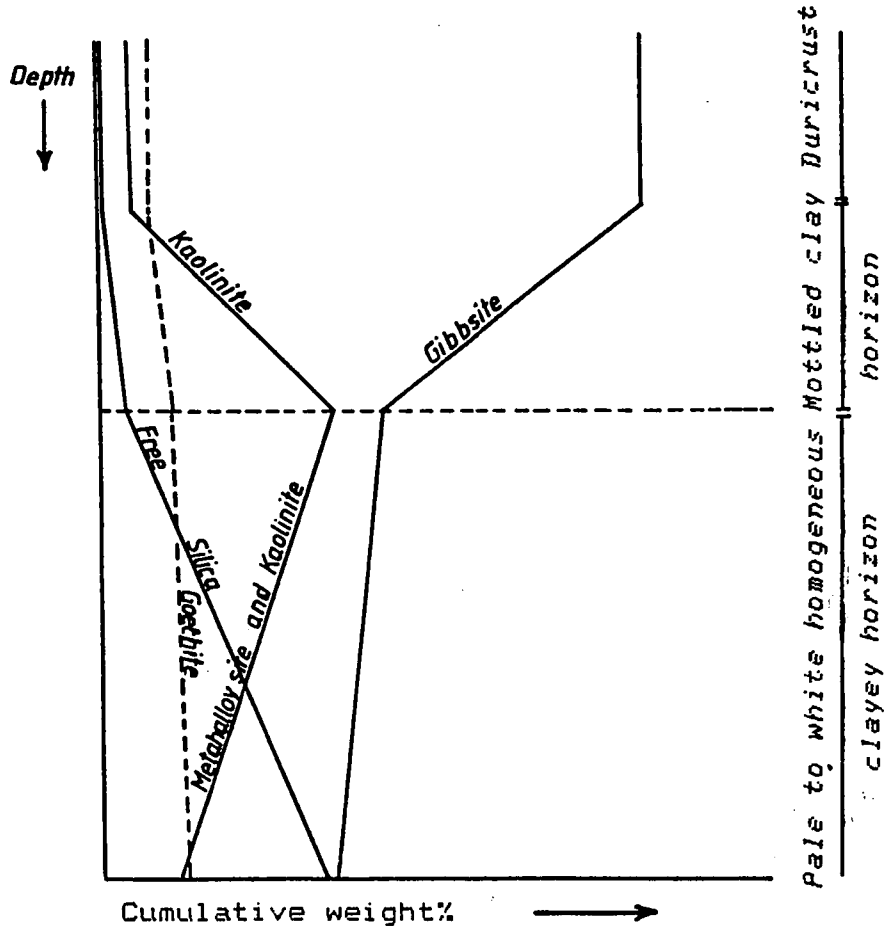

Fig. 62

Trends of major minerals along the weathering profile of Fongo Tongo and genetically related bauxite deposits

(2). Overlying this clay is the *mottled clay horizon*. Its thickness was not found, but is believed to vary with the topography. It is characterized by the hydrolysis of kaolinite with height and a corresponding increase in gibbsite. According to Grubb (1963) this reaction is common in the formation of residual bauxite, and takes place only above the watertable.

(3). The third and uppermost horizon is the *duricrust* which is about 10 meters thick. It is nearly devoid of silica, is low in kaolinite which amounts to less than 10% by weight, and is made up dominantly of gibbsite which reaches more than 80 wt%. The percentages of gibbsite and kaolinite are independent of depth and suggest that the invariant point where the two minerals are at equilibrium in the ternary system H_2O - SiO_2 - Al_2O_3 is reached in this horizon. This is confirmed by the depth independence of residual silica in this horizon.

Every bauxitic profile may not show the development of all three horizons. Direct bauxitization of a parent rock may take place without the formation of any intermediate clay zone, especially in the case of saprolitic bauxite. The field and laboratory data collected during this study support such a process in the case of the "Melan saprolite", and a similar saprolite on top of the weathered igneous rocks in Arkansas was described by Gordon et al. (1958). Nevertheless, this process is only valid for saprolitic bauxite.

The total absence of a relic trachytic texture in the "Fongo Tongo-type bauxite" strongly suggests that it was formed through the desilication of an intermediate lateritic clay horizon and the

cementation of the residual aluminum-rich material to yield a coherent duricrust.

GEOCHEMISTRY OF MAJOR AND TRACE ELEMENTS

In order to understand how the mineral trends shown in the preceeding section relate to bauxitic weathering, the chemical processes which led to the formation of the saprolite and to the Fongo Tongo lateritic bauxite will now be addressed. The dissolution processes of the major minerals of the parent rock will be considered along with the geochemical behavior of the major and trace elements during bauxitization.

GEOCHEMICAL BEHAVIOR OF MAJOR AND TRACE ELEMENTS DURING THEIR EXOGENIC CYCLE

Geochemical Behavior of Major Elements

During bauxitic weathering, the parent rocks are broken down and their minerals decomposed under the influence of various external factors such as climate, topography, microorganisms, etc. and are subjected to intense extractive leaching by meteoric water which results in important changes in the concentration of most of the major and trace elements. The weathering order of the rock-forming minerals in which these elements are originally locked was proposed by Goldich (1938) in a mineral stability series shown in fig. 63.

The stability of silicate minerals in a weathering environment is a function of the relative bond strengths of the various cations with

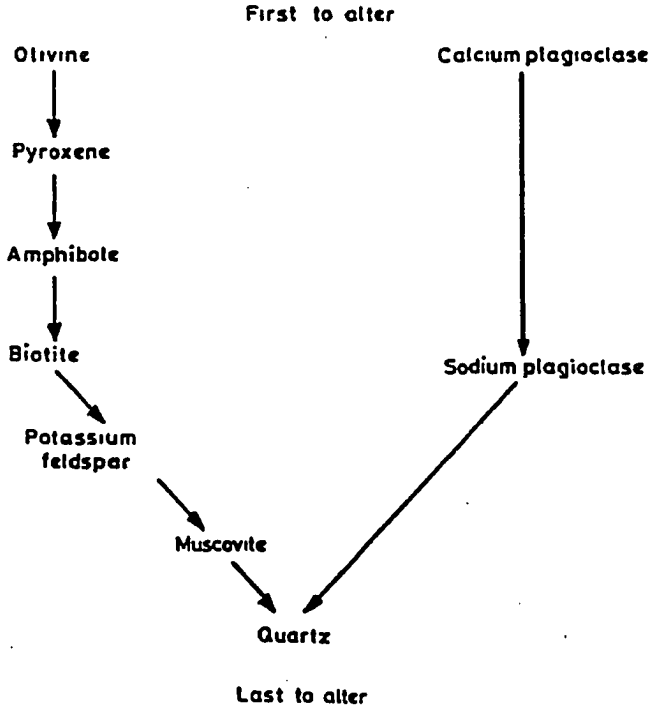

Fig. 63

Order of chemical alteration of primary minerals during weathering (Goldich, 1938).

oxygen (Blatt et al., 1980). Table 15 (Nicholls, 1963) gives the relative strengths of various cation-oxygen bonds in the common rock-forming minerals. The order of bond strengths very nearly similar to the amount of covalent bond character, and the Si-O bond, the strongest of those listed in table 15, is the most covalent (Blatt et al., 1980). Aluminum forms a weaker Al-O bond, and, as a result, the stability of the various silicate minerals is expected to decrease with increase in Al in the tetrahedral coordination site. One such example is the lower stability of calcic plagioclase as compared to albite which has a higher Si/Al ratio.

Once freed from mineral structures, some elements are carried away by weathering solutions while others such as aluminum, iron, and manganese may precipitate and form new compounds under favorable pH and Eh conditions. The development of bauxite depends on the geochemical behavior of these elements once they are liberated.

Geochemical Behavior of Trace Elements

The behavior of trace elements during weathering depends in part on their mineralogical occurence in the unweathered parent rocks. Their geochemical occurence in parent rocks was summarized by Vlassov (1966) as follows:

(1). Some trace elements enter into mineral lattices as ionic substitutes of major rock-forming elements.

(2). They can concentrate in residual magmatic solutions.

(3). At a definite stage during crystallization they start growing independent crystal lattices, but this growth may be inhibited by their

Table 15

Relative strengths of various cation-oxygen bonds
in common rock-forming minerals (after Nicholls, 1963)

Bond	Approximative relative strenght
Si-O	2.4
Ti-O	1.8
Al-O	1.65
Fe^{3+}-O	1.4
Mg-O	0.9
Fe^{2+}-O	0.85
Mn-O	0.8
Ca-O	0.7
Na-O	0.35
K-O	0.25

low concentration. They are then found dispersed in the rock in a rudimentary stage as minute segregations (accessory minerals).

Zirconium, for example, concentrates essentially in weathering-resistant zircon together with hafnium (Tsibul'chik and Ponomarchuk, 1980). Niobium and tantalum do not develop independant minerals and are dispersed in mafic minerals such as biotite and hornblende and in accessories such as zircon, ilmenite, and sphene because of their close geochemical relationship with zirconium and titanium (Tsibul'chik and Ponomarchuk, 1980). Upon the weathering of host minerals, these trace elements tend to form residual accumulations in ferric iron hydroxides in association with germanium, arsenic, vanadium, scandium, rare-earth elements and some other rare elements (Vlassov, 1966). This assemblage is more characteristic of bauxites (Vlassov, 1966).

Weathering processes promote the dispersion of rubidium and strontium in comparison with endogene processes, and only clay and argillaceous sediments have a rubidium content greater than its clarke value in supergene zones (Vlassov, 1966).

After the decomposition of its host minerals, barium is dissolved and brought into circulation, mainly in aqueous bicarbonate solutions (Goldschmidt, 1954). It nevertheless can concentrate in manganese oxy-hydroxides.

Cobalt is partially separated from nickel and carried in the weathering solutions as bicarbonate or colloidal hydroxide from which it may precipitate along with manganese (Rankama and Sahama, 1949). The Co/Ni ratio nevertheless tends to remain constant for a given rock; its

average for instance is 0.40 in hydrolizate sediments (Goldschmidt, 1937b).

Most of the lead in magmatic rocks is "locked" as a minor component in rather resistant silicates such as orthoclase and amphibole (Rankama and Sahama, 1949). In weathering zones, lead readily forms solute cations which may react with suitable anions to form insoluble compounds, or participate in processes of adsorption and ionic exchange with insoluble constituents of soil minerals, especially with the clay fraction (Goldschmidt, 1954). Goldschmidt also points out that a great variety of highly insoluble lead compounds are known in oxidation zones in which lead can be associated with other trace elements such as As, V, Mo and W. Lead which escapes these various possibilities of reprecipitation in the weathering profile is leached out as dissolved divalent cations (Goldschmidt, 1954).

Zinc and copper go into solution readily during weathering (Rankama and Sahama, 1949). These authors also point out that chromium follows ferric iron and aluminum during weathering because of the closeness of their ionic size and ionic charge.

GEOCHEMISTRY OF MAJOR AND TRACE ELEMENTS IN THE STUDY AREA

Geochemistry of Major Elements

The mean concentration ratios of the major elements present in the bauxites are shown in figure 64. Each number represents the ratio of the

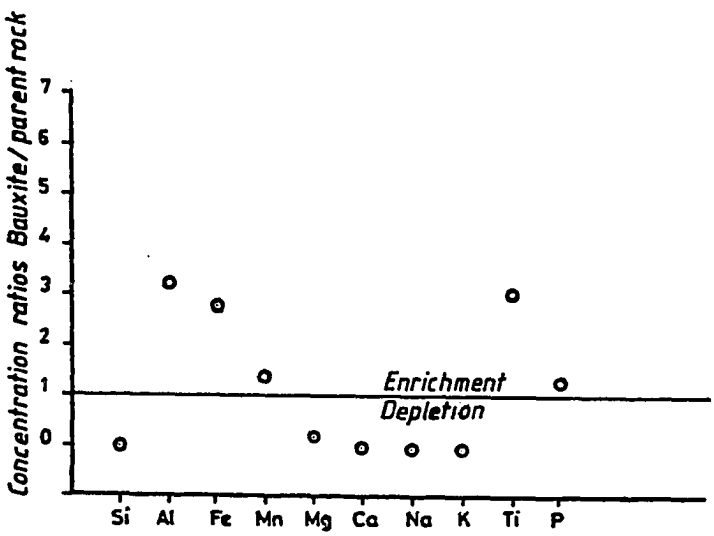

Fig. 64

Concentration ratios bauxite/parent rock
for major elements.

concentration of an element in the bauxite to its concentration in the parent rocks. These concentration ratios were individually calculated for each group of deposits with respect to its parent rock(s) and were averaged for each element. The numerical values are reported in table 16 which shows the concentration ratios of major elements for each group of deposits, as well as the arithmetic average of these ratios for each element. Ferrous iron found in bauxite outcrops was not considered because it is virtually absent in the bauxite, and what is present is believed to be related to biogenic reduction of Fe^{3+}.

Major elements can be divided into two separate groups depending on whether they undergo enrichment or depletion during bauxitization. Enriched elements are Al, Fe, Mn, P, and Ti. The trends of some of them and silica along profiles S2, PB and S4 are shown respectively in figs. 65, 66 and 67. The elements which are depleted are Si, Mg, Ca and K. Titanium has the highest concentration ratio, followed by aluminum, iron, and phosphorus. Aluminum and iron are essentially present as hydrated oxides, with the exception of kaolinite and traces of iron oxides. Titanium is present as anatase whereas phosphorus may be held in undissolved residual apatite (Rankama and Sahama, 1949).

The average concentration ratio of aluminum is 3.28 which is much lower than the 4- to 5-fold given by Goldschmidt (1937) for bauxites. Such low aluminum concentrations were also found in the Arkansas lateritic bauxites (Gordon et al., 1958). As pointed out by these authors, the 4- to 5-fold aluminum concentration can only be attained in bauxites containing alumina in the monohydrate form, such as the European bauxites to which Goldschmidt probably referred.

Table 16

Concentration ratios for major elements

	Fongo-Tongo	Djeu + Melan	Average
SiO_2	0.04	0.06	0.05
Al_2O_3	3.37	3.20	3.28
Fe_2O_3	2.22	3.40	2.81
MnO_2	1.40		1.40
MgO	0.02	0.4	0.21
CaO	0.025	0.02	0.022
Na_2O	0.02	0.02	0.02
K_2O	0.02	0.02	0.02
TiO_2	1.89	4.79	3.34
P_2O_5	0.41	2.16	1.28
LOI	20.68	20.68	20.68

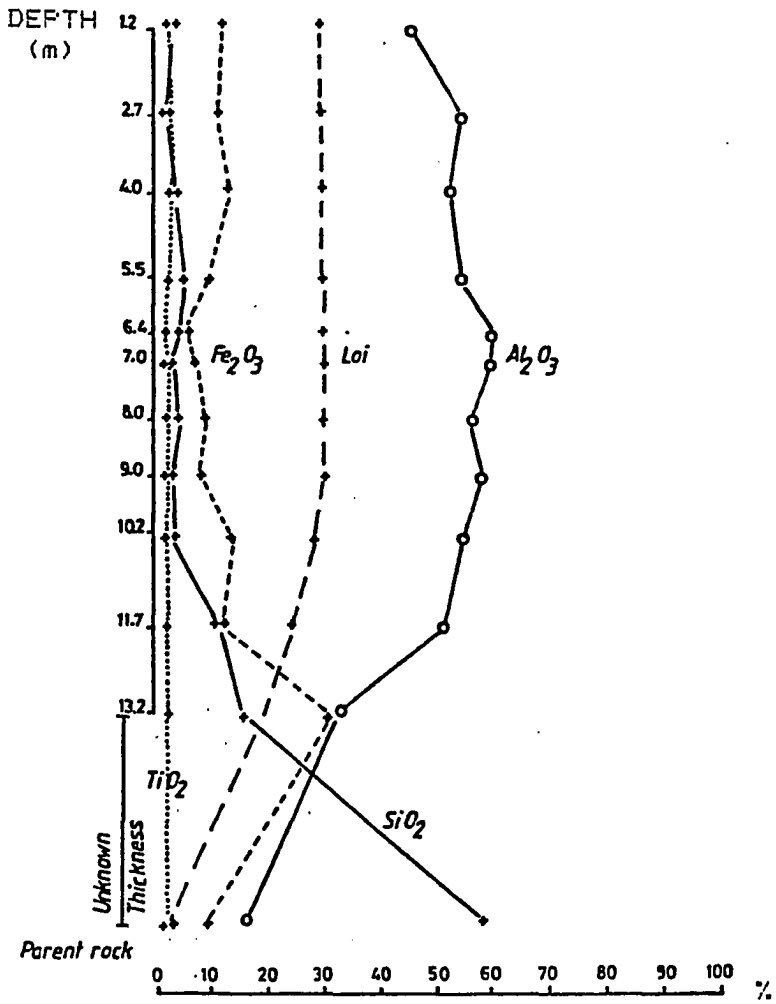

Fig. 65

Variation with depth of some enriched major elements and silica along profile S2.

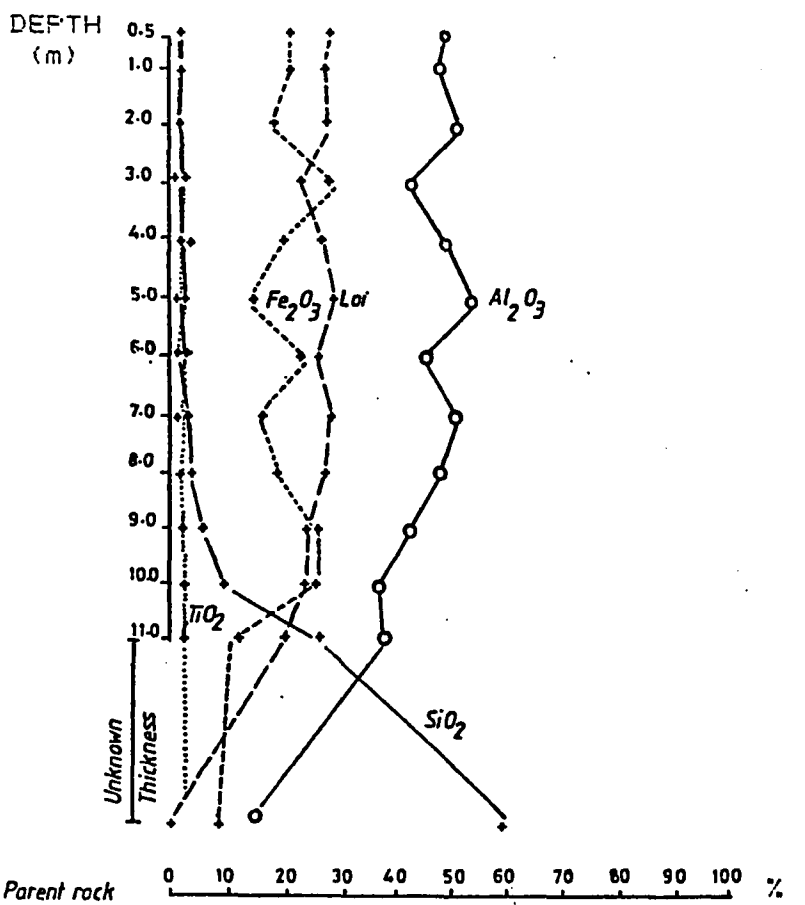

Fig. 66

Variation with depth of some enriched major elements and silica along profile PB.

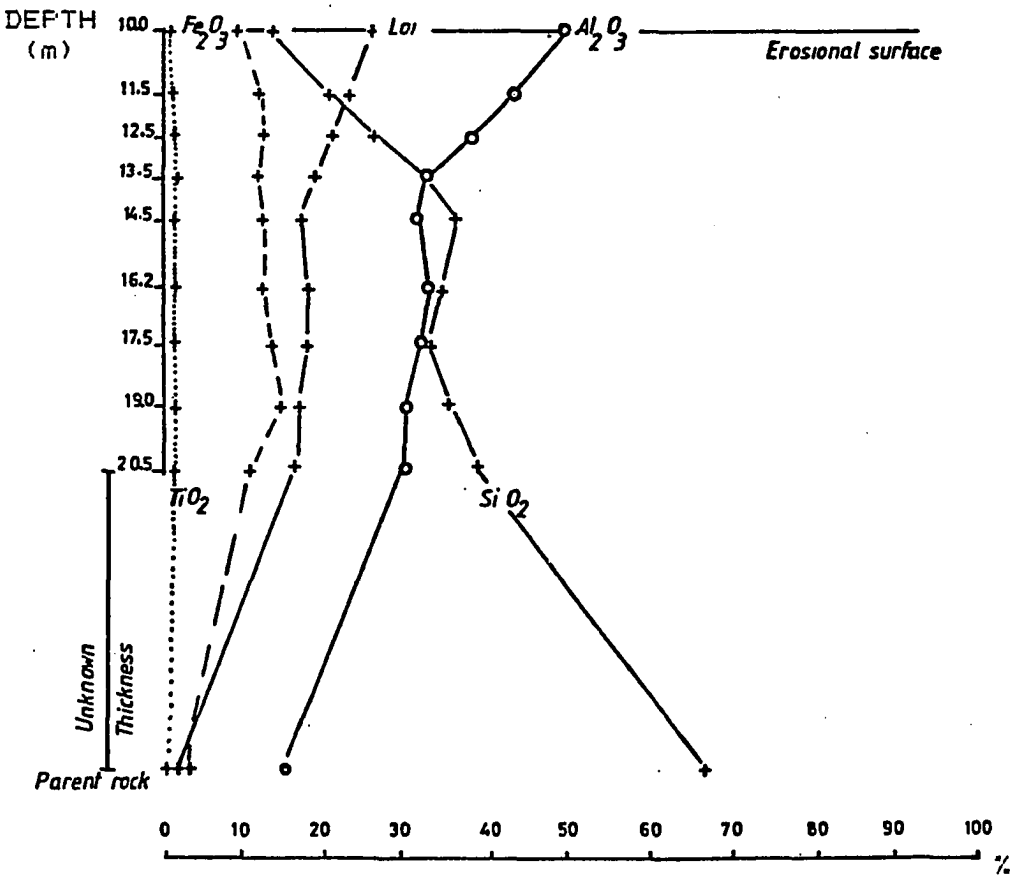

Fig. 67

Variation with depth of some enriched major elements and silica along profile S4.

It is difficult in a geochemical study of bauxitic profiles based on whole-rock analyses to quantitatively separate elemental first-generation enrichment from subsequent enrichment due to lateral and vertical migration of elements such as Fe and Al. Such examples were described above in the duricrust of Fongo Tongo and similar deposits, and are characterized by veins of goethite and gibbsite cutting across the original bauxitic matrix. Secondary redistribution of aluminum and iron has not been separately quantified in this study as the aim of this investigation is essentially to understand the overall behavior throughout the weathering profile of silicon and enriched elements.

Both the S2 and the PB profiles show an identical distribution for silicon which decreases rapidly with height within the mottled horizon and reaches its minimum in the duricrust. Silicon then remains constant throughout the duricrust. Iron and aluminum tend to have opposite trends, and titanium is nearly constant throughout the profile.

The behavior of aluminum in relation to silicon and iron in the weathering profile of Fongo Tongo and similar deposits is best characterized by the trends of the ratios SiO_2/Al_2O_3 and Fe_2O_3/Al_2O_3 along S2, PB and S4 profiles (Figs. 68, 69 and 70). The ratio SiO_2/Al_2O_3 decreases continously with height from the parent rocks all the way up to the duricrust where its lowest value is expressed. Its decrease with height reflects the metastability of the various hydrated alumino-silicates in the lower horizons of the profile. This ratio is essentially constant in the duricrust.

The change with height of the ratio Fe_2O_3/Al_2O_3 suggests limited enrichment of Al with respect to Fe in the duricrust. This trend is

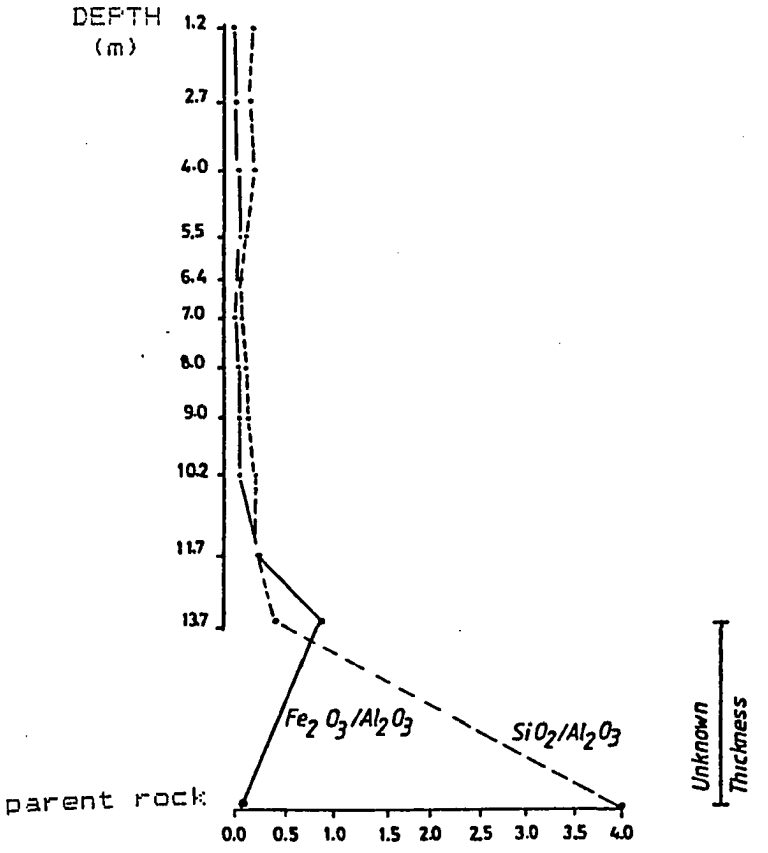

Fig. 68

Fe_2O_3/Al_2O_3 and SiO_2/Al_2O_3 trends along profile S2

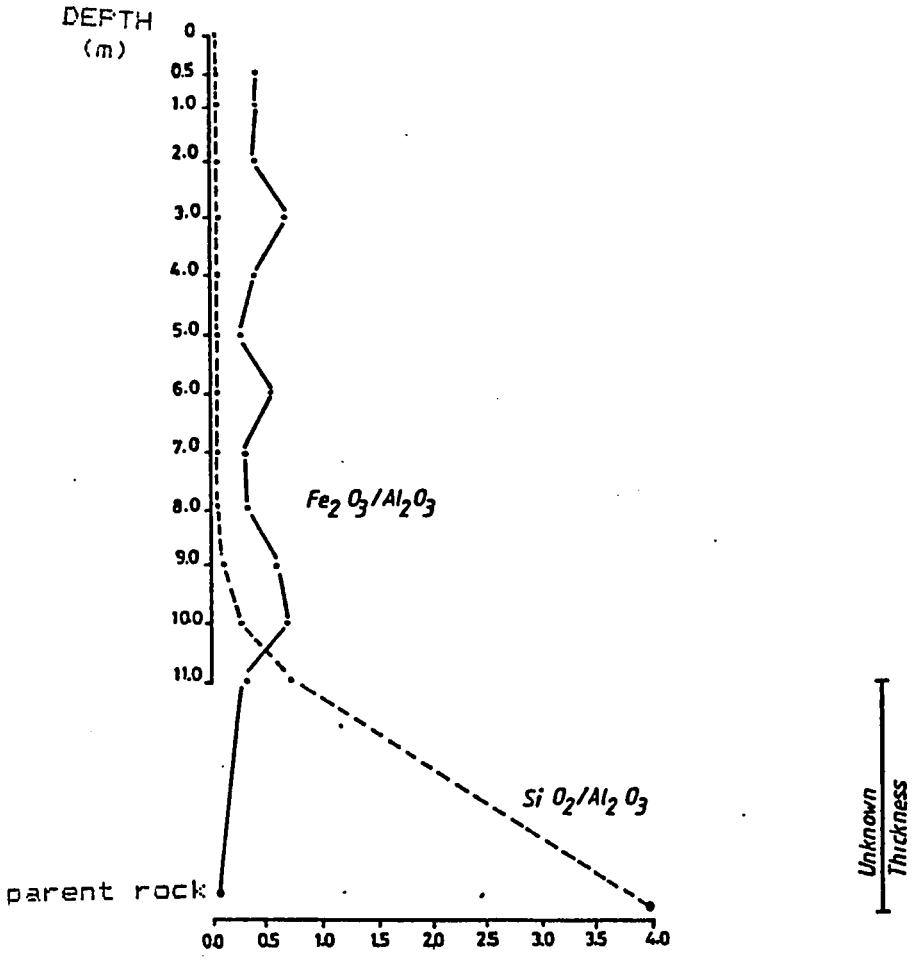

Fig. 69

Fe_2O_3/Al_2O_3 and SiO_2/Al_2O_3 trends along profile PB

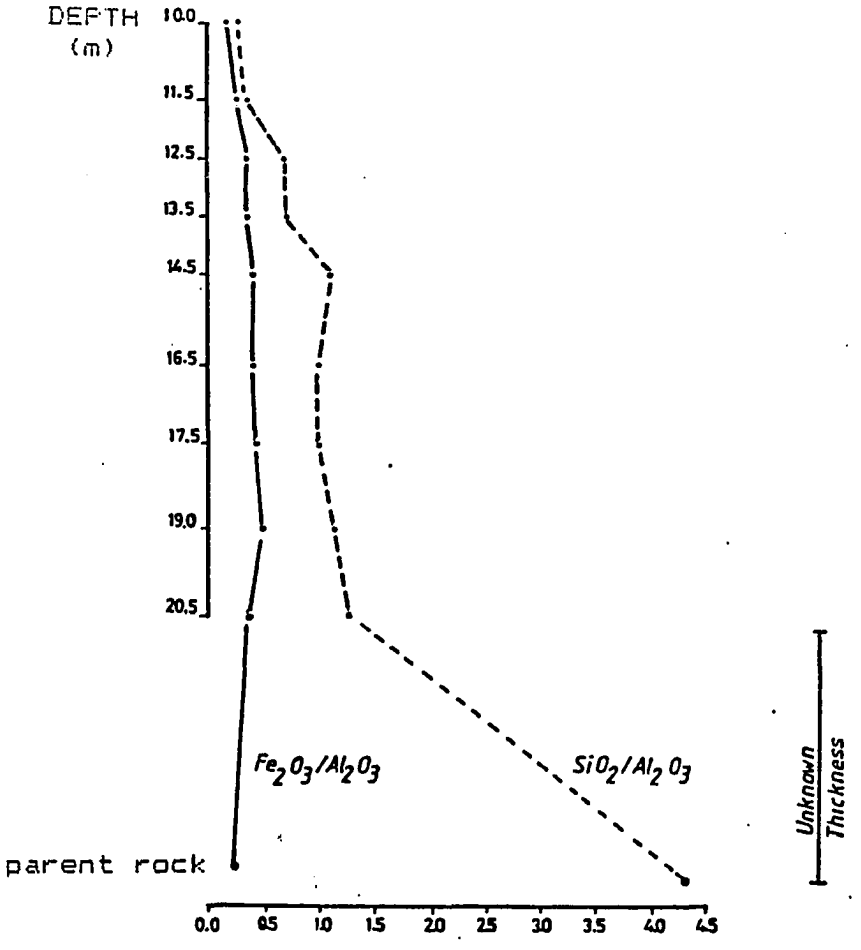

Fig. 70

Fe_2O_3/Al_2O_3 and SiO_2/Al_2O_3 trends along profile S4

somewhat erratic along profile PB because of the relatively higher mobility of iron along the trench from where this profile was sampled. Nevertheless this ratio is fairly constant throughout profile PB.

Among the group of depleted elements, those which have been almost completely leached out are Ca, Na, and K. These elements are characterized by weak structural bonds with oxygen. Their bonds are easily broken during weathering which results in solution of these cations. The very high loss of silica despite its strong structural bond is related to the ultimate depolymerization of all the silica tetrahedral networks in the parent minerals.

Geochemistry of Trace Elements

Fifteen outcrop samples of parent rocks and bauxites and twelve core samples from S2 were analysed for Cr, V, Ni, Rb, Sr, Ba, Co, Pb, Zn and Cu for the outcrop samples and Cr, Rb, Sr, Y, Nb and Zr for the core samples. In addition, thirteen samples from S4 were analysed for Cr, Rb, Sr, Y, Zr, Nb, Ba, Co and Ni. The resulting analyses are given in Appendix 1. The bauxite-to-parent-rock concentration ratios for 12 trace elements are shown in fig. 71 and the numerical values are reported in table 17. Fongo Tongo values were used for Cu and Sr. The average Ba, Zr, and Nb values obtained along profiles S2 and S4 were used.

One group of trace elements is enriched. It includes Cr, V, Ni, Co, Cu, Zr and Nb. This enrichment was expected based on discussion above of the geochemical behavior of these elements during their exogenic cycle, with the exception of Cu. However, copper may be adsorbed in oxidates together with other trace elements such as nickel,

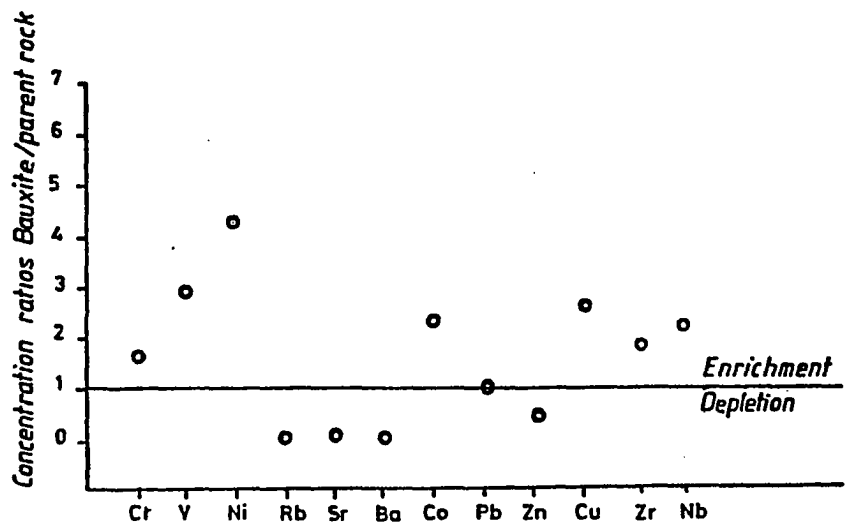

Fig. 71

Concentration ratios bauxite/parent rock
for trace elements.

Table 17

Concentration ratios for trace elements

	Fongo-Tongo	Djeu - Melan	Average
Cr	1.69		1.69
V	2.33	2.54	2.93
Ni	3.69	4.93	4.31
Rb	0.09	0.06	0.075
Sr	0.08		0.08
Ba	0.008		0.008
Co	2.86	1.85	2.35
Pb	1.05	1.12	1.08
Zn	0.70	0.17	0.43
Cu	3.96	1.30	2.63
Y	1.11		1.11
Zr	1.91		1.91
Nb	2.22		2.22

cobalt, zinc, lead, etc. (Rankama and Sahama, 1949). These authors have described adsorption compounds like $CuMn_2O_5$. Adsorption by oxidates could thus explain the enrichment in Cu detected in these deposits.

The parent rocks are exceptionally high in Co with respect to Ni. Their Co/Ni ratio is 4.35 for the greenish trachyte and 1.52 for the Fongo Tongo trachyte. This ratio falls to 0.375 in the bauxites derived from the greenish trachyte, and to 0.77 in the Fongo Tongo bauxite. This drop in the Co/Ni ratio is indicative of a relative depletion of Co with respect to Ni during bauxitic weathering, and thus of a higher mobility of cobalt relative to nickel.

Depleted trace elements include Rb, Sr, Ba and Zn. These elements are probably dispersed by weathering processes through aqueous solutions. Although not confirmed by whole-rock analysis, barium has been detected using EDS methods in the manganese ore which contains "cameroonite" and subordinate romanechite.

Figs. 72 and 73 show the trends of both Mn and Ba along profiles S2 and S4, and reveal a very close relationship between the two elements throughout the weathering profile. This relationship is also suggested by EDS qualitative analysis of "cameroonite" (Fig. 46), but was not quantitatively studied at the time of this writing .

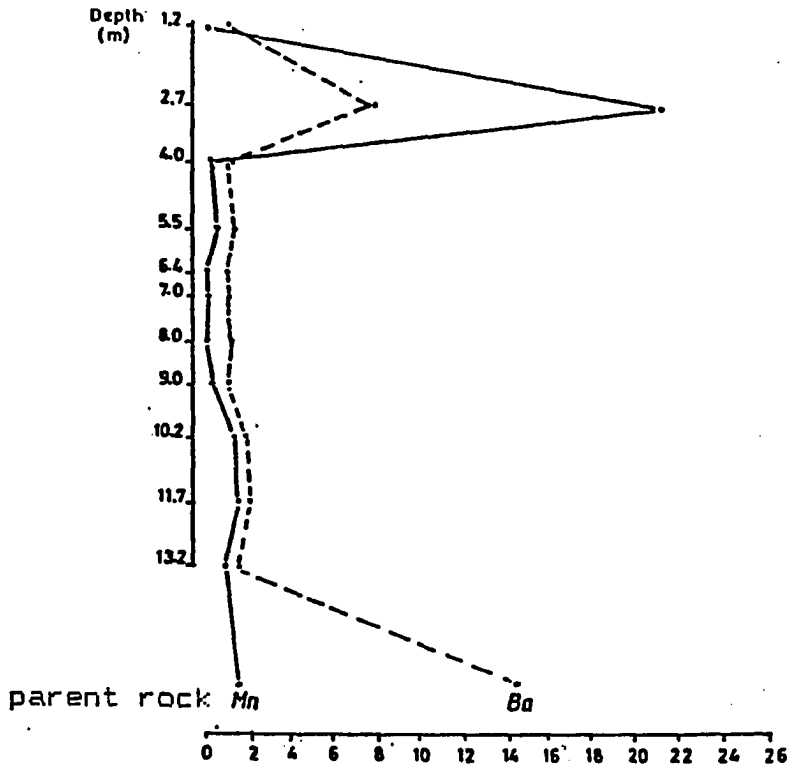

Fig. 72

Trends of Ba and Mn in profile S2

Mn: $x10^{-1}$ wt%
Ba: $x10^{2}$ ppm

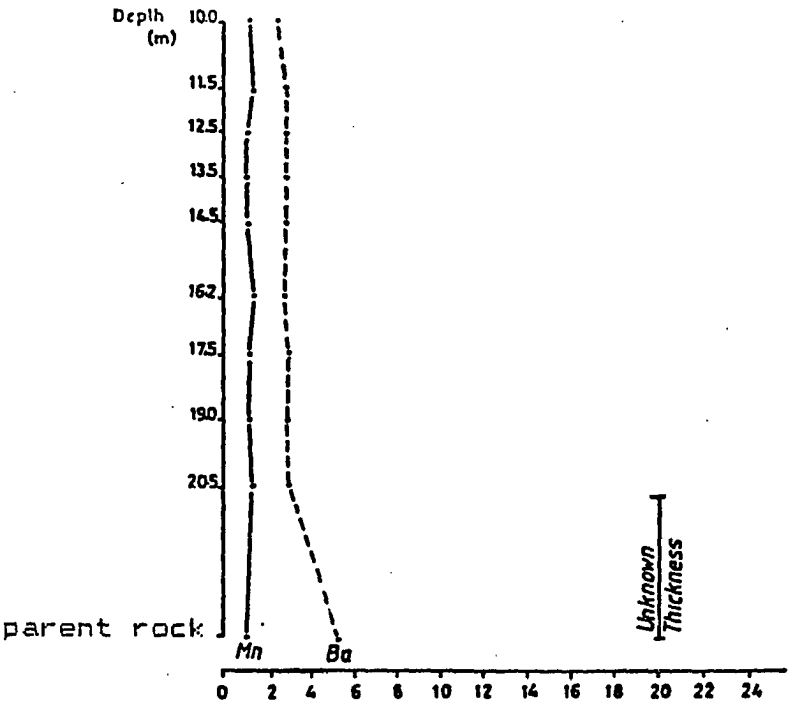

Fig. 73

Trends of Ba and Mn in profile S4

Mn: $x10^{-1}$ wt%
Ba: $x10^{2}$ ppm

Lead remains at about the same concentration as in the parent rocks. High lead concentration ratios were reported in the Arkansas bauxites where this element is believed to have undergone secondary enrichment due to events subsequent to bauxitization such as the burial of the deposits by Late Eocene sediments accompanied by a rise of the water table (Gordon and Murata, 1952). Such a burial was not recorded in the study area, and the non-depletion of lead there is rather attributed to its adsorption by oxidates or iron hydroxides.

GEOCHEMICAL BEHAVIOR OF ELEMENTS IN RELATION TO IONIC POTENTIAL

Concept of Ionic Potential and Theoretical Prediction of the Geochemical Behavior of Elements during Bauxitization

In order to obtain a comprehensive representation of the properties of ions and their compounds, Cartledge (1928) proposed to take into account the charge, structure and size of the ionic constituents of compounds and to develop a form of representation which would take into account all valence forms of all the elements. Realizing that the charge of an ion and its size act in opposite directions, and that the ratio of charge to radius is an important property of ions and determines their behavior, he proposed the following function also called "ionic potential":

$$I = Z/r$$

where "Z" is the charge of the ion and "r" its radius. This equation assumes that ions are charged spheres of finite size.

The concept of ionic potential was later applied in the earth sciences by Goldschmidt (1937a) who found that the radii and valency of atoms and ions regulate the distribution of elements, not only in the minerals of primary magmatic rocks, but also during the formation of sedimentary rocks and in various mineral-forming processes, especially those related to aqueous solutions.

Fig. 74 from Gordon and Murata (1952) after Goldschmidt (1937a) is a grouping of certain elements according to their ionic radii and charges. Elements of low ionic potential remain in solution during weathering, whereas those with intermediate potential are precipitated by hydrolysis. Elements with still higher ionic potential form anions containing oxygen and remain in solution. The three groups of elements are separated by lines of equal ionic potential. The first line represents an ionic potential of 3.0 and separates the field of soluble cations from the elements of hydrolysates. The second line has an ionic potential value of 12.0 and separates the elements of hydrolysates from the soluble complex anions. The dashed line with an ionic potential value of 9.5 was proposed by Gordon and Murata (1952) and represents more closely the upper limit of the elements concentrated in bauxite.

The concept of ionic potential, therefore, allows the grouping of elements which have similar Z/r ratios and are consequently expected to behave similarly during weathering.

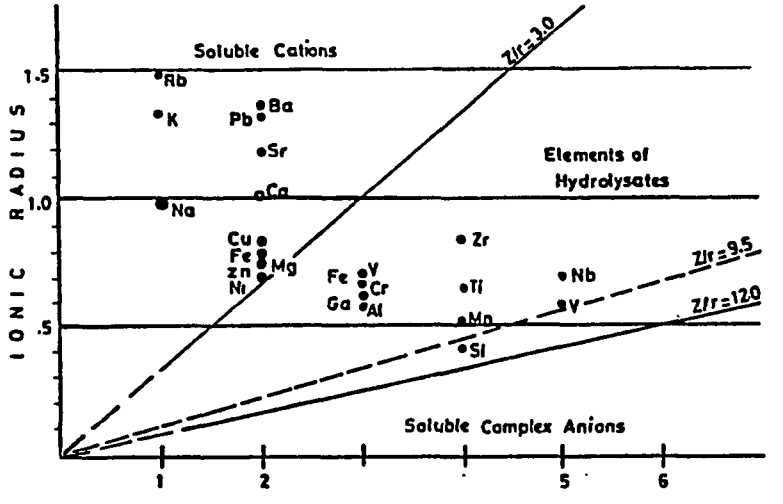

Fig. 74

Grouping of certain elements according to their ionic radii and charges. After Gordon and Murata, 1952.

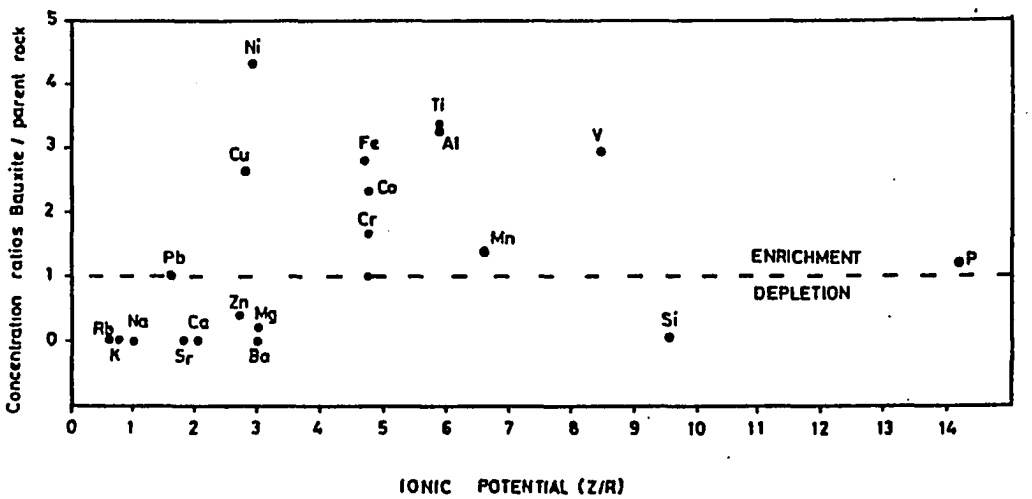

Fig. 75

Concentration of some major and trace elements in Fongo Tongo and areally related bauxite deposits grouped according to their ionic potentials.

Table 18

Ionic potentials of enriched and depleted elements.
(*)Magnetic measurements made on soil cobalt (Grn and Manasse, 1950) suggest that it is trivalent

ELEMENTS	Z/r	ELEMENTS	Z/r
Si^{4+}	9.52	Cr^{3+}	4.76
Al^{3+}	5.88	V^{5+}	8.48
Fe^{3+}	4.69	Ni^{2+}	2.89
Mn^{4+}	6.67	Rb^{1+}	0.68
Mg^{2+}	3.03	Sr^{2+}	1.78
Ca^{2+}	2.02	Ba^{2+}	1.49
Na^{1+}	1.03	Co^{3+}(*)	4.76
K^{1+}	0.75	Pb^{2+}	1.6
Ti^{4+}	5.88	Zn^{2+}	2.7
P^{5+}	14.28	Cu^{2+}	2.78

Geochemical Behavior of Elements in the Study Area Based on their Ionic Potentials

The behavior during bauxitic weathering in the study area of major and trace elements with respect to their ionic potentials is shown in fig. 75. The concentration ratios of the elements present in the bauxites are plotted on the ordinate and their ionic potentials (Table 18) are plotted on the abscissa. Comparison with the theoretically predicted behavior of elements (fig. 74) shows complete agreement between Fig 74 and Fig. 75 as follows:

(1). Elements with ionic potentials between 0 and 3 are depleted with the exception of Cu, Ni and Pb. These include K, Na, Ca, Ba, Mg, Rb, Sr and Zn. This depletion is in accordance with the predictions from fig. 74. Cu, and Pb may have been adsorbed by oxydates during weathering as discussed above. Contrary to Goldschmidt predictions, Ni is residually enriched in the study area. Similar Ni enrichement was reported in laterites by Sahu (1981).

(2). Elements with ionic potentials between 3.0 and 9.5 are enriched. They include Cr, Co, Fe, Ti, Mn, Al, and V. Most of the Mn is concentrated in the highly enriched manganese oxide masses which occur at a specific level in the profile. The fundamental reasons for this mode of occurrence have not been investigated.

(3). Silicon and phosphorous have ionic potentials greater than 9.5. Silicon is depleted as expected whereas phosphorus shows a slight enrichment which is attributed to the presence in the weathering profile of P-bearing resistates such as apatite.

BAUXITIZATION PROCESSES IN CAMEROON WESTERN HIGHLANDS

PHYSICO-CHEMICAL ENVIRONMENT OF BAUXITIZATION

Much research has been done on this matter by numerous researchers since the turn of the century. Some of the outstanding contributions on the subject were made by Harrison (1934), Lacroix (1934), Mohr (1944), Gordon and Murata (1952), Gordon et al. (1958), Carroll (1970a,b) and many others. The variables in rock weathering and soil formation according to most of these authors are climate, parent rocks, biological activity, topography and time. Physico-chemical constraints imposed on these variables for bauxitic weathering were summarized by Gordon and Murata (1952) as follows:

(1). The climate must be one of continuous moisture, with temperatures exceeding 25°C most of the time in order to ensure fast destruction of humus by microflora. High average temperatures in moist areas increase vegetation and rock weathering by chemical processes (Carroll, 1970b).

(2). Higher topographies favor better drainage and are more appropriate for bauxitization. Nevertheless, elevations above 2,500 meters seem to favor podzolization due to the prevalence of a more temperate climate. In any case the rock must be above the level of the permanent water table.

(3). All these conditions must last long enough to allow bauxitization.

According to Gordon and Murata (1952), the mineralogy of the parent rock is not a major physico-chemical constraint since bauxitic weathering has been reported on a variety of rocks including syenite, phonolite, trachyte, granite, diorite, gneiss, arkose, limestone, etc.

The climatograph for the study area in fig. 4 shows that the mean temperature varies between 19°C and 23°C and is slightly lower than the minimum of 25°C required for bauxitization (Gordon and Murata, 1952). Despite conclusions reached by Frakes and Kemp (1972), which suggest that present-day climatic conditions have been stable since the Mid-Oligocene, it is likely that the original climate which prevailed in the study area during bauxitization has changed slightly.

The high elevation of the study area was particularly favorable for bauxitic weathering which, together with an excellent microdrainage (Le Marechal, 1974), induced prolonged leaching.

PH AND EH CONTROL ON THE ENVIRONMENT OF BAUXITIZATION

Bauxites are essentially composed of hydroxides, hydrated oxides and oxides of Al, Fe, Mn, and, to a lesser degree, Si which expressed by phyllosilicates. The pH and Eh of the weathering environment play a key role in the behavior of these elements in aqueous solutions during

bauxitization. The stability of each of these elements during weathering can be summarized as follows:

Stability of Al^{3+}

According to published data on the stability of aluminum ions in acidic solutions, Al^{3+} tends to hydrolyse in solution at any pH above 3.0 (Hem and Roberson, 1967; Reesman et al, 1969; Smith and Hem, 1972).

The behavior of aluminum in alkaline solutions is different. Hydrolysis experiments by Hem and Roberson (1967) in the pH range 7.5-9.5 show that aluminum hydroxide colloids are partly redissolved as $Al(OH)_4^-$ as follows:

$$Al(OH)_{3coll} + H_2O = Al(OH)_4^- + H^+$$

Therefore, the stability of aluminum in natural dilute solutions is closely related to the pH of the environment. Fig. 76, after Reesmann et al. (1969), shows the relationship between the four main ionic forms of aluminum in solution as a function of the pH of the solution. It is important to note that aluminum shows no Eh dependency within the pH range of rock weathering (fig. 77).

Stability of Iron

Iron is found in nature in both divalent and trivalent states. Among the factors controlling its behavior during weathering, the pH and Eh of weathering solutions are the most important (Fig. 78). Divalent iron is stable in low Eh conditions, and converts into trivalent iron with increase in Eh.

On the pH dependency of the evolution of Fe-complexes, experiments made on perchlorate solutions containing $[(Fe(H_2O)_6]^{3+}$ have shown that

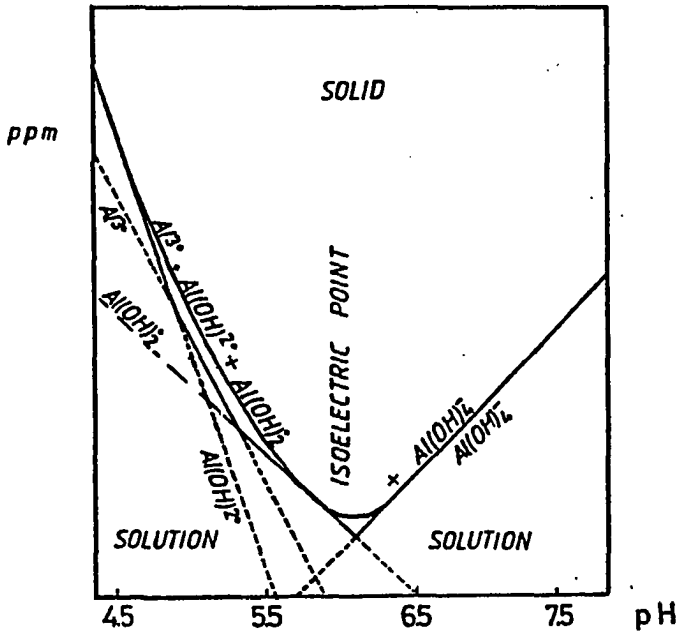

Fig. 76

Solubility diagram showing an idealized relationship between four forms of aluminum in solution and the pH of the solution. After Reesman et al, 1969.

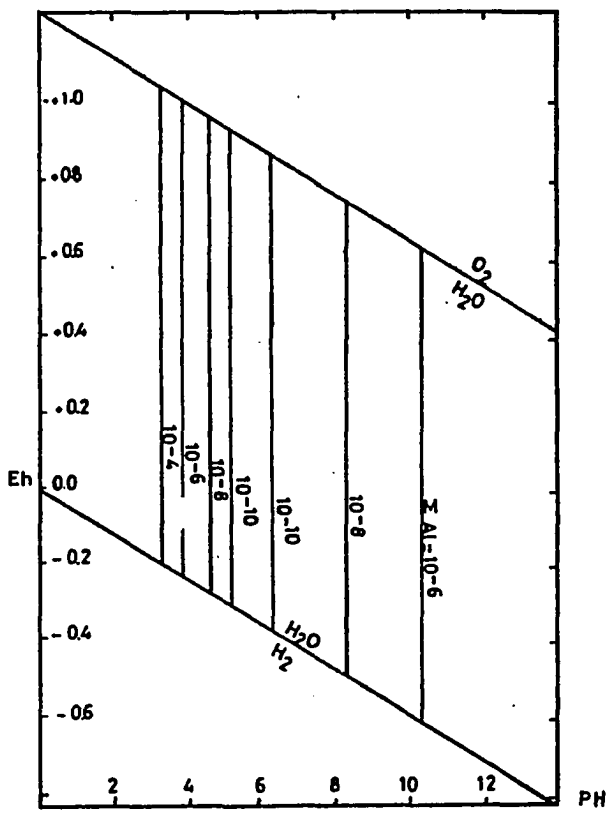

Fig. 77

Solubility relationship for the system aluminum-water at 25°C and 1 atm. After Norton, 1973.

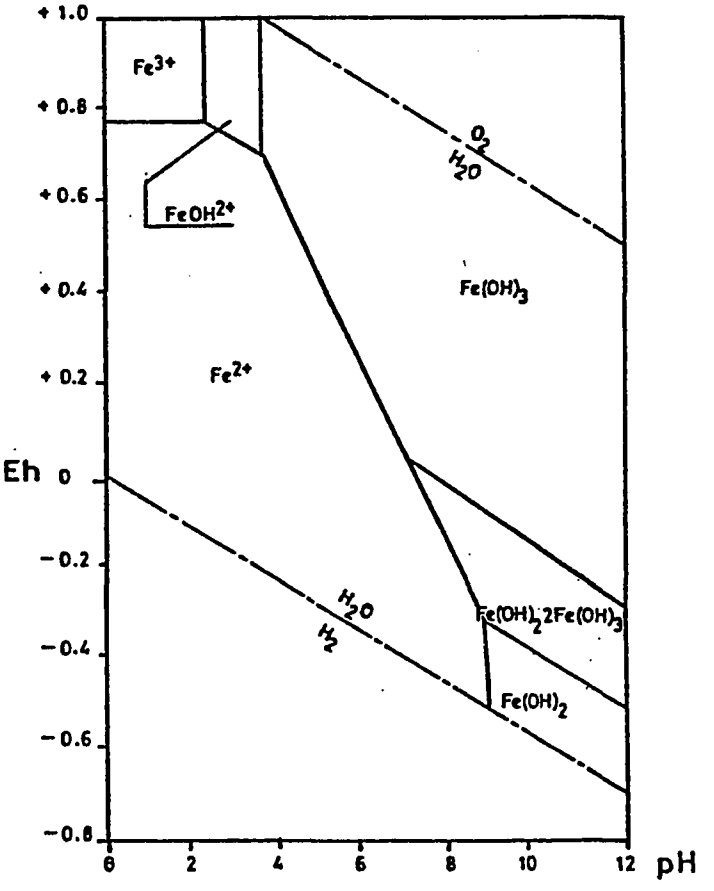

Fig. 78

PH-Eh diagram of Fe-ions and -hydroxides, at 25°C and 1 atm. After Guillet and Souchier, 1979.

with addition of a small amount of base, a process of progressive polymerization and condensation of iron hydrates takes place (Butty and Chappalaz, 1984) and, as a result, colloidal amorphous $Fe(OH)_3$ precipitates are formed together with crystalline α-FeO.OH (Valeton, 1972). According to these authors, with further ageing, the precipitate changes into a mixture of an amorphous hydroxide $[FeO_{n/2}(OH)_{3n-m}]$, and crystalline α-FeO.OH and α-Fe_2O_3. The evolution of iron complexes can be summarized as follows (Guillet and Souchier, 1972):

Mobile complex ⇒ amorphous precipitates ⇒ cryptocrystalline and crystalline phases.

Stability of Silicon

Silica is soluble throughout the entire pH range of natural weathering environments, but its solubility is very low because of the high activation energy required to break the Si-O bond (Stober, 1967). The solubility obtained for quartz by van Lier (1959) at 25°C is 10.8 ppm SiO_2. Carroll (1970) reported a much lower solubility of 6.0 ppm SiO_2 for quartz. Silica also has a very low precipitation rate, and, therefore, is unlikely to control any silica equilibria (Kittrick, 1969). Amorphous silica, much of which is related to biochemical activity (Kittrick, 1969), has a much higher solubility range between 115 and 150 ppm SiO_2 (Kittrick, 1969), and precipitates more readily than quartz. The solubility of silica shows no pH dependency in the range of bauxitic weathering. Fig. 79 shows comparative solubilities for crystalline quartz and amorphous silica as a function of pH.

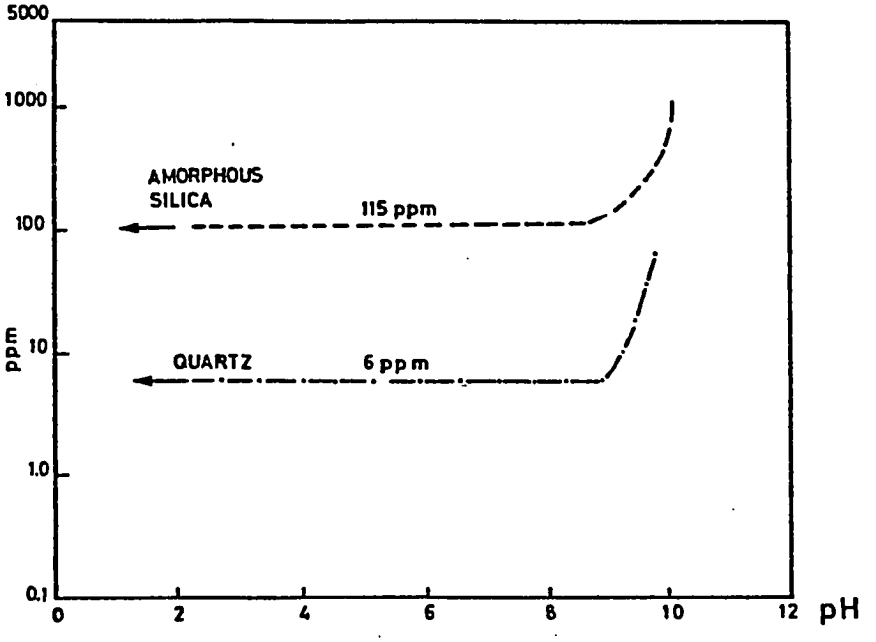

Fig. 79

Solubility of quartz and amorphous silica as a function of pH. After Carroll, 1970.

PH and Eh Control on Bauxitization and Lateritization

Selective enrichment of Fe^{3+} and/or Al^{3+}, on which preferential development of ferruginous laterite or bauxite

depends, is essentially controlled by the pH and Eh of the weathering environment. The chemistry of Al^{3+} and Fe^{3+} during lateritic and bauxitic weathering is summarized in figure 80. This diagram was obtained by superposing the pH-Eh diagram for the system iron-water at 25°C and 1 atm. and that for the system aluminum-water at 25°C and 1 atm. The areas thus defined are the following:

(1). *Area 1*. Al^{3+} is insoluble whereas Fe^{2+} is leached. According to the diagram, these conditions are highly favored by low Eh. Investigations on such reduced environments have revealed that the factors responsible for low Eh conditions are a large supply of organic matter and dense tropical forest (Grubb, 1970) which provides high moisture capture capacity, high humidity and low vertical erosion (Petersen, 1971). Under these conditions, Fe^{2+} remains in solution while Al^{3+} is residually enriched. These conditions are appropriate for bauxitization.

(2). *Area 2*. The pH is lower than 3.0 and Al^{3+} goes into solution while Fe^{3+} precipitates as hematite. This area is characterized by selective development of residual iron crusts.

(3). *Area 3*. This area is characterized by high pH and high Eh. Fe^{3+} and Al^{3+} are insoluble, and the resulting weathering product is a laterite whose Fe^{3+}/Al^{3+} ratio is proportional to that of the parent rock.

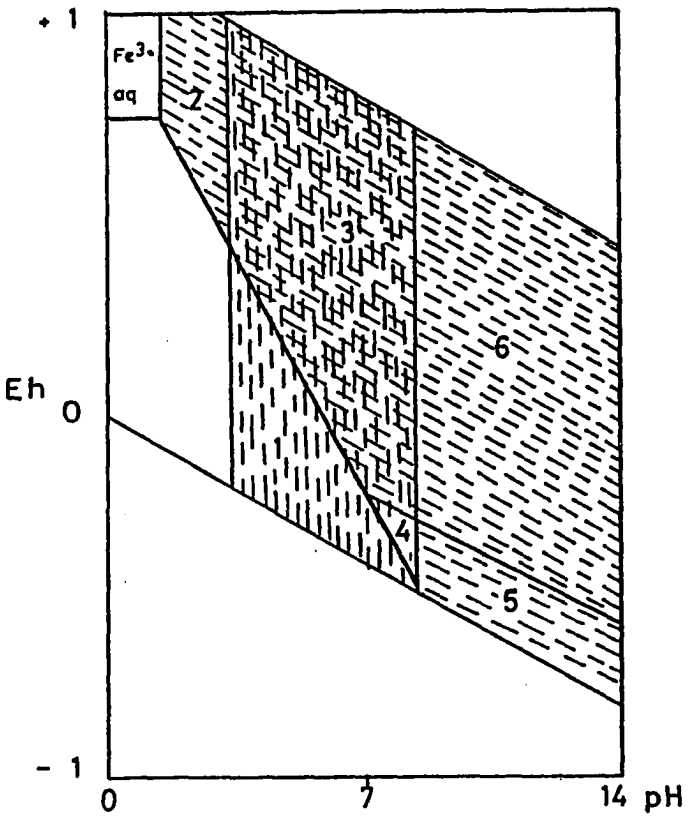

Fig. 80

PH-Eh control on bauxitization and lateritization
Modified after Petersen, 1971.

1_Zone of Fe^{2+} selective leaching.
Highly favorable for Bauxitization

2_Zone of Al selective leaching
Highly favorable for development of iron crust

3_Zone of Fe^{3+} and Al stability
Lateritization (hematite)

4_Zone of Al and Fe (Fe^{2+} and Fe^{3+}) stability
lateritization (magnetite)

5_Zone of Fe^{2+} and Fe^{3+} stability

6_Zone of Fe^{3+} stability.

(4). *Area 4*. This small area represents very exceptional low Eh-high pH conditions under which parent rocks weather into a laterite made up of aluminum hydroxides and magnetite.

(5). *Areas 5 and 6*. These areas are outside the pH of rock weathering and soil formation.

From this discussion, it is clear that bauxitization is favored by acidic to slightly alkaline pH conditions and moderately low Eh conditions. Laterization on the contrary seems to be favored in environments with high Eh and equally acidic to near alkaline conditions.

Stability of Manganese

The behavior of manganese during weathering is essentially pH-Eh dependent as illustrated by the pH-Eh diagram in fig. 81 for the system Mn-H_2O at 25°C and 1 atm. (Mason, 1966). Its chemistry closely resembles that of iron. While it is present in the parent rocks as Mn^{2+}, it is oxidized during weathering when sufficiently exposed to atmospheric oxygen. As conditions become more oxidizing due to weathering, divalent manganese becomes Mn^{3+}, then Mn^{4+}. Correspondingly, pyrochroite ($Mn(OH)_2$) is successively replaced by hausmanite (Mn_3O_4), manganite (MnO.OH) and pyrolusite (MnO_2). Manganese sometimes precipitates with a particular assortment of cations such as K^+, Ni^{2+}, Co^{2+}, Pb^{2+}, Ba^{2+} and Cu^{2+} (Krauskopf, 1978). Of particular interest is a manganese hydroxide found in this study area and discussed above. This mineral, which is referred to as "cameroonite", in this study precipitates in highly

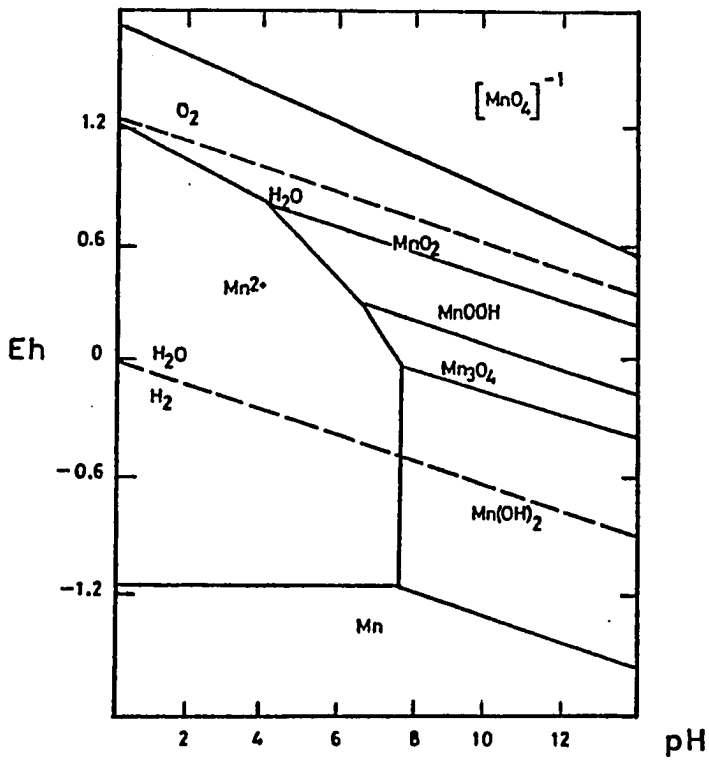

Fig. 81

PH-Eh diagram for the system Mn-H_2O at 25°C and 1 atm. After Mason, 1966.

enriched concretions near the surface. Infrared spectrometry has shown that manganese in "cameroonite" is essentially tetravalent.

OTHER PARAMETERS CONTROLLING BAUXITIZATION

The behavior of bauxite-forming elements is also controlled by other variables such as temperature and the concentration of other ions in solution (Valeton, 1972).

For example, in addition to its dependency on crystallinity, the solubility of silica in aqueous solutions also depends on the temperature and the alkalinity of the solution. These two factors were investigated by Okamoto et al. (1957) who found an increase in the solubility of $Si(OH)_4$ by 4 orders of magnitude when the temperature of the host solution is raised from 0°C to 73°C. They also found that the solubility of silica decreases with increasing aluminum concentration. Silica behaves the same way in the presence of iron hydroxides (Valeton, 1972). Another such example is provided by cations that form bases which have been reported to inhibit gibbsite formation in dolomitic terrains (Butty and Chapallaz, 1984).

From the brief discussion on this otherwise vast subject, it is evident that the solubility of the major bauxite-forming minerals is controlled dominantly by the pH and Eh of the weathering environment and subordinately by additional parameters such as temperature and the concentration of other ions in solution.

BAUXITIC WEATHERING IN THE AREA OF STUDY

Two texturally different types of bauxite have been observed in the study area, namely, the Melan bauxite, which is a saprolite, and the Fongo Tongo lateritic bauxite. The weathering processes which led to the development of each of these types of bauxites are discussed below.

Saprolite Development

This saprolite has a well-preserved trachytic texture and shows neither a volume change nor transportation of bauxite-forming alteration products either with the unaided eye or microscopically.

Saprolites have been widely studied by numerous geologists and soil scientists. Carroll (1970b) defines them as the final expression of geochemical weathering under continual moisture conditions, and relates their development to the inorganic breakdown of parent rocks.

The texture of the Melan saprolite suggests that the chemical conditions which prevailed during its formation highly favor the pseudomorphism of sanidine crystals by finely crystalline gibbsite aggregates.

Surface reactivity of microcline and augite was tested by Huang and Keller (1970) in the presence of deionized water, CO_2-charged water, and organic acids (tartaric and salycilic acids). They found that Al and Si were dissolved congruently in organic acids whereas deionized and CO_2-charged water favored the concentration in the solid of Al with respect to Si within the pH range of 5.75 to 8.63. Therefore, under favorable climatic and topographic conditions and in the presence of

deionized or CO_2-charged waters, feldspar and pyroxene would be expected to decompose with selective removal of Si. Huang and Keller (1970) also observed that unleached Al formed a shell around weathered aluminum silicates, and that further dissolution proceeded through this relatively stable envelope by diffusion.

Therefore, the preservation of the trachytic parental texture in the Melan saprolite may have resulted from the coating of sanidine crystals by an aluminum-rich residual envelope through which the other elements originally present in the mineral diffused out. Preserved sanidine twin planes, which were described above, may also have "fossilized" this way.

CO_2 reacts with water in the weathering environment to form HCO_3^- which, according to Le Marechal (1974), is ubiquitous in all the thermal springs found in the study area. On the origin of the CO_2 in this area, Le Marechal (1974) notes that its source is ascending waters of deep-seated origin. Evidence for ascending CO_2 in this region is also provided by two recent deadly CO_2 gas releases at Lake Monoun and Lake Nyos, both of which are crater lakes of volcanic origin along the Cameroon Line, not far from the study area.

Under acidic weathering conditions, Fe^{3+} also undergoes hydrolysis. The voids left by dissolved sanidine phenocrysts in the Melan saprolite are coated with a red film of iron hydroxide which is probably goethite derived from the hydrolysis of Fe^{3+} originally contained in the structure of the sanidine phenocrysts. Electron microprobe analysis of sanidine crystals of the greenish trachyte give an average total iron content of 1.7 wt%. Iron in sanidine is mostly

trivalent Fe^{3+} and can replace Al^{3+} up to 4 wt% in this mineral in highly differentiated volcanic rocks (Smith, 1974).

Therefore, in addition to climate and topography, the development of the Melan saprolite was also controlled by the presence of inorganic acids, the hydrolysis of Al^{3+} and Fe^{3+} and oxidation reactions.

The growth of the aluminum-rich shell which develops around primary minerals during saprolitic weathering can be explained in light of the chemistry of aluminum hydroxide complexes in dilute solutions. Under acidic weathering conditions, aluminum ions in solution in water are octahedrally coordinated with respect to water molecules and hydroxide ions and tend to polymerise by sharing OH^- situated at the edges of octahedra (Hem and Roberson, 1967). Fig. 82, based on this concept, was proposed by Hsu and Bates (1964) for the polymerization of aluminum hydroxide complexes. This figure suggests that polymerization starts from a single ring unit of six $Al(OH)_2^{1+}$ ions in the presence of NaOH as follows (Hsu and Bates, 1964):

$$Al^{3+} + OH^- = Al(OH)^{2+}$$

$$Al(OH)^{2+} + OH^- = Al(OH)_2^{1+}$$

$$6Al(OH)_2^{1+} = [Al_6(OH)_{12}]^{6+}$$

$$6Al^{3+} + 12OH^- = [Al_6(OH)_{12}]^{6+}$$

According to Hsu and Bates (1964), polymerization reactions are controlled by the ratio $[OH^-]/[Al^{3+}]$. When this ratio is in the range of 0 to 2, polymers nucleate from the unit ring through OH^- which serves as a bridge and double rings of the composition $Al_{10}(OH)_{22}^{8+}$, or triple rings of $Al_{13}(OH)_{30}^{9+}$ are obtained. Within this range no $Al(OH)_3$

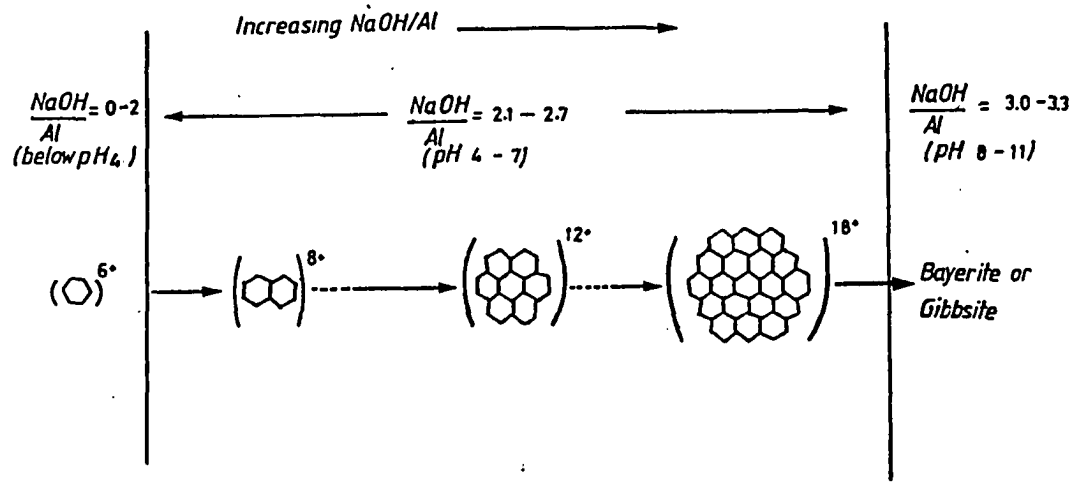

Fig. 82

Polymerization of aluminum hydroxide complexes.
After Hsu and Bates, 1964

molecules are obtained because of the net positive charge per aluminum. This net positive charge disappears when the ratio OH^-/Al^{3+} reaches 3.0, together with the repulsion between the polymer rings and their hydration water. Polymer rings then start clustering together and, with ageing, form crystalline $Al(OH)_3$.

On the basis of this discussion, the Melan saprolite can be defined as a product of geochemical weathering under acidic weathering conditions and a favorable topographic terrain. Weathering resulted in an incongruent dissolution of sanidine crystals and a polymerization of resulting hydroxyl-aluminum ions. As a result of this polymerization, insoluble shells developed around dissolving sanidine crystals and "fossilized" the texture of the parental greenish trachyte.

Lateritic Bauxite Development

As used here, the term "lateritic bauxite" applies to bauxites developed through the combined effects of geochemical and pedochemical weathering processes. In addition to the inorganic breakdown of the parent material, determining factors in the development of this bauxite are the humus provided by vegetation and microorganisms (Carroll, 1970). The resulting rock displays a profile with horizons similar to those developed by ordinary laterites.

The duricrust described in the Fongo Tongo profile corresponds to the B horizon of deposition of sesquioxides. This horizon is generally believed to be the one where the strongest pedochemical reactions occur (Carroll, 1970).

Saprolites and lateritic bauxites are usually genetically related. In many bauxite deposits, the standard saprolitic weathering profile

consists of a slightly altered to fresh parent rock successively overlain by a saprolite and a residual lateritic bauxite (Millot, 1964; Lelong, 1969). In a similar way, the Melan saprolite may have been overlain at one time by a lateritic bauxite.

The Fongo Tongo lateritic bauxite seems to have developed differently in that its profile shows no conservation of the parental texture above the weathering front which is instead overlain by a soft clayey zone. This zone is composed essentially of amorphous to poorly crystalline hydrated aluminum silicates, aluminum hydroxides, ferric iron oxides and residual minerals. If geochemical factors are essential for the initial breakdown of parent rocks, the formation of amorphous and cryptocrystalline oxides and hydroxides and their history throughout the weathering profile are related to pedochemical weathering processes in which organic compounds and microorganisms play an essential role (Carroll, 1970b) These pedochemical weathering processes can be summarized as follows:

Pedochemical Weathering by Organic Compounds:

The main chelating organometallic complexes which intervene in pedochemical weathering are citric acid, oxalic acid, amino acids, phenols, and poly- phenols (Stevenson, 1979). They contribute to the weathering of parent rocks by promoting the destruction of the crystal structure and selectively complexing such cations as Fe^{2+}, Fe^{3+}, Al, Mn^{2+}, Ti and Ca, and are responsible for the development of the characteristic features pertinent to lateritic bauxites (Butty and Chapallaz, 1984). These authors point out that lateral and vertical migration of Al^{3+} and Fe^{3+} essentially takes place through hydrosoluble

chelating compounds. Under moist conditions, Fe^{3+} can be taken up by chelates and transported over long distances (Bushinsky, 1975). It precipitates during drier seasons when chelates are no longer stable in transporting waters and forms iron-rich hard caps (Butty and Chapallaz, 1984). These authors also note that aluminum trends vertically from the highly biological "A" horizon, where it is removed by chelates, to the "B" horizon where it accumulates and forms a bauxitic horizon. Upon exposure, this horizon hardens and forms a duricrust.

The concretionary texture described above in the duricrust of the Fongo Tongo lateritic bauxite is the result of a later destruction of this duricrust by chelates through alternating seasonal mobilization and immobilization of Al^{3+} and Fe^{3+} (Butty and Chapallaz, 1984).

The stability of chelates is controlled by a number of external factors. Duchaufour (1977), for example, notes that chelate weathering depends on the pH and the Eh of the weathering environment, and that some cations such as Ca^{2+}, above a certain concentration, can cause chelates to precipitate.

Pedochemical Weathering by Biogenic Agents

Aside from their indirect leaching action through the synthesis of acids and the formation of organic compounds (Butty and Chapallaz, 1984), biologic agents control the geochemistry of iron and manganese in the weathering profile (Berthelin and Toutain, 1979) and contribute to the destruction of alumino-silicate lattices by extracting nutritive compounds such as nitrogen, phosphorous and potassium (Groudev and Genchev, 1979).

CHEMICAL WEATHERING AND THE SEPARATION OF "CAMEROONITE"

The geochemical cycles of iron and manganese show many similarities. Primary minerals of parent rocks containing Fe^{2+} often have Mn^{2+} in solid solution with iron, Fe^{2+} and Mn^{2+} being mutually replaceable because of the closeness of their ionic radii. During weathering, when surface conditions are favorable, both elements are oxidized and give highly insoluble oxides. Nevertheless, despite the many similarities they have during their exogenic cycles, the two elements are almost completely separated by supergene processes as shown by the formation of such secondary minerals as todorokite, birnessite, vernadite and "cameroonite". Mason (1966) explains the separation of Fe and Mn by the fact that iron precipitates at lower Eh values as hydrated ferric oxides whereas manganese remains in solution, and only precipitates under more oxidizing conditions. The pH of the weathering solutions is also a determining parameter in the separation of both elements. According to Krauskopf (1979), if manganese and iron bearing solutions derived from the weathering of parent rocks are exposed to air and made basic suddenly, both elements precipitate. However, if the pH is increased slowly, iron compounds reach their limit of solubility first and precipitate while manganese is left in solution.

Regardless of the thermodynamic mechanism involved in the separation of Mn^{4+} and Fe^{3+}, the pH and Eh conditions under which the two elements are separated are necessarily restricted, and separation

may not even be complete as indicated by "cameroonite" which also has Fe^{3+} in its structure.

Krauskopf (1979) remarks that microorganisms may also account for partial separation of manganese and iron inasmuch as both metals are solubilized by different species.

Separation of manganese and iron may take place through organo-metallic complexes. Like iron, manganese forms ligands with a number of organic compounds such as amines, organic acids and amino acids (Nakhshina, 1975). Nevertheless, iron complexes are more stable in aqueous solutions (Krauskopf, 1979). Manganese may then precipitate before iron when manganese and iron bearing complexes are present in a solution. This reversal in the order of precipitation of both elements has been observed in Finland (Carlson et al. 1977) in deposits from organic-rich waters.

Therefore, "cameroonite" may form from the precipitation, under appropriate oxidizing conditions, of manganese previously carried by organo-metallic complexes. Nevertheless, additional geochemical data are still needed in order to understand in detail the formation of this mineral.

SUMMARY AND CONCLUSIONS

The purpose of this investigation was to study the geologic setting of the Fongo Tongo and areally related bauxite deposits as well as their microtexture, mineralogy and geochemistry. For a better understanding of the regional setting of these bauxites, the entire southern flank of the Bambouto mountains was mapped, from the township of Dschang in the south to the southern border of the Bambouto caldera in the north. This investigation has revealed the nature and extent of a number of still unmapped or undefined volcanic units as well as additional bauxitic caps. The relationship between each flow and its related deposits was also investigated. Two discrete stages of bauxitization are revealed in the area, both separated in time by the collapse of the Bambouto caldera.

The first bauxitization stage occured under acidic weathering conditions and yielded the Melan saprolite. This saprolite developed on the greenish trachyte on top of the Bambouto Mountains. Evidence for limited pedochemical weathering of this saprolite was observed in the field. The saprolite is believed to have been dismantled during the collapse of the Bambouto caldera.

Saprolite blocks were transported downslope. Their major occurence is at Melan where they accummulated on a gently sloping hill forming a small 3.0-meter-thick bauxitic cap which overlies the greenish trachyte.

The deposits which are made up of boulders and pebbles of saprolite are para-autochthonous because, even though there is evidence for lateral movement, the distance traveled by the blocks is relatively

small and they still overlie the greenish trachyte from which they developed at higher elevations.

Saprolitization took place in a CO_2-rich weathering environment through a complex coating of dissolving sanidine crystals by gibbsite shells, and a selective removal of Si by diffusion through these shells.

Lateritic bauxite developed after the collapse of the Bambouto caldera during which the saprolite cap was destroyed. The volcanic units affected by this bauxitization phase are the greenish trachyte, the ash-flow tuffs and the plateau basalts.

The time relation between the two discrete bauxitization stages is given by the saprolite clasts which are found in the Fongo Tongo lateritic bauxite. It is concluded that these clasts are older than the enclosing lateritic bauxite, and that they were enclosed as xenoliths in the dark trachyte which subsequently underwent bauxitic weathering.

The topography was particularly favorable for high-level bauxitization. The study area underwent an uplift of about 1,000 meters in the Tertiary. Paleoclimatic studies also suggest that overall favorable climatic conditions prevailed during Mid- and Late-Tertiary time when these bauxites developed.

The main Fongo Tongo deposit has undergone erosion at places where the slope is relatively high, and limited downslope movement of bauxite blocks has taken place.

Mineralogical and geochemical studies of the Fongo Tongo lateritic bauxite suggest *in situ* bauxitic weathering. Weathering was essentially controlled by pedochemical agents which inhibited the development of a saprolite and contributed to the breakdown of parent rocks into

amorphous materials which then crystallized into maghemite, gibbsite, and cryptocrystalline halloysite. In addition, there were some unidentified amorphous hydrated alumino-silicates. This gel occurs in the vicinity of the weathering front and contains residual sanidine, magnetite and hornblende. The paragenesis of hydrated alumino-silicates from the base of the profile to the surface is essentially related to the gradual reduction with height of the (001) d-spacing of 10.0 Å halloysite which is successively replaced by metahalloysite and kaolinite. Desilication of kaolinite has been found to be the major reaction through which gibbsite is generated. This reaction takes place in the mottled clay horizon.

In situ development of the lateritic bauxite has also been demonstrated by the paragenesis of iron minerals. From the parent rock to the top of the profile, Fe^{2+}-bearing minerals are gradually replaced by Fe^{3+}-iron oxides and hydroxides, and magnetite is successively replaced by maghemite, hematite and goethite.

The action of climate during bauxitization was expressed through the control of the pH and Eh of aqueous environments on which the chemistry of Al and Fe depends. Highly favorable pH and Eh conditions allowed a selective removal of Fe^{3+} from the profile and the precipitation of gibbsite.

Minor- and trace-element investigation of the bauxites has revealed a good depletion/concentration correlation with theoretical expectations. Of special interest is the behavior of manganese which concentrates in bluish-black blocks composed essentially of a manganese mineral termed "cameroonite" in this study and minor romanechite.

Mineralogical study of "cameroonite" reveals similarities with vernadite, another manganese hydroxide. Nevertheless, the two minerals have different lattice parameters and chemical composition.

As a result of this study, the following additional investigations should be carried out in the future:

(1). The crystal chemistry, by electron microscopy and electron microprobe, of the two types of gibbsite crystals as defined in this study in the Fongo Tongo duricrust.

(2). A further characterization of the amorphous components of the clayey material below the mottled clay horizon, above the weathering front.

This study has also laid the lithostratigraphic foundations for future work on the geology and geochronology of the lava flows of the southern flank of the Bambouto Mountains, a step which was nessessary for a detailed characterization of these flows.

REFERENCES

Alexander, G. B., Heston, W. M. and Ihler, R. K., 1954. The solubility of amorphous silica in water. J. Phys. Chem. 59, 453-455.

Alexander, L. and Klug, H. P., 1948. Basic aspects of absorption in quantitative diffraction analysis of powder mixtures. Analyt. Chem. 20, 886-889.

_____, 1974. X-Ray Diffraction Procedures. 2nd ed. N. Y. Wiley.

Baker, P. E., 1969. Petrology of the volcanic rocks of Saint Helena Island, South Atlantic. Bull. G.S.A. 80, 1283-1310.

Balasubramaniam, K. S. and Paropkari, A. L., 1975. Mineralogy and genesis of bauxites of Nagardaswadi Plateau, Kolhapur District, Maharashtra State, India. Canadian Mineralogist. 13. pt.3, 222-226.

Bardossy, G., 1963. Die Entwicklung der Bauxitgeologie seit 1950. Symp. Bauxites. Zagreb, 1963. I. 31-50.

_____, 1977. Interrelations of bauxite texture, micromorphology, mineral individualism and heteromorphism: Economic Geol. 72, no.4, 573-581.

_____, 1982. Karst Bauxites. Elsevier Scientific Pub Co., 441p.

Becker, G. F., 1895. A Reconnaissance of gold fields of the Southern Appalachians, U. S. Geol. Surv. 16th annual Report. Pt.3, 251-331.

Benoit, P. H., 1987. Adaptation to microcomputer of the Appleman-Evans program for indexing and least square refinement of powder diffraction data for unit-cell dimension, Amer. Miner. v. 72 (in print).

Berner, R. A., 1971. Principles of Chemical Sedimentology, McGraw Hill Book Co. N. Y., 240p.

Berthelin, J. and Toutain, F., 1979. Biologie des sols, in Pedologie, (P. Duchaufour and B. Souchier, ed.). 2. Masson. Paris, 121-160.

Bessoles, B., 1969. Synthese simplifiee des connaissances sur la geologie du Cameroun, Bull. Dir. Mines et Geol. Cameroun. 5, 185-218.

_____ and Lasserre, M., 1977. Le complexe de base du Cameroun. Bull. Soc. Geol. Fr. 7. XIX. 5, 1085-1092.

_____ and Trompette, R., 1980. Geologie de l'Afrique: la chaine panafricaine "Zone mobile d'Afrique Centrale (partie sud) et zone mobile soudanaise", Mem. BRGM. 92, 101p.

Betekhtin, A. G., 1937. New mineral species of the group of manganese hydroxides. Zapishi Vseo. Mineralog. Obshch. v. 66, no. 4.

_____, 1940. Southern Ural manganese deposits as a resource base for the Magnitogorsk Metallurgical Trust. Trudy Inst. Geol. Nauk, Akad Nauk SSSR, no. 30, ser. Rudn. Mestorozhd. no. 4.

Black, R. and Girod, M., 1970. Late Paleozoic to Recent igneous activity in West Africa and its relationship to basement structure. In African Magmatism and Tectonics (T. N. Clifford, and I. G. Gass, ed.). Oliver and Boyd. Edingburg, 185-210.

Blatt, H., Middleton, G. and Murray, R., 1980. Origin of Sedimentary Rocks, Prentice-Hall, Inc. 782p.

Brindley, G. W., 1980. Quantitative x-ray mineral analysis of clays. In Crystal Structures of Clay Minerals and their X-Ray Identification (G. W. Brindley and G. Brown, ed.) Mineralogical Soc. London, 495p.

_____ and Goodyear J., 1948. The transition of halloysite to metahalloysite in relation to relative humidity. Mineralog. Mag. 28, 407-422.

_____ and Robinson K., 1948. X-ray studies of halloysite and metahalloysite. I. The structure of metahalloysite, an example of a random layer lattice. Mineralog. Mag. 28, 383-406.

Brosset, C., 1952. On the reaction of aluminum ion with water: Acta Chem. Scandin. 6, 910-940.

_____, Biedermann, G. and Sillen, L. G., 1954. Studies on the hydrolysis of metal ions. XI. The aluminum ion Al^{3+}. Acta Chem. Scandin. 8, 1917-1926.

Brown, G., 1980. Associated minerals. In Crystal Structure of Clay and their X-Ray Identification (G. W. Brindley and G. Brown, ed.). Mineralogical Soc. London, 361-410.

Brownlow, A. H., 1979. Geochemistry. Prentice Hall, N.J., 498p.

Brunt, M. and Hawkin, P., 1965. The Soils Ecology of West Cameroon. I. F.A.O. Rome, 290p.

Buchanan, F., 1807. A journey from Madras through the countries of Mysore, Canara and Malabar. East India Co., London, 2, 440-441.

Burke, K., 1969. Seismic areas of the Guinea coast where Atlantic fracture zones reach Africa. Nature 222, 655-657.

_____ and Wilson, J. T., 1972. Is the African Plate stationary? Nature. 239, 387-390.

_____ , Dessauvagie, T. F. J. and Whitenam, A. J., 1972. Geological history of the Benue valley and adjacent areas. In African Geology (T. F. J. Dessauvagie and A. J. Whitenam, ed.). Ibadan, 187-205.

Bushinsky, G. I., 1975. Geology of Bauxite. 2nd ed., Izd. Nedra, Moscow.

Butty, D. L. and Chapallaz, C. A., 1984. Bauxite genesis. In Bauxite - Proceedings of the 1984 Bauxite Symposium, Los Angeles, Ca. (L. Jacob Jr., ed.). Soc. Min. Eng. 111-151.

Caponi, A., 1944. La Lignite de Dschang, Bull. Soc. Et. Cameroun. 7, p75.

Carlson, L., Kolonen, T., Lahermo, P. and Rosenberg, R. I., 1977. Case study of a manganese and iron precipitation a groundwater discharge in Somero, Finland. Geol. Soc. Finland Bull. 49, 159-173.

Carroll, D., 1959. Ion exchange in clays and other minerals. Bull. GSA. 70, 749-780.

_____, 1970a. Clay Minerals: A Guide to their X-Ray Identification, GSA Special Paper 126, 80p.

_____, 1970b. Rock Weathering. Plenum Press, N.Y., 203p.

Cartledge, G. H., 1928. Studies on the Periodic System. I. The ionic potential as a periodic function. Jour. Am. Chem. Soc. 56, 2855-2863.

Champaud, J., 1973. Atlas regional. Ouest 2. Rep. Unie du Cameroon. ORSTOM, 115p.

Chukhrov, F. V., Gorshkov, A. I., Rudnitskaya, E. S., Berezovskaya, V. V. and Sivtsov, A. V., 1978. On vernadite. Bull. USSR Acad. Sci., ser. geol., 6, 5-19. [in russian].

_____, 1980. New data on supergene minerals. Akad. Nauk SSSR, Internatl. Geol. Congress, 26th Session, Paris, Paper by Soviet Geologists, Geochemistry and Mineralogy. 143-159.

_____, and Gorshkov, A. I., 1981. On the nature of some hypergene manganese minerals. Chem. Erde. 40, 207-216.

Courade, G., 1974. Atlas regional, Ouest I. Rep. Unie du Cameroun. ORSTOM, 191p.

Cross, W., Iddings, J. P., Pirsson, L. V. and Washington, H. S., 1903. Quantitative Classification of Igneous Rocks. Univ. of Chicago Press.

Cullity, B. D. 1978. Elements of X-Ray Diffraction. 2nd. ed. Addison-Wesley Publishing Co. Inc., 556p.

Douillet, P. and Nicolas, J., 1969. Les mineraux du kaolin. Bull. Soc. Fr. Ceram. 83, 87-114.

Duchaufour, P., 1977. Pedogenese et classification. In Pedologie (P. Duchaufour and B. Souchier, ed.). I. Masson, Paris.

Dumort, J. C., 1968. Carte geologigue de reconnaissance a 1:500,000 avec notice explicative. Feuille Douala- Ouest. Dir. Mines et Geol. du Cameroun, Yaounde, 69p.

Dunlop, H. M., 1983. Strontium Isotope Geochemistry and Potassium-Argon Studies on Volcanic Rocks from the Cameroon Line, West Africa. Univ. of Edingburgh. Ph. D. Dissertation, 347p. (Unpubl.).

Ekodeck, G. E., 1984. L'alteration des roches metamorphiques du Sud-Cameroun et ses aspects geotechniques. These d'Etat. Univ. Grenoble I. 368p. (Unpubl.).

Eno Belinga, M. S. and Ossah, N. H., 1974. Etude geologique de la region de Bamenda - premiers resultats petrographiques. Rapport polycop. Dept. Sci. Terre, Univ. Yaounde, 14p.

Eswaran, H. and Bin, W. C., 1978. A study of a deep weathering profile on granite in Peninsular Malayia: I. Physico - chemical and micromorphological properties. Soil Sci. Soc. Am. J. 42, 144-149.

Ferraro, J. R., ed., 1982. The Sadtler Infrared Spectra Handbook of Minerals and Clays, Sadtler Research Laboratories, Philadelphia. Pa., 440p.

Fitton J. G., 1980. The Benue trough and Cameroon Line - A migrating rift system in West Africa. Earth Planet. Sci. Lett. 51, 132-138.

Flock, W. M., 1966. Mineralogy and Petrology of the Andersonville, Georgia Bauxite District. Ph. D. Dissertation. University Park, Penn. State Univ. 228p. (Unpubl.).

Fondzeyuf, J. D., 1983. La Bauxite, une etude comparative du gisement de Djeu (secteur de Fongo Tongo) et du gisement de Bangan dans la region occidentale du Cameroun. Ecole Nat. Sup. Geol. Appl. et de Prosp. Min., 32p. (Unpubl.).

Foster, M. D., 1962. Interpretation of the composition and a classification of the chlorites. U. S. Geol. Surv. Prof. Pap. 414-A. 1-33.

Frakes, L. A. and Kemp, E. M., 1972. Influence of continental positions on Early Tertiary climates. Nature. 240. N.52376, 97-100.

Freeth, S., 1978a. Tectonic activity in West Africa and the Gulf of Guinea since Jurassic times: An explanation based on membrane tectonics. Earth Planet. Sci. Lett. 38, 298-300.

_____, 1978b. A Model for tectonic activity in West Africa and the Gulf of Guinea during the last 90 Ma based on membrane tectonics. Geol. Rundsch. 67, 675-688.

_____, 1979. Deformation on the African Plate as a consequence of membrane stress domains generated by Post-Jurassic drift. Earth Planet. Sci. Lett. 45, 93-104.

Garrels, R. M. and Christ, G. L., 1965. Solutions, Minerals and Equilibria. Harper and Row. N.Y., 450p.

Gass, I. G., Chapman, D. J., Pollack, H. M. and Thorpe, R.., 1978. Geological and geophysical parameters of mid-planete volcanism. Phil. Trans. R. Soc. A288, 581-597.

Gastuche, M. C., Bruggenwert, T. and Mortland, M. M., 1964. Crystallization of mixed iron and aluminum gels. Soil Sci. 98, 281-289.

Gayer, K. H., Thompson, L. C. and Zajicek, O. T., 1958. The olubility of aluminum hydroxide in acidic and basic media at 25°C. Canadian Jour. Chem. 36, 1268-1271.

Gazel, J., 1957. Note sur les Bauxites. Dir. Min. Cameroun. Yaounde.

_____, 1958. Geologie du Cameroun, 10p. In Atlas du Cameroun. IRCAM. Yaounde.

_____, Hourcq, V. and Nikles, M., 1956. Carte Geol. du Cameroun au 1:1 000 000. Bull. Dir. Min. Geol. 2. Cam. Imp. Nat. Paris.

Genieux, M. 1958. Climatologie du Cameroun, 4p. In Atlas du Cameroun. IRCAM. Yaounde.

Geze, B., 1943. Geographie physique et geologie du Cameroun Occidental. Mus. Nat. Hist. Nat. Paris, Mem. 17, 1-271.

Gheith, M. A., 1952. DTA of iron oxides. Am. Jour. Sci. 250, 677-695.

Gilkes, R.J. and Suddhiprakaran, A., 1981. Mineralogical and chemical aspects of lateritisation in Southwestern Australia. In Lateritisation Processes - Proceedings of the International Seminar on Lateritisation Processes. Trivandrum, India. Dec. 1979. Balkema/Rotterdam, 34-44.

Goldich, S. S., 1938. A study in rock weathering. Jour. Geol. 46, 17-58.

Goldschmidt, V. M., 1937a. The principles of distribution of chemical elements in minerals and rocks. Chem. Soc. London Jour. 655-673.

_____, 1937b. Geochemische Verteilungsgesetze der Elemente.IX. Die Mengeverhaltnisse der Elemente und der Atom-Arten. Skrifter Norske Videnskap-Akad. Oslo, I. Mat.-Naturv. Klasse. 4.

_____, 1954. Geochemistry. Oxford. Clarendon Press, 730p.

Gordon, M. Jr. and Murata, K. J., 1952. Minor elements in Arkansas bauxite. Econ. Geol. 47, 169-179.

_____, Tracey, J. I. and Ellis, M. W., 1958. Geology of the Arkansas bauxite region, U. S. Geol. Surv. Prof. Paper 299, 268p.

Gorini, M. A. and Bryan, G. M., 1976. Tectonic fabric of Equatorial Atlantic and adjoining continental margins. Gulf of Guinea to Northeastern Brazil. An. Acad. Brazil Cienc. 48, 101-119.

Gouhier, J., Nougier, J. and Nougier, D., 1974. Contribution a l'etude volcanologique du Cameroun ("Ligne du Cameroun" - Adamaoua). Ann. Fac. Sci. Univ. Yaounde, 17, 3-48.

Groudev, S. and Genchev, F., 1979. Bioleaching of bauxites by wild and laboratory - bred microbial strains, Proceedings 4th ICSOBA, 271-277.

Grubb, P. C. L., 1963. Critical factors in the genesis, extent, and grade of some residual bauxite deposits, Economic Geol. 58, 1267-1277.

_____, 1970. Mineralogy, geochemistry and genesis of the bauxite deposits on the Gove and Mitchell Plateaux, Northern Australia, Mineralium Deposita, 5, no.3, 248-272.

_____, 1971. Genesis of the Weiga bauxite deposits, N.E. Australia, Mineralium Deposita, 6, no 4, 265-274.

Grun, E. and Manasse, R., 1950. Referred to in Geochemistry by V. M. Goldschmidt, 1954. Oxford. Clarenton Press, 730p.

Guillemain, C. and Harbort, E. 1., 1909. Profil der Kreideschichten am Mungo: Beitrage zur Geologie von Kamerun, no. 17, Abhandl. kon. preuss. geol Landesanst., N. F. 62, 405-432.

Guillet, B. and Souchier, B. 1979. Les oxi - hydroxydes amorphes et crystallins dans les sols (fer, aluminium, silicium). In Pedologie (P. Duchaufour and B. Souchier ed.). 2, Masson, Paris, 16-37.

Harrassowitz, H., 1926. Laterit. Materal und Versuch erdgeschichtlicher Ausvertung. Fortchr. Geol. Palaont. 4 Heft 14.

Harrison, J. B., 1934. Katamorphism of Igneous Rocks under Tropical Conditions. Imp. Bur. of Soil Sci. Harpenden, England, 79p.

Hedberg, J. D., 1968. A Geological Analysis of the Cameroon Trend. Ph.D. Dissertation, Princeton Univ., 188p. (Unpubl.).

Hem, J. D. and Roberson, C. E., 1967. Form and stability of aluminum hydroxide complexes in dilute solution. U. S. Geol. Surv. Water Supply Paper, 1827-A, 55p.

Henmi, T. and Wada, K., 1976. Morphology and composition of allophane. Am. Miner. 61, 379-390.

Hieronymus, B., 1971. Note preliminaire sur l'alteration des trachytes de la zone bauxitique de Fongo Tongo. Ann. Fac. Sci. Univ. Yaounde. 6, p.39.

_____, 1972. Etude geologique de quelques types d'Alteration dans l'Ouest du Cameroun. Ann. Fac. Sci. Univ. Yaounde. 10, p.39.

_____, 1980. Mechanismes et facteurs de la bauxitization. Etude systematique d'un profil d'alteration bauxitique dans l'Ouest du Cameroun. 105e Congres National des Soc. Sav. Caen. 1980. Sci. Fasc. II, 153-165.

_____, and Bildgen, P., 1981. Precisions sur la nature mineralogique de l'alteration bauxitique dans l'Ouest du Cameroun. 106e Congres Nat. Soc. Sav. Perpignant. Sci. fasc. III, 421-432.

Hill, V. G., 1955. The mineralogy and genesis of the bauxite deposits of Jamaica. B.W.I. Amer. Miner. 40. nos.7-8, 676-688.

Hsu, P. H. and Bates, T. F., 1964. Formation of x-ray amorphous and crystalline aluminum hydroxides. Mineral. Magazine. 33, 749-768.

Huang, W. H. and Keller, W. D., 1970. Dissolution of rock - forming silicate minerals in organic acids: simulated first - stage weathering of fresh mineral surfaces. Amer. Miner. 55, 2076-2094.

Hunter, J. M., 1961. Morphology of a bauxite summit in Ghana. Geographical Journal. London. 127, pt.4, 469-476.

Kittrick, J. A., 1969. Soil minerals in the Al_2O_3-SiO_2-H_2O system and a theory of their formation. Clays and Clay Miner. 17, 157-167.

Klein, C. and Hurlbut, C. S. Jr., 1985. Manual of Mineralogy, 20th Ed. (After J. D. Dana). John Wiley and Sons, 596p.

Konta, J. 1958. Proposed classification and terminology of rocks in the series bauxite-clay-iron ore. J. Sedim. Petrol. 28, 83-86.

Krauskopf, K. B., 1956. Dissolution and precipitation of silica at low temperatures. Geochem. Cosmochem. Acta 10, 1-26.

_____, 1979. Introduction to Geochemistry. McGraw Hill Book Co., 617p.

Krumbein, W. E., 1983. Microbial Geochemistry. Blackwell Sci. Pub., 330p.

Lacroix, A. F. A., 1934. Les phenomenes d'alteration superficielle des roches silicatees alumineuses des pays tropicaux; leur consequence au point de vue minier. Bur. Etudes Geol. et Min. Coloniales. 25, 19-47.

Lasserre, M., 1966. Confirmation sur l'existence de granites Tertiaires du Cameroun: gisement, petrographie et geomorphologie. Bull. BRGM 2e serie. sect.IV, 143-159.

_____, 1967. Donnees geochronologiques nouvelles acquises au ler Janvier 1967 par la methode au strontium appliquee aux formations crystallines et cristallophylliennes du Cameroun. Ann. Fac. Sci. Clermont Ferrand, 36, Geol. Min. Fasc. 16.

_____, 1978. Mise au point sur les granitoides dits ultimes du Cameroun: gisement, petrographie et geochronologie. Bull. BRGM 2e serie. sect. IV, 143-159.

_____ and Soba, D., 1976. Ages Cambriens des granites de Nyibi et de Kongolo (Centre-Est Cameroun), C.R. Acad. Sci. Paris 283, 1695-1698.

_____, 1979. Migmatisation d'age Panafricain au sein des formations camerounaises appartenant a la zone mobile d'Afrique Centrale. C.R. Somm. Soc. Geol. France 2, 64-68.

Leet, D. L., Judson, S. and Kauffman, M. E., 1978. Physical Geology. 5th ed. Prentice-Hall Inc. N. J., 490p.

Lelong, F., 1969. Nature et genese des produits d'alteration des roches crystallines sous climat tropical humide. Sci. de la Terre, Mem. 14.

Le Marechal, A., 1976. Geologie et geochimie des sources thermominerales du Cameroun. Travaux et Documents de l'ORSTOM. 59, 176p.

Le Pichon, X. and Hayes, D. E., 1971. Marginal offsets, fracture zones and the early opening of the South Atlantic. J. Geophys. Res. 76, 6283-6293.

Leprun, J. C.,1981. Some principal features of the iron crust in dry Western Africa. In Lateritisation Processes - Proceedings of the

International Seminar on Lateritisation Processes. Trivandrum, India. Dec. 1979 Balkema/Rotterdam. 11-14.

Lindsley, D. H., 1976. The crystal chemistry and structure of oxide minerals as exemplified by the Fe-Ti oxides. In Oxide Minerals. (Rumble III, D. ed.). Reviews in Mineralogy. 3. Mineral. Soc. Amer. L.1-L.60.

Lorer, R. J., 1980. Geological evaluation of the Fongo Tongo Bauxite Deposit Cameroon. 1st Phase Feasibility Study. Alcan Int. Rpt. M-ER-222-80 (Unpubl.).

Loughnan, F. C., 1969. Chemical Weathering of the Silicate Minerals, Elsevier Publ. 154p.

_____ and Bayliss, P., 1961. The mineralogy of the bauxite deposits near Weiga, Queensland. Am. Miner. 46, 209-217.

Mackenzie, R. C., 1957. The Differential Thermal Investigation of Clays. Miner. Soc. London, 456p.

_____, and Caillere, S., 1979. Thermal analysis, DTA, TG, DTG. In Data Handbook of Clay Materials and other Non-Metallic Minerals. (H. Van Olphen and J. J. Fripiat, ed.). Pergamon Press, 243-261.

Mann, O., 1913. Gites mineraux. Rapp. arch. Serv. Mines. Cameroun. Mai 1913. 14p. (Unpubl.).

Marshall, P., 1935. Acid rocks of Taupo-Rotorua volcanic district. Royal Soc. New Zealand Trans. 64. pt.3, 323-366, [Off-Print Pagination 1-44].

Martin, D. and Segalen, P. 1966. Notice explicative de la carte pedologique du Cameroun Oriental. ORSTOM. 26, 134p.

Mascle, J., 1975. Geologie sous-marine du Golfe de Guinee. Univ. P. et M. Curie, These d'Etat, (Unpub.).

Mason, B., 1943. Mineralogical aspects of the system FeO - Fe_2O_3 - MnO - Mn_2O_3. Geol. Foren. Forh. Stockholm. 65, 97-180.

_____, 1966. Principles of Geochemistry. 3rd ed. John Wiley and Sons Inc, 329p.

McClune, W. F., Maguire, T. M., Mrose, M. E., Post, B. Weissmann, S., McMurdie, H. F., Zwell, L. and Morris, M. C., 1980 (eds.). Mineral Powder Diffraction File. Data Book. JCPDS International Center for Diffraction Data, Pennsylvania, USA.

Miller, J. P., 1961. Solutes in small streams draining single rock types. Sangre de Cristo Range, New Mexico. U. S. Geol. Surv. Water Supply Paper 1235-F, 23p.

Millot, G., 1964. Geologie des Argiles. Masson. Paris, 499p.

_____ and Bonifas, M., 1955. Transformatons isovolumetriques dans les phenomenes de laterisation et de bauxitisation. Bull. Serv. Carte Geol. Alsace Lorraine. 8(1), 3-19.

Mohr, E. C. J., 1944. Soils of equatorial regions with special reference to the Netherlands East Indies; Translated from Dutch by Pendleton. Ann. Arbor, Mich. J. W. Edwards Co. 766p.

_____, Van Baren, F. A. and Schuylenborgh, J. V. 1972. Tropical Soils. 3rd ed. Mouton-Ichtiar Baru-Van Hoeve 481p.

Moses, J. H. and Mitchell, W. D., 1963. Bauxite deposits of British Guiana and Surinam in relation to underlying unconsolidated sediments suggesting two step origin. Econ. Geol. 58, no.2, 250-262.

Munoz T. M., 1953. Clay mineralogy of some spanish soils. J. Soil Sci. 4, 48-55.

Nakhshina, Y. P., 1975. Manganese in fresh water. Hydrobiological Journal. 11, 77-90.

Nicholls, G. D., 1963. Environmental studies in sedimentary geochemistry Science Progress. 51, 12-31.

Nickles, M. and Hourq, V., 1952. Carte geologique de l'Afrique Equatoriale Francaise et du Cameroun a l'echelle de 1:2 000 000 (3 feuilles) avec notice. Publ. Dir. Min. Geol. A.E.F. et Serv. Min. Cameroun, 109p.

Norton, F. H., 1939. Identification of clay minerals by DTA. J. Amer. Ceram. Soc. 22, 54-63.

Norton, S. A., 1973. Laterite and bauxite formation. Econ. Geol. 68. no.3, 353-361.

Nyobe, J. B., 1984. Esquisse geologique du Cameroun-notice explicative Mango 1/50,000 no. 2. I.R.G.M., Yaounde.

Okamoto, G., Okura, T. and Goto, K., 1957. Properties of silica in water. Geochem. Cosmochem. Acta. 12, 123-132.

Pascual, J. F., 1983. Analyses realisees sur les bauxites des monts Bamboutos (Cameroun). Rapport: 1ere partie, Centre d'Etudes Geogr. Trop. du CNRS, 142p. (Unpubl.).

Passarge, S., 1910. Geomorphologische Probleme aus Kamerun. Zeitschr. Gessell. fur Erdkunde, Berlin, 448-465.

Pedro, G., 1966. Interet geochimique et signification mineralogique du parametre moleculaire K_i SiO_2/Al_2O_3 dans l'etude des laterites et

bauxites. Bull. Groupe Fr. Argiles. Nouvelle Ser. 13. Paris 18, 19-31.

Petersen, U., 1971. Laterite and bauxite formation. Econ. Geol. 66, no. 7, 1070-1071.

Porter, A. R. D. and Bliss, N. W., 1981. Reconnaissance evaluation of the bauxite deposits around Fongo Tongo and at Bangam, Cameroon. Rept. M-ER-231-81, I & 2. Alcan Inter. LTD. (Unpubl.).

Posnjak, E. and Merwin, H. E., 1919. Hydrated ferric oxides. Am. Jour. Sci. 47, 311-348.

Rankama, K. and Sahama, T. G., 1949. Geochemistry. The Unv. of Chicago Press, 911p.

Rao, J. J. and Krishnamurthy, C. V., 1981. Some observations on the mineralogy and geochemistry of Hazaridadar Raktidadar plateau areas, Madhya Pradesh, India. In Lateritisation Processes. Proceedings of the International Seminar on Laterisation Processes. Trivandrum, India. Dec.1979. Balkema/Rotterdam, 89-107.

Reesman, A. L., Pickett, E. E. and Keller, W. D., 1969. Aluminous ions in aqueous solutions. Am. Jour. Sci. 267, 99-113.

Rocci, G., 1965. Essai d'interpretation de mesures geochronologiques. La structure de l'Ouest Africain. Coll. Intern. Geochron. Nancy. Sci. Terre. X. 461-478.

Ross, C. S. and Smith, R. L., 1961. Ash - flow tuffs: Their origin, geologic relations and identification, U. S. Geol. Surv. Prof. Paper 366, 79p.

Sahu, K. C., 1981. Preliminary studies on formation of Ni-rich laterites over ultramafic rocks of Amjori sill in Similipal, Mayurbhanj District, Orissa. In Laterisation Processes. Proceedings of the International Seminar on Laterisation Processes. Trivandrum, India. Dec. Balkema/Rotterdam, 68-76.

Schellman, W., 1969. Die Bildungsbedingungen Sedimentarer Chamosit-und Hamatit - Eisenerze am Beispiel der Lagerstate Echte, Neues Jahrb. Mineral. Abh. 111,:1-31.

Schindler, P., Michaelis, W. and Feitknecht, W., 1963. Loslichkeits produkte von metall - oxiden und hydroxiden. Die loslichkeit gealterter Eisen (III) hydroxidfallungen. Helv. Chim. Acta. 46, 444-449.

Sibuet, J. C. and Mascle, J., 1978. Plate kinematic implications of Atlantic equatorial fracture zone trends. Jour. Geophys. Res. 83, 3401-3421.

Smith, J. V., 1974. Feldspar Minerals. 2. Chemical and Textural Properties. Springer-Verlag. Heidelberg, 690p.

Smith, R. W. and Hem, J. D. 1972. Effect of ageing on aluminum hydroxide complexes in dilute aqueous solutions. U. S. Geol. Sur. Water Supply Paper 1827-D, 51p.

Stark, J. T. and Hay, R. L., 1963. Geology and petrography of volcanic rocks of the Truck Islands, East Caroline Islands, U. S. Geol. Surv. prof. Paper 409, 41p.

Stevenson, F. J., 1979. "Humus" The Encyclopedia of Soil Science. (R. W. Fairbridge, and C. W. Finkl Jr., ed.). I. Dowden, Hutchinson and Ross. Pennsylvania. Stroudsburg, 155-205.

Stober, W., 1967. Formation of silicic acid in aqueous suspensions of different silica modifications. In Equilibrium Concepts in Natural Water Systems (R. F. Gould, ed.). Advan. Chem. ser. 67. Amer. Chem. Soc. Washington, D.C., 161-182.

Tchoua, F., 1974. Contribution a l'etude geologique et petrologique de quelques volcans de la Ligne du Cameroun: (Monts Manengoumba et Bambouto). Univ. Clermont-Ferrand. These d'Etat, 337p. (Unpubl.).

Thoenen, J. R., Malamphy, M. C. and Dale, G. K., 1945. Application of the ternary diagram to analysis and classification of bauxite reserves. AIME. Technical Publ. 1915, 13p.

Tsibul'chik, V. M. and Ponomarchuk, V. A., 1980. Niobium, tantalum, zirconium, and hafnium in weathering zones of Altai Foothills. Lithology and Mineral Ressources (USSR). 15. no.5, 408-418.

Turcotte, D. L. and Oxburgh, E. R., 1973. Mid-plate tectonics. Nature, 244, 337.

Vadasz, E., 1951. Bauxitfoldtan (Bauxite Geology). Akademiai Kialo. Budapest, 127p.

Valeton, I., 1972. Bauxites: Developments in Soil Sciences. Elsevier Pub. Co. Amsterdam, 226p.

_____, 1981. Bauxite on peneplained metamorphic and magmatic rocks, on detrital sediments, and on karst topography, their similarities and contrasts of genesis. In Lateritisation Processes -Proceedings of the International Seminar on Lateritisation Processes. Trivandrum, India. Dec. 1979. Balkema/Rotterdam, 15 - 23.

Van Der Marel, H. W., Beutelspacher, 1976. Atlas of Infrared Spectroscopy of Clay Minerals and their Admixtures. Elsevier Pub. 396p.

Van Lier, J. A., 1959. The Mobility of Quartz. Utrecht. Kermink en Zoon, 54p.

Van Schmus, W. R., Nyobe, J. B., Soba, D., Bickford, M. E. and Premo, W. R.. U - Pb zircon geochronology of the north end of the Congo Archean nucleus, Republic of Cameroon, West Africa (In prep.).

Vlassov, K. A., ed. 1966. Geochemistry and mineralogy of rare elements and genetic types of their deposits. I. Geochemistry of Rare Elements. Acad. Sci. USSR, 688p.

Wada, K. and Yoshinaga, N., 1969. The Structure of Imogolite. Amer. Miner. 54, 50-71.

Weeksteen, G., 1957. Le Gisement de bauxite de Fongo Tongo, Rapp. an. Dir. Min. Geol. Cameroun, Yaounde, 40p.

Weiser, H. B. and Milligan, W. O., 1939. Constitution of colloid systems of the hydrous oxides. Chem. Reviews, 25, 1-30.

Whitten, D. G. A. and Brooks, J. R. V. 1981. The Penguin Dictionary of Geology. Penguin, 495p.

Wright, J. B., 1976. Fracture system in Nigeria and initiation of fracture zones in the South Atlantic. Tectonophysics. 34, T34-T47.

APPENDIX 1

CHEMICAL ANALYSES

Bauxites and Weathered Rocks

Outcrop samples: whole-rock major elements, wt%

SAMPLES:	N37	N49	N50e	N53b	N59a	N63b	N68
SiO_2	11.23	3.83	0.01	3.94	3.66	0.22	0.75
TiO_2	0.59	1.44	1.83	1.02	4.57	1.12	5.22
Al_2O_3	57.45	49.63	48.00	54.01	46.80	56.15	41.01
Fe_2O_3	2.93	17.11	24.33	13.05	19.60	6.79	27.35
FeO	0.13	0.11	0.10	0.11	1.11	0.12	1.21
MnO_2	0.01	0.04	0.04	0.05	0.09	0.04	0.06
MgO	0.01	0.01	0.01	0.01	0.49	0.01	0.15
CaO	0.01	0.01	0.01	0.01	0.01	0.01	0.01
Na_2O	0.03	0.01	0.01	0.01	0.01	0.01	0.01
K_2O	0.05	0.02	0.01	0.01	0.02	0.01	0.02
P_2O_5	0.01	0.06	0.13	0.02	0.47	0.01	0.29
CO_2	0.00	0.00	0.00	0.00	0.00	0.00	0.00
LOI	27.81	27.46	26.98	29.89	24.37	29.04	23.85
SUM	100.26	99.73	101.46	102.13	101.20	101.3	99.93

Outcrop samples: whole-rock minor elements, ppm

Samples:	N37	N49b	N50e	N53b	N59a	N63b	N68
Cr	9.9	9.9	43.0	13.0	140.0	29.0	830.0
V	215.0	198.0	107.0	9.9	229.0	74.0	313.0
Ni	49.0	63.0	51.0	47.0	72.0	37.0	58.0
Rb	9.9	9.9	9.9	9.9	9.9	9.9	9.9
Sr	9.9	9.9	9.9	9.9	421.0	23.0	93.0
Ba	9.9	9.9	18.0	10.0	374.0	27.0	76.0
Co	36.0	51.0	37.0	62.0	90.0	92.0	92.0
Pb	21.0	18.0	23.0	19.0	44.0	18.0	24.0
Zn	14.0	91.0	105.0	127.0	66.0	35.0	24.0
Cu	15.0	9.9	9.9	98.0	9.9	9.9	19.0

Bore hole S2: whole-rock major elements, wt%

Depth: (m)	1.2	2.7	4.0	5.5	6.4	7.0
SiO_2	2.08	1.60	3.03	4.27	3.71	2.30
Al_2O_3	54.90	54.50	52.40	54.80	60.50	59.00
CaO	0.05	<0.01	<0.01	0.03	0.03	<0.01
MgO	0.16	0.12	0.13	0.25	0.12	0.17
Na_2O	0.02	<0.01	0.01	<0.01	0.05	0.02
K_2O	0.03	0.10	0.02	0.03	0.04	0.01
Fe_2O_3	11.30	10.40	12.90	9.01	4.91	6.88
MnO_2	0.04	2.16	0.04	0.06	0.02	0.02
TiO_2	1.76	1.86	2.58	1.82	1.19	1.64
P_2O_5	0.11	0.08	0.09	0.09	0.05	0.05
LOI	29.00	29.20	28.90	29.40	29.50	29.50
SUM	99.45	100.08	100.11	99.97	100.12	99.60

Depth: (m)	8.0	9.0	10.2	11.7	13.3
SiO_2	3.30	2.28	2.72	10.50	14.40
Al_2O_3	56.40	58.50	54.80	51.80	33.30
CaO	0.01	<0.01	<0.01	0.01	0.02
MgO	0.18	0.12	0.10	0.12	0.10
Na_2O	0.02	0.02	<0.01	<0.01	0.03
K_2O	0.03	0.02	0.03	0.03	0.04
Fe_2O_3	8.14	7.22	12.90	11.30	30.70
MnO_2	0.10	0.04	0.15	0.17	0.10
TiO_2	1.84	1.61	1.26	1.13	1.60
P_2O_5	0.06	0.06	0.07	0.06	0.10
LOI	29.80	29.80	27.90	23.90	18.60
SUM	99.88	99.66	99.95	99.03	99.09

Bore hole S2: whole-rock minor elements, ppm

Depth: (m)	1.2	2.7	4.0	5.5	6.4	7.0	8.0
Cr	180	120	130	120	100	70	110
Rb	<10	10	<10	<10	10	<10	10
Sr	<10	<10	<10	<10	20	<10	<10
Y	50	30	70	60	80	120	80
Zr	2230	2110	2460	2130	1700	2530	2180
Nb	430	420	490	430	340	500	430
Ba	210	800	120	150	110	120	130
V	100	60	130	90	50	58	70
Co	29	27	36	110	300	90	34
Mo	14	13	13	12	11	13	13

Depth: (m)	9.0	10.2	11.7	13.2
Cr	90	80	50	60
Br	<10	<10	30	10
Sr	<10	<10	<10	<10
Y	80	50	30	10
Zr	2240	1720	1320	1790
Nb	440	310	200	270
Ba	120	200	220	160
V	56	44	36	42
Co	28	35	23	26
Mo	11	11	12	8

Bore hole S4: whole-rock major elements, wt%

Depth: (m)	1.10	2.40	6.00	7.00	8.50
SiO_2	12.80	23.10	19.90	30.20	34.20
Al_2O_3	45.20	37.70	54.20	40.80	34.30
CaO	0.02	0.05	0.08	0.07	0.15
MgO	0.11	0.10	0.10	0.14	0.14
Na_2O	<0.01	<0.01	0.03	0.02	0.06
K_2O	0.10	0.09	0.06	0.15	0.07
Fe_2O_3	15.00	16.70	10.70	7.57	11.00
MnO_2	0.08	0.06	0.09	0.09	0.13
TiO_2	1.32	1.34	0.93	0.82	0.90
P_2O_5	0.13	0.12	0.10	0.09	0.10
LOI	25.10	20.20	22.70	20.10	18.50
SUM	99.87	99.47	108.89	100.05	98.55

Depth: (m)	10.0	11.5	12.5	13.5	14.5
SiO_2	13.70	20.10	26.30	32.60	36.00
Al_2O_3	49.90	43.30	37.70	34.80	31.50
CaO	0.04	0.05	0.05	0.06	0.04
MgO	0.01	0.01	0.01	0.01	0.01
Na_2O	0.02	0.02	<0.01	0.01	<0.01
K_2O	0.07	0.07	0.09	0.07	0.05
Fe_2O_3	9.50	12.20	12.70	11.90	12.80
MnO_2	0.10	0.12	0.09	0.09	0.09
TiO_2	0.85	1.07	1.19	1.18	1.19
P_2O_5	0.08	0.11	0.12	0.11	0.09
LOI	25.50	23.10	20.80	18.70	17.10
SUM	99.77	100.27	99.06	99.53	98.88

Depth: (m)	16.2	17.5	19.0	20.5
SiO_2	34.40	33.10	35.20	39.20
Al_2O_3	33.10	32.10	30.20	30.30
CaO	0.04	0.07	0.05	0.03
MgO	0.10	0.10	0.09	0.08
Na_2O	0.05	0.01	<0.01	<0.01
K_2O	0.08	0.07	0.07	0.06
Fe_2O_3	12.60	13.50	14.70	11.00
MnO_2	0.12	0.09	0.09	0.10
TiO_2	1.20	1.16	1.24	1.13
P_2O_5	0.10	0.11	0.12	0.12
LOI	17.80	17.90	16.90	16.30
SUM	99.59	98.21	98.67	98.43

Bore hole S4: whole-rock minor elements, ppm

Depth: (m)	1.10	2.40	6.00	7.00	8.50
Cr	140	70	50	50	50
Rb	40	20	<10	40	30
Sr	<10	10	<10	<10	<10
Y	10	40	50	40	60
Zr	1820	2710	2500	1610	2300
Nb	240	310	270	160	270
Ba	160	150	150	200	240

Depth: (m)	10.0	11.5	12.5	13.5	14.5
Cr	60	70	70	50	40
Rb	20	10	20	10	30
Sr	<10	<10	<10	<10	<10
Y	30	50	50	80	80
Zr	2070	2440	2410	2450	2690
Nb	230	270	270	270	270
Ba	160	210	250	250	210

Depth: (m)	16.2	17.5	19.0	20.5
Cr	40	40	40	40
Rb	<10	20	<10	<10
Sr	<10	<10	<10	<10
Y	80	60	80	180
Zr	2550	2770	2870	2310
Nb	260	280	280	240
Ba	240	190	190	200

Volcanic Rocks

(1) Data from Tchoua (1974)

Basaltic rocks: whole-rock major elements, wt%

SAMPLE NUMBER	N3	N35	N58	N67	N63	5083(1)
SiO_2	43.35	40.86	43.99	42.89	44.02	44.00
TiO_2	2.95	3.58	3.47	3.06	3.03	2.25
Al_2O_3	13.62	14.28	15.71	12.54	13.99	11.65
Fe_2O_3	3.22	4.02	2.72	3.13	1.37	8.35
FeO_2	8.44	9.79	8.72	9.08	10.19	7.45
MnO	0.20	0.21	0.23	0.18	0.19	0.20
MgO	8.48	7.39	6.21	12.36	8.43	7.50
CaO	10.95	10.63	10.30	10.60	9.82	8.80
Na_2O	2.76	3.23	3.41	2.92	3.18	2.90
K_2O	1.40	1.59	1.34	1.12	1.23	1.75
P_2O_5	0.83	1.58	1.33	1.03	1.11	1.90
CO_2	0.13	0.08	0.10	0.06	0.09	
H_2O^+	1.49	0.82	0.97	0.16	1.03	1.85
H_2O^-	0.36	0.24	0.13	0.19	0.33	0.40
SUM	98.18	98.30	98.68	99.32	98.01	100.60

CIPW norms:

Qz	0.00	0.00	0.00	0.00	0.00	0.00
Or	8.56	9.65	8.11	6.68	7.51	10.35
Ab	13.27	9.13	20.35	9.37	18.61	10.35
An	21.41	20.32	24.17	17.97	20.95	13.57
Ne	5.94	10.27	4.98	8.44	4.99	0.00
Di	23.49	19.44	15.64	22.96	17.97	14.80
Hy	0.00	0.00	0.00	0.00	0.00	8.95
Ol	15.77	16.34	13.30	22.68	19.12	8.95
Mt	3.08	3.61	2.99	3.14	2.06	12.11
Il	5.83	7.00	6.77	5.88	5.96	7.31
Ap	2.04	3.85	3.35	2.46	2.72	4.50
Ca	0.31	0.19	0.23	0.14	0.21	0.00
SUM	99.7	99.8	99.89	99.72	100.1	90.89

SAMPLE NUMBER	9316(1)	47(1)	5084(1)	9312(1)	9320(1)
SiO_2	42.59	43.40	43.80	43.23	45.60
TiO_2	3.91	3.90	3.60	4.15	3.33
Al_2O_3	13.51	15.50	12.50	15.14	16.88
Fe_2O_3	5.93	3.90	9.50	5.71	5.10
FeO	7.96	7.94	7.20	8.16	7.37
MnO	0.00	0.00	0.20	0.00	0.00
MgO	9.27	8.47	8.70	7.18	7.71
CaO	9.99	9.78	8.95	9.25	9.92
Na_2O	3.64	3.15	2.85	2.75	3.92
K_2O	1.37	1.72	1.45	1.75	1.73
P_2O_5	0.00	1.05	0.90	0.00	0.00
H_2O	1.24	0.00	2.56	1.60	1.82
SUM	99.41	98.61	100.30	99.93	101.38

CIPW norms:

SAMPLE NUMBER	9316(1)	47(1)	5084(1)	9312(1)	9320(1)
Qz	0.00	0.00	0.00	0.00	0.00
Or	8.10	10.00	8.58	10.35	10.23
Ab	10.43	15.72	24.09	18.81	17.22
An	16.45	23.07	17.00	23.76	23.31
Ne	11.02	5.70	0.00	2.40	8.62
Di	26.12	14.98	17.21		16.61
Hy	0.00	0.00	7.22		0.00
Ol	10.02	13.10	1.10	9.29	10.84
Mt	8.60	5.57	13.41	8.28	7.39
Il	7.43	7.47	6.84	7.88	6.33
Ap	0.00	2.35	2.13	0.00	0.00
Hm			0.25	0.00	0.00
SUM	98.17	97.96	97.83	80.79	100.55

Basaltic rocks: whole-rock minor elements, ppm

SAMPLE NUMBER	N3	N35	N58	N63	N67
Cr	382.0	93.0	93.0	266.0	535.0
V	242.0	155.0	276.0	220.0	163.0
Ni	150.0	106.0	80.0	165.0	376.0
Rb	32.0	36.0	28.0	24.0	33.0
Sr	1012.0	1390.0	2180.0	1114.0	1020.0
Ba	684.0	812.0	1317.0	765.0	605.0
Co	79.0	147.0	43.0	68.8	145.0
Zn	107.0	115.0	109.0	105.0	104.0
Cu	65.0	30.0	22.0	64.0	39.0

Trachytic rocks: whole-rock major elements, wt%

(2) Greenish trachyte
(3) Greyish trachyte
(4) Dark trachyte
(1) Superscripts are part of sample numbers.
Identical numbers with different subscripts represent different analyses of the same sample. Samples without one of the above three numbers are undifferentiated trachytes.

SAMPLE NUMBER	N2(3)	N7(3)	$N10_1$(2)	N28A(3)	N40(3)	N49a(4)
SiO_2	66.45	65.29	61.47	62.11	62.70	61.64
TiO_2	0.82	0.73	0.65	0.90	0.75	0.44
Al_2O_3	12.38	11.99	17.67	17.49	17.33	15.98
Fe_2O_3	3.82	2.89	2.58	2.99	2.90	3.89
FeO	2.91	4.22	2.76	0.74	1.88	3.20
MnO	0.16	0.46	0.18	0.18	0.13	0.19
MgO	0.20	0.25	0.42	0.53	0.34	0.28
CaO	0.07	0.13	0.17	0.90	0.06	2.20
Na_2O	5.24	5.08	6.04	5.87	6.16	4.75
K_2O	4.86	4.81	5.04	5.76	5.38	5.40
P_2O_5	0.01	0.02	0.02	0.23	0.15	0.05
CO_2	0.05	1.84	0.18	0.14	0.16	0.12
H_2O^+	1.04	2.26	1.36	0.82	1.27	1.46
H_2O^-	0.67	0.33	0.28	0.25	0.52	0.43
SUM	98.68	100.29	98.82	98.91	99.73	100.03

CIPW norms

SAMPLE NUMBER	N2(3)	N7(3)	$N10_1(2)$	N28A(3)	N40(3)	N49a(4)
Qz	16.83	18.48	3.90	2.63	4.22	5.55
Or	29.58	29.06	30.61	34.75	32.42	32.48
Ab	37.73	35.68	52.55	50.72	53.17	40.92
An	0.00	0.00	0.00	2.27	0.00	6.45
Ne	0.00	0.00	0.00	0.00	0.00	0.00
Ae	3.41	3.64	0.00	0.00	0.00	0.00
Ns	0.95	0.97	0.00	0.00	0.00	0.00
Di	0.00	0.00	0.00	0.00	0.00	0.00
Hy	9.30	6.06	7.41	4.93	6.07	7.93
Ol	0.00	0.00	0.00	0.00	0.00	0.00
Mt	0.00	0.00	1.37	0.92	1.20	1.79
Il	1.61	1.41	1.27	1.75	1.46	1.79
Ap	0.02	0.02	0.05	0.56	0.36	0.12
Cor	0.00	0.00	2.50	0.80	2.00	0.00
Ca	0.12	4.28	0.42	0.33	0.37	0.28
SUM	98.6	99.6	100.0	99.66	101.27	103.31

SAMPLE NUMBER	N47(2)	N57(2)	N66(3)	4206[1](1)	4870[1](1)	9323[3](1)
SiO_2	59.62	63.73	60.63	65.90	62.50	60.85
TiO_2	0.50	0.68	1.01	0.95	0.65	1.14
Al_2O_3	16.04	16.27	14.79	14.30	16.25	14.88
Fe_2O_3	3.29	2.21	4.02	3.30	1.40	5.09
FeO	4.59	2.92	2.05	0.45	2.50	3.58
MnO	0.20	0.19	0.72	0.05	0.25	0.00
MgO	0.13	0.41	0.72	0.90	1.05	0.40
CaO	2.58	0.21	0.77	0.60	1.40	2.55
Na_2O	4.74	6.27	5.86	6.10	6.85	5.22
K_2O	5.15	5.54	5.36	5.10	5.00	5.25
P_2O_5	0.27	0.01	0.01	0.35	0.20	0.00
CO_2	0.10	0.03	0.55			
H_2O^+	1.09	0.31	2.79	1.70	1.55}	
H_2O^-	0.31	0.18	0.46	0.55	0.00}	0.82
SUM	98.61	98.96	99.74	100.25	99.60	99.78

CIPW norms

SAMPLE NUMBER	N47(4)	N57(2)	N66(3)	4206[1](1)	4858[1](1)	9323[3](1)
Qz	3.93	2.65	2.00	10.89	0.00	6.53
Or	31.27	33.21	32.79	30.17	29.57	31.05
Ab	41.22	53.62	47.87	45.03	55.61	44.12
An	7.48	0.00	0.00	0.00	0.00	1.62
Ne	0.00	0.00				
Ae		0.19	3.06	5.75	2.02	0.00
Ns		0.00	0.00			
Di	3.01	0.70	0.26	0.72	4.82	6.09
Hy	8.82	6.71	10.23	1.92	2.59	0.00
Ol	0.00	0.00	0.00			
Mt	2.03	1.21	0.00			
Il	0.98	1.31	1.99	1.06	1.23	2.17
He				1.31	0.00	0.00
Ap	0.66	0.02	0.02	0.83	0.47	0.00
Ca	0.23	0.07	1.30			
Sum	99.63	99.69	99.52	97.68	96.31	91.58

whole rock minor-elements, ppm

SAMPLE NUMBER	N2(3)	N7(3)	N10(2)	N28a(3)	N40(3)
Cr	12.0	9.9	9.9	9.9	13.0
V	10.0	90.0	74.0	29.0	42.0
Ni	10.0	14.0	9.9	9.9	9.9
Rb	174.0	180.0	133.0	88.0	168.0
Sr	10.0	9.9	9.9	80.0	29.0
Ba	19.0	38.0	22.0	546.0	46.0
Co	22.0	97.0	29.0	9.9	9.9
Pb	26.0	30.0	17.0	9.0	17.0
Zn	221.0	401.0	98.0	130.0	161.0
Cu	9.9	9.9	9.9	9.9	9.9

SAMPLE NUMBER	$N47_1$(4)	N49a(4)	N57(2)	N66(3)	$N10_1$(2)	$N47_2$(4)
Cr	16.0	9.9	9.9	14.0		
V	15.0	75.0	9.9	12.0		
Ni	9.9	13.0	9.9	9.9		
Rb	105.0	110.0	169.0	212.0		
Sr	120.0	114.0	9.9	74.0		
Ba	1565.0	1725.0	18.0	67.0	60.0	1900.0
Co	9.9	25.0	9.9	9.9		
Pb	16.0	22.0	13.0	18.0		
Zn	152.0	154.0	109.0	351.0		
Cu	9.9	9.9	9.9	9.9		
Nb					310.0	84.0
Zr					1500.0	700.0
Y					50.0	64.0

Ash-Flow Tuffs: whole-rock major elements, wt%

SAMPLE NUMBER	N32	N44	N48	1546[4](1)	1547[4](1)	1549[4](1)
SiO_2	66.45	68.11	59.23	69.10	67.00	64.40
TiO_2	0.61	0.62	0.32	0.45	0.44	0.48
Al_2O_3	14.81	15.25	15.04	14.15	17.01	15.84
Fe_2O_3	2.35	1.92	5.59	3.25	2.50	3.98
FeO	0.69	0.53	1.01	0.43	0.50	0.50
MnO	0.06	0.03	0.06	0.00	0.00	0.00
MgO	0.03	0.01	0.25	0.00	0.00	0.00
CaO	0.01	0.01	0.98	0.16	0.26	0.56
Na_2O	5.39	5.59	0.70	5.75	4.10	2.92
K_2O	4.99	4.81	3.45	4.98	3.30	3.52
P_2O_5	0.07	0.14	0.01	0.06	0.01	0.03
CO_2	0.08	0.11	0.13			
H_2O^+	1.39	1.42	9.34	0.80	3.50	4.70
H_2O^-	0.76	0.50	2.98	1.60	2.00	2.10
SUM	99.98	99.05	99.09	100.67	100.65	99.06

CIPW norms

SAMP NUMB	N32	N44	N48	1546[4](1)	1547[4](1)	1549[4](1)
Qz	16.89	17.33	41.80	17.59	30.02	32.84
Or	30.39	29.23	23.47	28.98	19.52	20.83
Ab	47.01	48.66	6.82	45.38	34.65	24.68
An	0.00	0.00	4.58	0.00	1.23	2.60
Ne	0.00	0.00	0.00			
Ae	0.00	0.00	0.00	2.84	0.00	0.00
Ns	0.00	0.00	0.00			
Di	0.00	0.00	0.00			
Hy	3.08	2.18	9.69	0.00	0.00	0.00
Ol	0.00	0.00	0.00			
Mt	0.76	0.61	1.82	0.15	0.43	0.32
Il	1.20	1.21	0.70	0.85	0.84	0.91
Hm				2.17	2.20	3.76
Ap	0.17	0.34	0.03	0.14	0.02	0.07
Cor	0.82	1.43	10.20	0.00	6.23	6.26
Wo				0.18	0.00	0.00
Ca	0.19	0.26	0.34			
Sum	100.51	101.25	99.45	98.28	95.14	92.27

SAMPLE NUMBER	$8208^3(1)$	$8226^3(1)$	$8210^3(1)$
SiO_2	74.88	72.30	70.03
TiO_2	0.3	0.45	0.56
Al_2O_3	13.96	12.80	15.60
Fe_2O_3	0.41	3.32	1.24
FeO	0.43	0.28	0.57
MnO			
MgO		0.30	
CaO	0.32	0.40	
Na_2O	4.20	3.00	5.73
K_2O	4.77	4.80	5.57
P_2O_5			
CO_2			
H_2O	0.71	0.95	0.71
SUM	99.98	98.60	100.01

CIPW norms

SAMPLE NUMBER	$8208^3(1)$	$8226^3(1)$	$8210^3(1)$
Qz	31.54	35.19	15.43
Or	28 21	28.39	32.95
Ab	35.50	25.35	48.43
An	1.59	1.99	0.00
Cor		1.93	0.13
Hy		0.75	
Mt	0.52	0.00	0.21
Il	0.57	0.59	1.06
Hm	0.05	3.32	1.09
Ap	0.00	0.00	0.00
Ae	0.00	0.00	0.00
Sum	97.98	97.51	99.3

Whole-rock minor elements, ppm

SAMPLE NUMBER	N32	N44	$N48_1$	$N48_2$
Cr	9.9	31.0	9.9	
V	11.0	21.0	110.0	
Ni	9.9	9.9	25.0	
Rb	142.0	153.0	184.0	
Sr	18.0	29.0	50.0	
Ba	77.0	59.0	645.0	500.0
Co	9.9	9.9	23.0	
Pb	22.0	14.0	19.0	
Zn	149.0	60.0	277.0	
Cu	9.9	9.9	9.9	
Y				340.0
Nb				130.0
Zr				1000.0

Basement granites

SAMPLE N33

Whole-rock major elements, wt%		Whole-rock minor elem., ppm	
SiO_2	63.43	Cr	9.9
TiO_2	.86	V	11.0
Al_2O_3	16.72	Ni	9.9
Fe_2O_3	1.61	Rb	142.0
FeO	3.19	Sr	18.0
MnO	0.08	Ba	77.0
MgO	0.90	Co	9.9
CaO	2.01	Pb	22.0
Na_2O	3.35	Zn	149.0
K_2O	5.86	Cu	9.9
P_2O_5	0.49		
CO_2	0.11		
H_2O^+	1.02		
H_2O^-	0.14		
SUM	99.77		

CIPW norms

Qz	16.89
Or	30.39
Ab	47.01
An	0.00
Ne	0.00
Ae	0.00
Ns	0.00
Di	0.00
Hy	3.08
Ol	0.00
Mt	0.76
Il	1.20
Ap	0.17
Cor	0.89
Ca	0.19
	100.58

APPENDIX 2

X-RAY POWDER DIFFRACTION

List of samples analysed

Core Samples

Bore hole S2

Sample	Depth	Page
S21	1.0 m	303
S22	1.2 m	304
S23	2.7 m	305
S24	4.0 m	306
	and	307
S25	5.5 m	308
S26	6.4 m	309
S27	7.0 m	310
S28	8.0 m	311
S29	9.0 m	312
S210	0.2 m	313
S211	1.7 m	314
S213	3.2 m	315

Bore hole S4

Sample	Depth	Page
S41	1.1 m	316
S42	2.4 m	317
S44	5.0 m	318
S45	6.0 m	319
S46	7.0 m	320
S47	8.5 m	321
S48	0.5 m	322
S410	2.5 m	323
S411	3.5 m	324
S412	4.5 m	325
S413	6.2 m	326
S414	7.5 m	327
S416	20.5 m	328

Bore hole S3

S31	1.1 m	329
S32	2.6 m	330
S33	3.8 m	331
S34	4.3 m	332
S35	5.5 m	333

Bore hole S5

S51	1.1 m	334
S52	2.5 m	335
S53	3.8 m	336
S54	5.0 m	337
S55	6.0 m	338
S56	7.2 m	339

Sample from road cut: N-71 Page 340 and 341

N-7180 = N-71 heated at 80°C
Page 342 and 343

N-71380 = N-71 heated at 380°C
Page 344 and 345

Pit sample: N-74 ("cameroonite") Page 346

APD-3600 2ND DERIVATIVE PEAK ALGORITHM 11/15/85 15:19:16

RAW DATA FILE	: 521.RD
SAMPLE ID	: 521
RAW DATA FILE DATE	: 11/14/85
GENERATOR SETTINGS	: 45 KV 30 MA
STEP SIZE, CNT TIME	: 0.020 DEG 0.60 SEC
RANGE OF DATA	: 2.000 - 45.000 DEG
RANGE IN D	: 44.1716 - 2.0145 A
MAX PEAK CTS, CPS	: 1656. CTS 2761. CPS
SECF APPLIED	: NONE

2-THETA (DEG)	WIDTH (APPROX)	COUNTS PEAK	COUNTS BKGND	D (ANG)	I (NORM)	LINE TYPE A1	A2	BT	AM	OT
2.38	0.33	185.	50.	38.4107	11.17	X	X			
5.04	0.37	76.	81.	17.5332	4.57	X	X			
18.48	0.15	1656.	46.	4.8217	100.00	X	X			
20.37	0.20	317.	49.	4.3596	19.13	X	X			
20.65	0.13	169.	50.	4.3001	10.20	X	X			
21.62	0.18	90.	52.	4.1112	5.45	X	X			
24.32	0.37	26.	45.	3.6590	1.57	X	X			
25.32	0.32	67.	45.	3.5181	4.06	X	X			
26.68	0.28	193.	44.	3.3411	11.66	X	X			
27.01	0.14	142.	44.	3.3005	8.55	X	X			
28.06	0.19	128.	42.	3.1799	7.71	X	X			
28.54	0.15	778.	42.	3.1270	46.99	X	X			
33.23	0.33	94.	45.	2.6964	5.68	X	X			
33.98	0.34	55.	45.	2.6446	3.31	X	X			
35.78	0.27	112.	45.	2.5095	6.78	X	X			
36.51	0.19	182.	45.	2.4610	11.00	X	X			
36.74	0.19	253.	45.	2.4464	15.26	X	X			
37.19	0.24	190.	45.	2.4175	11.50	X	X			
37.77	0.26	335.	45.	2.3814	20.22	X	X			
39.46	0.31	53.	45.	2.2836	3.22	X	X			
40.22	0.32	114.	45.	2.2421	6.91	X	X			
41.79	0.27	156.	45.	2.1615	9.43	X	X			
44.27	0.32	231.	45.	2.0460	13.95	X	X			
3.75	10.00	66.	0.	23.5612						X

24 PEAKS IDENTIFIED 23 CRYSTALLINE 1 AMORPHOUS
24 PEAKS LISTED

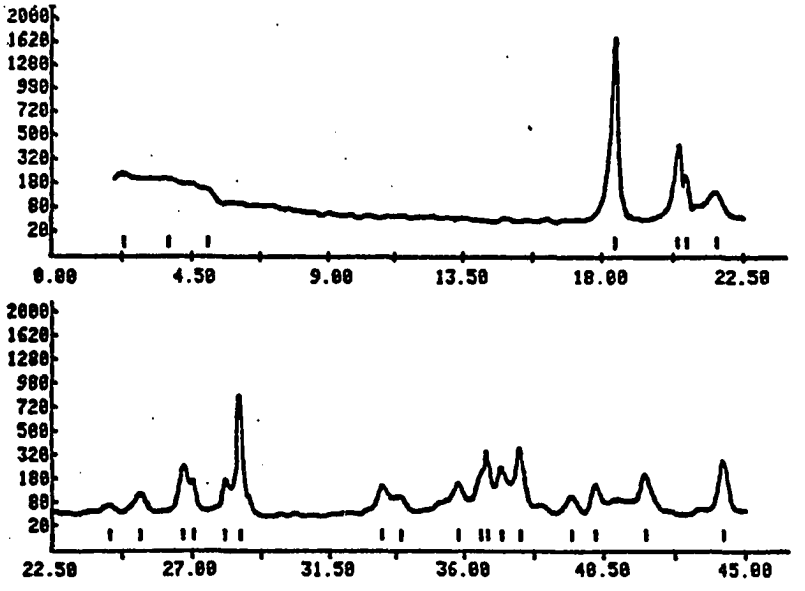

APD-3600 2ND DERIVATIVE PEAK ALGORITHM 10/ 1/85 10:20:21

RAW DATA FILE	: S22.RD
SAMPLE ID	: S22
RAW DATA FILE DATE	: 9/27/85
GENERATOR SETTINGS	: 45 KV 30 MA
STEP SIZE, CNT TIME	: 0.020 DEG 1.20 SEC
RANGE OF DATA	: 2.000 - 45.000 DEG
RANGE IN D	: 44.1716 - 2.0145 A
MAX PEAK CTS, CPS	: 6972. CTS 5815. CPS
SECF APPLIED	: NONE

2-THETA (DEG)	WIDTH (APPROX)	COUNTS PEAK	COUNTS BKGND	D (ANG)	I (NORM)	LINE TYPE A1	A2	BT	AM	OT
3.50	0.39	92.	243.	25.2435	1.32	x	x			
4.53	0.37	68.	207.	19.4844	1.27	x	x			
5.03	0.27	53.	198.	17.5690	0.76	x	x			
18.40	0.17	6972.	81.	4.8217	100.00	x	x			
20.37	0.21	1246.	81.	4.3607	17.87	x	x			
20.65	0.13	590.	81.	4.3011	8.47	x	x			
21.52	0.44	169.	81.	4.1282	2.42	x	x			
24.23	0.39	42.	79.	3.6739	0.61	x	x			
25.32	0.35	142.	77.	3.5181	2.03	x	x			
26.59	0.21	286.	76.	3.3523	4.10	x	x			
26.99	0.20	454.	76.	3.3041	6.51	x	x			
28.09	0.20	320.	74.	3.1771	4.60	x	x			
28.79	0.29	154.	72.	3.1009	2.21	x	x			
33.23	0.36	225.	74.	2.6960	3.23	x	x			
33.88	0.33	119.	74.	2.6454	1.70	x	x			
35.77	0.27	240.	76.	2.5102	3.45	x	x			
36.47	0.14	475.	77.	2.4636	6.82	x	x			
36.71	0.15	942.	77.	2.4480	13.52	x	x			
37.19	0.19	590.	77.	2.4175	8.47	x	x			
37.77	0.24	1116.	77.	2.3817	16.00	x	x			
38.46	0.25	94.	79.	2.3403	1.35	x	x			
39.39	0.19	243.	79.	2.2874	3.49	x	x			
40.23	0.28	416.	81.	2.2419	5.97	x	x			
41.79	0.27	538.	83.	2.1612	7.72	x	x			
43.47	0.26	44.	98.	2.0817	0.62	x	x			
44.27	0.29	790.	117.	2.0457	11.33	x	x			

26 PEAKS IDENTIFIED 26 CRYSTALLINE 0 AMORPHOUS
26 PEAKS LISTED

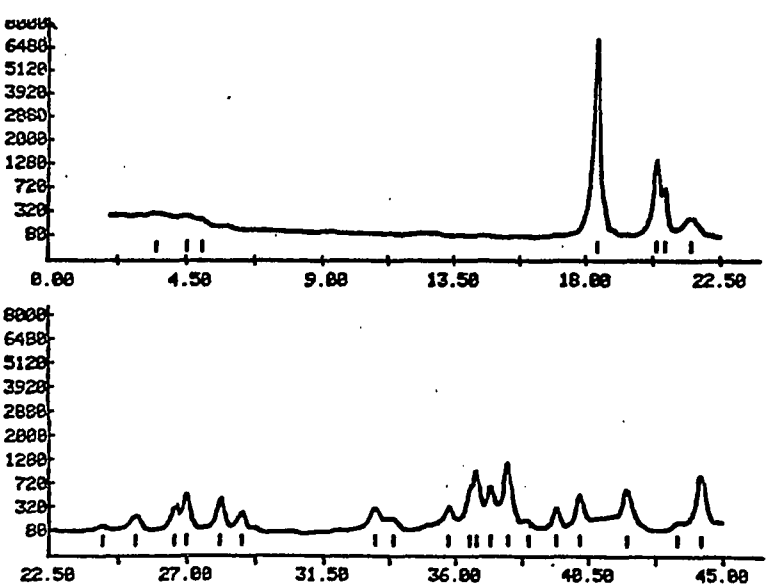

APD-3600 2ND DERIVATIVE PEAK ALGORITHM 11/15/85 15:28: 4

RAW DATA FILE	: S23.RD
SAMPLE ID	: S23
RAW DATA FILE DATE	: 11/14/85
GENERATOR SETTINGS	: 45 KV 30 MA
STEP SIZE, CNT TIME	: 0.020 DEG 0.60 SEC
RANGE OF DATA	: 2.000 - 45.000 DEG
RANGE IN D	: 44.1716 - 2.0145 A
MAX PEAK CTS, CPS	: 3528. CTS 5881. CPS
SECF APPLIED	: NONE

2-THETA (DEG)	WIDTH (APPROX)	COUNTS PEAK	COUNTS BKGND	D (ANG)	I (NORM)	LINE TYPE A1	A2	BT	AM	OT
5.18	0.37	44.	100.	17.3278	1.23	x	x			
18.40	0.13	3528.	40.	4.8217	100.00	x	x			
20.36	0.20	538.	38.	4.3617	15.25	x	x			
20.64	0.12	256.	38.	4.3032	7.26	x	x			
21.51	0.56	85.	37.	4.1311	2.40	x	x			
24.20	0.36	24.	38.	3.6776	0.68	x	x			
25.35	0.20	41.	40.	3.5127	1.16	x	x			
26.56	0.24	85.	42.	3.3560	2.40	x	x			
26.98	0.20	166.	44.	3.3047	4.72	x	x			
28.06	0.21	154.	42.	3.1799	4.36	x	x			
28.54	0.17	1218.	48.	3.1275	34.52	x	x			
33.21	0.31	106.	31.	2.6972	3.01	x	x			
33.87	0.36	56.	31.	2.6465	1.59	x	x			
35.76	0.31	92.	31.	2.5105	2.61	x	x			
36.66	0.33	328.	31.	2.4513	9.00	x	x			
37.18	0.19	259.	31.	2.4182	7.35	x	x			
37.76	0.27	408.	31.	2.3821	11.56	x	x			
38.46	0.25	41.	31.	2.3406	1.16	x	x			
39.41	0.38	92.	31.	2.2863	2.61	x	x			
40.22	0.25	166.	31.	2.2421	4.72	x	x			
41.79	0.36	284.	31.	2.1612	5.80	x	x			
43.47	0.23	27.	37.	2.0817	0.77	x	x			
44.29	0.26	313.	44.	2.0453	8.88	x	x			

23 PEAKS IDENTIFIED 23 CRYSTALLINE 0 AMORPHOUS
23 PEAKS LISTED

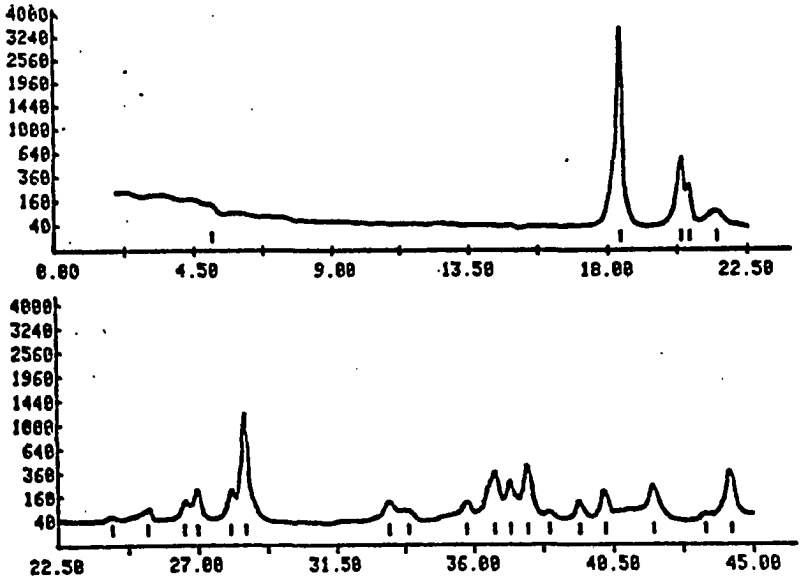

APD-3600 2ND DERIVATIVE PEAK ALGORITHM 9/25/85 8:32: 2
RAW DATA FILE : S24.RD
SAMPLE ID : S24
RAW DATA FILE DATE : 9/23/85
GENERATOR SETTINGS : 45 KV 30 MA
STEP SIZE, CNT TIME : 0.020 DEG 1.20 SEC
RANGE OF DATA : 3.000 - 75.000 DEG
RANGE IN D : 29.4496 - 1.2563 A
MAX PEAK CTS, CPS : 4238. CTS 3535. CPS
SECF APPLIED : NONE

2-THETA (DEG)	WIDTH (APPROX)	COUNTS PEAK	COUNTS BKGND	D (ANG)	I (NORM)	LINE TYPE A1	A2	BT	AM	OT
4.94	0.37	38.	282.	17.9060	0.91	X	X			
12.49	0.35	69.	90.	7.0868	1.63	X	X			
18.45	0.14	4238.	85.	4.8100	100.00	X	X			
20.43	0.15	1069.	85.	4.3488	25.23	X	X			
20.68	0.14	524.	85.	4.2960	12.37	X	X			
21.54	0.48	253.	85.	4.1244	5.97	X	X			
24.26	0.33	34.	83.	3.6687	0.79	X	X			
24.97	0.19	83.	81.	3.5639	1.95	X	X			
25.34	0.27	156.	81.	3.5147	3.69	X	X			
26.62	0.25	219.	77.	3.3492	5.17	X	X			
27.83	0.19	369.	77.	3.2987	8.70	X	X			
28.11	0.22	296.	76.	3.1743	6.98	X	X			
28.85	0.26	119.	74.	3.0951	2.80	X	X			
33.26	0.27	193.	98.	2.6941	4.56	X	X			
33.91	0.27	119.	94.	2.6431	2.80	X	X			
35.11	0.31	44.	98.	2.5559	1.03	X	X			
35.79	0.33	219.	98.	2.5085	5.17	X	X			
36.51	0.15	376.	98.	2.4613	8.88	X	X			
36.71	0.31	635.	98.	2.4480	14.98	X	X			
37.21	0.15	488.	98.	2.4163	11.52	X	X			
37.80	0.19	942.	98.	2.3796	22.24	X	X			
38.50	0.25	85.	98.	2.3383	2.00	X	X			
39.45	0.30	202.	98.	2.2844	4.76	X	X			
40.24	0.24	328.	98.	2.2413	7.73	X	X			
40.35	0.08	199.	98.	2.2349	4.69		X	X		
41.82	0.38	467.	98.	2.1597	11.01	X		X		
43.53	0.31	41.	98.	2.0790	0.97	X	X			
44.32	0.26	718.	96.	2.0440	16.95	X	X			
45.59	0.25	502.	94.	1.9898	11.84	X	X			
46.35	0.26	83.	92.	1.9591	1.95	X	X			
47.54	0.21	350.	90.	1.9124	8.25	X	X			
48.07	0.24	86.	90.	1.8929	2.04	X	X			
49.56	0.44	66.	81.	1.8393	1.55	X	X			
50.69	0.31	581.	79.	1.8009	13.70	X	X			
52.35	0.29	581.	86.	1.7478	13.70	X	X			
52.79	0.16	81.	88.	1.7339	1.91	X	X			
54.07	0.25	357.	92.	1.6962	8.43	X	X			
54.52	0.18	645.	94.	1.6831	15.22	X	X			
54.63	0.12	524.	96.	1.6800	12.37		X	X		
55.55	0.27	182.	100.	1.6542	4.30	X	X			
56.24	0.48	94.	102.	1.6355	2.22	X	X			
58.11	0.42	142.	117.	1.5874	3.34	X	X			
58.74	0.28	118.	123.	1.5720	2.80	X	X			
59.65	0.25	76.	125.	1.5500	1.79	X	X			
60.46	0.29	45.	117.	1.5313	1.06	X	X			
61.51	0.23	44.	112.	1.5076	1.03	X	X			
62.61	0.44	222.	112.	1.4837	5.24	X	X			
63.89	0.14	529.	112.	1.4578	12.48	X	X			
64.13	0.20	339.	112.	1.4522	7.99		X	X		
64.74	0.17	313.	112.	1.4399	7.39	X	X			
64.96	0.08	174.	112.	1.4356	4.11		X	X		
66.24	0.19	342.	112.	1.4108	8.08	X	X			
66.84	0.36	240.	112.	1.3997	5.67	X	X			
67.98	0.35	104.	112.	1.3790	2.45	X	X			
68.96	0.24	151.	108.	1.3616	3.57	X				
69.12	0.14	142.	108.	1.3590	3.34		X	X		
70.78	0.20	104.	100.	1.3311	2.45	X	X	X		
71.26	0.16	74.	98.	1.3234	1.75	X	X	X		
71.66	0.24	137.	96.	1.3168	3.23	X	X	X		
72.84	0.45	26.	90.	1.2985	0.61	X	X			

60 PEAKS IDENTIFIED 60 CRYSTALLINE 0 AMORPHOUS

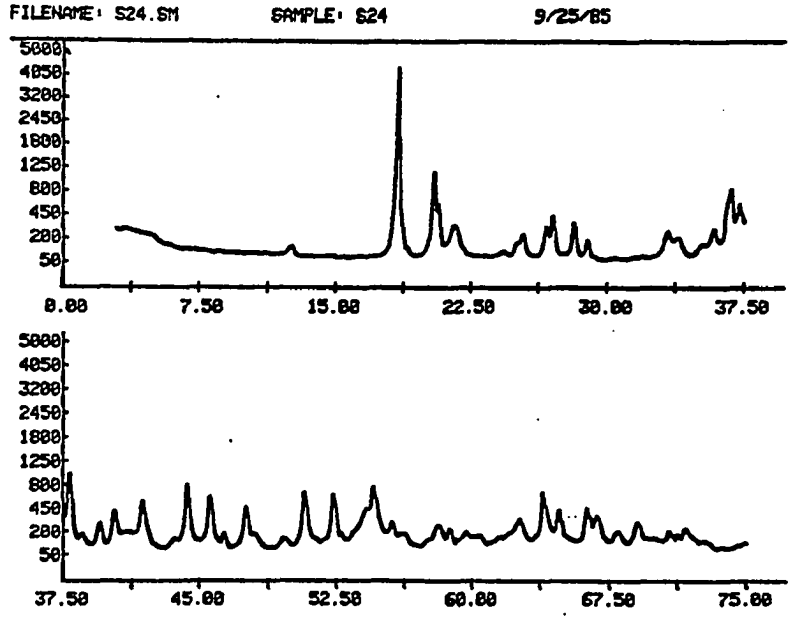

APD-3600 2ND DERIVATIVE PEAK ALGORITHM 11/15/85 15:33:58
RAW DATA FILE : S25.RD
SAMPLE ID : S25
RAW DATA FILE DATE : 11/14/85
GENERATOR SETTINGS : 45 KV 30 MA
STEP SIZE, CNT TIME : 0.020 DEG 0.60 SEC
RANGE OF DATA : 2.000 - 45.000 DEG
RANGE IN D : 44.1716 - 2.0145 A
MAX PEAK CTS, CPS : 1436. CTS 2394. CPS
SECF APPLIED : NONE

2-THETA (DEG)	WIDTH (APPROX)	COUNTS PEAK	COUNTS BKGND	D (ANG)	I (NORM)	LINE TYPE A1	A2	BT	AM	OT
3.68	0.17	62.	156.	24.0418	4.34		x	x		
5.05	0.28	38.	123.	17.5158	2.68					
12.36	0.26	27.	92.	7.1610	1.88					
18.35	0.19	1436.	42.	4.8334	100.00					
20.35	0.15	586.	42.	4.3628	40.77					
20.68	0.11	282.	42.	4.3184	19.65					
21.46	0.58	72.	42.	4.1415	5.03					
24.98	0.34	45.	42.	3.5751	3.13					
25.33	0.29	40.	41.	3.5161	2.76					
26.54	0.23	102.	40.	3.3585	7.10					
26.94	0.21	198.	40.	3.3095	13.87					
28.02	0.19	151.	39.	3.1843	10.53					
28.52	0.18	1218.	38.	3.1256	84.88					
28.84	0.15	77.	37.	3.0962	5.39					
33.16	0.37	52.	35.	2.7012	3.61					
33.62	0.38	46.	35.	2.6648	3.22					
35.09	0.22	38.	32.	2.5573	2.68					
35.69	0.32	77.	32.	2.5136	5.39					
36.45	0.17	231.	31.	2.4652	16.08					
36.65	0.28	357.	31.	2.4519	24.87					
37.15	0.23	164.	30.	2.4197	11.41					
37.74	0.23	454.	30.	2.3833	31.59					
38.46	0.23	68.	29.	2.3406	4.82					
39.37	0.28	125.	28.	2.2883	8.73					
40.23	0.21	164.	27.	2.2416	11.41					
41.73	0.25	216.	26.	2.1647	15.04					
43.43	0.31	37.	28.	2.0836	2.59					
44.26	0.23	335.	37.	2.0466	23.31					

28 PEAKS IDENTIFIED 28 CRYSTALLINE 0 AMORPHOUS
28 PEAKS LISTED

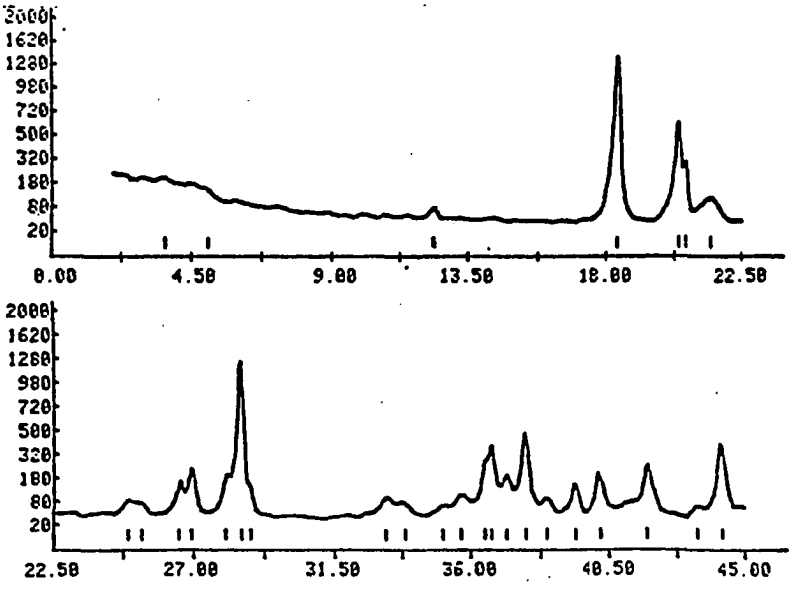

APD-3600 2ND DERIVATIVE PEAK ALGORITHM 10/ 1/85 18:32:58

RAW DATA FILE	: S26.RD
SAMPLE ID	: S26
RAW DATA FILE DATE	: 9/27/85
GENERATOR SETTINGS	: 45 KV 30 MA
STEP SIZE, CNT TIME	: 0.020 DEG 1.20 SEC
RANGE OF DATA	: 2.000 - 45.000 DEG
RANGE IN D	: 44.1716 - 2.0145 A
MAX PEAK CTS, CPS	: 6241. CTS 5205. CPS
SECF APPLIED	: NONE

2-THETA (DEG)	WIDTH (APPROX)	COUNTS PEAK	COUNTS BKGND	D (ANG)	I (NORM)	LINE TYPE A1	A2	BT	AM	OT
3.47	0.43	81.	225.	25.4984	1.30	X	X			
4.97	0.26	31.	185.	17.7578	0.50	X	X			
9.02	0.36	22.	114.	9.7983	0.35	X	X			
12.49	0.27	56.	98.	7.0868	0.90	X	X			
18.45	0.13	6241.	92.	4.8068	100.00	X	X			
20.42	0.17	2016.	96.	4.3491	32.28	X	X			
20.68	0.13	938.	96.	4.2919	14.91	X	X			
21.57	0.24	130.	98.	4.1197	2.08	X	X			
22.09	0.19	76.	98.	4.0239	1.21	X	X			
23.23	0.28	14.	102.	3.8257	0.23	X	X			
24.96	0.25	128.	104.	3.5666	2.05	X	X			
25.40	0.20	90.	102.	3.5059	1.45	X	X			
26.63	0.22	582.	98.	3.3473	9.04	X	X			
27.02	0.19	686.	98.	3.2993	11.00	X	X			
28.09	0.24	520.	94.	3.1771	8.33	X	X			
28.65	0.25	193.	92.	3.0951	3.10	X	X			
31.67	0.30	49.	81.	2.8252	0.79	X	X			
33.26	0.35	177.	79.	2.6941	2.83	X	X			
33.93	0.31	106.	81.	2.6416	1.70	X	X			
35.06	0.32	85.	86.	2.5594	1.36	X	X			
35.82	0.29	204.	90.	2.5068	3.28	X	X			
36.51	0.12	745.	92.	2.4613	11.94	X	X			
36.75	0.19	1253.	94.	2.4455	20.08	X	X			
37.18	0.15	538.	96.	2.4179	8.62	X	X			
37.81	0.23	1444.	98.	2.3793	23.14	X	X			
38.52	0.26	164.	102.	2.3368	2.63	X	X			
39.44	0.29	376.	106.	2.2847	6.03	X	X			
40.25	0.24	576.	110.	2.2405	9.23	X	X			
41.63	0.31	734.	117.	2.1595	11.77	X	X			
44.31	0.28	1197.	161.	2.0442	19.18	X	X			

38 PEAKS IDENTIFIED 38 CRYSTALLINE 0 AMORPHOUS
38 PEAKS LISTED

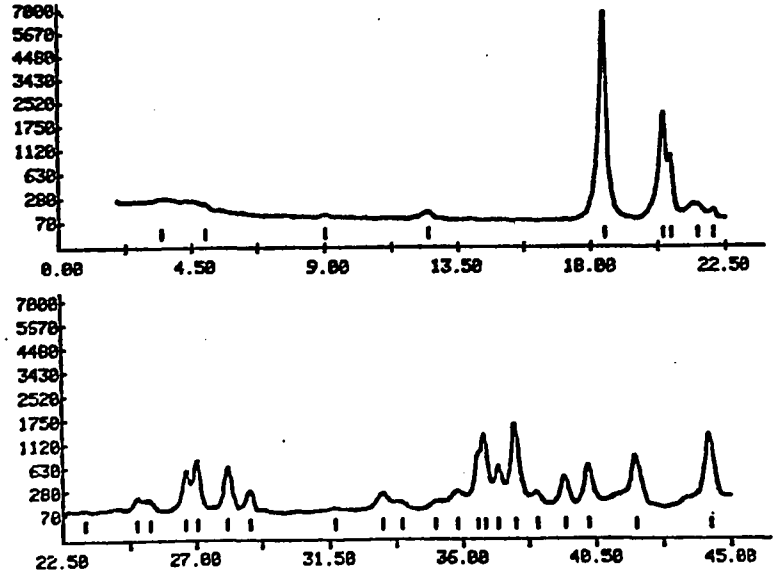

APD-3600 2ND DERIVATIVE PEAK ALGORITHM 10/ 1/85 10:39:39

RAW DATA FILE	: S27.RD
SAMPLE ID	: S27
RAW DATA FILE DATE	: 9/27/85
GENERATOR SETTINGS	: 45 KV 30 MA
STEP SIZE, CNT TIME	: 0.020 DEG 1.20 SEC
RANGE OF DATA	: 2.000 - 45.000 DEG
RANGE IN D	: 44.1716 - 2.0145 A
MAX PEAK CTS, CPS	: 17371. CTS 14488. CPS
SECF APPLIED	: NONE

2-THETA (DEG)	WIDTH (APPROX)	COUNTS PEAK	COUNTS BKGND	D (ANG)	I (NORM)	LINE TYPE A1	A2	BT	AM	OT
12.45	0.28	55.	94.	7.1066	0.32		X	X		
18.02	0.12	538.	88.	4.9225	3.10		X	X		
18.42	0.14	17371.	88.	4.8165	100.00		X	X		
20.48	0.15	1815.	90.	4.3343	10.45		X	X		
20.65	0.13	708.	90.	4.3011	4.07		X	X		
21.48	0.58	130.	92.	4.1368	0.75		X	X		
24.26	0.28	37.	90.	3.6694	0.21		X	X		
24.97	0.36	100.	88.	3.5659	0.58		X	X		
25.32	0.29	149.	88.	3.5168	0.86		X	X		
26.60	0.20	358.	85.	3.3516	2.01		X	X		
26.99	0.19	640.	85.	3.3029	3.68		X	X		
28.11	0.19	475.	81.	3.1743	2.74		X	X		
28.80	0.24	213.	79.	3.0993	1.23		X	X		
33.23	0.37	228.	88.	2.6964	1.31		X	X		
33.92	0.21	98.	90.	2.6427	0.56		X	X		
35.76	0.29	234.	90.	2.5105	1.35		X	X		
36.48	0.13	697.	92.	2.4633	4.01		X	X		
36.72	0.21	1096.	92.	2.4474	6.31		X	X		
37.18	0.14	1076.	92.	2.4185	6.19		X	X		
37.77	0.23	1376.	92.	2.3814	7.92		X	X		
38.46	0.25	130.	94.	2.3406	0.75		X	X		
39.40	0.24	331.	94.	2.2872	1.91		X	X		
40.22	0.25	552.	94.	2.2421	3.18		X	X		
41.76	0.24	635.	96.	2.1627	3.66		X	X		
41.98	0.12	441.	96.	2.1568	2.54					
43.47	0.24	100.	118.	2.0817	0.58		X	X		
44.27	0.18	1056.	125.	2.0457	6.08		X	X		

27 PEAKS IDENTIFIED 27 CRYSTALLINE 0 AMORPHOUS
27 PEAKS LISTED

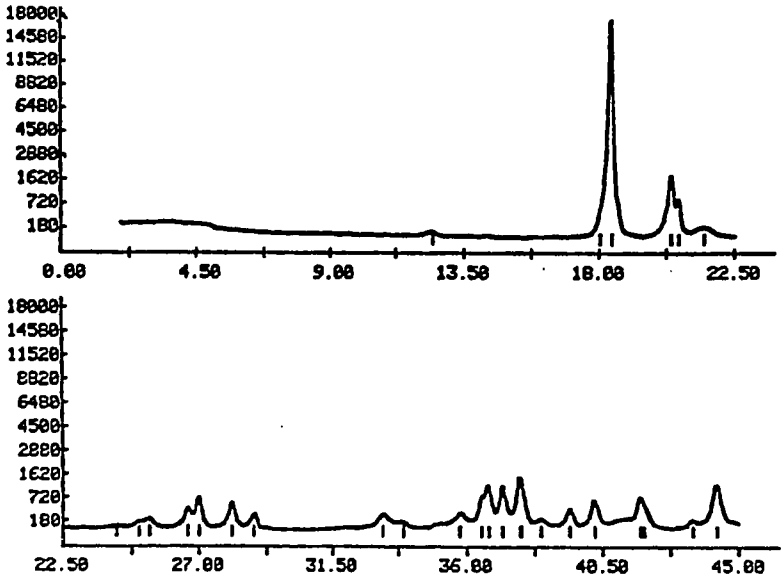

APD-3600 2ND DERIVATIVE PEAK ALGORITHM 11/15/85 15:40: 8
RAW DATA FILE : S28.RD
SAMPLE ID : S28
RAW DATA FILE DATE : 11/14/85
GENERATOR SETTINGS : 45 KV 30 MA
STEP SIZE, CNT TIME : 0.020 DEG 0.60 SEC
RANGE OF DATA : 2.000 - 45.000 DEG
RANGE IN D : 44.1716 - 2.0145 A
MAX PEAK CTS, CPS : 4789. CTS 7981. CPS
SECF APPLIED : NONE

2-THETA (DEG)	WIDTH (APPROX)	COUNTS PEAK	COUNTS BKGND	D (ANG)	I (NORM)	LINE TYPE A1	A2	BT	AM	OT
12.37	0.29	25.	49.	7.1524	0.52	x	x			
18.38	0.13	4789.	44.	4.8269	100.00	x	x	x	x	
20.35	0.16	767.	44.	4.3628	16.02	x	x	x	x	
20.62	0.12	324.	44.	4.3073	6.77	x	x	x	x	
21.49	0.43	64.	44.	4.1358	1.34	x	x	x	x	
24.18	0.24	18.	41.	3.6814	0.39	x	x	x	x	
25.38	0.22	56.	38.	3.5282	1.17	x	x	x	x	
26.56	0.20	142.	37.	3.3568	2.96	x	x	x	x	
26.99	0.20	202.	36.	3.3041	4.21	x	x	x	x	
28.85	0.21	193.	35.	3.1004	4.03	x	x	x	x	
28.52	0.12	999.	35.	3.1296	20.85	x	x	x	x	
28.82	0.13	83.	34.	3.0977	1.73	x	x	x	x	
33.28	0.35	81.	35.	2.6908	1.69	x	x	x	x	
33.85	0.32	52.	35.	2.6484	1.08	x	x	x	x	
35.73	0.24	90.	34.	2.5129	1.88	x	x	x	x	
36.45	0.15	256.	34.	2.4649	5.35	x	x	x	x	
36.69	0.21	420.	34.	2.4493	8.78	x	x	x	x	
37.19	0.19	234.	34.	2.4175	4.89	x	x	x	x	
37.75	0.15	506.	34.	2.3838	10.57	x	x	x	x	
38.43	0.24	58.	34.	2.3423	1.21	x	x	x	x	
39.37	0.28	121.	32.	2.2886	2.53	x	x	x	x	
40.18	0.29	210.	32.	2.2448	4.39	x	x	x	x	
41.76	0.32	240.	32.	2.1629	5.02	x	x	x	x	
43.43	0.31	36.	35.	2.0836	0.75	x	x	x	x	
44.23	0.24	392.	44.	2.0477	8.19	x	x			

23 PEAKS IDENTIFIED 25 CRYSTALLINE 0 AMORPHOUS
25 PEAKS LISTED

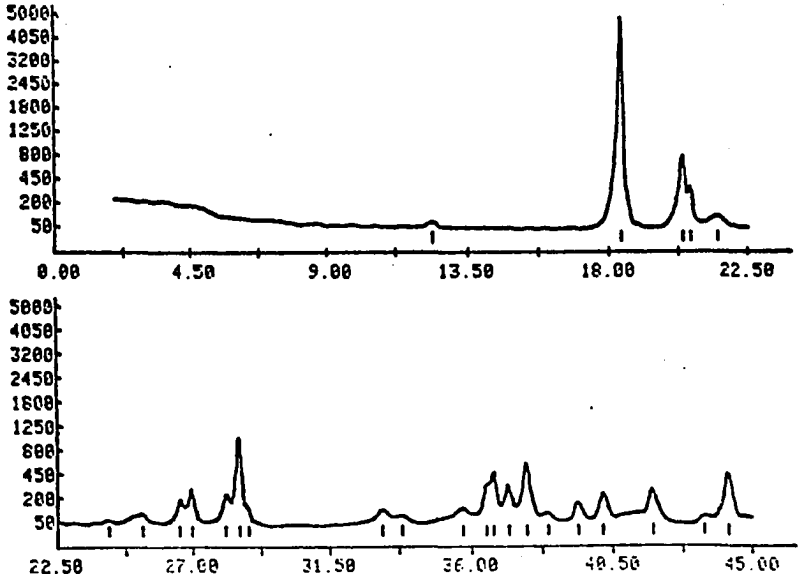

APD-3600 2ND DERIVATIVE PEAK ALGORITHM 11/15/85 15:46:17

RAW DATA FILE	: S29.RD
SAMPLE ID	: S29
RAW DATA FILE DATE	: 11/14/85
GENERATOR SETTINGS	: 45 KV 30 MA
STEP SIZE, CNT TIME	: 0.020 DEG 0.60 SEC
RANGE OF DATA	: 2.000 - 45.000 DEG
RANGE IN D	: 44.1716 - 2.0145 A
MAX PEAK CTS, CPS	: 3733. CTS 6222. CPS
SECF APPLIED	: NONE

2-THETA (DEG)	WIDTH (APPROX)	COUNTS PEAK	COUNTS BKGND	D (ANG)	I (NORM)	LINE TYPE A1	A2	BT	AM	OT
3.66	0.36	45.	177.	24.1483	1.20	X	X			
5.00	0.37	26.	130.	17.6733	0.70	X	X			
10.41	0.15	3733.	42.	4.8191	100.00	X	X			
20.38	0.17	595.	44.	4.3565	15.95	X	X			
20.63	0.13	299.	44.	4.3011	8.02	X	X			
21.52	0.42	52.	44.	4.1282	1.39	X	X			
24.18	0.34	28.	44.	3.6806	0.54	X	X			
25.36	0.48	25.	42.	3.5128	0.67	X	X			
26.59	0.21	102.	40.	3.3523	2.73	X	X			
26.99	0.19	207.	40.	3.3041	5.55	X	X			
28.07	0.19	151.	38.	3.1793	4.05	X	X			
28.54	0.17	1325.	38.	3.1278	35.49	X	X			
29.24	0.24	20.	37.	3.0537	0.54	X	X			
33.22	0.35	83.	38.	2.6968	2.22	X	X			
33.91	0.29	37.	38.	2.6431	1.00	X	X			
35.77	0.33	90.	36.	2.5099	2.42	X	X			
36.62	0.45	292.	36.	2.4542	7.83	X	X			
37.21	0.19	306.	35.	2.4163	8.20	X	X			
37.79	0.19	445.	35.	2.3802	11.93	X	X			
38.48	0.31	46.	34.	2.3394	1.24	X	X			
39.48	0.31	186.	32.	2.2872	2.84	X	X			
40.21	0:30	177.	32.	2.2429	4.74	X	X			
41.79	0.32	259.	30.	2.1617	6.94	X	X			
44.26	0.32	339.	46.	2.0462	9.07	X	X			

24 PEAKS IDENTIFIED 24 CRYSTALLINE 0 AMORPHOUS
24 PEAKS LISTED

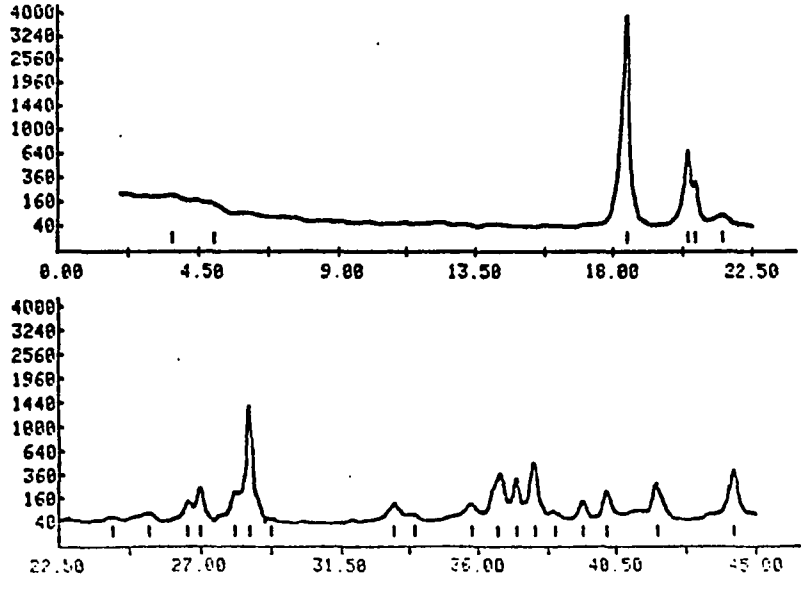

APD-3600 2ND DERIVATIVE PEAK ALGORITHM 11/15/85 16:20:21

RAW DATA FILE	: S210.RD
SAMPLE ID	: S210
RAW DATA FILE DATE	: 11/14/85
GENERATOR SETTINGS	: 45 KV 30 MA
STEP SIZE, CNT TIME	: 0.020 DEG 0.60 SEC
RANGE OF DATA	: 2.000 - 45.000 DEG
RANGE IN D	: 44.1716 - 2.0145 A
MAX PEAK CTS, CPS	: 3770. CTS 6283. CPS
SECF APPLIED	: NONE

2-THETA (DEG)	WIDTH (APPROX)	COUNTS PEAK	COUNTS BKGND	D (ANG)	I (NORM)	LINE TYPE A1	A2	BT	AM	OT
12.37	0.48	4.	52.	7.1524	0.12	x	x			
18.34	0.19	3770.	44.	4.8387	100.00	x	x			
20.32	0.18	524.	42.	4.3702	13.91	x	x			
20.59	0.13	231.	42.	4.3135	6.13	x	x			
21.43	0.58	59.	42.	4.1463	1.57	x	x			
24.13	0.35	40.	37.	3.6874	1.05	x	x			
25.29	0.26	32.	34.	3.5209	0.86	x	x			
26.52	0.24	79.	32.	3.3609	2.10	x	x			
26.93	0.21	164.	32.	3.3107	4.35	x	x			
28.01	0.24	121.	32.	3.1868	3.21	x	x			
28.49	0.16	870.	32.	3.1334	23.08	x	x			
30.22	0.31	15.	32.	2.9573	0.40	x	x			
33.15	0.35	132.	37.	2.7024	3.51	x	x			
33.62	0.26	25.	37.	2.5619	0.66	x	x			
35.63	0.33	132.	37.	2.5197	3.51	x	x			
36.59	0.37	289.	37.	2.4558	7.67	x	x			
37.13	0.25	237.	37.	2.4216	6.29	x	x			
37.71	0.23	369.	37.	2.3857	9.78	x	x			
39.33	0.33	67.	37.	2.2900	1.78	x	x			
40.16	0.30	149.	37.	2.2451	3.95	x	x			
41.73	0.32	159.	37.	2.1647	4.21	x	x			
43.41	0.31	30.	37.	2.0845	0.80	x	x			
44.22	0.30	328.	37.	2.0482	8.69	x	x			

23 PEAKS IDENTIFIED 23 CRYSTALLINE 0 AMORPHOUS

23 PEAKS LISTED

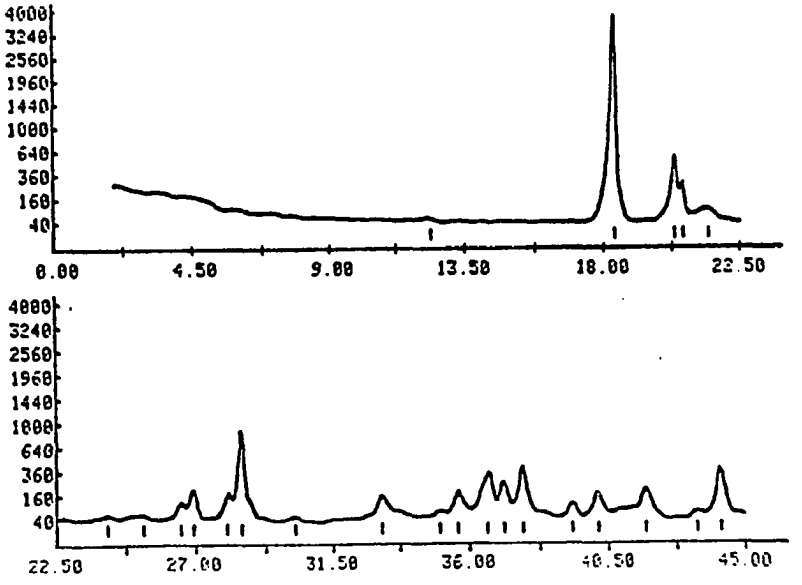

APD-3600 2ND DERIVATIVE PEAK ALGORITHM 11/15/85 16:26:18

RAW DATA FILE	: S211.RD
SAMPLE ID	: S211
RAW DATA FILE DATE	: 11/14/85
GENERATOR SETTINGS	: 45 KV 30 MA
STEP SIZE, CNT TIME	: 0.020 DEG 0.60 SEC
RANGE OF DATA	: 2.000 - 45.000 DEG
RANGE IN D	: 44.1716 - 2.0145 A
MAX PEAK CTS, CPS	: 1998. CTS 3330. CPS
SECF APPLIED	: NONE

2-THETA (DEG)	WIDTH (APPROX)	COUNTS PEAK	COUNTS BKGND	D (ANG)	I (NORM)	LINE TYPE A1	A2	BT	AM	OT
3.51	0.51	149.	92.	25.1716	7.45	X				X
5.10	0.36	79.	85.	17.3101	3.96	X				X
12.38	0.41	71.	55.	7.1466	3.53	X				X
18.36	0.20	1998.	45.	4.8321	100.00	X				X
20.35	0.19	376.	42.	4.3649	18.84	X				X
20.62	0.12	210.	42.	4.3084	10.52	X				X
21.48	0.31	98.	41.	4.1538	4.91	X				X
24.18	0.36	69.	37.	3.6799	3.45	X				X
24.90	0.35	100.	37.	3.5758	5.00	X				X
26.54	0.24	92.	36.	3.3578	4.61	X				X
26.97	0.25	130.	36.	3.3059	6.50	X				X
28.05	0.31	114.	37.	3.1804	5.73	X				X
28.79	0.40	46.	38.	3.1009	2.31	X				X
30.29	0.36	35.	40.	2.9507	1.74	X				X
33.19	0.33	180.	42.	2.6992	8.99	X				X
35.02	0.38	52.	45.	2.5619	2.59	X				X
35.71	0.25	243.	45.	2.5146	12.18	X				X
36.63	0.32	228.	46.	2.4532	11.41	X				X
37.16	0.21	172.	46.	2.4191	8.59	X				X
37.76	0.26	276.	48.	2.3824	13.79	X				X
38.49	0.25	92.	48.	2.3391	4.61	X				X
39.37	0.32	85.	49.	2.2888	4.24	X				X
40.18	0.29	110.	50.	2.2448	5.52	X				X
41.82	0.41	59.	50.	2.2002	2.97	X				X
41.79	0.37	110.	52.	2.1617	5.52	X				X
43.37	0.29	20.	53.	2.0863	1.01	X				X
44.24	0.30	204.	55.	2.0471	10.23	X				X

27 PEAKS IDENTIFIED 27 CRYSTALLINE 0 AMORPHOUS
27 PEAKS LISTED

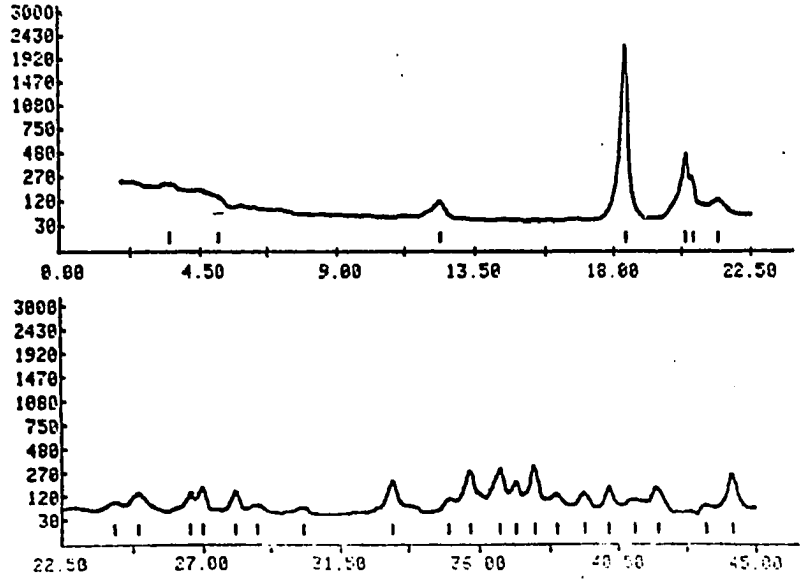

APD-3600 2ND DERIVATIVE PEAK ALGORITHM 11/15/85 16:32: 2

RAW DATA FILE	: S213.RD
SAMPLE ID	: S213
RAW DATA FILE DATE	: 11/14/85
GENERATOR SETTINGS	: 45 KV 30 MA
STEP SIZE, CNT TIME	: 0.020 DEG 0.60 SEC
RANGE OF DATA	: 2.000 - 45.000 DEG
RANGE IN D	: 44.1716 - 2.0145 A
MAX PEAK CTS, CPS	: 598. CTS 984. CPS
SECF APPLIED	: NONE

2-THETA (DEG)	WIDTH (APPROX)	COUNTS PEAK	COUNTS BKGND	D (ANG)	I (NORM)	LINE TYPE A1	A2	BT	AM	OT
12.41	0.53	53.	49.	7.1294	9.82	X	X			
18.45	0.19	550.	44.	4.8100	100.00	X	X			
20.43	0.28	154.	42.	4.3478	26.04	X	X			
21.46	0.37	151.	41.	4.1396	25.62	X	X			
24.98	0.35	83.	40.	3.5652	14.82	X	X			
26.60	0.29	41.	38.	3.3504	6.94	X	X			
27.06	0.21	38.	38.	3.2951	6.51	X	X			
28.16	0.33	22.	37.	3.1688	3.74	X	X			
30.37	0.25	49.	31.	2.9431	8.38	X	X			
33.35	0.55	98.	29.	2.6870	16.68	X	X			
35.08	0.36	96.	29.	2.5580	16.26	X	X			
35.75	0.28	182.	29.	2.5116	30.86	X	X			
36.77	0.37	182.	29.	2.4439	30.86	X	X			
37.15	0.36	172.	29.	2.4201	29.06	X	X			
37.81	0.25	106.	29.	2.3793	17.97	X	X			
38.56	0.35	72.	29.	2.3348	12.24	X	X			
39.41	0.35	53.	29.	2.2861	9.02	X	X			
40.26	0.43	62.	29.	2.2408	10.57	X	X			
41.82	0.39	66.	29.	2.1597	11.11	X	X			
43.43	0.39	30.	29.	2.0836	5.12	X	X			
44.30	0.29	46.	29.	2.0444	7.83	X	X			

21 PEAKS IDENTIFIED 21 CRYSTALLINE 0 AMORPHOUS
21 PEAKS LISTED

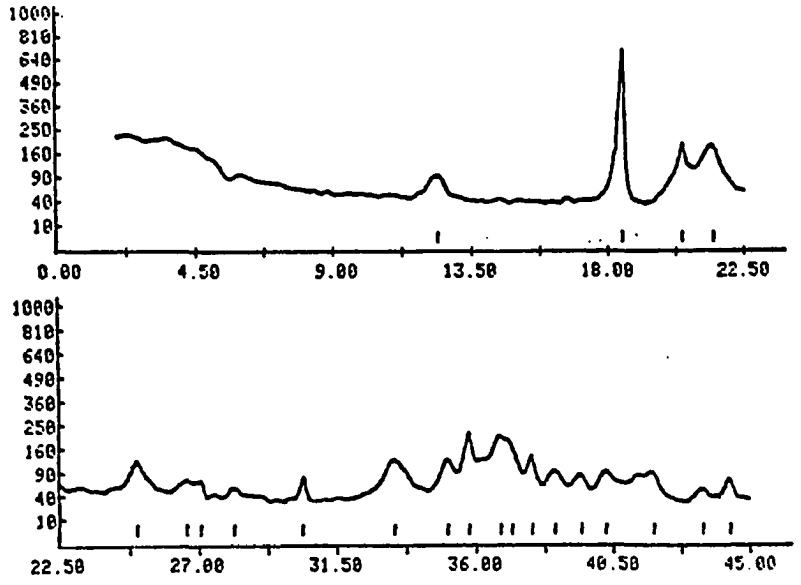

APD-3600 2ND DERIVATIVE PEAK ALGORITHM 10/ 1/85 12: 7: 5

RAW DATA FILE	: S41.RD
SAMPLE ID	: S41
RAW DATA FILE DATE	: 9/27/85
GENERATOR SETTINGS	: 45 KV 30 MA
STEP SIZE, CNT TIME	: 0.020 DEG 1.20 SEC
RANGE OF DATA	: 2.000 - 45.000 DEG
RANGE IN D	: 44.1716 - 2.0145 A
MAX PEAK CTS, CPS	: 2107. CTS 1757. CPS
SECF APPLIED	: NONE

2-THETA (DEG)	WIDTH (APPROX)	COUNTS PEAK	COUNTS BKGND	D (ANG)	I (NORM)	LINE TYPE A1	A2	BT	AM	OT
3.65	0.35	42.	296.	24.1734	2.01	X	X			
12.40	0.42	108.	100.	7.1409	5.13	X	X			
18.36	0.19	2107.	92.	4.8256	100.00	X	X			
20.36	0.18	847.	104.	4.3617	40.19	X	X			
20.64	0.13	428.	106.	4.3032	20.34	X	X			
20.99	0.12	188.	100.	4.2332	8.91	X	X			
21.37	0.24	182.	110.	4.1578	8.65	X	X			
24.94	0.29	169.	117.	3.5702	8.02	X	X			
25.35	0.28	83.	112.	3.5127	3.93	X	X			
26.68	0.25	515.	104.	3.3418	24.46	X	X			
27.01	0.14	246.	102.	3.3017	11.70	X	X			
28.08	0.25	177.	94.	3.1777	8.40	X	X			
28.80	0.25	90.	88.	3.0993	4.28	X	X			
30.34	0.29	15.	83.	2.9464	0.72	X	X			
33.24	0.39	210.	92.	2.6952	9.98	X	X			
35.05	0.24	144.	94.	2.5597	6.83	X	X			
35.73	0.32	276.	94.	2.5133	13.08	X	X			
36.63	0.32	660.	94.	2.4516	31.35	X	X			
37.18	0.25	317.	96.	2.4185	15.04	X	X			
37.74	0.24	640.	96.	2.3833	30.38	X	X			
38.46	0.29	177.	96.	2.3403	8.40	X	X			
39.40	0.36	210.	96.	2.2872	9.98	X	X			
40.21	0.31	282.	98.	2.2424	13.40	X	X			
41.01	0.35	86.	98.	2.2010	4.11	X	X			
41.77	0.32	310.	98.	2.1625	14.70	X	X			
42.54	0.25	32.	100.	2.1248	1.54	X	X			
43.43	0.32	42.	100.	2.0836	2.01	X	X			
44.24	0.22	529.	100.	2.0473	25.11	X	X			
23.50	6.94	117.	0.	3.7850						X

29 PEAKS IDENTIFIED 28 CRYSTALLINE 1 AMORPHOUS
29 PEAKS LISTED

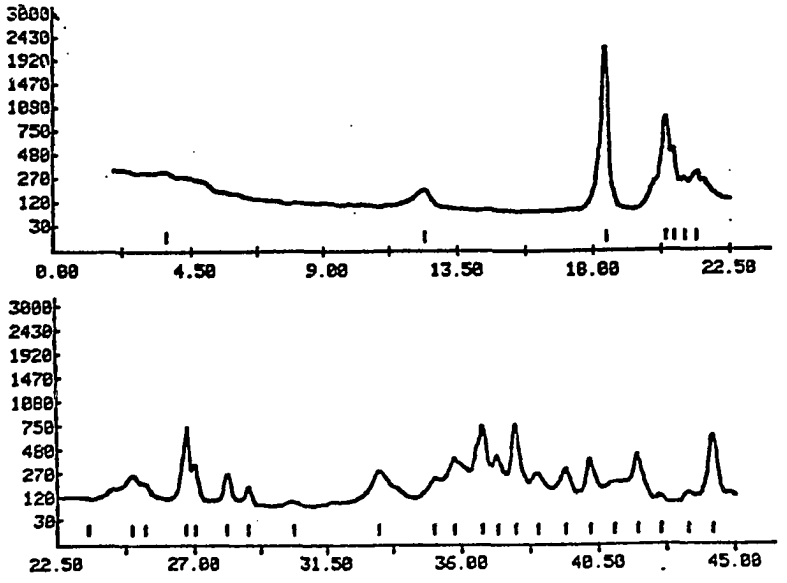

APD-3600 2ND DERIVATIVE PEAK ALGORITHM 10/ 1/85 12:15:58
RAW DATA FILE : S42.RD
SAMPLE ID : S42
RAW DATA FILE DATE : 9/27/85
GENERATOR SETTINGS : 45 KV 30 MA
STEP SIZE, CNT TIME : 0.020 DEG 1.20 SEC
RANGE OF DATA : 2.000 - 45.000 DEG
RANGE IN D : 44.1716 - 2.0145 A
MAX PEAK CTS, CPS : 1274. CTS 1063. CPS
SECF APPLIED : NONE

2-THETA (DEG)	WIDTH (APPROX)	COUNTS PEAK	COUNTS BKGND	D (ANG)	I (NORM)	LINE TYPE A1	A2	BT	AM	OT
3.63	0.55	64.	282.	24.3398	5.02	X	X			
12.35	0.27	161.	108.	7.1639	12.66	X	X			
18.38	0.18	1274.	66.	4.8256	100.00	X	X			
19.93	0.15	196.	77.	4.4549	15.38	X	X			
20.40	0.11	671.	88.	4.3543	52.63	X	X			
20.65	0.12	488.	94.	4.3022	31.39	X	X			
21.35	0.27	231.	112.	4.1607	18.13	X	X			
21.88	0.23	207.	128.	4.0621	16.27	X	X			
23.23	0.30	26.	154.	3.8298	2.04	X	X			
24.96	0.36	210.	146.	3.5681	16.50	X	X			
26.66	0.21	219.	123.	3.3436	17.19	X	X			
27.00	0.17	161.	117.	3.3023	12.66	X	X			
28.07	0.25	128.	100.	3.1782	10.02	X	X			
28.81	0.19	66.	88.	3.0988	5.15	X	X			
30.30	0.26	42.	83.	2.9497	3.32	X	X			
33.21	0.37	266.	86.	2.6976	20.85	X	X			
35.07	0.23	196.	86.	2.5583	15.38	X	X			
35.73	0.26	412.	86.	2.5133	32.33	X	X			
36.64	0.31	416.	86.	2.4526	32.65	X	X			
37.18	0.28	222.	86.	2.4182	17.42	X	X			
37.74	0.18	497.	86.	2.3836	39.02	X	X			
38.48	0.31	237.	86.	2.3397	18.61	X	X			
39.39	0.44	202.	86.	2.2874	15.82	X	X			
40.21	0.27	219.	86.	2.2427	17.19	X	X			
41.07	0.37	139.	86.	2.1977	10.93	X	X			
41.79	0.25	231.	86.	2.1617	18.13	X	X			
43.43	0.19	45.	94.	2.0833	3.52	X	X			
44.28	0.30	346.	108.	2.0455	27.15	X	X			
24.25	6.19	149.	0.	3.6702						X

29 PEAKS IDENTIFIED 28 CRYSTALLINE 1 AMORPHOUS
29 PEAKS LISTED

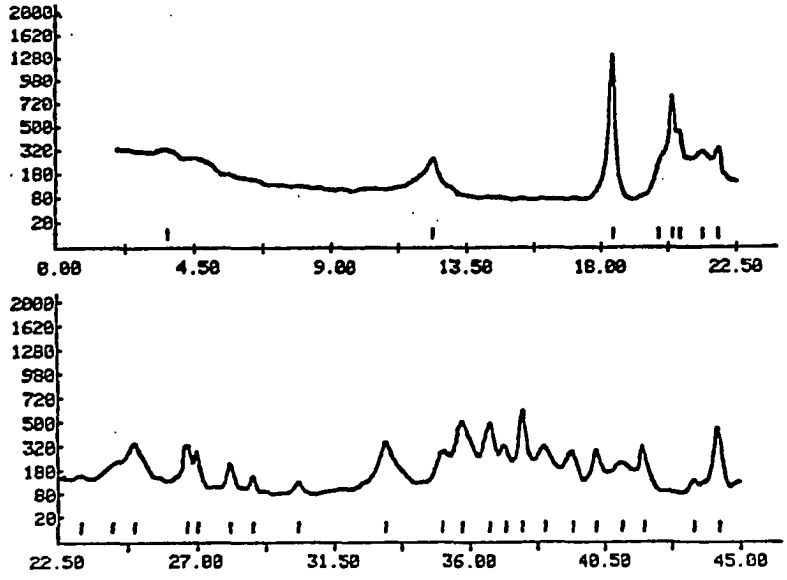

APD-3600 2ND DERIVATIVE PEAK ALGORITHM 10/ 1/85 12:22:22
RAW DATA FILE : S44.RD
SAMPLE ID : S44
RAW DATA FILE DATE : 9/28/85
GENERATOR SETTINGS : 45 KV 30 MA
STEP SIZE, CNT TIME : 0.020 DEG 1.20 SEC
RANGE OF DATA : 2.000 - 45.000 DEG
RANGE IN D : 44.1716 - 2.0145 A
MAX PEAK CTS, CPS : 2421. CTS 2019. CPS
SECF APPLIED : NONE

2-THETA (DEG)	WIDTH (APPROX)	COUNTS PEAK	COUNTS BKGND	D (ANG)	I (NORM)	LINE TYPE A1	A2	BT	AM	DT
4.87	0.38	66.	188.	18.1448	2.71	X	X			
12.44	0.32	108.	102.	7.1100	4.47	X	X			
18.40	0.17	2421.	74.	4.8230	100.00	X	X			
20.40	0.16	1204.	71.	4.3543	49.74	X	X			
20.63	0.11	615.	72.	4.3053	25.41	X	X			
21.63	0.12	515.	74.	4.1084	21.29	X	X			
22.84	0.17	262.	74.	4.0338	10.84	X	X			
23.32	0.27	94.	76.	3.8136	3.89	X	X			
24.90	0.40	182.	77.	3.5751	7.53	X	X			
26.63	0.25	256.	81.	3.3479	10.58	X	X			
26.99	0.18	339.	81.	3.3035	13.99	X	X			
27.48	0.18	100.	83.	3.2457	4.13	X	X			
28.09	0.21	282.	83.	3.1766	11.66	X	X			
28.79	0.23	119.	85.	3.1004	4.91	X	X			
30.28	0.25	98.	86.	2.9516	4.05	X	X			
31.49	0.35	36.	94.	2.8409	1.49	X	X			
33.18	0.35	196.	102.	2.6996	8.10	X	X			
35.04	0.30	166.	100.	2.5612	6.87	X	X			
35.74	0.29	543.	100.	2.5126	22.43	X	X			
36.46	0.14	428.	100.	2.4646	17.70	X	X			
36.68	0.26	655.	100.	2.4503	27.07	X	X			
37.19	0.23	276.	102.	2.4175	11.38	X	X			
37.76	0.17	876.	102.	2.3827	36.20	X	X			
38.47	0.33	225.	102.	2.3400	9.30	X	X			
39.38	0.30	262.	102.	2.2877	10.84	X	X			
40.21	0.21	369.	104.	2.2424	15.23	X	X			
41.02	0.39	112.	104.	2.2000	4.64	X	X			
41.77	0.22	346.	104.	2.1625	14.29	X	X			
43.43	0.26	76.	106.	2.0833	3.13	X	X			
44.26	0.27	639.	108.	2.0464	26.83	X	X			

30 PEAKS IDENTIFIED 30 CRYSTALLINE 0 AMORPHOUS
30 PEAKS LISTED

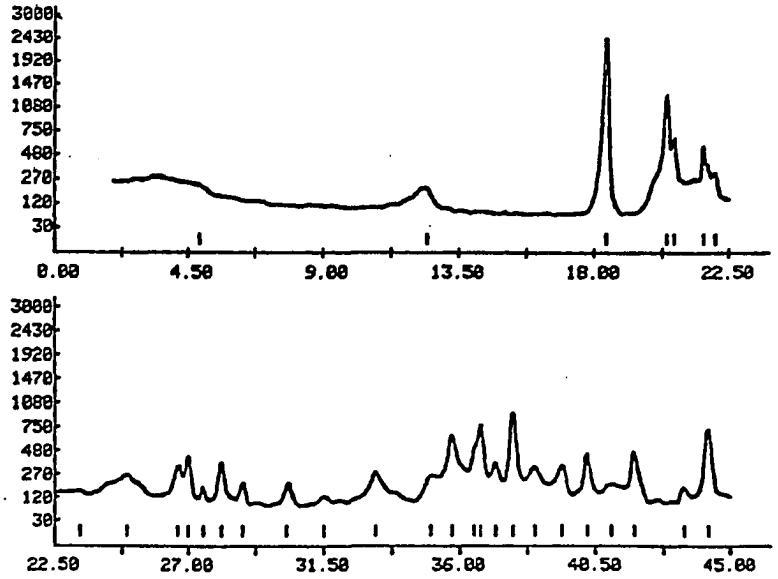

APD-3600 2ND DERIVATIVE PEAK ALGORITHM 10/ 1/85 12:27:53

RAW DATA FILE	: S45.RD
SAMPLE ID	: S45
RAW DATA FILE DATE	: 9/28/85
GENERATOR SETTINGS	: 45 KV 30 MA
STEP SIZE, CNT TIME	: 0.020 DEG 1.20 SEC
RANGE OF DATA	: 2.000 - 45.000 DEG
RANGE IN D	: 44.1716 - 2.0145 A
MAX PEAK CTS, CPS	: 6416. CTS 5351. CPS
SECF APPLIED	: NONE

2-THETA (DEG)	WIDTH (APPROX)	COUNTS PEAK	COUNTS BKGND	D (ANG)	I (NORM)	LINE TYPE A1	A2	BT	AM	OT
3.61	0.32	31.	289.	24.4408	0.49	x	x			
18.35	0.15	6416.	81.	4.8334	100.00	x	x			
20.32	0.16	2362.	79.	4.3692	36.81	x	x			
20.59	0.13	1102.	79.	4.3135	17.18	x	x			
21.98	0.19	350.	79.	4.0447	5.45	x	x			
25.55	0.35	86.	77.	3.4863	1.35	x	x			
26.54	0.24	445.	76.	3.3591	6.94	x	x			
26.94	0.17	801.	76.	3.3095	12.48	x	x			
28.84	0.19	615.	76.	3.1827	9.59	x	x			
28.76	0.23	292.	76.	3.1041	4.56	x	x			
30.28	0.24	128.	76.	2.9516	1.99	x	x			
31.45	0.32	40.	77.	2.8449	0.62	x	x			
33.16	0.35	125.	81.	2.7016	1.96	x	x			
33.85	0.30	76.	83.	2.6481	1.18	x	x			
35.02	0.27	100.	85.	2.5619	1.56	x	x			
35.69	0.23	497.	85.	2.5156	7.75	x	x			
36.42	0.12	882.	86.	2.4669	13.75	x	x			
36.66	0.19	1362.	86.	2.4510	21.22	x	x			
37.13	0.19	475.	88.	2.4213	7.41	x	x			
37.73	0.23	1815.	88.	2.3845	28.28	x	x			
38.37	0.18	180.	90.	2.3456	2.80	x	x			
39.37	0.24	445.	92.	2.2888	6.94	x	x			
40.16	0.24	702.	94.	2.2453	10.95	x	x			
41.74	0.30	778.	96.	2.1637	12.13	x	x			
43.38	0.29	149.	114.	2.0856	2.32	x	x			
44.20	0.22	1406.	133.	2.0498	21.92	x	x			
44.84	0.19	74.	154.	2.0213	1.15	x	x			

27 PEAKS IDENTIFIED 27 CRYSTALLINE 0 AMORPHOUS
27 PEAKS LISTED

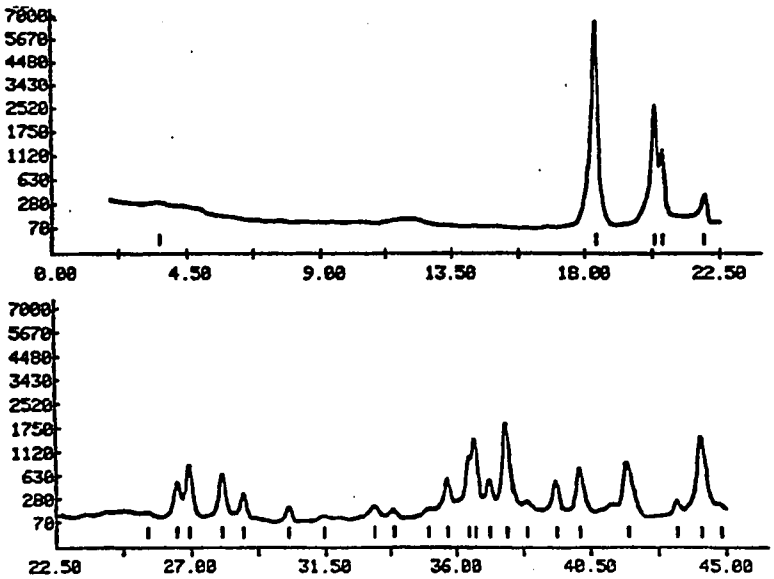

APD-3600 2ND DERIVATIVE PEAK ALGORITHM 10/ 1/85 12:33:45

RAW DATA FILE	S46.RD
SAMPLE ID	S46
RAW DATA FILE DATE	9/28/85
GENERATOR SETTINGS	45 KV 30 MA
STEP SIZE, CNT TIME	0.020 DEG 1.20 SEC
RANGE OF DATA	2.000 - 45.000 DEG
RANGE IN D	44.1716 - 2.0145 A
MAX PEAK CTS, CPS	2200. CTS 1835. CPS
SECF APPLIED	NONE

2-THETA (DEG)	WIDTH (APPROX)	COUNTS PEAK	COUNTS BKGND	D (ANG)	I (NORM)	LINE TYPE A1	A2	BT	AM	OT
3.55	0.45	44.	266.	24.8881	1.98	X	X			
12.42	0.27	119.	112.	7.1266	5.40	X	X	X	X	
18.48	0.19	2200.	79.	4.8217	100.00	X	X	X	X	
20.41	0.15	999.	77.	4.3512	45.40	X	X	X	X	
20.69	0.15	557.	77.	4.2939	25.32	X	X	X	X	
22.84	0.25	240.	79.	4.8328	10.92	X	X	X	X	
23.35	0.31	88.	81.	3.8087	4.02	X	X	X	X	
24.25	0.32	156.	83.	3.6782	7.10	X	X	X	X	
24.96	0.31	210.	83.	3.5681	9.56	X	X	X	X	
26.64	0.23	296.	85.	3.3461	13.45	X	X	X	X	
27.01	0.19	320.	86.	3.3005	14.57	X	X	X	X	
28.15	0.15	256.	86.	3.1705	11.64	X	X	X	X	
28.84	0.38	100.	88.	3.0962	4.55	X	X	X	X	
30.35	0.38	64.	90.	2.9445	2.91	X	X	X	X	
31.57	0.14	41.	98.	2.8335	1.86	X	X	X	X	
33.24	0.29	259.	112.	2.6956	11.78	X	X	X	X	
35.03	0.31	139.	117.	2.5615	6.33	X	X	X	X	
35.74	0.29	520.	114.	2.5126	23.63	X	X	X	X	
36.48	0.12	437.	112.	2.4633	19.86	X	X	X	X	
36.68	0.25	543.	110.	2.4497	24.68	X	X	X	X	
37.21	0.21	292.	110.	2.4166	13.29	X	X	X	X	
37.79	0.19	762.	108.	2.3805	34.63	X	X	X	X	
38.49	0.25	204.	106.	2.3391	9.30	X	X	X	X	
39.42	0.32	259.	104.	2.2858	11.78	X	X	X	X	
40.23	0.28	328.	102.	2.2416	14.89	X	X	X	X	
41.01	0.36	128.	100.	2.2018	5.81	X	X	X	X	
41.80	0.27	361.	98.	2.1607	16.41	X	X	X	X	
43.46	0.26	69.	100.	2.0822	3.13	X	X	X	X	
44.29	0.25	566.	125.	2.0453	25.75	X	X	X	X	
35.00	6.62	112.	0.	2.5636						X

30 PEAKS IDENTIFIED 29 CRYSTALLINE 1 AMORPHOUS
30 PEAKS LISTED

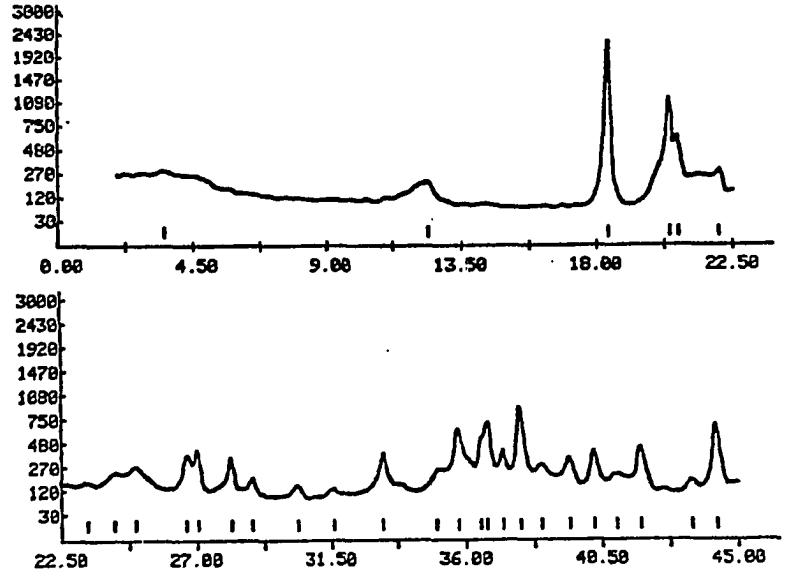

APD-3600 2ND DERIVATIVE PEAK ALGORITHM 10/ 1/85 12:39:37
RAW DATA FILE : S47.RD
SAMPLE ID : S47
RAW DATA FILE DATE : 9/28/85
GENERATOR SETTINGS : 45 KV 30 MA
STEP SIZE, CNT TIME : 0.020 DEG 1.20 SEC
RANGE OF DATA : 2.000 - 45.000 DEG
RANGE IN D : 44.1716 - 2.0145 A
MAX PEAK CTS, CPS : 2285. CTS 1906. CPS
SECF APPLIED : NONE

2-THETA (DEG)	WIDTH (APPROX)	COUNTS PEAK	COUNTS BKGND	D (ANG)	I (NORM)	LINE TYPE A1	A2	BT	AM	OT
3.57	0.43	64.	282.	24.7141	2.80	x			x	
10.61	0.23	26.	125.	8.3379	1.14				x	
12.39	0.49	361.	108.	7.1437	15.80				x	
18.48	0.19	2285.	86.	4.8204	100.00				x	
20.38	0.17	1018.	88.	4.3565	44.54				x	
20.69	0.13	515.	88.	4.2929	22.55				x	
20.98	0.12	686.	90.	4.2352	30.04				x	
21.86	0.28	310.	90.	4.0657	13.56				x	
23.43	0.11	112.	92.	3.7967	4.92				x	
24.96	0.52	449.	94.	3.5681	19.67				x	
26.75	0.15	2025.	98.	3.3326	88.63				x	
27.02	0.13	420.	98.	3.2993	18.39				x	
28.18	0.21	256.	98.	3.1755	11.20				x	
28.83	0.26	121.	100.	3.0967	5.30				x	
30.29	0.27	35.	98.	2.9502	1.52				x	
31.55	0.24	28.	102.	2.8356	1.23				x	
33.22	0.25	156.	106.	2.6968	6.84				x	
35.04	0.37	144.	106.	2.5604	6.30				x	
35.76	0.29	388.	106.	2.5112	16.99				x	
36.49	0.15	484.	106.	2.4623	21.18	x			x	
36.68	0.29	708.	106.	2.4497	30.97				x	
37.21	0.20	286.	106.	2.4166	12.50				x	
37.77	0.20	894.	106.	2.3817	39.13				x	
38.46	0.25	210.	106.	2.3403	9.20				x	
39.46	0.32	279.	106.	2.2833	12.21				x	
40.27	0.48	289.	106.	2.2395	12.65				x	
41.79	0.27	357.	106.	2.1615	15.63				x	
42.54	0.20	146.	106.	2.1248	6.41				x	
43.47	0.26	62.	114.	2.0817	2.73				x	
44.29	0.27	610.	135.	2.0451	26.70	x			x	

30 PEAKS IDENTIFIED 30 CRYSTALLINE 0 AMORPHOUS
30 PEAKS LISTED

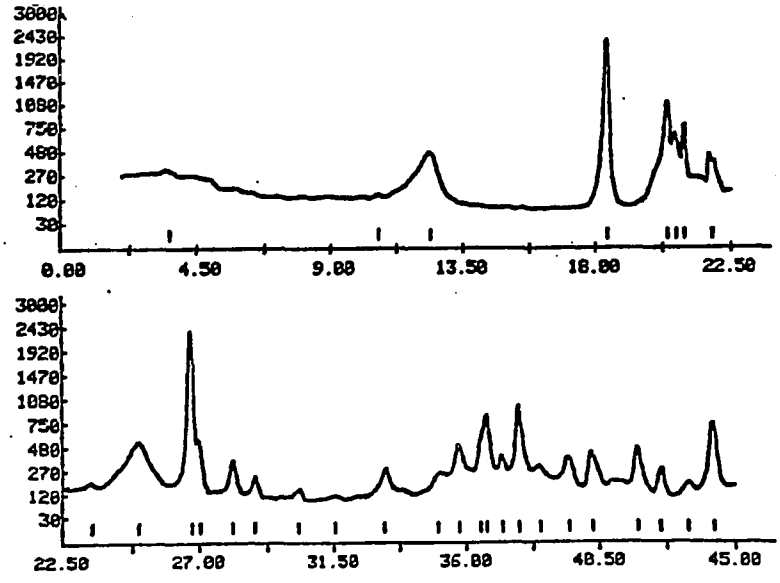

APD-3600 2ND DERIVATIVE PEAK ALGORITHM 10/ 1/85 12:45:36
RAW DATA FILE : S48.RD
SAMPLE ID : S48
RAW DATA FILE DATE : 9/28/85
GENERATOR SETTINGS : 45 KV 30 MA
STEP SIZE, CNT TIME : 0.020 DEG 1.20 SEC
RANGE OF DATA : 2.000 - 45.000 DEG
RANGE IN D : 44.1716 - 2.0145 A
MAX PEAK CTS, CPS : 681. CTS 568. CPS
SECF APPLIED : NONE

2-THETA (DEG)	WIDTH (APPROX)	COUNTS PEAK	COUNTS BKGND	D (ANG)	I (NORM)	LINE TYPE A1	A2	BT	AM	OT
3.58	0.44	69.	299.	24.6796	10.11	X	X			
12.39	0.43	243.	117.	7.1437	35.72	X	X			
18.38	0.15	681.	94.	4.8269	100.00	X	X			
19.95	0.29	365.	123.	4.4584	53.55	X	X			
20.35	0.15	576.	137.	4.3639	84.56	X	X			
21.54	0.26	282.	177.	4.1254	41.43	X	X			
21.98	0.19	108.	198.	4.0447	15.88	X	X			
24.86	0.30	219.	222.	3.5815	32.15	X	X			
26.65	0.25	159.	177.	3.3435	23.31	X	X			
27.46	0.18	49.	159.	3.2480	7.19	X	X			
28.07	0.27	69.	144.	3.1788	10.11	X	X			
28.82	0.25	45.	138.	3.0972	6.59	X	X			
30.29	0.34	58.	119.	2.9511	8.48	X	X			
33.23	0.23	159.	128.	2.6968	23.31	X	X			
35.01	0.39	240.	128.	2.5629	35.27	X	X			
35.78	0.37	441.	138.	2.5158	64.74	X	X			
36.66	0.25	342.	138.	2.4518	50.24	X	X			
37.16	0.21	246.	138.	2.4194	36.18	X	X			
37.74	0.21	416.	138.	2.3836	61.09	X	X			
38.48	0.38	234.	138.	2.3394	34.36	X	X			
39.37	0.44	182.	132.	2.2883	26.73	X	X			
40.20	0.29	164.	132.	2.2432	24.05	X	X			
40.94	0.39	92.	132.	2.2044	13.53	X	X			
41.75	0.31	154.	132.	2.1634	22.57	X	X			
42.54	0.31	24.	135.	2.1251	3.52	X	X			
43.39	0.33	31.	135.	2.0854	4.68	X	X			
44.25	0.32	190.	135.	2.0468	27.96	X	X			
23.75	6.58	225.	0.	3.7463						X

28 PEAKS IDENTIFIED 27 CRYSTALLINE 1 AMORPHOUS
28 PEAKS LISTED

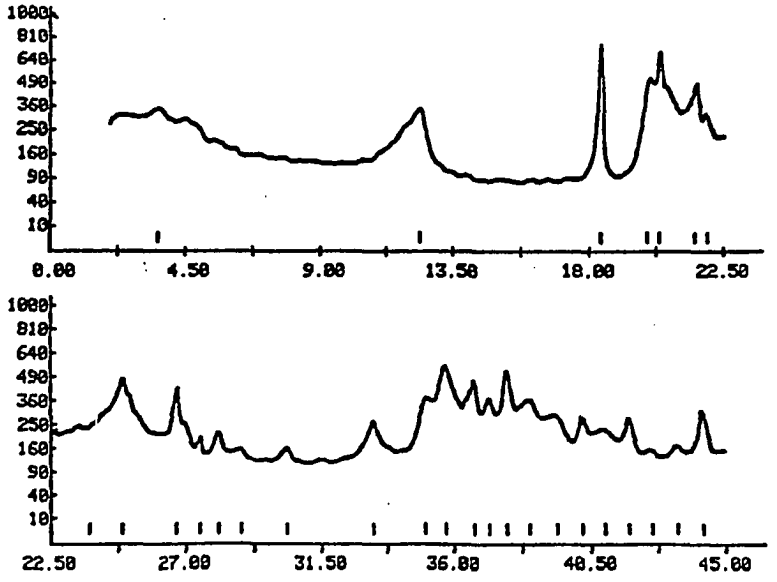

APD-3600 2ND DERIVATIVE PEAK ALGORITHM 10/ 1/85 12:51:15

RAW DATA FILE	: S410.RD
SAMPLE ID	: S410
RAW DATA FILE DATE	: 9/28/85
GENERATOR SETTINGS	: 45 KV 30 MA
STEP SIZE, CNT TIME	: 0.020 DEG 1.20 SEC
RANGE OF DATA	: 2.000 - 45.000 DEG
RANGE IN D	: 44.1716 - 2.0145 A
MAX PEAK CTS, CPS	: 3295. CTS 2748. CPS
SECF APPLIED	: NONE

2-THETA (DEG)	WIDTH (APPROX)	COUNTS PEAK	COUNTS BKGND	D (ANG)	I (NORM)	LINE TYPE A1	A2	BT	AM	OT
3.57	0.42	67.	256.	24.7487	2.04		X	X		
4.99	0.32	45.	282.	17.7087	1.36		X	X		
12.36	0.42	88.	102.	7.1610	2.68		X	X		
18.40	0.18	3295.	88.	4.8204	100.00		X	X		
20.39	0.17	1232.	88.	4.3554	37.39		X	X		
20.66	0.14	615.	88.	4.2981	18.67		X	X		
21.69	0.10	475.	88.	4.0972	14.42		X	X		
21.90	0.11	1608.	88.	4.0584	48.81		X	X		
23.42	0.29	88.	88.	3.7983	2.68		X	X		
24.19	0.28	188.	88.	3.6791	3.84		X	X		
24.99	0.19	151.	88.	3.5624	4.59		X	X		
26.62	0.24	266.	88.	3.3485	8.06		X	X		
27.00	0.20	396.	88.	3.3023	12.02		X	X		
28.09	0.24	266.	88.	3.1765	8.06		X	X		
28.81	0.27	128.	88.	3.0988	3.88		X	X		
30.31	0.33	86.	90.	2.9488	2.63		X	X		
31.54	0.31	25.	94.	2.8378	0.76		X	X		
33.24	0.37	193.	96.	2.6956	5.86		X	X		
35.06	0.23	119.	100.	2.5594	3.61		X	X		
35.74	0.27	437.	100.	2.5126	13.26		X	X		
36.47	0.14	515.	102.	2.4636	15.64		X	X		
36.70	0.26	724.	102.	2.4487	21.96		X	X		
37.19	0.28	324.	102.	2.4175	9.83		X	X		
37.78	0.26	938.	104.	2.3811	28.23		X	X		
38.48	0.31	182.	104.	2.3394	5.53		X	X		
39.48	0.30	228.	106.	2.2869	6.92		X	X		
40.23	0.29	317.	108.	2.2419	9.62		X	X		
41.74	0.19	384.	118.	2.1639	11.66		X	X		
43.42	0.35	81.	123.	2.0848	2.46		X	X		
44.28	0.27	697.	132.	2.0455	21.15		X	X		
44.85	0.18	55.	142.	2.0206	1.66		X	X		

31 PEAKS IDENTIFIED 31 CRYSTALLINE 0 AMORPHOUS
31 PEAKS LISTED

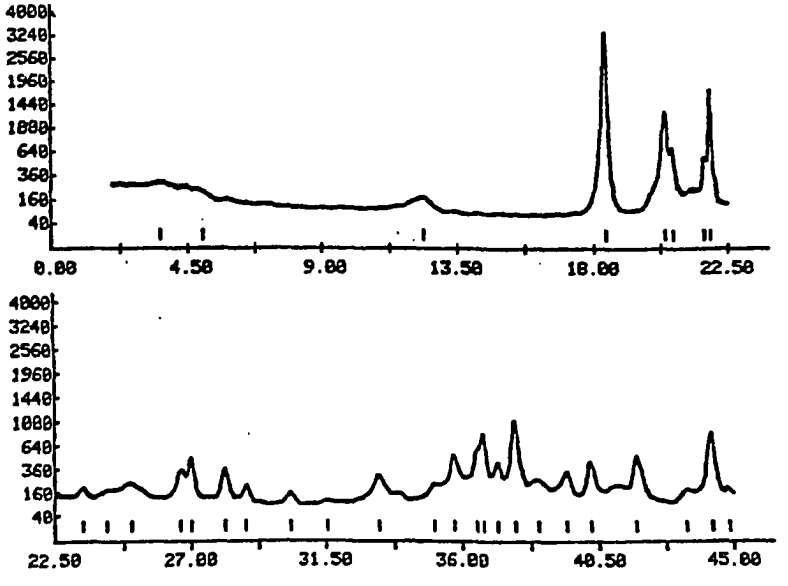

APD-3600 2ND DERIVATIVE PEAK ALGORITHM 10/ 1/85 12:57: 6

RAW DATA FILE	: S411.RD
SAMPLE ID	: S411
RAW DATA FILE DATE	: 9/28/85
GENERATOR SETTINGS	: 45 KV 30 MA
STEP SIZE, CNT TIME	: 0.020 DEG 1.20 SEC
RANGE OF DATA	: 2.000 - 45.000 DEG
RANGE IN D	: 44.1716 - 2.0145 A
MAX PEAK CTS, CPS	: 2834. CTS 1696. CPS
SECF APPLIED	: NONE

2-THETA (DEG)	WIDTH (APPROX)	COUNTS PEAK	COUNTS BKGND	D (ANG)	I (NORM)	LINE TYPE A1	A2	BT	AM	OT
3.69	0.35	35.	286.	23.9442	1.71			X	X	
12.29	0.56	123.	104.	7.2016	6.06			X	X	
18.40	0.15	2834.	88.	4.8238	100.00			X	X	
19.99	0.17	276.	88.	4.4427	13.55			X	X	
20.38	0.15	1024.	88.	4.3575	50.34			X	X	
20.65	0.13	571.	88.	4.3022	28.08			X	X	
21.79	0.14	454.	86.	4.0777	22.31			X	X	
22.05	0.14	204.	86.	4.0311	10.05			X	X	
23.36	0.39	100.	85.	3.8079	4.92			X	X	
24.21	0.37	146.	85.	3.6761	7.20			X	X	
24.95	0.31	219.	83.	3.5688	10.77			X	X	
26.64	0.19	289.	81.	3.3461	14.21			X	X	
26.99	0.19	313.	81.	3.3041	15.40			X	X	
28.07	0.26	219.	81.	3.1793	10.77			X	X	
28.80	0.23	106.	79.	3.0998	5.22			X	X	
30.29	0.35	94.	83.	2.9507	4.63			X	X	
33.21	0.32	177.	104.	2.6980	8.70			X	X	
35.02	0.37	180.	106.	2.5622	8.83			X	X	
35.73	0.26	576.	108.	2.5133	28.32			X	X	
36.63	0.33	493.	108.	2.4535	24.23			X	X	
37.18	0.22	272.	108.	2.4182	13.38			X	X	
37.76	0.25	686.	110.	2.3821	33.75			X	X	
38.49	0.32	169.	110.	2.3385	8.31			X	X	
39.38	0.31	216.	112.	2.2877	10.62			X	X	
40.24	0.25	250.	112.	2.2411	12.27			X	X	
41.81	0.31	108.	114.	2.2010	5.32			X	X	
41.76	0.23	306.	114.	2.1632	15.06			X	X	
41.88	0.08	190.	114.	2.1570	9.36			X	X	
43.39	0.29	66.	114.	2.0854	3.23			X	X	
44.27	0.30	458.	112.	2.0468	22.52			X	X	

30 PEAKS IDENTIFIED 30 CRYSTALLINE 0 AMORPHOUS
30 PEAKS LISTED

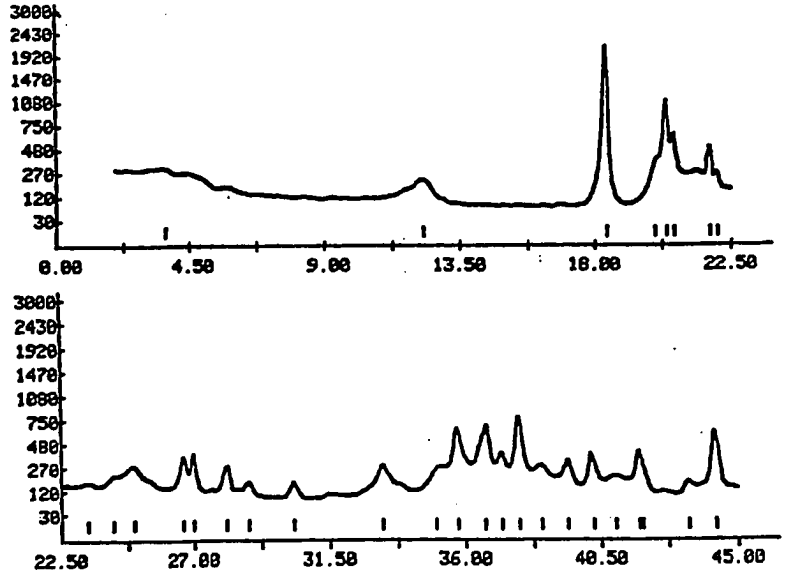

APD-3600 2ND DERIVATIVE PEAK ALGORITHM 10/ 1/85 13: 3: 4

RAW DATA FILE	: S412.RD
SAMPLE ID	: S412
RAW DATA FILE DATE	: 9/28/85
GENERATOR SETTINGS	: 45 KV 30 MA
STEP SIZE, CNT TIME	: 0.020 DEG 1.20 SEC
RANGE OF DATA	: 2.000 ~ 45.000 DEG
RANGE IN D	: 44.1716 ~ 2.0145 A
MAX PEAK CTS, CPS	: 1082. CTS 903. CPS
SECF APPLIED	: NONE

2-THETA (DEG)	WIDTH (APPROX)	COUNTS PEAK	COUNTS BKGND	D (ANG)	I (NORM)	LINE TYPE A1	A2	BT	AM	DT
2.18	0.20	282.	0.	40.6179	26.08	X	X			
2.40	0.20	98.	202.	36.8873	9.05					
12.31	0.42	139.	106.	7.1929	12.86					
18.40	0.15	1082.	86.	4.8217	100.00					
19.95	0.26	276.	112.	4.4504	25.46					
20.38	0.18	618.	123.	4.3575	56.36					
20.66	0.14	524.	132.	4.2981	48.45					
21.75	0.13	475.	164.	4.0860	43.91					
24.93	0.42	142.	172.	3.5723	13.08					
26.67	0.25	121.	151.	3.3424	11.18					
27.04	0.20	188.	144.	3.2959	16.59					
28.18	0.25	110.	128.	3.1760	10.19					
28.82	0.32	53.	119.	3.0972	4.92					
30.34	0.27	59.	104.	2.9464	5.48					
33.28	0.30	137.	106.	2.6984	12.63					
35.10	0.23	228.	118.	2.5569	21.07					
35.73	0.35	449.	112.	2.5129	41.52					
36.71	0.25	408.	112.	2.4488	37.70					
37.20	0.22	250.	114.	2.4172	23.06					
37.76	0.21	493.	114.	2.3821	45.53					
38.51	0.37	210.	117.	2.3377	19.42					
39.42	0.35	180.	119.	2.2858	16.59					
40.21	0.23	154.	119.	2.2427	14.21					
41.79	0.33	188.	123.	2.1617	17.34					
43.41	0.27	36.	125.	2.0845	3.33					
44.26	0.29	296.	125.	2.0462	27.33	X	X			

26 PEAKS IDENTIFIED 26 CRYSTALLINE 0 AMORPHOUS
26 PEAKS LISTED

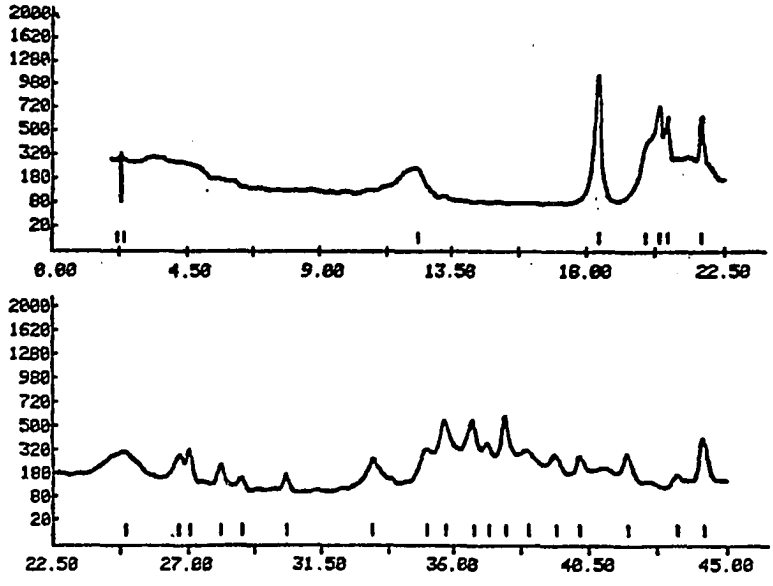

APD-3600 2ND DERIVATIVE PEAK ALGORITHM 10/29/85 11:21:54

RAW DATA FILE	: S413.RD
SAMPLE ID	: 6413
RAW DATA FILE DATE	: 10/23/85
GENERATOR SETTINGS	: 45 KV 30 MA
STEP SIZE, CNT TIME	: 0.020 DEG 1.20 SEC
RANGE OF DATA	: 2.000 - 45.000 DEG
RANGE IN D	: 44.1716 - 2.0145 A
MAX PEAK CTS, CPS	: 467. CTS 389. CPS
SECF APPLIED	: NONE

2-THETA (DEG)	WIDTH (APPROX)	COUNTS PEAK	COUNTS BKGND	D (ANG)	I (NORM)	LINE TYPE A1	A2	BT	AM	OT
3.68	0.36	100.	420.	24.0092	21.43	X	X			
4.51	0.40	100.	346.	19.6141	21.43	X	X			
12.24	0.50	174.	121.	7.2288	37.35	X	X			
18.32	0.22	342.	74.	4.8413	73.36	X	X			
19.94	0.25	420.	100.	4.4527	90.07	X	X			
20.33	0.19	467.	114.	4.3681	100.00	X	X			
20.60	0.17	335.	123.	4.3115	71.78	X	X			
21.65	0.26	164.	164.	4.1056	35.12	X	X			
22.04	0.12	112.	100.	4.0329	24.00	X	X			
24.15	0.29	90.	196.	3.6851	19.34	X	X			
24.91	0.39	156.	190.	3.5737	33.49	X	X			
26.57	0.23	44.	169.	3.3541	9.34	X	X			
27.02	0.25	79.	159.	3.2999	16.90	X	X			
28.10	0.33	22.	135.	3.1760	4.73	X	X			
30.26	0.26	76.	96.	2.9530	16.22	X	X			
33.10	0.31	112.	90.	2.7000	24.00	X	X			
34.99	0.39	199.	90.	2.5647	42.61	X	X			
35.66	0.26	462.	90.	2.5177	99.00	X	X			
36.65	0.31	202.	90.	2.4519	43.22	X	X			
37.74	0.30	250.	90.	2.3839	53.51	X	X			
38.43	0.43	185.	90.	2.3421	39.64	X	X			
39.40	0.34	125.	90.	2.2869	26.89	X	X			
40.16	0.35	90.	90.	2.2451	21.01	X	X			
40.99	0.32	69.	90.	2.2015	14.77	X	X			
41.71	0.27	74.	90.	2.1654	15.85	X	X			
43.37	0.29	45.	90.	2.0863	9.62	X	X			
44.23	0.33	106.	90.	2.0479	22.74	X	X			
24.00	7.06	159.	0.	3.7078						X

28 PEAKS IDENTIFIED 27 CRYSTALLINE 1 AMORPHOUS
28 PEAKS LISTED

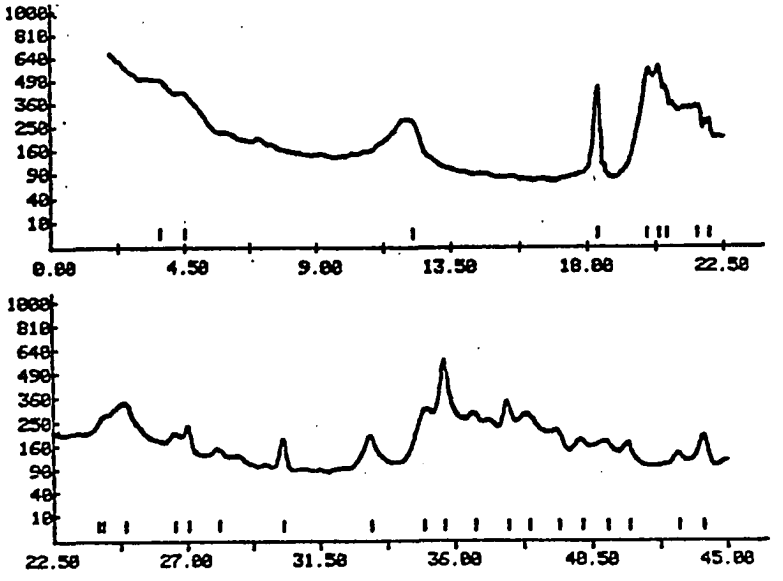

APD-3600 2ND DERIVATIVE PEAK ALGORITHM 10/ 1/85 14:38:14

RAW DATA FILE	: S414.RD
SAMPLE ID	: S414
RAW DATA FILE DATE	: 9/28/85
GENERATOR SETTINGS	: 45 KV 30 MA
STEP SIZE, CNT TIME	: 0.020 DEG 1.20 SEC
RANGE OF DATA	: 2.000 - 45.000 DEG
RANGE IN D	: 44.1716 - 2.0145 A
MAX PEAK CTS, CPS	: 681. CTS 568. CPS
SECF APPLIED	: NONE

2-THETA (DEG)	WIDTH (APPROX)	COUNTS PEAK	COUNTS BKGND	D (ANG)	I (NORM)	LINE TYPE A1	A2	BT	AM	OT
4.98	0.31	34.	262.	17.7621	4.94	X	X			
12.18	0.09	188.	112.	7.3113	26.36	X	X			
18.34	0.24	199.	85.	4.8387	29.18	X	X			
19.96	0.39	493.	123.	4.4471	72.35	X	X			
20.35	0.19	467.	137.	4.3639	68.49	X	X			
20.62	0.24	296.	146.	4.3073	43.43	X	X			
21.43	0.42	161.	174.	4.1463	23.68	X	X			
24.89	0.52	125.	216.	3.5772	18.41	X	X			
26.90	0.28	14.	182.	3.3137	2.01	X	X			
30.29	0.25	92.	119.	2.9511	13.53	X	X			
33.16	0.32	164.	112.	2.7812	24.05	X	X			
34.99	0.36	383.	112.	2.5643	44.44	X	X			
35.71	0.28	681.	114.	2.5146	100.00	X	X			
36.65	0.26	228.	114.	2.4516	33.47	X	X			
37.74	0.25	306.	114.	2.3833	44.96	X	X			
38.42	0.63	253.	114.	2.3429	37.11	X	X			
39.27	0.31	159.	117.	2.2939	23.31	X	X			
40.90	0.36	117.	117.	2.2052	17.12	X	X			
41.74	0.36	79.	119.	2.1639	11.63	X	X			
43.38	0.23	94.	119.	2.0861	13.81	X	X			
44.21	0.37	154.	119.	2.0488	22.57	X	X			
24.00	7.12	222.	0.	3.7078						X

22 PEAKS IDENTIFIED 21 CRYSTALLINE 1 AMORPHOUS
22 PEAKS LISTED

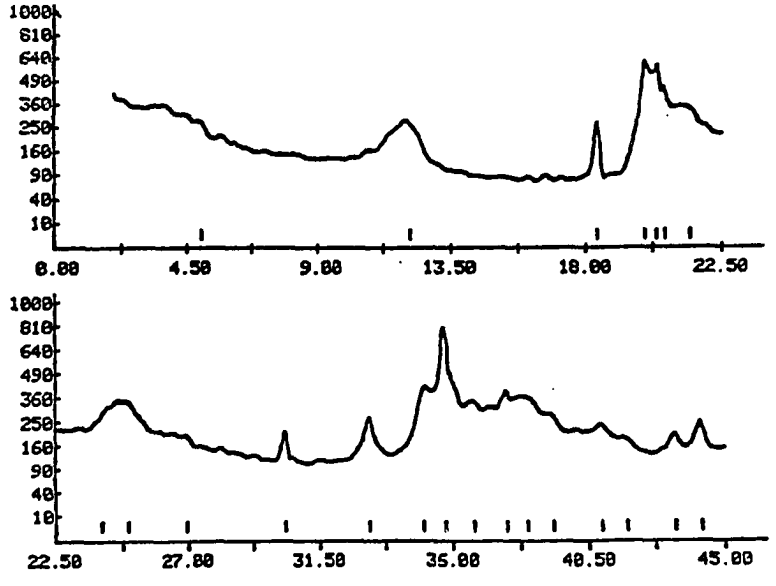

APD-3600 2ND DERIVATIVE PEAK ALGORITHM 10/ 1/85 15: 4:30

RAW DATA FILE	:	S416.RD
SAMPLE ID	:	S416
RAW DATA FILE DATE	:	9/28/85
GENERATOR SETTINGS	:	45 KV 30 MA
STEP SIZE, CNT TIME	:	0.020 DEG 1.20 SEC
RANGE OF DATA	:	2.000 - 45.000 DEG
RANGE IN D	:	44.1716 - 2.0145 A
MAX PEAK CTS, CPS	:	692. CTS 577. CPS
SECF APPLIED	:	NONE

2-THETA (DEG)	WIDTH (APPROX)	COUNTS PEAK	COUNTS BKGND	D (ANG)	I (NORM)	LINE TYPE A1	A2	BT	AM	OT
3.68	0.30	22.	328.	24.0418	3.19	X	X			
12.00	0.76	164.	112.	7.3264	23.69	X	X			
18.35	0.21	190.	81.	4.8360	27.53	X	X			
19.96	0.34	497.	112.	4.4471	71.89	X	X			
20.35	0.15	475.	125.	4.3639	68.71	X	X			
24.99	0.45	135.	219.	3.5638	19.45	X	X			
28.10	0.31	10.	149.	3.1749	1.39	X	X			
30.29	0.27	79.	117.	2.9511	11.45	X	X			
33.18	0.36	161.	119.	2.7000	23.32	X	X			
34.99	0.27	276.	123.	2.5648	39.84	X	X			
35.65	0.19	692.	125.	2.5100	100.00	X				
35.76	0.00	562.	125.	2.5109	81.21		X			
37.73	0.28	269.	130.	2.3842	38.88	X	X			
38.46	0.37	231.	130.	2.3406	33.40	X	X			
39.24	0.31	146.	132.	2.2956	21.17	X	X			
40.93	0.43	121.	135.	2.2051	17.49	X	X			
41.77	0.32	67.	137.	2.1622	9.72	X	X			
43.37	0.27	72.	142.	2.0865	10.45	X	X			
44.17	0.33	81.	146.	2.0504	11.71	X	X			
24.00	6.75	225.	0.	3.7078						X

20 PEAKS IDENTIFIED 19 CRYSTALLINE 1 AMORPHOUS.
20 PEAKS LISTED

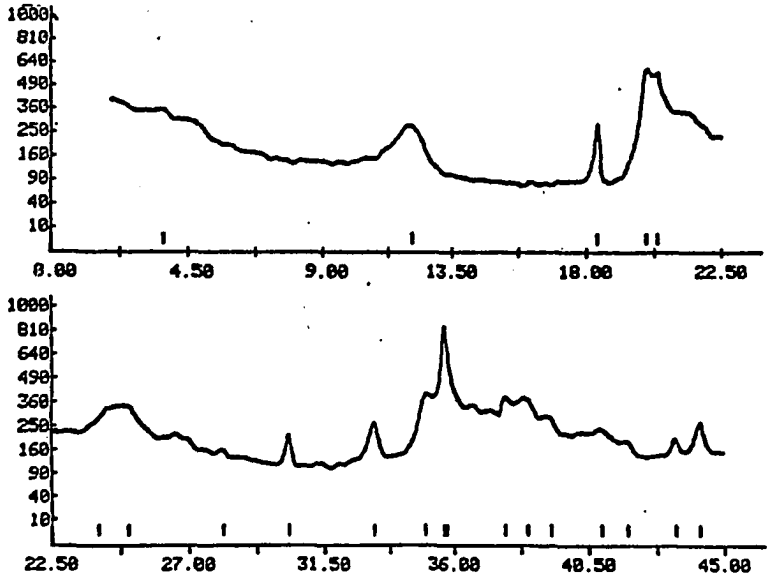

APD-3690 2ND DERIVATIVE PEAK ALGORITHM 11/4/85 11:18:51
RAW DATA FILE : S31.RD
SAMPLE ID : S31
RAW DATA FILE DATE : 10/27/85
GENERATOR SETTINGS : 45 KV 30 MA
STEP SIZE, CNT TIME : 0.020 DEG 1.20 SEC
RANGE OF DATA : 2.000 - 45.000 DEG
RANGE IN D : 44.1716 - 2.0145 A
MAX PEAK CTS, CPS : 5610. CTS 4679. CPS
SECF APPLIED : NONE

2-THETA (DEG)	WIDTH (APPROX)	COUNTS PEAK	COUNTS BKGND	D (ANG)	I (NORM)	LINE TYPE A1	A2	BT	AM	OT
2.16	0.25	94.	458.	40.8055	1.68	X	X			
5.09	0.30	61.	253.	17.3781	1.08	X	X			
12.29	0.46	94.	188.	7.2016	1.68	X	X			
18.48	0.13	5610.	188.	4.8238	100.00	X	X			
20.36	0.16	1325.	112.	4.3617	23.62	X	X			
20.62	0.12	640.	112.	4.3084	11.41	X	X			
21.43	0.42	139.	119.	4.1463	2.48	X	X			
24.83	0.45	112.	106.	3.5857	2.00	X	X			
26.54	0.21	237.	98.	3.3585	4.23	X	X			
26.96	0.20	428.	96.	3.3077	7.64	X	X			
28.05	0.27	296.	88.	3.1810	5.27	X	X			
28.74	0.25	102.	86.	3.1056	1.82	X	X			
30.11	0.29	27.	81.	2.9679	0.48	X	X			
33.23	0.27	110.	81.	2.6960	1.97	X	X			
33.82	0.31	83.	83.	2.6503	1.48	X	X			
34.99	0.35	92.	83.	2.5647	1.64	X	X			
35.58	0.37	177.	83.	2.5232	3.15	X	X			
36.43	0.15	529.	85.	2.4659	9.43	X	X			
36.71	0.18	778.	85.	2.4484	13.88	X	X			
37.15	0.23	502.	85.	2.4204	8.94	X	X			
37.75	0.21	1024.	85.	2.3830	18.25	X	X			
38.44	0.29	164.	86.	2.3418	2.92	X	X			
39.35	0.30	266.	86.	2.2894	4.74	X	X			
40.18	0.26	376.	86.	2.2443	6.71	X	X			
41.77	0.31	441.	88.	2.1622	7.86	X	X			
43.35	0.31	53.	100.	2.0870	0.95	X	X			
44.23	0.24	676.	119.	2.0479	12.85	X	X			
22.75	7.19	117.	0.	3.9086						X

28 PEAKS IDENTIFIED 27 CRYSTALLINE 1 AMORPHOUS.
28 PEAKS LISTED

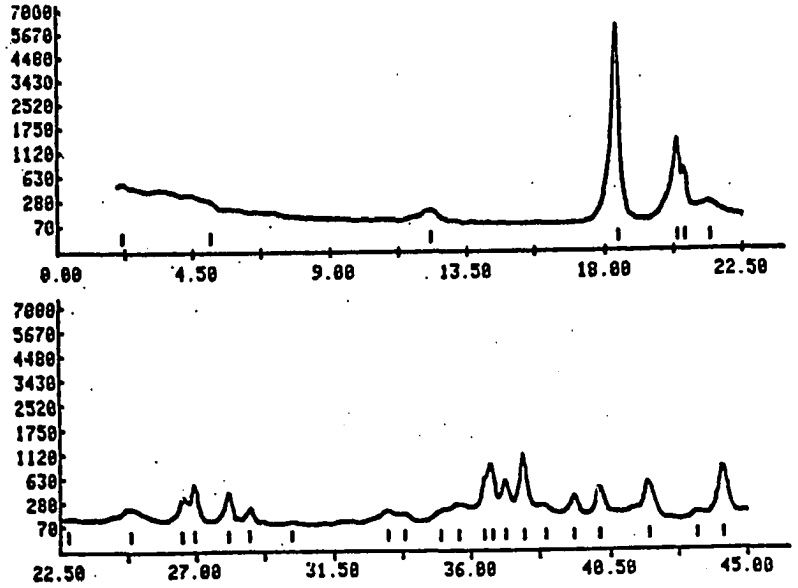

APD-3600 2ND DERIVATIVE PEAK ALGORITHM 10/31/85 16:47: 9
RAW DATA FILE : S32.RD
SAMPLE ID : S32
RAW DATA FILE DATE : 10/29/85
GENERATOR SETTINGS : 45 KV 30 MA
STEP SIZE, CNT TIME : 0.020 DEG 1.20 SEC
RANGE OF DATA : 2.000 - 45.000 DEG
RANGE IN D : 44.1716 - 2.0145 A
MAX PEAK CTS, CPS : 2134. CTS 1780. CPS
SECF APPLIED : NONE

2-THETA (DEG)	WIDTH (APPROX)	COUNTS PEAK	COUNTS BKGND	D (ANG)	I (NORM)	LINE TYPE A1	A2	BT	AM	OT
3.66	0.45	72.	369.	24.1403	3.38	X	X			
4.55	0.37	85.	299.	19.4415	3.97	X	X			
5.10	0.31	55.	259.	17.3448	2.57	X	X			
10.91	0.25	11.	112.	8.1056	0.51	X	X			
12.30	0.48	98.	104.	7.1958	4.59	X	X			
18.40	0.17	2134.	94.	4.8230	100.00	X	X			
20.38	0.16	876.	106.	4.3586	41.05	X	X			
20.65	0.13	449.	108.	4.3022	21.06	X	X			
21.46	0.35	234.	112.	4.1415	10.97	X	X			
24.86	0.40	110.	108.	3.5815	5.17	X	X			
26.60	0.26	193.	96.	3.3504	9.05	X	X			
26.98	0.19	256.	94.	3.3047	11.99	X	X			
28.10	0.18	196.	86.	3.1760	9.18	X	X			
28.77	0.25	71.	83.	3.1025	3.31	X	X			
33.24	0.50	144.	77.	2.6948	6.75	X	X			
33.77	0.40	98.	76.	2.6538	4.59	X	X			
34.96	0.35	137.	76.	2.5665	6.41	X	X			
35.84	0.33	228.	74.	2.5055	10.68	X	X			
36.63	0.37	543.	74.	2.4529	25.43	X	X			
37.17	0.23	342.	72.	2.4188	16.03	X	X			
37.77	0.23	618.	72.	2.3817	28.58	X	X			
38.42	0.21	159.	72.	2.3429	7.44	X	X			
39.38	0.32	207.	71.	2.2888	9.71	X	X			
40.21	0.23	256.	71.	2.2427	11.99	X	X			
41.77	0.32	318.	69.	2.1625	14.51	X	X			
43.50	0.21	31.	79.	2.0804	1.47	X	X			
44.26	0.34	437.	94.	2.0464	20.46	X	X			
23.80	7.25	114.	0.	3.8667						X

28 PEAKS IDENTIFIED 27 CRYSTALLINE 1 AMORPHOUS
28 PEAKS LISTED

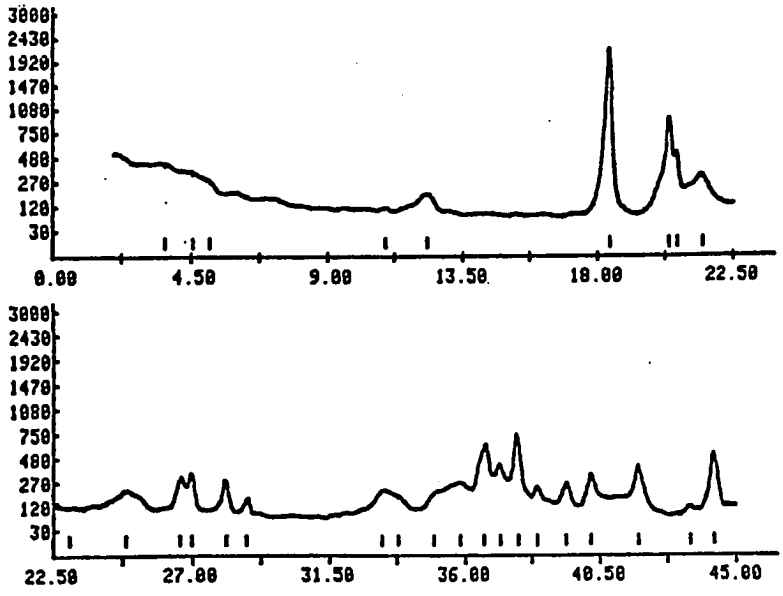

APD-3600 2ND DERIVATIVE PEAK ALGORITHM 10/31/85 21:44:18

RAW DATA FILE	: S33.RD
SAMPLE ID	: S33
RAW DATA FILE DATE	: 10/29/85
GENERATOR SETTINGS	: 45 KV 30 MA
STEP SIZE, CNT TIME	: 0.020 DEG 1.20 SEC
RANGE OF DATA	: 2.000 - 45.000 DEG
RANGE IN D	: 44.1716 - 2.0145 A
MAX PEAK CTS, CPS	: 5944. CTS 4958. CPS
SECF APPLIED	: NONE

2-THETA (DEG)	WIDTH (APPROX)	COUNTS PEAK	COUNTS BKGND	D (ANG)	I (NORM)	LINE TYPE A1	A2	BT	AM	OT
2.16	0.24	53.	552.	40.8855	0.90	X	X			
3.56	0.39	58.	408.	24.7834	0.97	X	X			
5.06	0.32	62.	276.	17.4639	1.05	X	X			
10.46	0.12	266.	130.	8.4571	4.47	X	X			
12.09	0.58	159.	114.	7.3203	2.67	X	X			
13.72	0.12	751.	100.	6.4564	12.63	X	X			
15.19	0.25	6.	98.	5.8307	0.10	X	X			
18.34	0.17	392.	86.	4.8387	6.60	X	X			
19.98	0.26	339.	86.	4.4449	5.70	X	X			
20.31	0.28	350.	86.	4.3724	5.88	X	X			
20.64	0.27	216.	86.	4.3032	3.64	X	X			
21.24	0.38	164.	86.	4.1848	2.76	X	X			
21.91	0.23	259.	86.	4.0556	4.36	X	X			
23.68	0.31	365.	88.	3.7572	6.14	X	X			
24.66	0.36	196.	88.	3.6101	3.30	X	X			
25.03	0.20	139.	88.	3.4491	2.34	X	X			
26.23	0.19	112.	88.	3.3981	1.89	X	X			
27.57	0.18	5944.	90.	3.2353	100.00	X	X			
27.85	0.09	745.	90.	3.2028	12.54	X	X			
28.34	0.19	299	90.	3.1496	5.03	X	X			
29.94	0.44	92.	90.	2.9844	1.55	X	X			
30.71	0.49	125.	90.	2.9108	2.11	X	X			
31.65	0.20	59.	92.	2.8274	1.00	X	X			
32.57	0.25	90.	98.	2.7495	1.52	X	X			
32.93	0.20	102.	100.	2.7203	1.72	X	X			
35.43	0.30	276.	106.	2.5338	4.64	X	X			
36.59	0.30	199.	106.	2.4561	3.34	X	X			
37.24	0.30	204.	106.	2.4147	3.44	X	X			
37.71	0.22	199.	106.	2.3851	3.34	X	X			
38.37	0.30	125.	106.	2.3456	2.11	X	X			
40.20	0.29	79.	106.	2.2432	1.33	X	X			
41.85	0.24	1764.	106.	2.1583	29.67	X	X			
44.16	0.31	110.	106.	2.0506	1.85	X	X			

33 PEAKS IDENTIFIED 33 CRYSTALLINE 0 AMORPHOUS
33 PEAKS LISTED

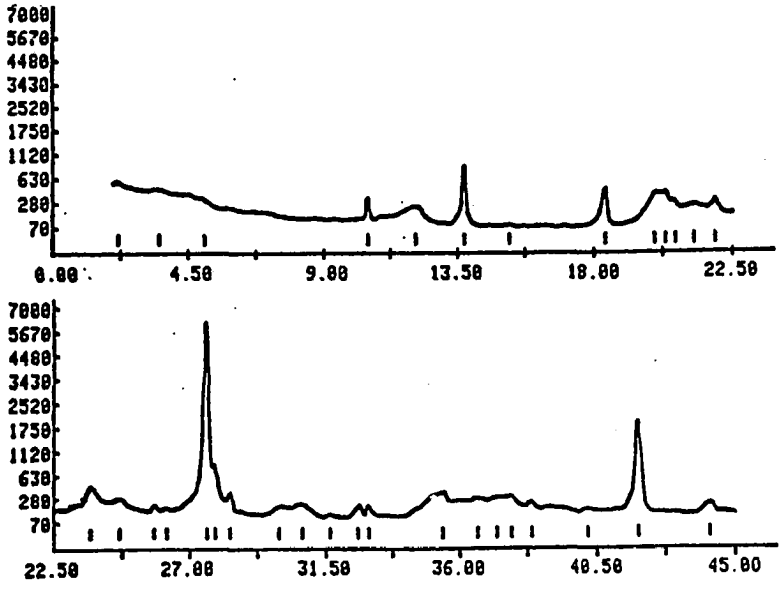

APD-3600 2ND DERIVATIVE PEAK ALGORITHM 10/31/95 21:27:30

RAW DATA FILE	: S34.RD
SAMPLE ID	: S34
RAW DATA FILE DATE	: 10/29/95
GENERATOR SETTINGS	: 45 KV 30 MA
STEP SIZE, CNT TIME	: 0.020 DEG 1.20 SEC
RANGE OF DATA	: 2.000 - 45.000 DEG
RANGE IN D	: 44.1716 - 2.0145 A
MAX PEAK CTS, CPS	: 19937. CTS 16628. CPS
SECF APPLIED	: NONE

2-THETA (DEG)	WIDTH (APPROX)	COUNTS PEAK	COUNTS BKGND	D (ANG)	I (NORM)	LINE TYPE A1	A2	BT	AM	OT
5.08	0.25	83.	199.	17.3952	0.42	X	X			
10.56	0.12	310.	102.	8.3773	1.55	X	X			
11.01	0.19	79.	98.	8.0358	0.40	X	X			
12.18	0.29	56.	98.	7.2664	0.28					X
13.79	0.12	2981.	85.	6.4192	14.95	X	X			
15.28	0.33	41.	83.	5.7985	0.21	X	X			
18.48	0.32	18.	85.	4.8217	0.09	X	X			
20.12	0.33	90.	85.	4.4143	0.45	X	X			
21.26	0.43	125.	85.	4.1801	0.63	X	X			
21.99	0.20	266.	85.	4.0420	1.33	X	X			
23.80	0.18	1190.	85.	3.7262	5.97	X	X			
24.76	0.25	123.	85.	3.5950	0.62					
25.98	0.19	292.	85.	3.4393	1.47	X	X			
27.63	0.14	19937.	85.	3.2278	100.00	X	X			
27.96	0.18	2411.	85.	3.1916	12.09	X	X			
28.43	0.19	357.	85.	3.1393	1.79	X	X			
29.97	0.36	289.	85.	2.9814	1.45	X	X			
30.55	0.24	324.	85.	2.9257	1.63	X	X			
30.98	0.26	388.	85.	2.8865	1.95	X	X			
31.74	0.21	114.	85.	2.8195	0.57	X	X			
32.55	0.24	132.	85.	2.7504	0.66	X	X			
33.15	0.31	119.	85.	2.7027	0.60	X	X			
34.98	0.20	177.	85.	2.5651	0.89	X	X			
35.49	0.35	412.	86.	2.5294	2.07	X	X			
37.38	0.43	266.	98.	2.4054	1.33	X	X			
38.49	0.30	59.	92.	2.3391	0.30	X	X			
39.04	0.24	96.	94.	2.3074	0.48	X				
39.20	0.15	59.	94.	2.2984	0.30		X			
41.94	0.24	5227.	106.	2.1541	26.22	X	X			
42.74	0.32	114.	110.	2.1156	0.57	X	X			
44.20	0.31	69.	119.	2.0493	0.35	X	X			
44.79	0.30	61.	121.	2.0234	0.31	X	X			

32 PEAKS IDENTIFIED 32 CRYSTALLINE 0 AMORPHOUS
32 PEAKS LISTED

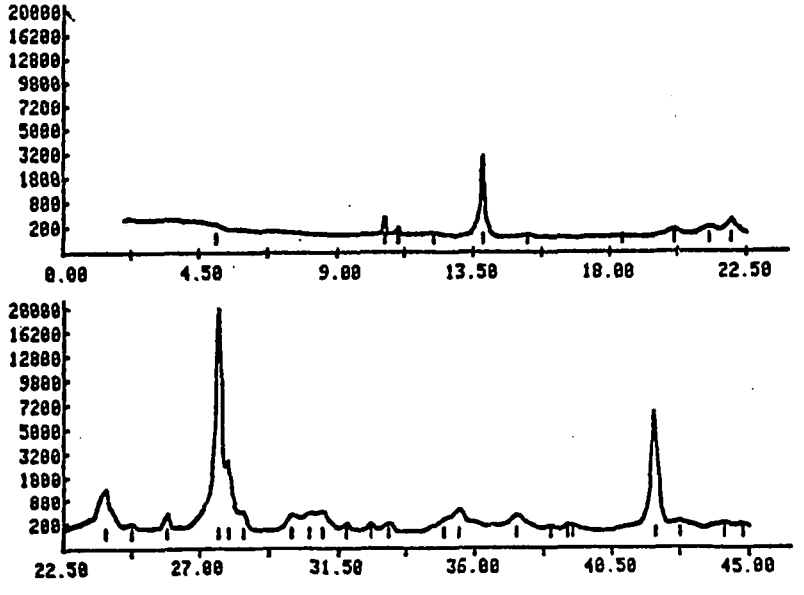

APD-3600 2ND DERIVATIVE PEAK ALGORITHM 10/31/95 19: 7:15
RAW DATA FILE : S35.RD
SAMPLE ID : S35
RAW DATA FILE DATE : 10/23/95
GENERATOR SETTINGS : 45 KV 30 MA
STEP SIZE, CNT TIME : 0.020 DEG 1.20 SEC
RANGE OF DATA : 2.000 - 45.000 DEG
RANGE IN D : 44.1715 - 2.0145 A
MAX PEAK CTS, CPS : 13340. CTS 11126. CPS
SECF APPLIED : NONE

2-THETA (DEG)	WIDTH (APPROX)	COUNTS PEAK	COUNTS BKGND	D (ANG)	I (NORM)	LINE TYPE A1	A2	BT	AM	OT
3.65	0.43	186.	386.	24.1734	0.88	X	X			
10.60	0.17	123.	182.	8.3418	0.92	X	X			
11.07	0.24	41.	98.	7.9888	0.31	X	X			
13.85	0.13	1325.	85.	6.3938	9.93	X	X			
15.40	0.30	55.	79.	5.7536	0.41	X	X			
21.35	0.35	130.	69.	4.1617	0.97	X	X			
22.05	0.29	286.	67.	4.0311	2.14	X	X			
23.34	0.20	282.	64.	3.8120	2.12	X	X			
23.90	0.37	930.	64.	3.7231	6.97	X	X			
24.81	0.29	123.	62.	3.5886	0.92			X		
25.96	0.19	424.	61.	3.4315	3.18	X	X			
27.71	0.15	13340.	58.	3.2198	100.00	X	X			
28.02	0.15	3457.	56.	3.1838	25.92	X	X			
28.51	0.16	310.	56.	3.1307	2.32	X	X			
29.96	0.13	412.	53.	2.9829	3.09	X	X			
30.72	0.18	412.	52.	2.9103	3.09	X	X			
31.04	0.20	458.	52.	2.8806	3.43	X	X			
31.75	0.15	125.	50.	2.8162	0.94	X	X			
32.62	0.24	190.	49.	2.7454	1.43	X	X			
33.20	0.30	114.	49.	2.6988	0.86	X	X			
35.06	0.17	216.	52.	2.5594	1.62	X	X			
35.58	0.32	471.	55.	2.5232	3.53	X	X			
36.13	0.19	135.	58.	2.4857	1.01	X	X			
37.43	0.39	276.	64.	2.4023	2.07	X	X			
39.12	0.30	144.	74.	2.3029	1.08	X	X			
40.99	0.43	44.	86.	2.2028	0.33	X	X			
41.95	0.14	4007.	92.	2.1530	30.04	X				
42.09	0.08	2391.	94.	2.1470	17.92		X	X		
42.77	0.29	112.	98.	2.1142	0.84		X	X		
44.22	0.39	59.	128.	2.0482	0.44	X	X			

30 PEAKS IDENTIFIED 30 CRYSTALLINE 0 AMORPHOUS
30 PEAKS LISTED

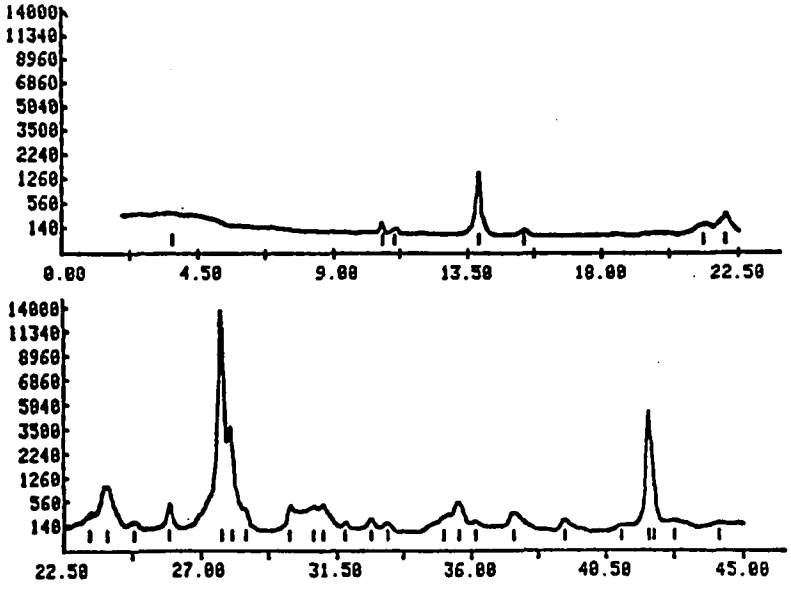

APD-3A98 2ND DERIVATIVE PEAK ALGORITHM 10/29/85 11:28: 0
RAW DATA FILE : S51.RD
SAMPLE ID : S51
RAW DATA FILE DATE : 10/23/85
GENERATOR SETTINGS : 45 KV 30 MA
STEP SIZE, CNT TIME : 0.020 DEG 1.20 SEC
RANGE OF DATA : 2.000 - 45.000 DEG
RANGE IN D : 44.1715 - 2.0145 A
MAX PEAK CTS, CPS : 4225. CTS 3524. CPS
SECF APPLIED : NONE

2-THETA (DEG)	WIDTH (APPROX)	COUNTS PEAK	COUNTS BKGND	D (ANG)	I (NORM)	LINE TYPE A1	A2	BT	AM	OT
2.15	0.25	58.	412.	41.0901	1.19	X	X			
12.42	0.37	28.	100.	7.1266	0.66	X	X			
18.41	0.18	4225.	79.	4.8178	100.00	X	X			
20.48	0.18	798.	72.	4.3533	18.69	X	X			
20.67	0.13	324.	72.	4.2978	7.67	X	X			
21.49	0.43	121.	69.	4.1358	2.86	X	X			
24.26	0.29	135.	61.	3.6679	3.18	X	X			
25.37	0.35	52.	58.	3.5113	1.23	X	X			
26.68	0.23	272.	55.	3.3418	6.44	X	X			
27.82	0.18	276.	53.	3.2999	6.52	X	X			
28.13	0.19	250.	50.	3.1727	5.91	X	X			
28.83	0.24	114.	49.	3.0967	2.71	X	X			
30.35	0.36	77.	45.	2.9445	1.83	X	X			
33.23	0.29	428.	44.	2.6964	10.14	X	X			
35.76	0.33	462.	45.	2.5105	10.94	X	X			
36.65	0.43	384.	46.	2.4519	9.09	X	X			
37.21	0.23	335.	46.	2.4168	7.93	X	X			
37.82	0.21	506.	46.	2.3787	11.98	X	X			
38.49	0.38	58.	48.	2.3385	1.37	X	X			
39.43	0.29	139.	48.	2.2852	3.30	X	X			
40.25	0.32	228.	48.	2.2405	5.40	X	X			
40.97	0.29	142.	49.	2.2028	3.35	X	X			
41.80	0.29	266.	49.	2.1607	6.29	X	X			
43.46	0.26	50.	59.	2.0822	1.19	X	X			
44.31	0.30	353.	77.	2.0442	8.37	X	X			

25 PEAKS IDENTIFIED 25 CRYSTALLINE 0 AMORPHOUS
25 PEAKS LISTED

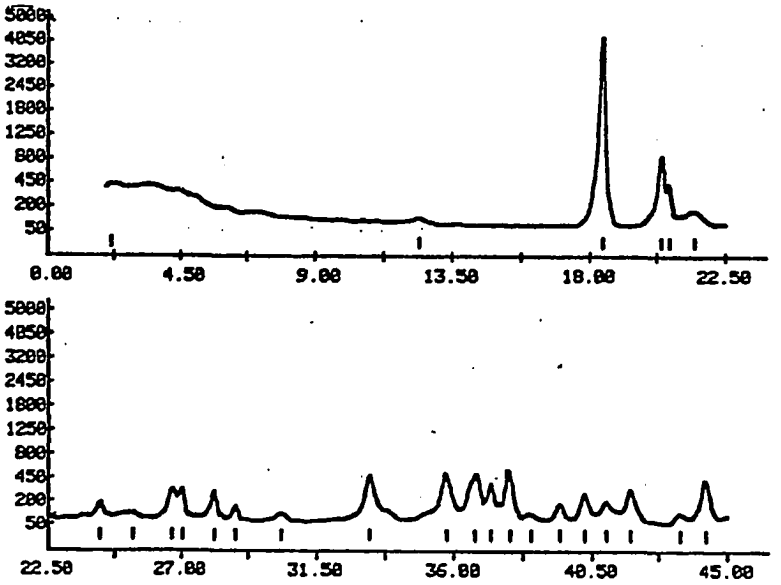

APD-3600 2ND DERIVATIVE PEAK ALGORITHM 12/29/93 11:34:41

RAW DATA FILE	: SS2.RD
SAMPLE ID	: SS2
RAW DATA FILE DATE	: 10/23/85
GENERATOR SETTINGS	: 45 KV 30 MA
STEP SIZE, CNT TIME	: 0.020 DEG 1.20 SEC
RANGE OF DATA	: 2.000 - 45.000 DEG
RANGE IN D	: 44.1716 - 2.0145 A
MAX PEAK CTS, CPS	: 4298. CTS 3578. CPS
SECF APPLIED	: NONE

2-THETA (DEG)	WIDTH (APPROX)	COUNTS PEAK	COUNTS BKGND	D (ANG)	I (NORM)	LINE TYPE A1	A2	BT	AM	OT
2.15	0.33	428.	112.	40.9948	9.99	X	X			
3.74	0.38	328.	149.	23.5926	7.64	X	X			
5.12	0.25	132.	185.	17.2426	3.08	X	X			
12.38	0.37	67.	184.	7.1495	1.57	X	X			
18.35	0.13	4298.	72.	4.8347	100.00	X	X			
20.34	0.13	1156.	66.	4.3671	26.94	X	X			
20.59	0.12	534.	66.	4.3146	12.44	X	X			
21.41	0.39	204.	66.	4.1492	4.77	X	X			
24.16	0.31	94.	66.	3.6836	2.19	X	X			
24.88	0.35	74.	66.	3.5786	1.72	X	X			
25.23	0.35	69.	66.	3.5278	1.61	X	X			
26.55	0.26	222.	66.	3.3572	5.17	X	X			
26.95	0.14	262.	66.	3.3053	6.12	X	X			
28.81	0.25	237.	66.	3.1049	5.53	X	X			
28.74	0.21	100.	66.	3.1067	2.33	X	X			
30.28	0.43	18.	62.	2.9516	0.43	X	X			
33.16	0.25	306.	62.	2.7016	7.14	X	X			
33.81	0.29	74.	61.	2.6511	1.72	X	X			
35.67	0.26	310.	58.	2.5178	7.22	X	X			
36.42	0.12	361.	56.	2.4669	8.41	X	X			
36.67	0.28	595.	56.	2.4506	13.88	X	X			
37.12	0.25	324.	55.	2.4216	7.55	X	X			
37.71	0.21	668.	55.	2.3851	15.48	X	X			
38.44	0.36	86.	53.	2.3418	2.02	X	X			
39.35	0.31	185.	52.	2.2897	4.31	X	X			
40.18	0.32	256.	50.	2.2445	5.97	X	X			
40.90	0.25	139.	49.	2.2062	3.25	X	X			
41.73	0.29	313.	48.	2.1647	7.38	X	X			
43.48	0.31	69.	52.	2.0852	1.61	X	X			
44.22	0.31	493.	62.	2.0482	11.49	X	X			
4.88	9.62	154.	0.	22.8891						X

31 PEAKS IDENTIFIED 30 CRYSTALLINE 1 AMORPHOUS
31 PEAKS LISTED

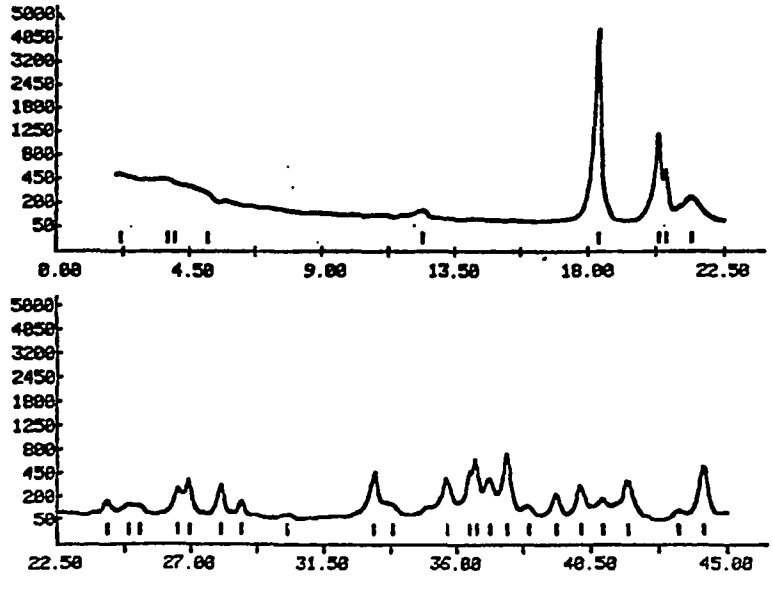

APD-3600 2ND DERIVATIVE PEAK ALGORITHM 10/29/35 11:40: 9
RAW DATA FILE : S53.RD
SAMPLE ID : S53
RAW DATA FILE DATE : 10/23/85
GENERATOR SETTINGS : 45 KV 30 MA
STEP SIZE, CNT TIME : 0.020 DEG 1.20 SEC
RANGE OF DATA : 2.000 - 45.000 DEG
RANGE IN D : 44.1716 - 2.0145 A
MAX PEAK CTS, CPS : 3668. CTS 3053. CPS
SECF APPLIED : NONE

2-THETA (DEG)	WIDTH (APPROX)	COUNTS PEAK	COUNTS BKGND	D (ANG)	I (NORM)	LINE TYPE A1	A2	BT	AM	OT
2.20	0.43	42.	520.	40.0653	1.15	X	X			
3.59	0.33	106.	400.	24.6109	2.90	X	X			
12.36	0.38	142.	104.	7.1581	3.87	X	X			
18.38	0.17	3668.	90.	4.8269	100.00	X	X			
20.35	0.18	756.	96.	4.3639	20.66	X	X			
20.63	0.12	400.	98.	4.3063	10.93	X	X			
21.40	0.45	193.	100.	4.1538	5.28	X	X			
23.14	0.21	32.	98.	3.8436	0.89	X	X			
24.18	0.26	79.	86.	3.6814	2.16	X	X			
24.91	0.31	202.	85.	3.5737	5.51	X	X			
26.61	0.38	199.	79.	3.3498	5.43	X	X			
26.97	0.20	219.	77.	3.3059	5.98	X	X			
28.06	0.38	169.	74.	3.1799	4.62	X	X			
28.77	0.31	81.	71.	3.1038	2.21	X	X			
30.29	0.33	25.	66.	2.9511	0.68	X	X			
33.19	0.32	269.	69.	2.6992	7.35	X	X			
35.81	0.35	114.	67.	2.5626	3.13	X	X			
35.69	0.26	339.	67.	2.5156	9.25	X	X			
36.61	0.37	361.	67.	2.4545	9.86	X	X			
37.15	0.22	276.	67.	2.4204	7.53	X	X			
37.74	0.26	488.	67.	2.3839	13.34	X	X			
38.49	0.24	139.	66.	2.3388	3.80	X	X			
39.36	0.36	172.	66.	2.2891	4.69	X	X			
40.21	0.32	188.	66.	2.2429	5.13	X	X			
40.97	0.38	100.	66.	2.2028	2.73	X	X			
41.74	0.27	256.	64.	2.1642	6.99	X	X			
43.43	0.25	34.	64.	2.0836	0.92	X	X			
44.21	0.31	365.	64.	2.0484	9.97	X	X			
22.25	6.69	96.	0.	3.9953						X

29 PEAKS IDENTIFIED 28 CRYSTALLINE 1 AMORPHOUS
29 PEAKS LISTED

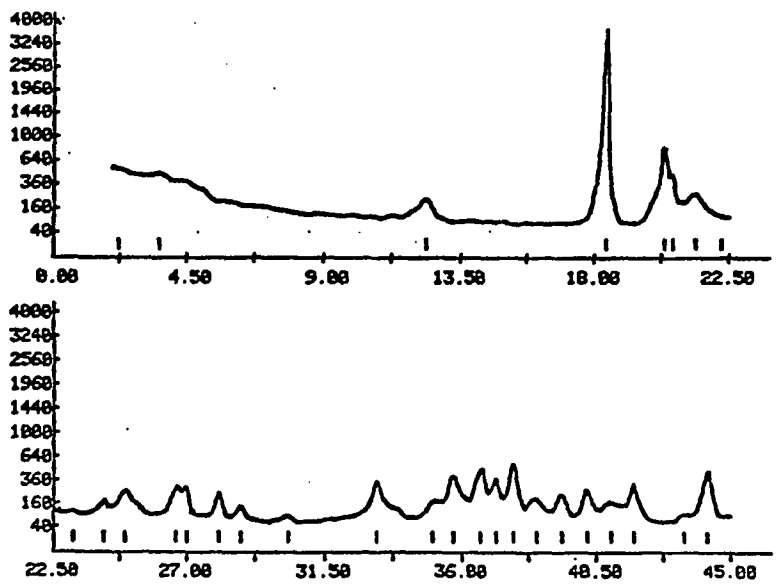

APD-3600 2ND DERIVATIVE PEAK ALGORITHM 10/29/85 11:46:23

RAW DATA FILE	: S54.RD
SAMPLE ID	: S54
RAW DATA FILE DATE	: 10/23/85
GENERATOR SETTINGS	: 45 KV 30 MA
STEP SIZE, CNT TIME	: 0.020 DEG 1.20 SEC
RANGE OF DATA	: 2.000 - 45.000 DEG
RANGE IN D	: 44.1715 - 2.0145 A
MAX PEAK CTS, CPS	: 6708. CTS 5584. CPS
SECF APPLIED	: NONE

2-THETA (DEG)	WIDTH (APPROX)	COUNTS PEAK	COUNTS BKGND	D (ANG)	I (NORM)	LINE TYPE A1	A2	BT	AM	OT
3.65	0.51	186.	335.	24.2397	1.58	X	X			
12.42	0.32	237.	180.	7.1266	3.54	X	X			
18.18	0.14	286.	98.	4.8996	4.26	X	X			
18.44	0.14	6708.	92.	4.8113	100.00	X	X			
20.48	0.17	853.	184.	4.3322	12.71	X	X			
20.68	0.12	365.	186.	4.2968	5.44	X	X			
21.43	0.44	216.	118.	4.1473	3.22	X	X			
23.21	0.34	31.	114.	3.8322	0.47	X	X			
24.25	0.25	66.	188.	3.6782	0.98	X	X			
24.96	0.35	303.	184.	3.5666	4.51	X	X			
26.68	0.26	144.	98.	3.3518	2.15	X	X			
27.01	0.17	222.	86.	3.3005	3.31	X	X			
27.54	0.31	12.	83.	3.2387	0.17	X	X			
28.12	0.24	172.	77.	3.1738	2.56	X	X			
28.84	0.27	94.	72.	3.0962	1.40	X	X			
30.29	0.25	49.	64.	2.9587	0.73	X	X			
33.29	0.14	320.	59.	2.6909	4.78	X	X			
35.86	0.27	149.	58.	2.5594	2.22	X	X			
35.74	0.21	529.	56.	2.5122	7.89	X	X			
36.51	0.18	306.	56.	2.4607	4.57	X	X			
36.74	0.21	437.	56.	2.4461	6.51	X	X			
37.21	0.28	420.	55.	2.4160	6.27	X	X			
37.88	0.21	552.	55.	2.3799	8.23	X	X			
38.45	0.29	284.	55.	2.3412	3.85	X	X			
39.39	0.36	282.	55.	2.2874	3.81	X	X			
40.24	0.35	284.	52.	2.2411	3.85	X	X			
40.99	0.38	139.	52.	2.2020	2.08	X	X			
41.79	0.26	253.	50.	2.1612	3.77	X	X			
43.43	0.27	52.	56.	2.0833	0.77	X	X			
44.32	0.28	357.	69.	2.0448	5.33	X	X			
23.25	7.75	110.	0.	3.8257						X

31 PEAKS IDENTIFIED 30 CRYSTALLINE 1 AMORPHOUS
31 PEAKS LISTED

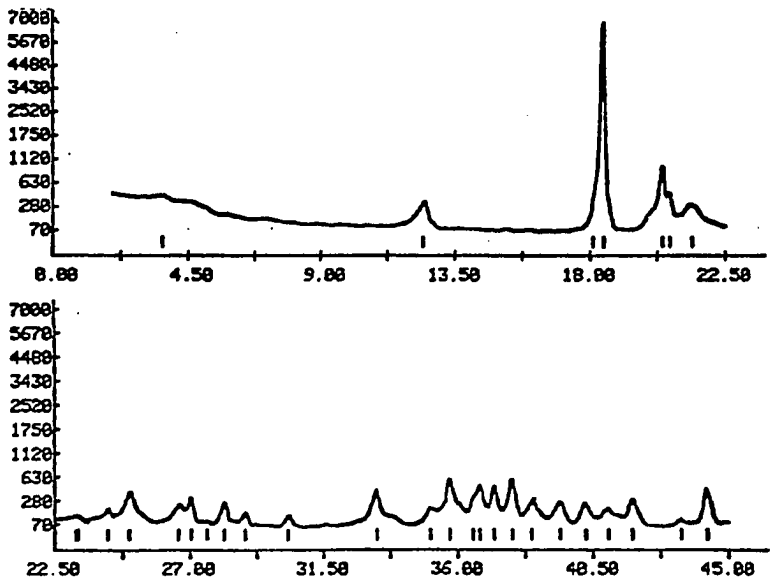

APD-3600 2ND DERIVATIVE PEAK ALGORITHM 10/29/85 11:32:48

RAW DATA FILE	: S55.RD
SAMPLE ID	: S55
RAW DATA FILE DATE	: 10/23/85
GENERATOR SETTINGS	: 45 KV 30 MA
STEP SIZE, CNT TIME	: 0.020 DEG 1.20 SEC
RANGE OF DATA	: 2.000 - 45.000 DEG
RANGE IN D	: 44.1716 - 2.0145 A
MAX PEAK CTS, CPS	: 4651. CTS 3879. CPS
SECF APPLIED	: NONE

2-THETA (DEG)	WIDTH (APPROX)	COUNTS PEAK	COUNTS BKGND	D (ANG)	I (NORM)	LINE TYPE A1	A2	BT	AM	OT
2.38	0.62	188.	588.	38.4197	2.33	X	X			
12.41	0.25	83.	184.	7.1323	1.78	X	X			
18.38	0.18	4651.	79.	4.8259	100.00	X	X			
20.36	0.17	858.	76.	4.3617	18.46	X	X			
20.63	0.14	424.	76.	4.3053	9.12	X	X			
21.39	0.47	166.	74.	4.1548	3.58	X	X			
24.19	0.25	142.	71.	3.6791	3.04	X	X			
24.98	0.31	123.	69.	3.5758	2.65	X	X			
26.55	0.24	188.	67.	3.3572	3.86	X	X			
26.95	0.22	253.	66.	3.3083	5.44	X	X			
28.07	0.23	204.	64.	3.1788	4.48	X	X			
28.77	0.27	66.	64.	3.1039	1.41	X	X			
30.32	0.32	36.	62.	2.9473	0.77	X	X			
33.21	0.23	433.	58.	2.6972	9.30	X	X			
34.99	0.23	71.	55.	2.5648	1.52	X	X			
35.68	0.27	437.	55.	2.5168	9.39	X	X			
36.62	0.36	488.	53.	2.4542	10.31	X	X			
37.16	0.28	361.	52.	2.4191	7.76	X	X			
37.76	0.23	543.	52.	2.3824	11.67	X	X			
38.43	0.28	108.	50.	2.3421	2.33	X	X			
39.36	0.31	161.	49.	2.2891	3.47	X	X			
40.21	0.33	234.	49.	2.2429	5.03	X	X			
40.91	0.29	166.	48.	2.2059	3.58	X	X			
41.79	0.32	262.	46.	2.1617	5.64	X	X			
43.46	0.19	55.	53.	2.0824	1.18	X	X			
44.22	0.21	488.	61.	2.0482	0.77	X	X			

26 PEAKS IDENTIFIED 26 CRYSTALLINE 0 AMORPHOUS
26 PEAKS LISTED

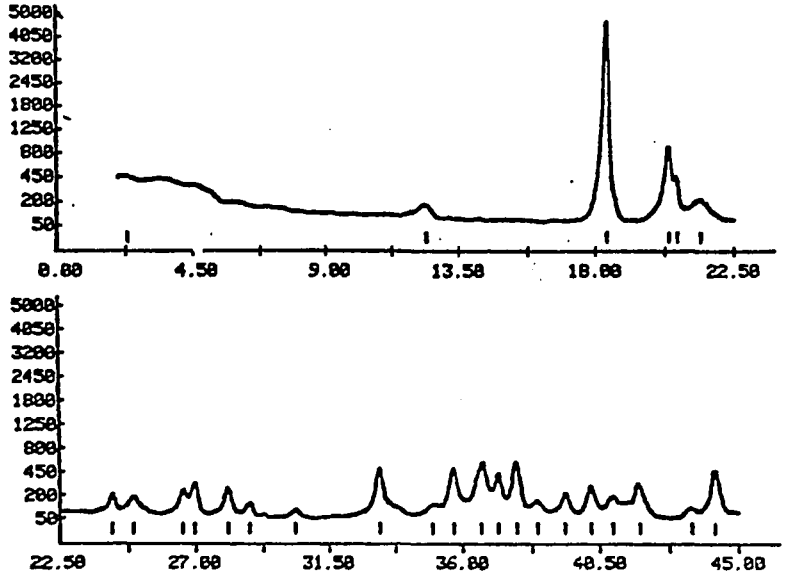

APD-3520 2ND DERIVATIVE PEAK ALGORITHM 10/23/85 11:58:38

RAW DATA FILE	: S56.RD
SAMPLE ID	: S56
RAW DATA FILE DATE	: 10/23/85
GENERATOR SETTINGS	: 45 KV 30 MA
STEP SIZE, CNT TIME	: 0.020 DEG 1.20 SEC
RANGE OF DATA	: 2.000 - 45.000 DEG
RANGE IN D	: 44.1715 - 2.0145 A
MAX PEAK CTS, CPS	: 3869. CTS 2568. CPS
SECF APPLIED	: NONE

2-THETA (DEG)	WIDTH (APPROX)	COUNTS PEAK	COUNTS BKGND	D (ANG)	I (NORM)	LINE TYPE A1 A2 BT AM OT
12.44	0.36	269.	102.	7.1158	8.76	X X
18.43	0.19	3869.	76.	4.8125	100.00	X X
20.43	0.14	795.	74.	4.3478	25.91	X X
20.63	0.12	433.	72.	4.2958	14.10	X X
21.51	0.46	174.	72.	4.1311	5.68	X X
24.26	0.27	199.	69.	3.6694	6.48	X X
24.98	0.34	313.	67.	3.5645	10.21	X X
26.63	0.25	137.	66.	3.3473	4.46	X X
27.83	0.19	213.	66.	3.2987	6.95	X X
28.13	0.26	149.	64.	3.1727	4.85	X X
28.87	0.29	72.	62.	3.0930	2.35	X X
30.37	0.39	35.	61.	2.9436	1.13	X X
33.26	0.19	471.	58.	2.6937	15.34	X X
35.12	0.14	108.	55.	2.5555	3.52	X X
35.77	0.29	520.	53.	2.5102	16.94	X X
36.73	0.23	429.	52.	2.4455	13.96	X X
37.24	0.15	279.	52.	2.4141	9.09	X X
37.82	0.19	506.	50.	2.3784	16.49	X X
38.58	0.29	196.	50.	2.3383	6.39	X X
39.42	0.32	188.	49.	2.2858	6.12	X X
40.26	0.26	180.	48.	2.2397	5.85	X X
40.96	0.38	166.	46.	2.2031	5.42	X X
41.82	0.38	222.	45.	2.1597	7.23	X X
43.54	0.38	37.	53.	2.0786	1.21	X X
44.31	0.29	324.	62.	2.0442	10.56	X X

25 PEAKS IDENTIFIED 25 CRYSTALLINE 0 AMORPHOUS
25 PEAKS LISTED

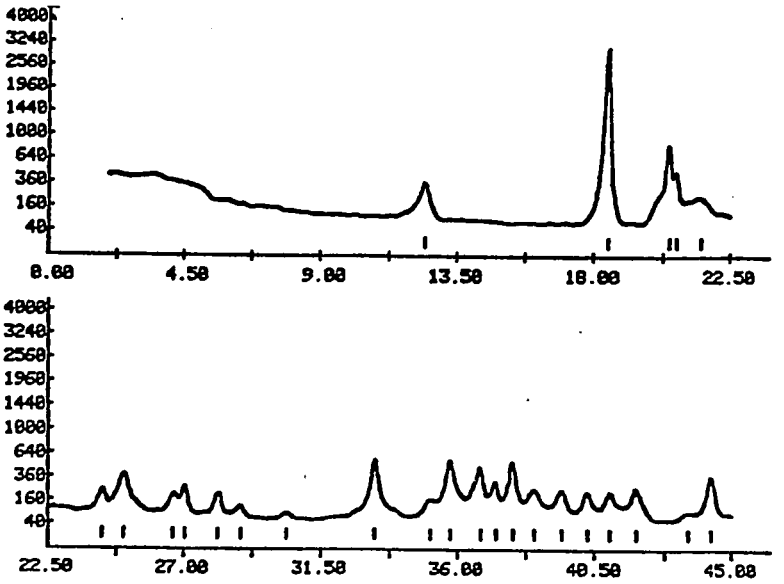

APD-3600 2ND DERIVATIVE PEAK ALGORITHM 10/28/85 9:22:11

RAW DATA FILE : 71.RD
SAMPLE ID : 71
RAW DATA FILE DATE : 10/28/85
GENERATOR SETTINGS : 45 KV 30 MA
STEP SIZE, CNT TIME : 0.010 DEG 1.20 SEC
RANGE OF DATA : 2.000 - 69.999 DEG
RANGE IN D : 44.1716 - 1.5419 A
MAX PEAK CTS, CPS : 2421. CTS 2019. CPS
SECF APPLIED : NONE

2-THETA (DEG)	WIDTH (APPROX)	COUNTS PEAK	COUNTS BKGND	D (ANG)	I (NORM)	LINE TYPE A1	A2	B1	AM	OT
13.66	0.14	253.	184.	6.4799	10.44	X	X			
15.28	0.13	28.	96.	5.7985	0.84					
18.33	0.17	79.	98.	4.8388	3.27					
19.98	0.37	259.	182.	4.4438	10.71					
21.54	0.19	299.	186.	4.1244	12.36					
21.99	0.18	655.	188.	4.0429	27.07					
22.83	0.19	207.	110.	3.8857	8.57					
23.71	0.29	936.	112.	3.7517	38.68					
24.69	0.17	185.	114.	3.6057	7.64					
25.26	0.16	121.	117.	3.5258	5.00					
25.79	0.17	292.	119.	3.4544	12.08					
27.48	0.16	2421.	123.	3.2457	100.00					
27.79	0.15	841.	125.	3.2096	34.74					
28.42	0.19	100.	128.	3.1404	4.13					
30.12	0.23	346.	121.	2.9674	14.29					
30.82	0.19	306.	114.	2.9007	12.65					
31.48	0.11	92.	118.	2.8418	3.81					
32.43	0.20	149.	108.	2.7611	6.15					
35.19	0.24	437.	135.	2.5502	18.05					
35.60	0.16	350.	139.	2.5218	14.45	X	X			
36.07	0.12	289.	144.	2.4988	11.94	X	X			
36.62	0.17	213.	149.	2.4535	8.81					
37.24	0.15	219.	156.	2.4144	9.05					
41.21	0.16	72.	159.	2.1905	2.98					
41.73	0.25	718.	146.	2.1647	29.67					
42.63	0.19	76.	137.	2.1206	3.13					
43.26	0.19	81.	142.	2.0916	3.35					
44.13	0.20	250.	149.	2.0524	10.31					
44.88	0.14	37.	154.	2.0228	1.54					
48.54	0.26	83.	177.	1.8757	3.42					
50.95	0.28	256.	135.	1.7923	10.58					
52.76	0.19	24.	169.	1.7348	0.99					
56.66	0.21	85.	159.	1.6245	3.58	X	X			

33 PEAKS IDENTIFIED 33 CRYSTALLINE 0 AMORPHOUS
33 PEAKS LISTED

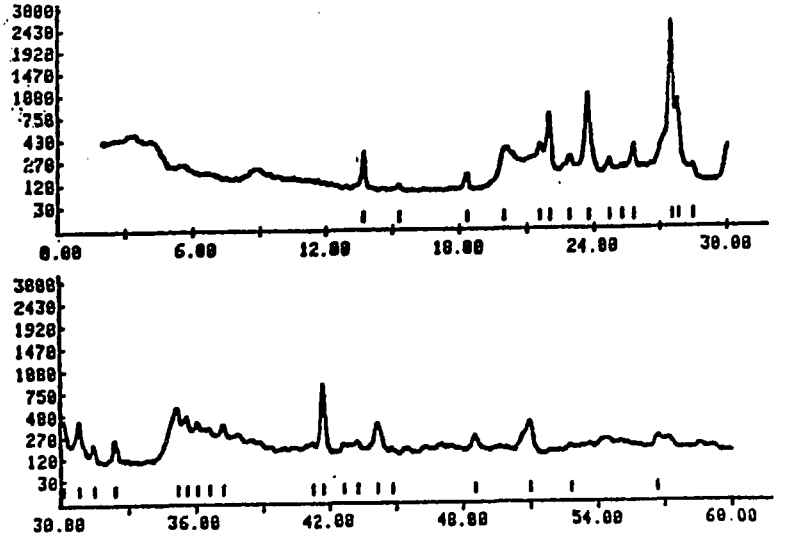

APD-3600 2ND DERIVATIVE PEAK ALGORITHM 10/29/86 20:57:52

RAW DATA FILE	: 718.RD
SAMPLE ID	: 718
RAW DATA FILE DATE	: 10/29/86
GENERATOR SETTINGS	: 45 KV 30 MA
STEP SIZE, CNT TIME	: 0.020 DEG 2.40 SEC
RANGE OF DATA	: 1.000 - 9.000 DEG
RANGE IN D	: 88.3397 - 9.8255 A
MAX PEAK CTS, CPS	: 515. CTS 215. CPS
SECF APPLIED	: NONE

2-THETA (DEG)	WIDTH (APPROX)	COUNTS PEAK	COUNTS BKGND	D (ANG)	I (NORM)	LINE TYPE A1	A2	BT	AM	DT
3.37	0.40	515.	676.	26.1782	100.00	X	X			
4.28	0.40	454.	590.	21.0377	88.05	X	X			
5.57	0.46	77.	484.	15.8668	15.03	X	X			
8.76	0.38	94.	369.	10.0999	18.26	X	X			

4 PEAKS IDENTIFIED 4 CRYSTALLINE 0 AMORPHOUS

4 PEAKS LISTED

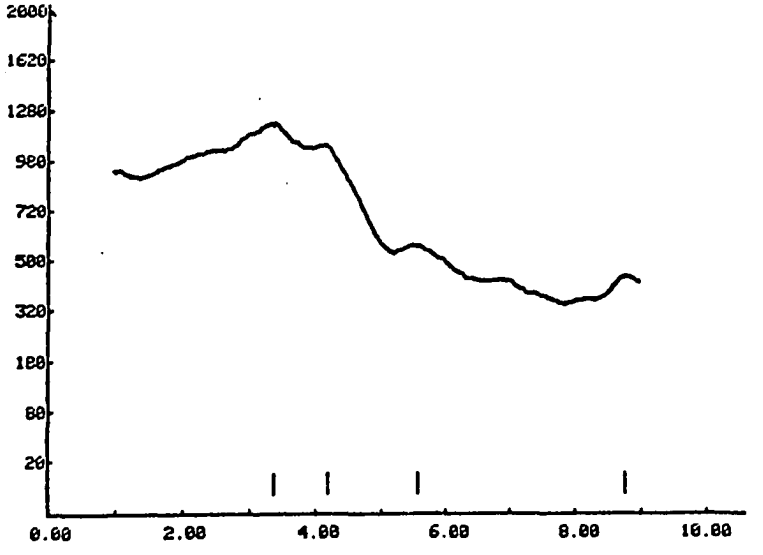

APD-3600 2ND DERIVATIVE PEAK ALGORITHM 10/29/86 21: 5: 6

RAW DATA FILE	7180.RD
SAMPLE ID	7180
RAW DATA FILE DATE	10/29/86
GENERATOR SETTINGS	45 KV 30 MA
STEP SIZE, CNT TIME	0.020 DEG 2.40 SEC
RANGE OF DATA	1.000 - 65.000 DEG
RANGE IN D	88.3397 - 1.4348 A
MAX PEAK CTS, CPS	4109. CTS 1713. CPS
SECF APPLIED	NONE

2-THETA (DEG)	WIDTH (APPROX)	COUNTS PEAK	COUNTS BKGND	D (ANG)	I (NORM)	LINE TYPE A1	A2	BT	AM	DT
3.34	0.51	520.	756.	26.4921	12.65	X	X			
4.30	0.55	420.	615.	20.5487	10.23	X	X			
5.65	0.48	72.	488.	15.6415	1.76	X	X			
12.08	0.51	243.	253.	7.3728	5.92	X	X			
13.65	0.15	313.	228.	6.4847	7.62	X	X			
15.21	0.36	27.	213.	5.8250	0.66	X	X			
18.29	0.26	125.	202.	4.8505	3.05	X	X			
19.96	0.32	548.	199.	4.4493	13.33	X	X			
21.46	0.19	484.	199.	4.1415	11.78	X	X			
21.99	0.14	1197.	199.	4.0429	29.14	X	X			
22.86	0.25	380.	199.	3.8901	9.25	X	X			
23.71	0.21	1624.	199.	3.7517	39.53	X	X			
24.63	0.32	458.	199.	3.6137	11.15	X	X			
25.78	0.21	484.	199.	3.4557	11.78	X	X			
27.49	0.15	4109.	199.	3.2431	100.00	X	X			
27.78	0.17	1568.	199.	3.2113	37.97	X	X			
28.43	0.21	193.	199.	3.1393	4.70	X	X			
30.06	0.43	581.	199.	2.9727	14.14	X	X			
30.81	0.27	497.	199.	2.9020	12.10	X	X			
31.46	0.29	193.	199.	2.8436	4.70	X	X			
32.40	0.27	196.	199.	2.7636	4.77	X	X			
35.15	0.31	750.	219.	2.5534	15.22	X	X			
35.62	0.18	595.	225.	2.5208	14.49	X	X			
36.07	0.22	538.	231.	2.4897	13.10	X	X			
37.22	0.25	488.	246.	2.4157	11.89	X	X			
37.96	0.38	339.	256.	2.3706	8.24	X	X			
38.91	0.14	169.	269.	2.3146	4.11	X	X			
41.10	0.19	79.	289.	2.1961	1.93	X	X			
41.73	0.25	1274.	276.	2.1644	31.02	X	X			
42.68	0.48	67.	317.	2.1187	1.64	X	X			
43.21	0.36	71.	317.	2.0937	1.72	X	X			
44.16	0.39	412.	320.	2.0506	10.03	X	X			
45.43	0.32	49.	279.	1.9962	1.19	X	X			
46.27	0.18	69.	269.	1.9619	1.68	X	X			
46.98	0.27	29.	324.	1.9341	0.71	X	X			
47.51	0.24	-3.	335.	1.9135	-0.08	X	X			
48.53	0.38	154.	339.	1.8759	3.74	X	X			
49.62	0.50	48.	328.	1.8372	1.16	X	X			
50.92	0.31	493.	279.	1.7933	11.99	X	X			
51.94	0.39	3.	289.	1.7604	0.08	X	X			
52.70	0.31	40.	303.	1.7370	0.97	X	X			
54.31	0.50	161.	289.	1.6891	3.93	X	X			
56.66	0.28	222.	276.	1.6245	5.40	X	X			
57.25	0.44	166.	276.	1.6091	4.05	X	X			
59.13	0.33	81.	276.	1.5624	1.97	X	X			
60.77	0.25	85.	296.	1.5240	2.06	X	X			
62.22	0.55	734.	328.	1.4920	17.87	X	X			
62.86	0.27	428.	346.	1.4784	10.43	X	X			
63.82	0.26	72.	369.	1.4583	1.76	X	X			
41.00	0.56	286.	0.	2.2013						X

50 PEAKS IDENTIFIED 49 CRYSTALLINE 1 AMORPHOUS
50 PEAKS LISTED

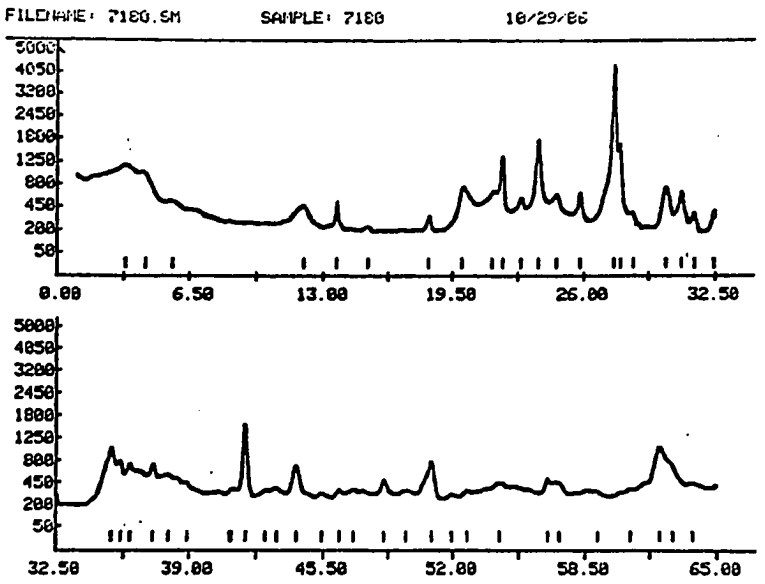

APD-3600 2ND DERIVATIVE PEAK ALGORITHM 10/29/86 21:12:11

RAW DATA FILE	: 71380.RD
SAMPLE ID	: 71380
RAW DATA FILE DATE	: 10/29/86
GENERATOR SETTINGS	: 45 KV 30 MA
STEP SIZE, CNT TIME	: 0.020 DEG 2.40 SEC
RANGE OF DATA	: 1.000 - 65.000 DEG
RANGE IN D	: 89.3397 - 1.4348 A
MAX PEAK CTS, CPS	: 4476. CTS 1866. CPS
SECF APPLIED	: NONE

2-THETA (DEG)	WIDTH (APPROX)	COUNTS PEAK	COUNTS BKGND	D (ANG)	I (NORM)	LINE TYPE A1	LINE TYPE A2	LINE TYPE BT	LINE TYPE AM	LINE TYPE OT
3.31	0.52	473.	666.	26.7325	10.62	X	X			
4.27	0.56	449.	557.	20.6688	10.04	X	X			
5.72	0.37	110.	437.	15.4637	2.46	X	X			
12.29	0.37	328.	225.	7.1987	7.32	X	X			
13.70	0.12	454.	207.	6.4635	10.14	X	X			
15.24	0.32	23.	196.	5.8136	0.51	X	X			
19.99	0.34	497.	199.	4.4427	11.11	X	X			
21.57	0.18	562.	202.	4.1287	12.55	X	X			
22.81	0.19	1136.	202.	4.0393	25.38	X	X			
22.89	0.27	361.	204.	3.8851	8.07	X	X			
23.74	0.24	1756.	204.	3.7486	39.23	X	X			
24.74	0.37	778.	207.	3.5979	17.39	X	X			
25.82	0.19	388.	210.	3.4511	8.67	X	X			
27.03	0.20	480.	210.	3.2987	10.72	X	X			
27.51	0.19	4476.	210.	3.2416	100.00	X	X			
27.82	0.14	1452.	213.	3.2073	32.43	X	X			
28.43	0.23	164.	213.	3.1393	3.66	X	X			
30.09	0.42	581.	216.	2.9698	12.98	X	X			
30.85	0.23	506.	216.	2.8979	11.31	X	X			
31.49	0.24	169.	216.	2.8403	3.78	X	X			
32.46	0.24	228.	216.	2.7586	5.09	X	X			
35.15	0.41	692.	219.	2.5530	15.45	X	X			
35.71	0.19	655.	222.	2.5139	14.64	X	X			
36.13	0.23	529.	222.	2.4860	11.82	X	X			
37.27	0.27	511.	222.	2.4122	11.41	X	X			
37.99	0.25	328.	225.	2.3688	7.32	X	X			
41.13	0.24	161.	228.	2.1944	3.60	X	X			
41.76	0.25	1376.	231.	2.1627	30.75	X	X			
42.74	0.31	137.	231.	2.1156	3.06	X	X			
44.18	0.32	493.	234.	2.0497	11.01	X	X			
46.33	0.19	112.	237.	1.9597	2.51	X	X			
46.99	0.35	135.	237.	1.9335	3.01	X	X			
47.59	0.23	128.	237.	1.9107	2.85	X	X			
48.60	0.36	243.	240.	1.8731	5.44	X	X			
50.93	0.44	548.	243.	1.7928	12.23	X	X			
52.78	0.44	85.	250.	1.7344	1.89	X	X			
54.29	0.43	190.	256.	1.6897	4.26	X	X			
56.72	0.27	240.	269.	1.6229	5.37	X	X			
57.45	0.27	139.	272.	1.6040	3.11	X	X			
58.61	0.33	90.	279.	1.5758	2.02	X	X			
59.24	0.27	59.	282.	1.5599	1.32	X	X			
60.24	0.22	46.	296.	1.5362	1.03	X	X			
62.27	0.50	756.	357.	1.4908	16.90	X	X			
63.89	0.19	266.	388.	1.4735	5.94	X	X			

44 PEAKS IDENTIFIED 44 CRYSTALLINE 0 AMORPHOUS
44 PEAKS LISTED

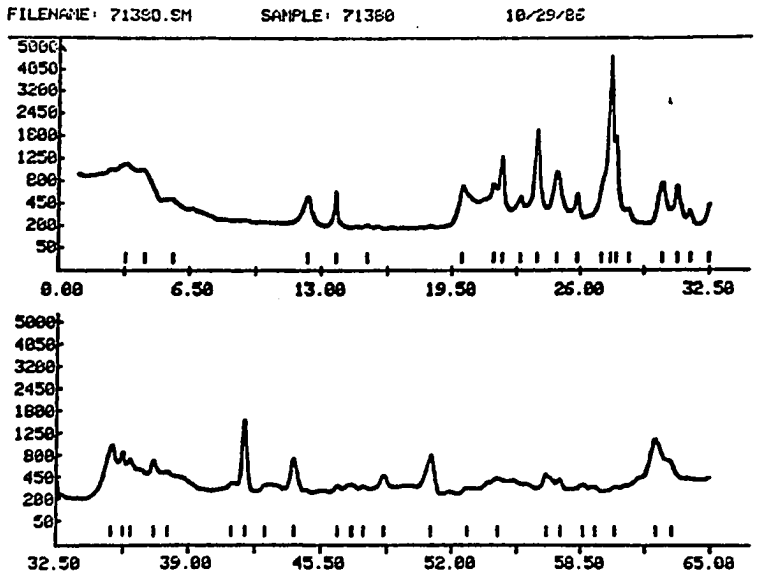

APD-3500 2ND DERIVATIVE PEAK ALGORITHM 9/30/86 1: 4: 0

RAW DATA FILE	: 74.RD
SAMPLE ID	: 74
RAW DATA FILE DATE	: 9/29/86
GENERATOR SETTINGS	: 45 KV 30 MA
STEP SIZE, CNT TIME	: 0.020 DEG 1.20 SEC
RANGE OF DATA	: 15.000 - 60.000 DEG
RANGE IN D	: 5.9061 - 1.5418 A
MAX PEAK CTS, CPS	: 607. CTS 673. CPS
SECF APPLIED	: NONE

2-THETA (DEG)	WIDTH (APPROX)	COUNTS PEAK	COUNTS BKGND	D (ANG)	I (NORM)	LINE TYPE A1	A2	BT	AM	OT
18.46	0.13	607.	42.	4.8075	100.00	x	x			
20.51	0.33	27.	42.	4.3291	3.33					
21.43	0.38	28.	42.	4.1454	3.48					
25.74	0.32	35.	37.	3.4617	4.32					
28.77	0.51	188.	35.	3.1025	22.26					
35.05	0.35	34.	29.	2.5597	4.17					
37.67	0.38	310.	28.	2.3878	38.41					
41.07	0.38	76.	27.	2.1974	9.38					
42.01	0.73	130.	27.	2.1507	16.11					
44.26	0.36	30.	26.	2.0464	3.73					
45.39	0.32	27.	26.	1.9990	3.33					
47.54	0.34	41.	29.	1.9125	5.08					
49.84	0.54	104.	32.	1.8298	12.90					
52.36	0.31	8.	40.	1.7473	0.97					
54.57	0.39	11.	55.	1.6815	1.33					
59.90	0.44	8.	112.	1.5443	1.04	x	x			

16 PEAKS IDENTIFIED 16 CRYSTALLINE 0 AMORPHOUS
16 PEAKS LISTED

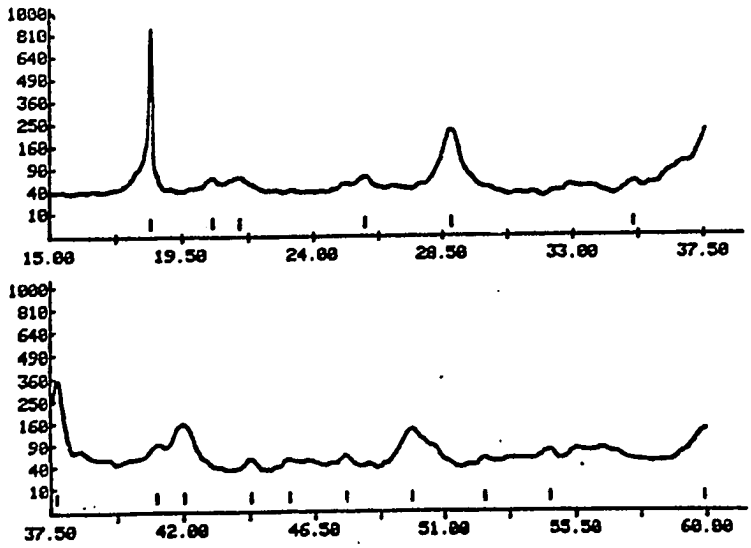

APPENDIX 3

DESCRIPTION OF KEY OUTCROPS

Number	Location	Description
N-1	Lingan Falls	biotite granite
N-2	Cliff north of Fongo Tongo market place	greyish trachyte with macroperthitic sanidine phenocrysts
N-3	Mamy Watta village	olivine basalt
N-6	same as N-2	
N-7	Mamy Watta falls	greyish trachyte
N-9	Road-cut 1.0km east of Mamy Watta village	ash-flow tuff with granitic and trachytic clasts
N-10	Melan bauxite deposit	greenish trachyte
N-11	same	olivine basalt
N-16	road-cut 1.0km north of Djeu on the road to Melan	greenish trachyte with macroperthitic sanidine phenocrysts. Contains dark organic enclaves
N-17	same as N-16	
N-21	about 2.5kms north of Fongo Tongo market place, along the base of a greyish trachyte cliff	ash-flow tuff with trachyte and black organic matter
N-22	1.0km north of N-21	highly compacted ash-flow tuff unit
N-32	road-cut 1.0km north of Foyangem	ash-flow tuff
N-33	300m south of N-32	biotite-granite with

		amphibolite enclaves
N-35	400m south of Mamy Watta falls along a creek	olivine basalt
N-37	1.5km from Tongo Tongo market place driving westward	outcrop of weathered greyish trachyte
N-38	same as N-22	
N-39	2.0km NW of Mamy Watta village, on the road to King Place	greenish trachyte
N-44	1.2km west of Fossong Tchuentcheu	ash-flow tuff
N-45	500m south of N-44	same as N-44
N-46	500m north of Mangha along a stream bed	same as N-45
N-47	road-cut 2.5km west of Fongo Tongo market place	outcrop of dark trachyte
N-48	Fondjoumetah village (not shown in map)	ash-flow tuff with clasts of organic matter. The ash-flow tuff overlies the biotite-granite
N-49a	Fongo Tongo Mountains	partially weathered dark trachyte sample (collected by a creek)
N-49b	Fongo Tongo Mountains	Fongo Tongo bauxite
N-50	same	same
N-51	same	same
N-52	Fongo Tongo Mountains	partially weathered dark trachyte sample (collected by a creek)
N-53	Fowondji'i village	Fongo Tongo bauxite
N-54	Atsanwoua village	same

N-55	about 4.0km north of the Fongo Tongo mountains	biotite-granite
N-57	1.0km north of Long	greenish trachyte
N-58	500m east of N-57	olivine basalt dike
N-59	southern Djeu deposit	Fongo Tongo bauxite
N-63	Melan deposit	Melan saprolite
N-73 N-74 N-75	south of Foyangem village	samples from a pit N-73 Fongo Tongo loose bauxitic block (surface) N-74 block of "cameroonite" (upper B horizon) N-75 bauxitic clay (lower B horizon)
N-76	1.5km north of Tzinza village	granulites and biotite granites
N-77	1.0km NW of N-76	greyish trachyte with columnar structure. At this outcrop, the greyish trachyte contains ash-flow tuffs xenoliths
N-78	Kuetetsa village	ash-flow tuff with brecciated texture
N-79	Djuttitsa village	greenish trachyte
N-80	Lap village, also known as Fiala	plateau basalt
N-81	1.0km north of Nza on the Nza-Levoni road	amphibolite
N-82	1.5km north of	folded granulites
N-83	Levoni village	contact between the ash-flow tuff (north)

		and the granites (south)
N-84	near Lefe	plateau basalt
N-85	2.5km south of Kuetetsa on the road to Fonou	the road follows the contact between the greenish trachyte which forms a cliff on the left- hand side and the ash-flow tuff on the right-hand side
N-86	close to N-85	olivine-basalt dike with columnar structure
N-89	3.0kms west of Kuetetsa on the road to Mena	greenish trachyte
N-94	less than 1.0km west of Djeu village	main Djeu bauxite deposit
N-95	about 2.0km south of "Le rocher Rond"	vesicular olivine basalt cone
N-98	Fosimobin, about 10.0kms west of "Le Rocher Rond"	ash-flow tuffs
N-100	south of Mve village	bauxitic weathering on olivine basalt
N-101	Ngoua village, southwest of Dschang	outcrop of volcano-sedimentary formations
N-102	same	same
N-103	Dschang city quarry	gneisses and amphibolites
N-104	Fongo Tongo Mountains, on top of the 1695m-high summit	Fongo Tongo bauxite deposit
N-105	150m west of N-104	same
N-106	Fongo Tongo Mountains	outcrop of the dark trachyte

N-107	Fotendza village	outcrop of Fongo Tongo bauxite
N-108	same	same
N-111	west of the "Rocher Rond", near the southern edge of the caldera	outcrop of dark trachyte overlain by loose rounded pebbles of greenish trachyte saprolite
N-112	road-cut south of the "Rocher Rond"	loose blocks of greenish trachyte saprolite
N-113	Djuttitsa quarry	Djuttitsa bauxite deposit
N-114	"Le Rocher Rond"	greyish trachyte

VITA

Jean Blaise Nyobe, the son of Jacques Nyobe Mandeng and Catherine Mezene Endomo, was born on July 25, 1948 in Abong-Mbang, Republic of Cameroon. He obtained his undergraduate education at the University of Yaounde in Cameroon during the period September, 1969 to June, 1972 and graduated with honors with a B.S. in Geological Sciences.

He continued his education in the Department of Geological Sciences at Lehigh University in the Spring of 1973 as an M. S. candidate under the guidance of Professor. J. D. Ryan. He held an African-American Institute Fellowship during his Master's program.

He obtained an M. S. degree in 1975 and passed the Ph. D. qualifying examination in June, 1975. He went back to Cameroon the same year and began employment with the Cameroon Institute for Geological and Mining Research (IRGM) in December, 1975. In 1980, he was appointed Chief of the Center for Geological and Mining Research (CRGM) in Garoua, Cameroon. He has largely contributed in getting that newly created Center started, and in designing the ongoing geologic mapping of the Republic of Cameroon at the scale of 1:50,000, a first order priority research program in IRGM.

He resumed his graduate studies at Lehigh University in the fall of 1985 as a doctoral candidate under the supervision of Professor Charles B. Sclar. Mr. Nyobe is married. He and his wife Florence have three children, Annick Marie, Albert Blaise and Jacques Eithel.

PLATE 1

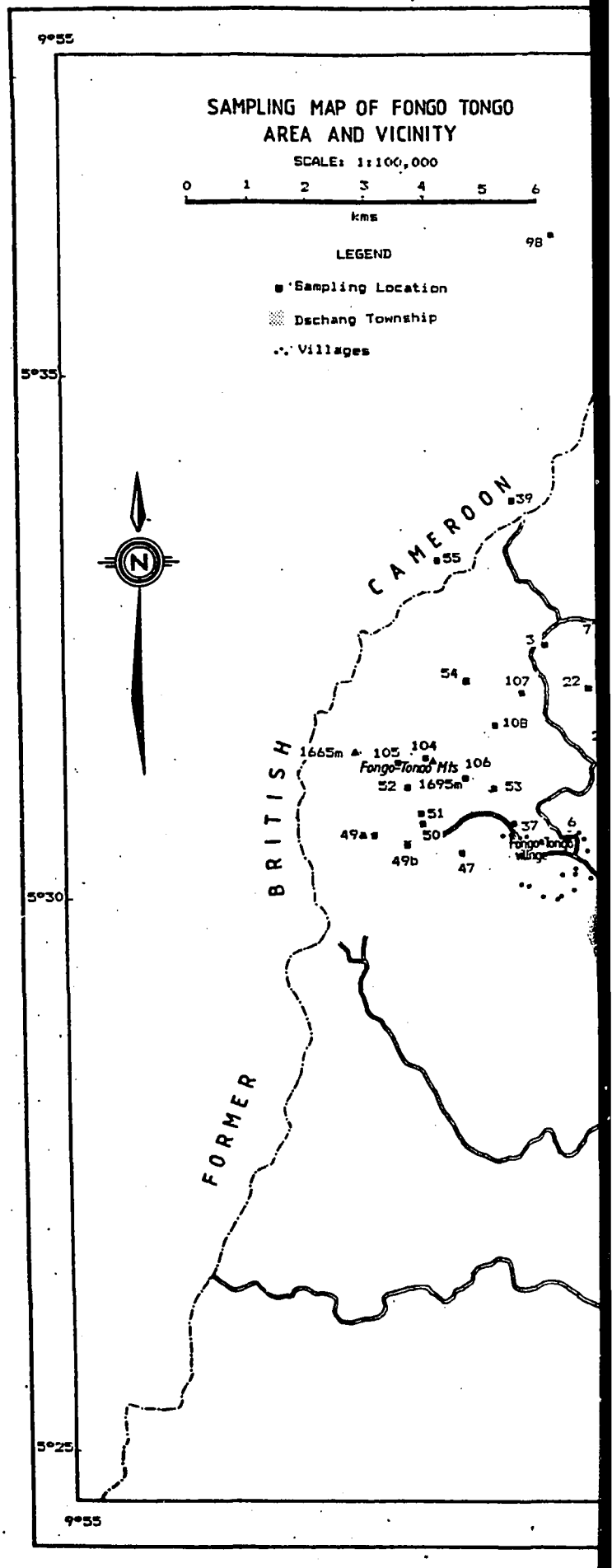

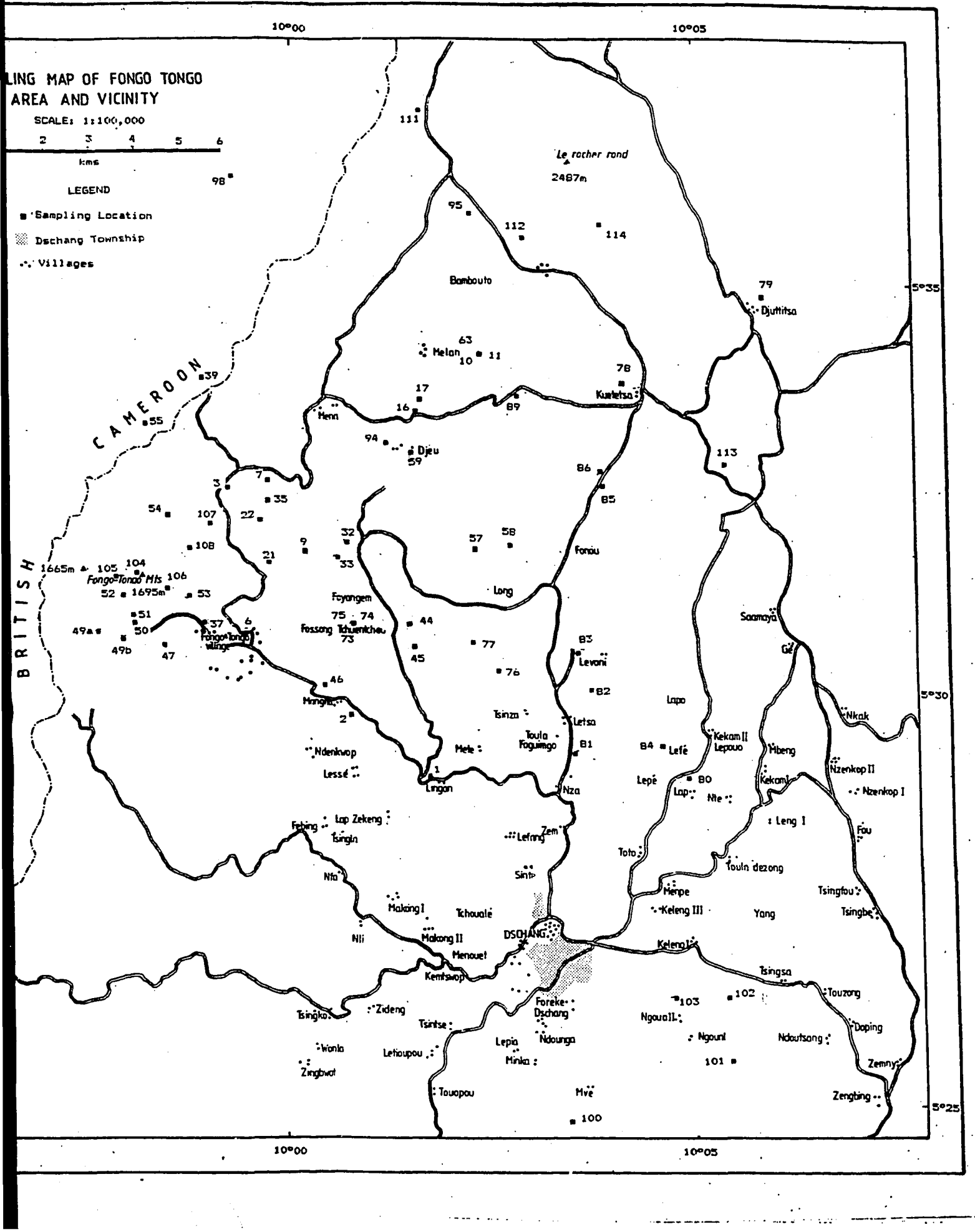
LING MAP OF FONGO TONGO
AREA AND VICINITY
SCALE: 1:100,000
2 3 4 5 6
kms
LEGEND
■ Sampling Location
▨ Dschang Township
∴ Villages
10°00
10°05
5°35
5°30
5°25
BRITISH CAMEROON
Le rocher rond
2487m
Bambouto
Melan
Djuttitsa
Kuetetsa
Menn
Djeu
Fonau
Long
Foyangem
Fossong Tchuentcheu
1665m
1695m
Fongo-Tongo Mts
Fongo-Tongo village
Mangia
Ndenkwop
Lessé
Lingan
Mele
Tsinzo
Toula Foguimgo
Letsa
Levoni
Lapo
Lefé
Kekam II Lepouo
Saamaya
Gé
Nkak
Mbeng
Nzenkop II
Nzenkop I
Kekam I
Lepé
Lap
Nte
Nza
Lap Zekeng
Febing
Tsingin
Lefang
Zem
Sinto
Toto
Leng I
Touln dezong
Fou
Nfo
Makang I
Tchouale
Menpe
Keleng III
Yang
Tsingfou
Tsingbe
Nli
Makong II
DSCHANG
Menouet
Keleng I
Kemtswop
Tsingsa
Touzong
Tsingko
Zideng
Foreke Dschang
Ngoual I
Ngoual
Ndoutsong
Doping
Tsintse
Wonla
Letioupou
Lepia
Minka
Ndounga
Zemny
Zingbwat
Touopou
Mvé
Zengbing
1 2 3 6 7 9 10 11 16 17 21 22 32 33 35 37 39 44 45 46 47 49a 49b 50 51 52 53 54 55 57 58 59 63 73 74 75 76 77 78 79 80 81 82 83 84 85 86 89 94 95 98 100 101 102 103 104 105 106 107 108 111 112 113 114

PLATE 2

GEOLOGIC MAP OF THE SOUTHERN FLANK OF THE BAMBOUTO MOUNTAINS

J. B. Nyobe, 1987

SCALE: 1:100,000

0 1 2 3 4 5 6

kms

LEGEND

- Bauxites
- Basalts
- Greyish trachyte
- Dark trachyte
- Greenish trachyte
- Ash-Flow tuffs

Tertiary volcanics

- Granites, amphibolites & granulites

Panafrican basement units

- Faults
- Dips
- Geologic contours
- C Basaltic cones
- •S Drilling sites
- ▲ Heights
- Lineations